UNIVERSITÀ
DI PAVIA

Department of Electrical, Computer and Biomedical
Engineering

Design, Modeling and Diagnostics of Closed-Loop Inverter-Fed Electrical Machines

a dissertation submitted for
the degree of doctor of sciences
by **Lorenzo Mantione**

supervised by
Prof. Lucia Frosini

reviewed by
Prof. Joan Pons-Llinares
Dr. Panagiotis Panagiotou

XXXVI Cycle - A.Y. 2022/2023

Abstract

This thesis aims to present the main research activities carried on by the author during his doctoral studies. Two main topics have been studied during this period: the design and modeling of synchronous brushless machines and the diagnostics of closed-loop controlled induction motors.

The design of Interior Permanent Magnet (IPM) machines, nowadays, has a crucial role in developing the whole electric drive. After reviewing the existing body of literature in this field of research, two design procedures will be presented in this thesis. As will be explained in the first part of this thesis, the design of a machine is strongly influenced by the requirements and the application. An important focus will be given to the behavior of the machine in the field-weakening region, implementing models that also take into account the thermal and mechanical limits of the machine under certain conditions. More in detail, an analysis of the reduction of the torque ripple by adopting specific skewing techniques will be provided. Moreover, a detailed study of the costs of different materials for the manufacturing of this kind of machine will be given.

Induction motors represent the most widely used rotating electrical machine typology. In the second part of this thesis, based on a literature review of the topic, a method for the detection of the broken rotor bar fault while the motor is operating under closed-loop conditions based on the Motor Current Signature Analysis (MCSA) will be proposed. The key point behind the detection of fault under these operating conditions is the problem that arises from the non-constant frequency of the fundamental harmonic even when the start-up transient is already depleted. Moreover, the control loop operation introduces a high noise level in the signals, which increases the difficulties in the identification of the

harmonics. Several signal analysis techniques will be presented, together with their theoretical background. Signals from the phase current of healthy and faulty induction motors operating in different control conditions will be analyzed using traditional methods such as the fast Fourier transform and the short-time Fourier transform. The same signals are analyzed through the Dragon Transform and the Short-Time Min-Norm. These methods ensure high resolution in frequency and time, allowing the detection of trajectories of the harmonics in all the analyzed conditions.

Contents

List of Abbreviations

BRB/BB	Broken Rotor Bar/Broken Bar
CL	Closed Loop
CTFT	Continuous Time Fourier Transform
DFT	Discrete Fourier Transform
DRFOC	Direct Rotor Field Oriented Control
DT	Dragon Transform
DTC	Direct Torque Control
DWT	Discrete Wavelet Transform
EHD	Enlarged Heisenberg Box
EMD	Empirical Mode Decomposition
EMF	Electromotive Force
FE	Finite Element
FEM/FEA	Finite Element Method/Analysis
FFT	Fast Fourier Transform
FM	Frequency Modulated
FOC	Field Oriented Control
FRF	Frequency Response Function
FT	Fourier Transform

HB	Heisenberg Box
ICE	Internal Combustion Engine
IIR	Infinite Impulse Response
IM	Induction Motor
IMC	Internal Model Control
IPM/IPMSM	Interior Permanent Magnet (Synchronous Motor)
IRFOC-FC	Indirect Field Oriented Control with Flux Control loop
LSH	Lower Sideband Harmonic
MCSA	Motor Current Signature Analysis
MMF	Magnetomotive Force
MN	Minimum-Normalization, Min-Norm
MTPA	Maximum Torque Per Ampere
MTPV	Maximum Torque Per Volt
MUSIC	Multiple Signal Classification
OL	Open Loop
PD	Partial Discharge
PID	Proportional, Integral, Derivative controller
PM	Permanent Magnet
PMSM	Permanent Magnet Synchronous Machine
RMS	Root Mean Square value
rpm	Revolutions per Minute
RSH	Rotor Slot Harmonics
RUL	Remaining Useful Life
SFSA	Stray Flux Signature Analysis

SPM	Surface Permanent Magnet
SRM	Switched Reluctance Machine
ST-MUSIC	Short-Time Multiple Signal Classification
STFT	Short-Time Fourier Transform
STMN	Short-Time Minimum Normalization
SynRM	Synchronous Reluctance Machine
TFD	Time-Frequency Distribution
UPS	Uninterruptable Power Supply
USH	Upper Sideband Harmonic
VMM	Vienna Monitoring Method
VSD	Variable Frequency Drive
WT	Wavelet Transform
WVD	Wigner-Ville Distribution
ZSC	Zero Sequence Current

List of Symbols

Chapter 1

μ_R	Relative permeability
(a, b, c)	Stator reference frame
θ_e	Rotor electrical angle
θ_R	Rotor mechanical angle
p	Number of pole pairs
v_a, v_b, v_c	Stator phase voltages
i_a, i_b, i_c	Stator phase currents
$\lambda_a, \lambda_b, \lambda_c$	Instantaneous phase flux linkages
R	Stator phase resistance
T_e	Torque produced by the motor
T_r	Load torque of the system
$\lambda_{a,i}, \lambda_{b,i}, \lambda_{c,i}$	Flux linkages generated by the stator currents
$\lambda_{m,a}, \lambda_{m,b}, \lambda_{m,c}$	Flux linkages generated by the permanent magnets
λ_M	Peak value of the flux linkages generated by the PMs
L_a, L_b, L_c	Stator phase inductances
$M_{a,b}, M_{b,c}, M_{c,a}$	Phase mutual inductances
$L_{\sigma s}$	Stator leakage inductance

M_S	Average mutual inductance coefficient
L_{ms0}	Constant magnetization inductance
L_m	Anisotropic magnetization inductance
ω_R	Rotor mechanical angular speed, expressed in $\left[\frac{rad}{s}\right]$
P_e	Motor electrical power
P_m	Shaft output power
(α, β)	Two-phase fixed reference frame
$(d, q, 0)$	Two-phase rotating reference frame
v_d, v_q	Direct and quadrature axis voltages
i_d, i_q	Direct and quadrature axis currents
λ_d, λ_q	Direct and quadrature axis flux linkages
L_d, L_q	Direct and quadrature axis inductances
λ_{PM}	Permanent magnet flux linkage in the $d, q, 0$ reference frame
n_R	Rotor mechanical speed, expressed in $[rpm]$
f_s	Fundamental supply frequency
ω_n	Motor rated speed
T_n	Motor rated torque

Chapters 2, 3 & 4

J_s	Saturation magnetic polarization
μ_r	Relative permeability
f_s	Fundamental supply frequency
k_h	Hysteresis losses coefficient
α_h	Exponent of the flux density for the hysteresis losses

β_h	Exponent of the supply frequency for the hysteresis losses
k_c	Eddy current losses coefficient
α_c	Exponent of the flux density and the frequency for the eddy current losses
k_e	Excess losses coefficient
α_e	Exponent of the flux density and the frequency for the excess losses
B_{pk}	Flux density peak value
H_c **(or** H_{cJ}**)**	Coercitive field of a PM material
B_r	Remaining flux density of a PM material
$(BH)_{max}$	Maximum energy product of hard magnetic materials
Ψ	Control angle for IPMSMs
E	Electromotive force
T_n	Motor rated torque
η	Machine efficiency
$\cos\phi$	Power factor
V_{Lmax}	Maximum line-to-line RMS voltage
J_{max}	Maximum current density

Chapter 5

F_s	Sampling frequency
BW_{max}	Maximum analyzable bandwidth
f_{res}	Frequency resolution
N	Number of acquired samples
T_{acq}	Time duration of acquisitions

f_s	Fundamental supply frequency
f_r	Rotational frequency of the rotor
s	Motor slip
p	Number of pole pairs
R	Number of rotor slots
k	Integer ($k = 1, 2, 3, \dots$)
n	Harmonic order ($n = 1, 3, 5, \dots$)
n_d	Eccentricity order ($n_d = 1$: dynamic eccentricity, $n_d = 0$: static eccentricity)
N	Number of balls of the bearing
D_b	Diameter of a bearing ball
D_c	Diameter of a bearing ball pitch
β	Contact angle of a bearing ball
f_{ecc}	Characteristic frequency for the eccentricity harmonic signature
f_{sc}	Characteristic frequency for the short circuit harmonic signature
f_{bb} **(or** f_{brb}**)**	Characteristic frequency for the broken rotor bar harmonic signature
$\frac{z}{p}$	Integer ($\frac{z}{p} = 1, 3, 5, \dots$)
i_d	Component of the current along the direct axis in the $(d, q, 0)$ reference frame

Chapter 6

f	Variable in the frequency domain
t	Variable in the time domain
$t - f$	Time - frequency

k	Variable in the discrete time domain
$X(f)$	Representation of the signal in the frequency domain
$x(t)$	Representation of the signal in the frequency domain
ω	Angular frequency corresponding to f
j	Imaginary unit
$x(k)$	Discretization of the signal in the time domain $x(t)$
$X[k]$	Discrete Fourier transform of the signal $x(k)$
F_s	Sampling frequency
N	Number of samples
T	Acquisition time
$S(t;f)$	STFT of the signal in time $g(t)$
τ	Defined time instant
$w(\tau)$	Time window defined in τ
$g[n]$	Discretization of the signal in time domain $g(t)$
$w[n]$	Discretization of the time window $w(t)$
$S[n;f]$	Discrete STFT of the signal $g[n]$
Δf	Frequency resolution
Δt	Time resolution
C_σ	Constant to define a Gabor function
σ	Deviation parameter of Dragon and Gabor Atoms
t_c	Time coordinate of the center of a Gabor Atom
f_c	Modulation Frequency of a Gabor function
$\phi(t)$	Gabor and Dragon Atoms
σ_t	Time side of the Heisenberg Box of the Gabor function

σ_f	Frequency side of the Heisenberg Box of the Gabor function
$\theta(t)$	Modulating angle in the complex exponential of the Gabor function to define a Dragon Atom
$s_p(t)$	$p-th$ harmonic component of the spectrum of a signal $s(t)$
$v(\omega_p)$	Uniformly sampled complex sinusoid array
ω_p	Angular frequency of a uniformly sampled complex sinusoid array
$\eta(t)$	Noise from the measurement
f_f	Fault-related frequencies
$\mathbf{A}$	$N \times M$ Vandermonde matrix
$\mathbf{S_x}$	Decomposition of the signal $s(t)$ in the frequency domain
$\mathbf{V}(\omega)$	Representation of $v(\omega_p)$ in the frequency domain
σ_w^2	Spectral covariance
λ_i	$i-th$ eigenvalue of $\mathbf{S_x}$
$\mathbf{\Phi_i}$	$i-th$ eigenvector of $\mathbf{S_x}$
$\mathbf{U_s}$	Signal subspace of eigendecomposition-based spectral estimator
$\mathbf{U_n}$	Noise subspace of eigendecomposition-based spectral estimator
$\mathbf{d}$	Noise vector of the MN spectral estimator technique, linear combination of the $N-D$ vectors in $\mathbf{U_n}$
$\hat{Q}_{MN}$	Null spectra of the MN
$S_{xx}(t,\omega)$	STMN of a signal $s(t)$

Chapter 7

I_{alt}	Stator current of the DC alternator
V_{alt}	Voltage of the DC alternator

ω	Rotor speed of the DC alternator
P_{loss}	Losses of the DC alternator
P_R	Power dissipated by the DC alternator
T_l **(or** T_{load}**)**	Load torque
R	Bank of resistors
$R_{PID}(s)$	Transfer function of the PID controller
K_P	Proportional gain of the PID controller
T_i	Integration time of the PID controller
T_d	Derivative time of the PID controller
T	Time constant of the response to a variation in the goal frequency for the IMC tuning rule
τ	Time delay for the IMC tuning rule
T_f	Arbitrary parameter for the IMC tuning rule
T_s	Sampling time
F_s	Sampling frequency

Chapter 8

f_s	Fundamental supply frequency
s	Motor slip
k	Integer ($k = 1, 2, 3, \dots$)
σ_f	Frequency resolution of the FFT
f_{bb} **(or** f_{brb}**)**	Characteristic frequency for the broken rotor bar harmonic signature
T	Load torque
I_{rms}	RMS value of the current

f_{3bb}	Characteristic frequency for the third component of the broken rotor bar harmonic signature
$t - f$	Time - frequency
F_s	Sampling frequency
K	Integer ($K = \frac{z}{p} = 1, 3, 5, \dots$)

List of Figures

List of Tables

Introduction

In this thesis, the most relevant scientific works carried out by the candidate during his doctoral studies are reported. The thesis is divided into two parts:

- Part I, aimed at the design of Interior Permanent Magnet Synchronous Machines (IPMSMs);
- Part II, focused on techniques to detect rotor faults in closed-loop inverter-fed Induction Motors (IMs).

Both Part I and Part II are divided into four chapters. In chapters 1 and 5 a general background and an accurate literature review will be reported respectively on the design of IPMSMs and the diagnostics of IMs faults. After the literature review, Part I is organized as follows:

- in chapter 2 the analysis will be focused on general aspects of the IPMSMs design and, in particular, on the approach to the choice of the number of poles, the topology of rotor poles and the analysis of the materials;
- in chapters 3 and 4 two design procedures will be proposed, highlighting the differences between them and providing a solution for the high values of torque ripple found in the results of the simulations.

The other chapters of Part II, instead, are organized as follows:

- in chapter 6 the main signal analysis techniques studied for this work will be introduced, focusing on the behavior and the mathematical equations behind each analyzed method;

- in chapter 7 the experimental setup of the laboratory will be presented, with particular attention on the tuning of the controller and on the problems related to the speed signal;
- in chapter 8 the results of the signal analysis will be reported and discussed, focusing on different harmonics and trajectories related to the rotor fault of IMs.

Finally, in chapter 9 general conclusions will be drawn for the two parts of this thesis, followed by a discussion pertaining to future direction in terms of potential future work.

Part I

Design of Interior Permanent Magnet Machines

Chapter 1

Theoretical background in IPM machine design

The increasing need for energy-efficient technologies in the last decades, together with the advances in the field of power electronics and control of electric drives, have triggered notable technological advancements and novelties in electric machines. Among these, synchronous motors have emerged as a promising technology in energy conversion, offering nowadays ease in the control strategy and very high efficiency, power density and torque density as well as power factor. In fact, in the past, these motors were considered motors for constant-speed applications, due to the fixed supply frequency given by the grid reflected in a fixed synchronous speed of the rotor. In this way, their use was mainly limited to specific applications such as the power factor correction in the grids using wounded rotor machines. For such application, speed or position control is not necessary [1]. Moreover, the synchronous motor was suitable for low-speed applications (i.e. compressors), thanks to its high efficiency in a wide speed range [2].

Synchronous machines spread into a broad family tree that can be divided into different types. This classification is reported in Fig. 1.1. These kinds of machines differ in the way the rotor field is generated. In separated excited machines the rotor iron core is wounded. To create the field, it is a common practice to manufacture the rotor winding from copper and supply it with DC current by the use of brushes.

In reluctance machines, the rotor core is made with a strong saliency, and no magnets or windings are used. This family can be further divided into switched reluctance machines

(SRM) and synchronous reluctance machines (SynRM). The first category has salient poles both on the rotor and on the stator, which also has concentrated windings on the poles. By supplying two windings on opposite stator poles, the rotor is aligned to the minimum reluctance position. Alternating the time in which every pair of poles is supplied, the torque is generated as the output of the rotor shaft. In synchronous reluctance machines, on the other hand, the stator has distributed winding like induction machines, and the saliency is present only in the rotor. In this family of motors, the difference between direct axis inductance and quadrature axis inductance of the rotor core allows the generation of the so-called reluctance torque. In this part of this thesis, the study will focus on the design of interior permanent magnet synchronous machines, whose rotor is made by inserting permanent magnets in the laminated core to produce the rotor magnetic field. The goal of this study is to achieve improved performance throughout the speed range of the machine, keeping low the torque ripple and the total cost of manufacture.

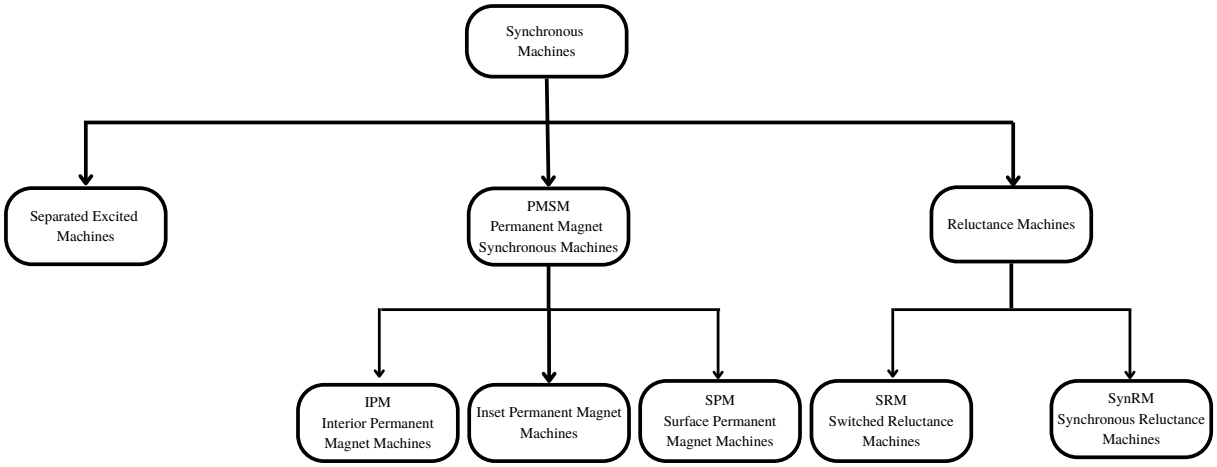

Figure 1.1: Types of synchronous machines.

1.1 Permanent Magnet Synchronous Motors

In many industrial sectors, and in the field of electric and hybrid vehicles, permanent magnet synchronous motors (PMSMs) are nowadays considered the best choice among electrical motors, due to their superiority in terms of torque density, high efficiency, wide speed range, dynamic performance and reliability, despite of the usage of costly rare-earth

materials and the presence of torque ripple. In the field of transportation or electric vehicles, especially for light-duty electric and hybrid vehicles [3], many examples of PMSM motors are already present in the market, both as a single propulsion system and combined with an internal combustion engine (ICE). For medium- and heavy-duty vehicles instead, induction motors are still considered the best choice.

A first example can be made by citing the hybrid 2005 Honda Accord, which was equipped with a 12 kW Surface Permanent Magnet (SPM) motor (whose rotor is shown in Fig. 1.2) with concentrated stator winding and a maximum speed of 6500 rpm. In this case, the small PMSM assists the main ICE which has a maximum power of around 180 kW [4].

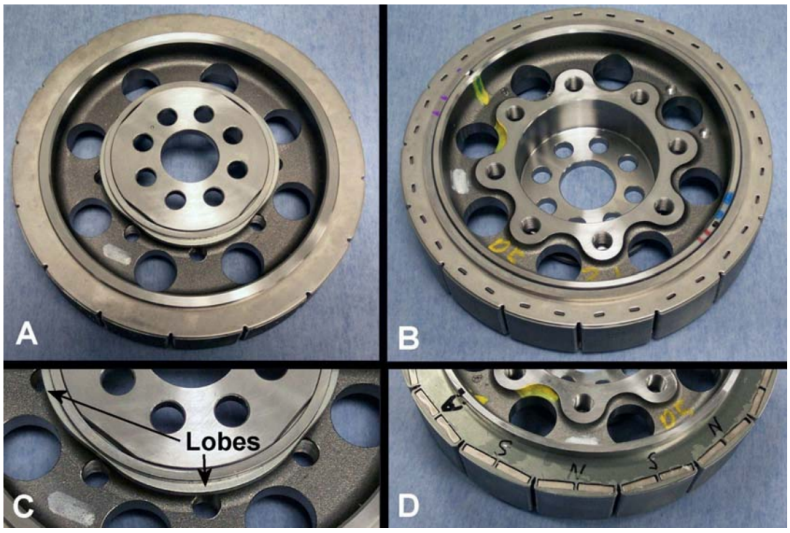

Figure 1.2: Details of the rotor from the 2005 Honda Accord [4].

On the Lexus LS 600H a hybrid system is mounted. This combines an ICE and a generator with an Interior Permanent Magnet (IPM) motor that can produce up to 165 kW of mechanical power at 5250 rpm of rotor speed, while the maximum speed is 10200 rpm. Magnets inside the rotor are arranged in 8 poles with a triangular (or "delta") configuration, as shown in Fig. 1.3 [5, 6].

Fig. 1.3 also shows the rotor lamination of the motor of the Toyota Camry (2008). This motor has a peak speed of 14 krpm, with a rated power of 105 kW reached at 4500 rpm. As for the motor of the Lexus, Camry has an IPM machine with magnets divided into 8 poles. In this case, each pole has two permanent magnets with a single "V-shape" configuration [7]. Both SPM and inset PM machines have magnets on the surface of the rotor. In SPM motors, arc-shaped permanent magnets are mounted on the surface of its

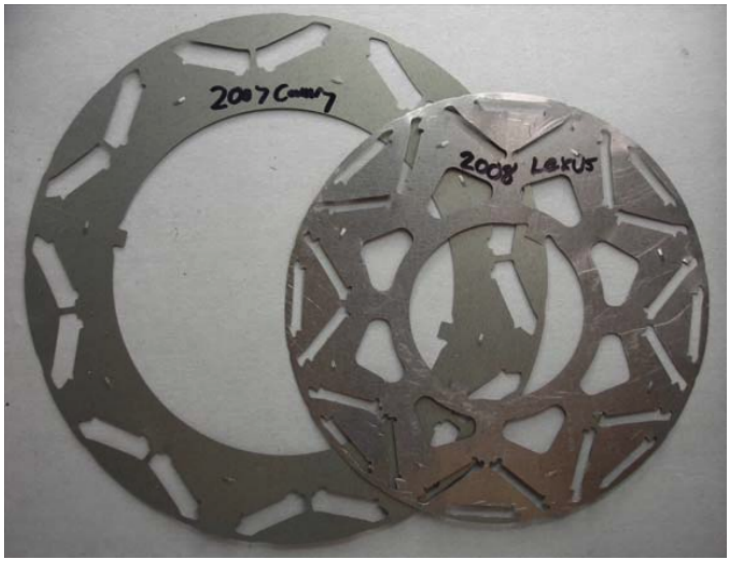

Figure 1.3: Comparison of motor rotor laminations, Toyota Camry (left) vs. Lexus LS 600H (right) [5].

cylindrical rotor. Since this machine is completely without saliency (isotropic structure), the torque produced during operation is only dependent on the field of the permanent magnets on the rotor surface. This is due to the relative permeability of the magnets which is almost equal to the one of the air ($\mu_R = 1.04 - 1.05$). For inset PM motors, instead, magnets are still visible on the surface of the rotor but inserted inside a slot in the lamination, that is no more perfectly cylindrical. For this reason, the rotor has a small magnetic anisotropy, and the saliency is slightly higher. In IPM motors, magnets are completely buried inside the lamination, and the resulting air gap is usually thinner than the one of the machines described previously. This structure offers higher resistance to mechanical stress compared to the rotors of SPM and inset PM machines, which makes the IPM motor more suitable for high-speed applications [8]. Furthermore, the strong anisotropic structure of the rotor, due to the magnets deep in the lamination, allows for a greater field-weakening region during the operation control and the possibility of using sensorless control strategies which is easier to implement if compared to the ones of SPM motors [9]. Finally, the shape of the buried magnets can be improved to optimize the saliency ratio of the machine or the distribution of the flux inside the rotor lamination [10, 11].

Thanks to these properties, besides the already cited automotive sector, IPM motors are

more and more employed in many sectors, such as electrohydrostatic actuators (EHA) for aerospace applications as described in [12, 13], nautical [14–16], railway transportation and trains [17, 18] but also for process automation [19, 20], drones [21] and biomedical application, as proposed in [22].

1.2 PMSM working principles

1.2.1 Motor equations in the *a,b,c* reference frame

In this section, a brief description of the conventional mathematical model of the PMSM will be presented. The analysis can be made under the following assumption [23]:

- magnetomotive force has a sinusoidal distribution at the air gap;
- linear magnetic behavior of the machine for the analysis (no saturation);
- no hysteresis and eddy currents in the iron;
- no cross-coupling effects;
- no slot harmonics effects;
- no temperature effects on the machine.

The general model of the machine can be represented from the three voltage equations and the general torque equation as in (1.1):

$$\begin{cases} v_a(t) = Ri_a(t) + \frac{d\lambda_a(t,\theta_e)}{dt} \\ v_b(t) = Ri_b(t) + \frac{d\lambda_b(t,\theta_e)}{dt} \\ v_c(t) = Ri_c(t) + \frac{d\lambda_c(t,\theta_e)}{dt} \\ J\frac{d\omega_R}{dt} = T_e - T_r \end{cases} \tag{1.1}$$

where:

- θ_e is the rotor electrical angle $\theta_e = p\theta_R$;
  - p is the number of pole pairs;

  - θ_R is the rotor mechanical angle;

- v_a, v_b, v_c are the phase voltages;
- i_a, i_b, i_c are the phase currents;
- $\lambda_a, \lambda_b, \lambda_c$ are the instantaneous phase flux linkages;
- R is the stator phase resistance, equal for all the phases if the system is balanced;
- J is the moment of inertia of the rotor $[kg \cdot m^2]$;
- T_e and T_r are the produced torque of the motor and the load torque of the system, respectively.

The values of the flux linkage of each phase can be rewritten as follows:

$$\begin{cases} \lambda_a(t) = \lambda_{a,i}(t) + \lambda_{m,a}(t) \\ \lambda_b(t) = \lambda_{b,i}(t) + \lambda_{m,b}(t) \\ \lambda_c(t) = \lambda_{c,i}(t) + \lambda_{m,c}(t) \end{cases} \tag{1.2}$$

where $\lambda_{a,i}$, $\lambda_{b,i}$, $\lambda_{c,i}$ are the flux linkages generated from the stator currents of phase a, b, and c, respectively, and $\lambda_{m,a}$, $\lambda_{m,b}$, $\lambda_{m,c}$ are the flux linkages produced by the permanent magnets on the rotor. By the initial assumptions, the flux linkage $\lambda_{m,i}$ from the permanent magnets can be assumed as sinusoidal, resulting in:

$$\begin{cases} \lambda_{m,a}(t) = \lambda_M \cos\theta_e \\ \lambda_{m,b}(t) = \lambda_M \cos\left(\theta_e - \frac{2}{3}\pi\right) \\ \lambda_{m,c}(t) = \lambda_M \cos\left(\theta_e - \frac{4}{3}\pi\right) \end{cases} \tag{1.3}$$

where λ_M represents the peak value of the flux linkage from the permanent magnets. By taking into account the different values of stator inductance, the flux linkage related to the stator current can be divided in:

$$\begin{cases} \lambda_{a,i}(t) = L_a i_a + M_{a,b} i_b + M_{a,c} i_c \\ \lambda_{b,i}(t) = L_b i_b + M_{a,b} i_a + M_{b,c} i_c \\ \lambda_{c,i}(t) = L_c i_c + M_{a,c} i_a + M_{b,c} i_b \end{cases} \tag{1.4}$$

where L_a, L_b, L_c are the self inductances of the stator phases and $M_{a,b}, M_{b,c}, M_{a,c}$ are the mutual inductances between the phases. The instantaneous values of self inductances and mutual inductances are dependent on the position of the rotor, and therefore on the value of θ_e. Moreover, if the three windings are symmetrical: $L_a = L_b = L_c$; $M_{a,b} = M_{b,a}$; $M_{b,c} = M_{c,b}$; $M_{a,c} = M_{c,a}$, resulting in the following equations:

$$\begin{cases} L_a = L_{\sigma s} + L_{ms0} + L_m \cos 2\theta_e \\ L_b = L_{\sigma s} + L_{ms0} + L_m \cos\left(2\theta_e - \frac{2}{3}\pi\right) \\ L_c = L_{\sigma s} + L_{ms0} + L_m \cos\left(2\theta_e - \frac{4}{3}\pi\right) \\ M_{a,b} = M_{b,a} = -M_S + L_m \cos\left(2\theta_e - \frac{2}{3}\pi\right) \\ M_{b,c} = M_{c,b} = -M_S + L_m \cos\left(2\theta_e\right) \\ M_{c,a} = M_{a,c} = -M_S + L_m \cos\left(2\theta_e - \frac{4}{3}\pi\right) \end{cases} \tag{1.5}$$

where $L_{\sigma s}$ is constant and represents the leakage inductance of the stator winding flux linkage in air, M_S is the average mutual inductance coefficient and L_{ms0} and L_m represents, respectively, the two components of the magnetizing inductance (constant magnetization inductance and anisotropic magnetization inductance). The equations of the voltages in the system 1.1, together with the ones of the flux linkage in 1.2 can be rewritten in compact matrix form as the following stator equation:

$$[v] = [R][i] + \omega_R \frac{d[L]}{d\theta_R}[i] + [L]\frac{d[i]}{dt} + \omega_R \frac{d[\lambda]}{d\theta_R} \tag{1.6}$$

In equation 1.6, the first term $[R][i]$ represents the voltage drops in the stator phases, $[L]\frac{d[i]}{dt}$ represents the self-induced and mutual-induced back electromotive force (back-EMF) in the stator winding, $\omega_R \frac{d[L]}{d\theta_R}[i]$ represents the rotational back-EMF due to the anisotropy of the machine and $\omega_R \frac{d[\lambda]}{d\theta_R}$ represent the rotational back-EMF due to the flux produced by the permanent magnets. Multiplying this equation by the transposed matrix of the currents $[i]^T$, the expression of the electrical power of the motor is obtained:

$$P_e = [v][i]^T = [i]^T[R][i] + \omega_R[i]^T \frac{d[L]}{d\theta_R}[i] + [i]^T[L]\frac{d[i]}{dt} + \omega_R[i]^T \frac{d[\lambda]}{d\theta_R} \tag{1.7}$$

where $[i]^T[R][i]$ represents the Joule losses in the stator winding, $[i]^T[L]\frac{d[i]}{dt}$ represents the variation of magnetic energy and $\omega_R[i]^T \frac{d[L]}{d\theta_R}[i] + \omega_R[i]^T \frac{d[\lambda]}{d\theta_R}$ represents the rotating

mechanical power P_m at the output the shaft of the motor. Finally, dividing the expression of the mechanical power by the rotational speed ω_R of the rotor it is possible to write the expression of the torque for a brushless machine, as:

$$T = \frac{P_m}{\omega_R} = [i]^T \frac{d[\lambda]}{d\theta_R} + [i]^T \frac{d[L]}{d\theta_R}[i] \tag{1.8}$$

Equation 1.8 shows that the expression of the mechanical torque has two different components: the first term, $[i]^T \frac{d[\lambda]}{d\theta_r}$, represents the torque produced by the interaction of the flux generated by the permanent magnets with the currents in the three stator windings, while the other term, $[i]^T \frac{d[L]}{d\theta_R}[i]$, represents the reluctance torque of the machine, that is equal to zero for SPM motors that have a perfect isotropic rotor structure.

1.2.2 Motor equations in the *d,q,0* reference frame

The mathematical model outlined in subsection 1.2.1 explains how the motor behaves in the stator reference frame. It consists of three differential equations with variable coefficients. To make it easier to understand and control the motor, a simplified model is needed. Specifically, we should replace the changing coefficients with fixed parameters. This simplification will make it easier to analyze and control the motor's behavior. The transition to a simpler reference system is generally done by applying the Park transformation to the system, which allows to switch from a fixed three-phase reference frame to a rotating reference system composed by two phases [24]. The new reference system is rotating at the rotor mechanical speed ω_R. The biggest advantage of the new reference frame, *d, q, 0* is the reduction of the number of equations in the system, together with the independence of the coefficients on the rotor position θ_R. The transformation can be seen as divided into two different steps [25].

During the first coordinate transformation, from the stator reference system (a,b,c), shown in Fig. 1.4a, the two-phase fixed reference system (α,β) is obtained, as displayed in Fig. 1.4b. In this system, only two equivalent winding are present, magnetically decoupled and arranged with a displacement of 90° each other. However, in this reference system some coefficients, as the inductive ones, are still dependent on the rotor position. A further transformation is made to obtain a reference system in which the model of the motor has constant parameters. This is done by switching to the rotating two-phase reference

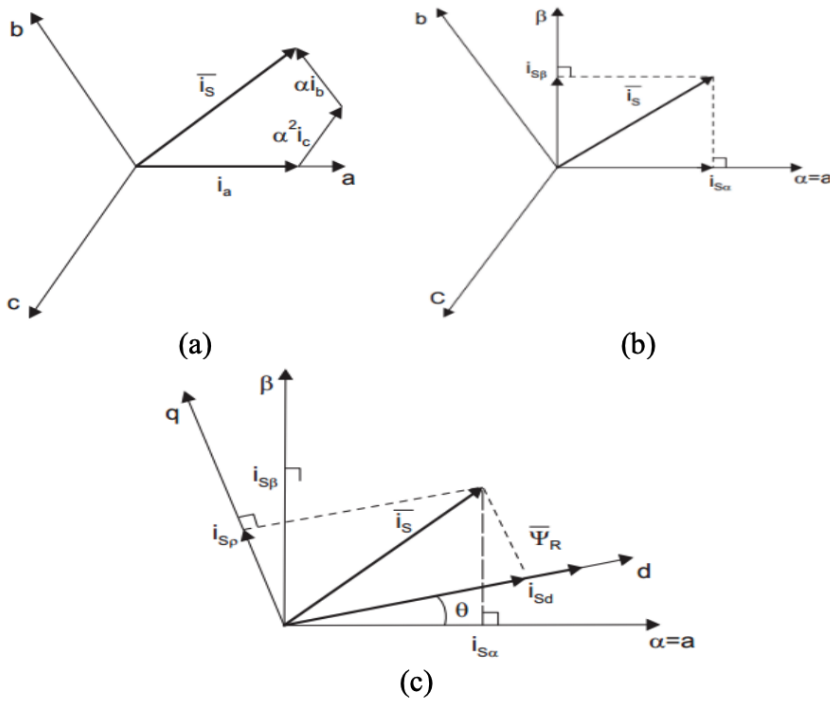

Figure 1.4: Reference systems: a) Stator three-phase reference system (a,b,c). b) Fixed two-phase reference system (α,β). c) rotating reference system $(d,q,0)$ [26].

system $(d,q,0)$, shown in Fig. 1.4c [27, 28].

The transformation from the stator reference system (a,b,c) to the one rotating at the rotor reference speed $(d,q,0)$ is done through the transformation matrix [28]:

$$[T] = \frac{2}{3}\begin{bmatrix} \cos p\theta_R & \cos\left(p\theta_R - \frac{2}{3}\pi\right) & \cos\left(p\theta_R - \frac{4}{3}\pi\right) \\ -\sin p\theta_R & -\sin\left(p\theta_R - \frac{2}{3}\pi\right) & -\sin\left(p\theta_R - \frac{4}{3}\pi\right) \\ \frac{1}{2} & \frac{1}{2} & \frac{1}{2} \end{bmatrix} \tag{1.9}$$

To switch from the rotating coordinate system $(d,q,0)$ to the three-phase (a,b,c) stator one, instead, the transformation matrix is defined as [28]:

$$[T]^{-1} = \frac{2}{3}\begin{bmatrix} \cos p\theta_R & -\sin p\theta_R & 1 \\ \cos\left(p\theta_R - \frac{2}{3}\pi\right) & -\sin\left(p\theta_R - \frac{2}{3}\pi\right) & 1 \\ \cos\left(p\theta_R - \frac{4}{3}\pi\right) & -\sin\left(p\theta_R - \frac{4}{3}\pi\right) & 1 \end{bmatrix} \tag{1.10}$$

By applying this transformation, all the equations that describe the motor can be rewritten with the following relationships [28]:

$$[v_{d,q,0}] = [T][v_{a,b,c}] \tag{1.11}$$

$$[i_{d,q,0}] = [T][i_{a,b,c}] \tag{1.12}$$

$$[\lambda_{d,q,0}] = [T][\lambda_{a,b,c}] \tag{1.13}$$

By applying it to the flux equation of the motor, it is possible to reach:

$$\begin{gathered}[\lambda_{d,q,0}] = [T][\lambda_{a,b,c}] = [T][L][i_{a,b,c}] + [T][\lambda_{a,b,c}] = \\ = [T][L][T]^{-1}[i_{d,q,0}] + [T][T]^{-1}[\lambda_{d,q,0}] = \begin{bmatrix} L_d & 0 & 0 \\ 0 & L_q & 0 \\ 0 & 0 & L_0 \end{bmatrix} \begin{bmatrix} i_d \\ i_q \\ i_0 \end{bmatrix} + \begin{bmatrix} \lambda_{PM} \\ 0 \\ 0 \end{bmatrix}\end{gathered} \tag{1.14}$$

In this reference system, the input power of the motor can be written as:

$$P_i = [i_{a,b,c}]^T[v_{a,b,c}] = [i_{d,q,0}]([T]^{-1})^T[T]^{-1}[v_{d,q,0}] = \frac{3}{2}(v_d i_d + v_q i_q + v_0 i_0) \tag{1.15}$$

Equation 1.15 can be developed as:

$$\begin{gathered}P_i = [i_{d,q,0}]([T]^{-1})^T[T]^{-1}[v_{d,q,0}] = \\ = [i_{d,q,0}]([T]^{-1})^T[T]^{-1}\left([R][i_{d,q,0}] + [L_{d,q,0}]\tfrac{d}{dt}[i_{d,q,0}] + p\omega_R \begin{bmatrix} -\lambda_q \\ \lambda_d \\ 0 \end{bmatrix} \right) = \\ = [i_{d,q,0}]([T]^{-1})^T[T]^{-1}[R][i_{d,q,0}] + [i_{d,q,0}]([T]^{-1})^T[T]^{-1}[L_{d,q,0}]\tfrac{d}{dt}[i_{d,q,0}] + \\ + [i_{d,q,0}]([T]^{-1})^T[T]^{-1}p\omega_R \begin{bmatrix} -\lambda_q \\ \lambda_d \\ 0 \end{bmatrix}\end{gathered} \tag{1.16}$$

In equation 1.16, three terms compose the total electrical power in the motor. The first term represents the Joule losses in the stator winding, the middle one is related to the variation of energy stored in the produced magnetic field, and the last one represents the mechanical output power at the rotor shaft, P_m. By carrying out the calculation in the expression of P_m, it is possible to obtain:

$$\begin{gathered}P_m = [i_{d,q,0}]([T]^{-1})^T[T]^{-1}p\omega_R \begin{bmatrix} -\lambda_q \\ \lambda_d \\ 0 \end{bmatrix} = p\omega_R \frac{3}{2}[\lambda_d i_q - \lambda_q i_d] = \\ = p\omega_R \frac{3}{2}[\lambda_{PM} i_q + (L_d - L_q) i_d i_q]\end{gathered} \tag{1.17}$$

Finally, from 1.17 it is possible to obtain the expression of the mechanical torque as follows:

$$T = \frac{P_m}{\omega_R} = p\frac{3}{2}[\lambda_d i_q - \lambda_q i_d] = p\frac{3}{2}[\lambda_{PM} i_q + (L_d - L_q) i_d i_q] \tag{1.18}$$

The expression of the mechanical torque in the $d,q,0$ reference system, like the equation 1.8, is composed of two different terms. The first one is directly linked to the flux produced by the permanent magnets in the rotor along the q-axis, while the second term, the reluctance torque, is developed on both d-and q-axis and is produced by the saliency of the machine (for SPM motors in which $L_d = L_q$, only the first term is different from zero).

1.3 IPMSM control principles and working regions

The speed of the rotating field in a brushless motor, as for all the synchronous machines, is directly proportional to the supply frequency f_s and inversely proportional to the pole number of the stator winding [27]:

$$\omega_R = \frac{\omega_s}{p} = \frac{2\pi f_s}{p} \qquad \left[\frac{rad}{s}\right] \tag{1.19}$$

$$n_R = \frac{60 f_s}{p} \qquad [rpm] \tag{1.20}$$

Due to this constraint, when the machine is directly powered from the grid, torque generation is typically feasible only at a fixed speed. This necessitates the employment of a

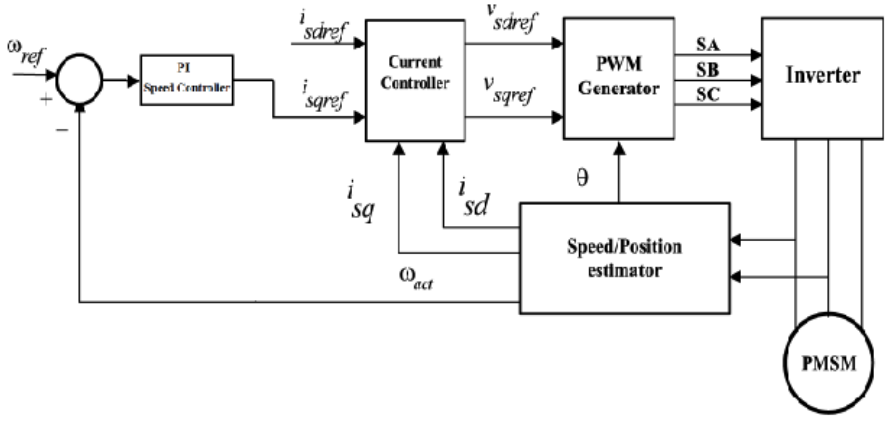

Figure 1.5: Example of PMSM control scheme [29].

Variable Frequency Drive (VSD) to regulate the speed and, more broadly, the operational parameters of the motor. Additionally, to accurately determine the rotor's position and speed, the inclusion of a sensor (i.e. encoder) was generally required in the past. Recently, there has been a surge of interest in sensorless control methods, such as sensorless direct torque control (DTC), which obviates the necessity for a physical sensor [30–32]. As an example, the block diagram of a drive system of a permanent magnet synchronous machine is represented in Fig. 1.5. The operation of the motor is limited by physical constraints. For this reason, the torque-speed characteristic of the motor is generally divided in two regions, in which the control strategies are different. An example of the ideal characteristics of an IPM synchronous motor is shown in Fig. 1.6. The first region,

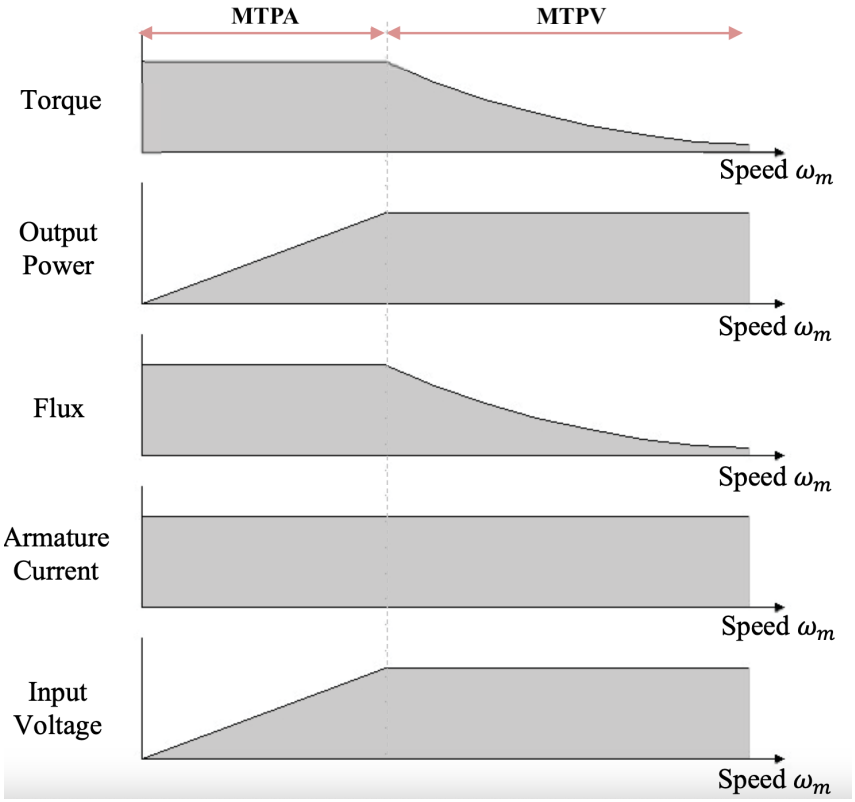

Figure 1.6: Ideal characteristics of an IPMSM.

referred to as the *Maximum Torque Per Ampere* (MTPA) region, exhibits a linear increase in voltage with rising speed until it reaches its rated and maximum values. Within this region, output power escalates in tandem with speed and voltage. Consequently, both current and torque remain constant within the MTPA region. For this reason, it is pos-

sible to refer to the MTPA as the *constant torque region*. At the working point at the edge between the two regions, the motor has reached the rated speed ω_n at the rated torque T_n [33]. To reach values of the speed higher than the rated one, it is necessary to keep voltages within the operating limits. This is done in the *Maximum Torque Per Volt* (MTPV) region where, controlling the direct and quadrature components of the stator current i_d (on the axis of the magnets) and i_q(on the axis between two rotor poles), the field weakening is implemented [33]. By decoupling these two currents, it becomes possible to independently control torque and flux. To have a constant power speed range, the negative d-axis current (I_d) magnitude is increased to weaken the magnetic flux and keep the voltage constant. At the same time, the q-axis current (I_q) must be reduced to keep a constant armature current. The maximum speed that can be reached by the motor during the operation along the flux-weakening region at constant speed has two main limits. The first one is related to the total losses and consequently the rms value of the armature current, which impact the increase of the temperature in the motor [34]. The second limit is due to the saliency ratio of the rotor in the machine: the higher it is, the higher the theoretical speed that can be achieved during the operation will be [35–37].

1.4 IPMSM rotor topologies

As discussed in section 1.1, IPM motors can be designed with different configurations and shapes of the magnets inside the rotor lamination. Some examples are displayed in Fig. 1.7.

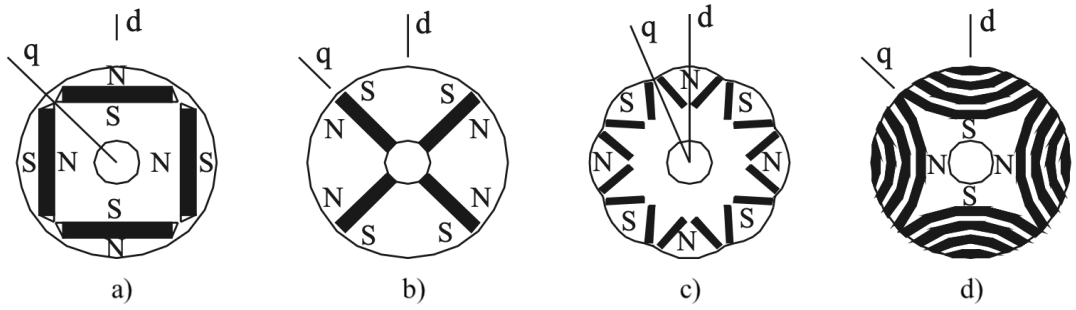

Figure 1.7: Examples of magnets configurations for IPMSM: single segment per pole (a), spoke configuration (b), "V" shaped (c), and multilayer configuration (d) [38].

All these types of magnets, as well as their arrangement and orientation, render a machine topology for which the quadrature-axis synchronous inductance is higher than the direct-axis synchronous inductance. Fig. 1.7a shows the simplest pole configuration for an IPM machine in terms of manufacture, with tangentially embedded magnets. This type of IPM machine is the easiest to construct because just one magnet per pole is present in the rotor. Moreover, the leakage flux produced by the magnets due to the need for magnetization of the lamination is minimized because of the small portion of iron between the rotor surface and the magnets. At the same time, however, the structure does not offer a very good saliency ratio between the direct and the quadrature-axis, and the speed range for flux-weakening operation is limited if compared to the other types of IPM motors. Moreover, the large magnet pole surface causes larger magnet losses if compared to other configurations [39].

By employing at least two magnets per pole, as in the configuration shown in Fig. 1.7c and Fig. 1.7d, it is possible to reach a high magnet airgap flux even in machines that have magnets buried deep inside the lamination [38]. The best configuration to reach a very high saliency ratio is represented by the multilayer rotor, which can also have a high quantity of magnets if compared to the other rotors displayed in Fig. 1.7. The disadvantages, however, are the high mechanical stresses on the lamination due to centrifugal forces while operating in the high-speed range and the quite high complexity of the manufacture of this typology, which involves more segments of permanent magnets that have to be inserted in the lamination [40].

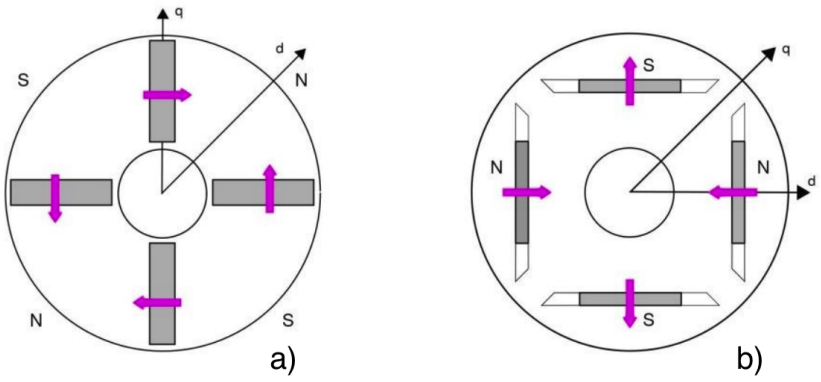

Figure 1.8: Different types of magnetizations: tangential magnetization (a), radial magnetization (b) [41].

Finally, Fig. 1.7b shows the rotor of a machine that has magnets inserted in spoke configuration. In this type of machine, as shown in Fig. 1.8, the direction of the magnetization, of the permanent magnets that is tangential to the rotor surface, creates an equivalent pole in the lamination between two different magnets. For this reason, the direct axis of this kind of machine does not coincide with the radial axis of the magnet as in the other IPM rotor described.

1.5 Literature review

Over the past fifteen years, there has been a significant emphasis in the literature on assessing the performance of IPM Synchronous Motors, with a particular focus on traction applications. In this section, a general review of the topic will be provided. As briefly described at the end of section 1.1, IPM motors offer some advantages compared to the other types of brushless PM machines. These advantages make its performance competitive for various applications. The first benefit of IPM is that, as seen in section 1.4, various shapes of magnets can be inserted in the rotor, even rectangular-shaped and with standardized dimensions, reducing the cost with respect to the arc-shaped magnets that are used in SPM motors, which can be difficult to manufacture, as they increase manufacturing complexity and cost [42]. Moreover, the magnet geometry generally adopted in SPM can lead to higher eddy current losses in the magnets, as analyzed in the study of Yamazaki et al. [43].

A second important positive aspect of IPM motors is the production of a considerable reluctance torque, coming from the higher value of inductance along the q-axis (L_q) with respect to the inductance along the d-axis (L_d), which is added to the magnet torque. As explained by Pellegrino et al. in [44], in order to have high saliency in the IPM rotor, multiple flux barriers may be required, but this can ensure a much larger overload torque over the entire speed range of the machine. Furthermore, as studied in [45] the back-EMF has safer values in case of uncontrolled generator operation. Related to this aspect, the permanent magnets are also less sensitive to temperature variations.

As already described, IPM motors offer performance (in terms of peak torque and efficiency) that remains high even in a wide flux-weakening region, at high-speed and

constant-power operation, which is one of the main requirements for Variable Speed Drives (VSD), especially in electric propulsion systems. The first researcher who filed a patent on synchronous motors with buried permanent magnets for flux-weakening application was Steen in 1977 [46]. Among the earliest studies conducted referred to the field-weakening potential of an IPM motor drive, one was carried out by Jahns in 1987 [47], while three years later, another important research was published by Schiferl and Lipo [48]. More recently, an interesting study about this aspect was conducted by Zhu et al. in [49], where the efficiency of IPM motors has been compared along a wide speed range to the performance of induction and switched reluctance motors, with the purpose of electric and hybrid vehicles application. A similar analysis has been carried out in [50] by Pellegrino and Vagati et al. In this paper, keeping constant the size of power electronics and the external volumes of the machine, a comparison has been presented on the different efficiencies that two four-pole machines, an SPM motor with concentrated winding and a distributed winding IPM motor with four flux barriers per pole, have along all the required speed range. From this study, the superior overload capability of the IPMSM is confirmed by both an analytical model and a finite element analysis (FEA).
Another important aspect of IPM machines is that if it is compared to the other topologies of brushless motors, the risk of demagnetization is reduced, as the magnets are not directly adjacent to the air gap. This was demonstrated for example by Chlebosz and Ombach in [51], where a demagnetization test on an IPM and a SPM motors was carried out both with 2D Finite Element Analysis (FEA) and in the laboratory, proving that the amount of demagnetization is lower for the motor with magnets buried in the lamination. Because of the magnets buried inside the rotor core, also the risk of their detachment at high speed due to centrifugal and magnetic forces is avoided, without the need for additional bindings. Among the points of strength of the IPM motor typology, another one is that many geometries of the rotor can be designed, in order to optimize the features of the motor according to the specific application. In the analysis made by Liu at al. in [52] for example, four different topologies of pole shape in the rotor have been tested. The goal of the investigation was to find the best pole shape of an IPM motor for electric vehicle applications by means of an inductance calculation based on FEA, which has been validated with experimental results. The result proved that, for the requirement of the

study, the V-shape motor is more satisfying with comprehensive consideration of costs, torque ripple, and overall efficiency if compared to the other three IPMSMs with different rotor topologies. The same typology of rotor poles has been chosen in [53] by Kim et al., where the goal of the study was to find the optimal shape of the rotor for the motor of a compressor in an air conditioning system. In [54], Chen et al. studied two different IPM shapes with outer rotor. In this case, the goal was to find the best geometry for high-reliability operation. The rotors under analysis were a V-shape and a spoke-type. The results of this analysis confirm that both motors can offer high fault tolerance in terms of demagnetization. The spoke-type motor results better suited for generating a trapezoidal back electromotive force (EMF) and is cost-effective. On the other hand, the V-shape motor produces a sinusoidal back EMF, leading to smoother torque output and minimal torque fluctuations. As Liu et al. in [52], Yang et al. studied in [55] the performance of different geometries for traction application. In this case, however, the geometries under investigation were V-shape, double V-shape and delta-shape rotors. Considering the requirements of the electric traction, the single V-shape magnet configuration has been chosen, due to its good torque-speed performance, best demagnetization performance, smallest mechanical stress and tolerable radial force harmonic content. Furthermore, the skew optimization has been applied, obtaining a minimum torque ripple below 5% at the peak torque region. In a subsequent study, the same research group also investigated the effects of two different stator winding configurations (integer slot and fractional slot) combined with the three rotor configurations already analyzed in the previous work [56]. Simulation results show that fractional slot winding generally improves torque quality, although each combination of rotor and stator configuration offers advantages and disadvantages over the others.

As mentioned, one of the objectives in the design of IPM brushless machines is often the reduction of the torque oscillations. In fact, the presence of a high level of torque ripple during the operation is one of the weaknesses of IPM motors and, in general, of PMSMs. This goal can be pursued in different ways, both by applying design techniques such as the skewing of the geometry and by using control strategies. A first example can be represented by the analysis from Zhu and Howe [57], where the combination between the number of stator slots and rotor poles has been studied. The authors have concluded

that a proper combination of these parameters, together with the choice of the optimal magnet pole-arc to pole-pitch ratio and the optimal skew can keep low the torque ripple during the operation. Moreover, they proposed a factor to indicate if a slot and pole number combination has good behavior from the point of view of the cogging torque. Another study on the number of stator slots and rotor poles was conducted by Hwang et al. in [58]. In the mentioned paper, also the effect of the width ratio of armature teeth to magnet pole arc was investigated with a FEA method, concluding that an optimal choice can lead to a significative improvement in the torque ripple. In [59] Xintong et al. studied the influence of the width of stator teeth on the torque ripple by creating simulation models, concluding that for a brushless DC (BLDC) machine, by adopting a nonuniformed tooth width, the reduction of the cogging torque can be related to a certain geometrical parameter. Azar et al. in [60] investigated the benefits of having fractional-slot winding with alternate slot opening in IPM machines by adopting a comparative study. The study was carried out by using 2D FEA, concluding that the cogging torque sensitivity against the additional stator gaps strongly depends on the slot opening. The non-uniformity of such gaps causes a significant increase in the cogging torque and also diminishes the effectiveness of rotor skewing. In [61], a different approach was used by Ge et al., focusing on introducing and analyzing an optimal step-skew technique through 2D and 3D FEA in order to diminish cogging torque in IPMSMs. Experimental validation on prototypes confirmed the method's efficacy in reducing cogging torque, which cannot be completely eliminated, primarily due to end leakage flux and axial interaction between adjacent rotor steps. It is noteworthy to highlight two additional papers that delve into the analysis of various skewing techniques using FEA to mitigate cogging torque and on-load torque ripple in SPMSMs. In [62], Chu and Zhu state that on-load torque ripple presents challenges for analytical modeling due to magnetic saturation, while 3D FEA is intricate and time-consuming. Hence, they opt for a 2D FEA multi-slice approach utilizing OPERA software. Their findings suggest that although cogging torque can be entirely eliminated through skewing, achieving the same for on-load torque ripple is impractical. In another work from the same research group [63], the authors employed both 2D and 3D FEA methods using the software package JMAG-Designer 10.5 to assess cogging torque reduction achieved through conventional and herringbone rotor step skewing. Their analysis

demonstrated that both skewing techniques can mitigate cogging torque, with conventional skewing proving more effective compared to herringbone skewing, particularly with smaller steps. Experimental measurements on prototypes validated the FEA simulations. Regarding the rotor configuration, the V-shape pole typology has been proposed in different variants. For example, in [64] by Xiao et al. a symmetrical V-shape PM geometry is modified by adding asymmetric spoke-type flux barriers between poles, obtaining an improvement in the torque, thanks to the magnetic-field-shifting effect. In a subsequent work from the same authors [65], the rotor geometry was furtherly modified, by proposing a combination of V-shape and spoke-type PM rotors, as well as an extra asymmetric flux barrier close to the rotor surface in each pole. This asymmetric rotor configuration allowed the increase of the maximum torque and the decrease of the cogging torque simultaneously, even in the constant power speed range. The results presented in the discussed paper are obtained with both 2D and 3D FEA and validated with experimental measurements on a prototype. Other recent papers have evaluated the performance of different IPMSM configurations, with particular focus on their field-weakening capability. In [66], by Zhou and Gerling, a baseline motor with single-layer, tangential-form rotor magnets and concentrated stator winding is modified, by removing part of the iron core with half-circle-form flux barriers and by increasing the stator tooth width; the new design improves the field-weakening capability and reduces the cogging torque, at the price of higher current density. In [67], Abdelrahman et al. outlined a comparative study between delta-shape and double-V-shape rotor magnets within the context of a dual three-phase IPMSM. Simulated outcomes indicated that the delta-shape rotor requires 10% less permanent magnet mass compared to the double-V-shape rotor, resulting in higher torque at the base speed. However, the double-V-shape rotor demonstrates superior flux-weakening capability. Additionally, it is noted that the bar magnet configuration in the delta-shape design is more susceptible to demagnetization in the event of a short circuit. The target of demagnetization robustness has been considered in the design of IPMSM in other research. For example, in [68] by Ruoho et al., some demagnetization models for NdFeB magnets have been implemented in a FEA software and studied by the authors. Results of the demagnetization models have been compared with the measured recoil behavior of a Nd–Fe–B magnet material. Among these models, the linear one offers realistic results that

are appropriate for practical applications, whereas the limited model offers considerably robust outcomes specifically concerning demagnetization. More recently, Jong and Hur proposed in [69] an optimization in the design of permanent magnet synchronous motor using hybrid-type permanent magnets (defined as using both neodymium PM and ferrite PM in a rotor) considering irreversible demagnetization. The analysis has been carried out on finite elements simulations and validated on prototypes in the laboratory, stating that, when the motor is designed using hybrid permanent magnets, the effect on ferrite permanent magnets by flux leakage of NdFeB magnets has to be considered and analyzed through the magnetic equivalent circuit. Another research in the field was carried out by Kladas and Sakkas in [70], where three different magnet configurations and various permanent magnet material grades are investigated. In conclusion, the authors emphasize the critical significance of selecting appropriate magnet grades, as the choice directly impacts the potential for extended demagnetization. Unsuitable material can significantly increase the risk of demagnetization, underscoring the importance of meticulous magnet grade selection in design considerations.

Regarding the materials used for the PM in the rotor, most of the papers cited only considered neodymium ones during the design procedure. In [71] by Kimiabeigi et al., an interesting study on the usage of ferrite magnets in IPM motors for electric vehicle applications is proposed. The authors concluded that, with proper optimization of the rotor topology and geometry, it is possible to reach high torque, power density, and efficiency keeping low the risks of demagnetization using low-cost ferrite magnets. Another important study on the performance of ferrite magnet machines is reported in [72]. In this paper by Cai et al., the performance of the commercial neodymium motor from the Toyota Prius is compared with a ferrite-assisted SynRM. The results showed how the proposed geometry, which is composed of three flux barriers per pole, reaches similar performance to the already existing neodymium IPM motor, with just a 15% reduction in the maximum torque. Nevertheless, the estimated reduction in terms of the cost of material for the permanent magnets was around 50%. In [73] by Sekerák et al., another comparison between interior permanent magnet motors with ferrite and neodymium PM was conducted. The authors demonstrated through FEA simulations that, for some applications, ferrite magnets can replace NdFeB inside the machine. Finally, a comprehensive

analysis was made by Chi-Kwong Luk et al. in [74]. In the latter study, several works on the usage of ferrite magnets inside the rotor have been compared in terms of performance and torque density to give a general overview of the prospective of this kind of machine.

Chapter 2

Design considerations

In this chapter, some preliminary aspects of the design of the IPM machines will be discussed. In particular, the discussion will be on the type of stator and winding, the number of poles and the choice of the topology of the barriers inside the rotor, together with an analysis of the performance and total costs for different magnet materials. Moreover, the method used to create the models (through the software Altair Flux and FluxMotor), that is based on the finite element analysis, will be briefly introduced in section 2.1.

2.1 Finite element software

The Finite Element Method (FEM) is a numerical method that allows the solution of physical problems. In the field of design and, in general, modeling of electrical machines, it is widely used nowadays, thanks to the extremely high precision in the results. The magnetic behavior of IPM machines can be described as the interaction of two electromagnetic fields: the one created by the permanent magnets in the rotor with the field created by the armature reaction. The machine's performance can be predicted by solving Maxwell's equations, which describe the electromagnetic fields involved. This can be done through various methods, as described in Fig. 2.1. While analytical methods offer quicker solving times in comparison to numerical techniques, their applicability is confined to relatively easy problems. Among the numerical techniques, Finite Elements Method can offer some advantages, as reported in [75]:

- no restrictions on boundary conditions;

- can be applied to different fields (i.e. electromagnetic, mechanical stress analysis, heat transfer);
- no restrictions on material properties;
- no restrictions on geometrical shape for the analysis;
- the accuracy strictly depends on the size of the mesh;
- the finite element solution closely mirrors the actual field distribution within the region.

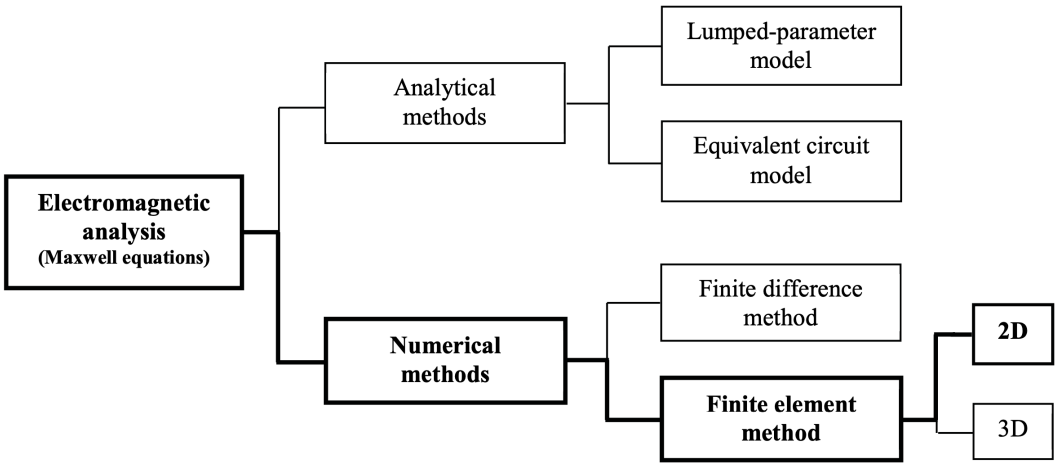

Figure 2.1: Methods for modeling and studying the electromagnetic behavior of electrical machines [8].

In the FEM, the domain is divided into a fixed number of sub-domains to minimize the complexity of the problem. The solving of the problem consists of several steps, that are summarized in Table 2.1. In particular, a crucial role of the pre-processing step is the meshing of the domain. This step consists of dividing the whole geometry into smaller regions, allowing the reduction of the complexity of the problem to analyze. The mesh is made of a finite number of elements. For each component of the mesh, a differential Maxwell equation is computed: for this reason, it is important to accurately decide the dimension of the components of the mesh. The smaller the components of the grid, the higher the precision in the calculation. Nevertheless, also the computational burden of

Table 2.1: FEM steps for the analysis of the domain of an electrical machine.

Pre-processing	- Construction of the geometry - Construction of the mesh - Creation of the sources of excitation - Creation of the electrical circuit - Assignment of the boundary conditions
Solving	- Derivation and assembly of the matrix equations - Solving the equations for each element
Post-processing	- Analysis of the results

the calculation increases with the number of elements of the mesh. The mesh elements can take on various forms, each defined by its vertices. These vertices, commonly referred to as nodes, collectively set up the mesh structure. Based on the type of domain, the elements can be:

- volume elements, for a volume domain (3D domain);
- surface elements, for a surface domain (2D domain);
- line elements, for a line domain (1D domain).

The quality of the solution in the mesh not only depends on the dimension of each element. In fact, it also depends on the interpolation functions in each element, which can be 1st or 2nd-order polynomial functions and on the continuity conditions imposed on the sub-domain boundaries [76].

In this thesis, the approach to the FEM is mainly carried out by studying a 2D domain. The main topologies of elements in the 2D FEA approach are the triangular one and the rectangular element, as reported in Fig. 2.2. The elements shown in Fig. 2.2.a and Fig. 2.2.b have only nodes in the vertices of the element: these are first-order elements. The software calculates the approximated potential between each node through a linear function (1st-order polynomial). Consequently, the field, which is calculated through a derivation of the potential, is constant over the single 1st-order element. The other examples represented in Fig. 2.2.c and Fig. 2.2.d also have nodes in the middle of each edge of

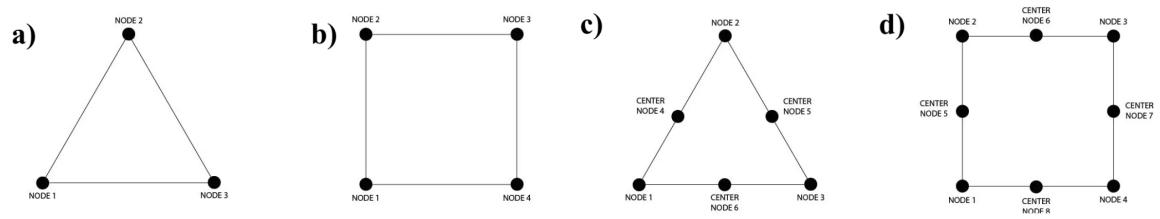

Figure 2.2: Types of mesh elements: triangular, 1st-order (a); rectangular, 1st-order (b); triangular, 2nd-order (c); rectangular, 2nd-order (d) [77].

the element. These are 2nd-order elements: in this typology, the potential is calculated with a quadratic function (2nd-order polynomial) and the resulting approximation of the field in the element has a linear behavior [78].

To reduce the computational burden of a FEA simulation, some boundary conditions can be applied to the domain. The first method that can be applied is the Dirichlet boundary condition, which consists of assigning a constant value to the potential of a certain line of the domain [79, 80]. For the model of an electrical machine, the application of the Dirichlet condition is usually made by creating the so-called infinite box around the external iron of the machine. By applying this condition, the leakage flux outside the infinite box is assumed to be zero. A second boundary condition that can be applied to the finite element analysis is the Neumann boundary condition. The application of the Neumann condition allows to avoid the repetition of calculations where a symmetry in the geometry takes place [79, 80]. Finally, another important boundary condition is represented by the periodic condition. The periodic condition is applied to structures demonstrating a repetition of electromagnetic fields. It is typically assigned to two boundary lines utilizing symmetries within the geometry. Such boundary conditions prove beneficial in structures where scaling down the overall geometry allows for accurate analysis on a single part, reducing computational time significantly. As the Neumann boundary condition, the periodic condition is useful during the design of a machine. Still, it cannot be applied to specific applications in which the symmetry or the periodicity of the fields are not respected (i.e. in models for the simulation of a motor fault). Dirichlet and periodic conditions will be applied to the design study carried out for this thesis, where the models are built in a 2D domain. This choice is made to reduce the computational burden,

decreasing the precision in the calculation of the magnetic effects and losses in the end windings.

2.2 Stator configuration and number of poles

2.2.1 Stator and winding configurations

The configuration of the stator in an IPM motor is a critical choice during the design process. The most important parameters of the shape, like the tooth height and width or the area of a slot, can significantly affect the performance of the machine in terms of efficiency and power density, mainly due to the saturation of the flux in the magnetic circuit. For example, if the stator tooth-tips are too thin, the saturation of the flux in this region creates an effect similar to that of a wider slot-opening, increasing the cogging torque and the rotor eddy current losses [27]. Moreover, also the number of slots is an important parameter that impacts the machine's performance, especially in terms of torque ripple. For the design analysis carried out during the work of this thesis, the basic configuration of the stator has been chosen in order to simplify both the design and the manufacturing process. An already-existent stator geometry from an induction machine has been used during the design process. The lamination of the stator was built for a 4-pole machine with single-layer distributed winding. The axial height of the motor is 160 mm, and the outer diameter of the stator is equal to 292 mm. The inner diameter of the stator lamination has been designed to be 190 mm. The geometry of the slots from a model built in the FEA software FluxMotor from Altair is shown in Fig.2.3. The stator has 48 slots, which for a 4-pole machine are equal to 4 slots per pole per phase.

The choice of using distributed windings allows to reach a magnetomotive force (MMF) in the airgap which has a distribution as close as possible to a sinusoidal one. It has been proven, for example in [81], that a sinusoidal distribution of the MMF in the airgap significantly reduces the torque ripple of the IPM machine during the operation. As already seen in chapter 1, the oscillations in the torque are one of the main weaknesses of the IPM machines. In order to further reduce the harmonic content of the MMF produced by the stator and consequently improve the shape of the output torque of the motor, the stator winding has been divided into two layers. The winding scheme of this configuration is

reported in Fig. 2.4.

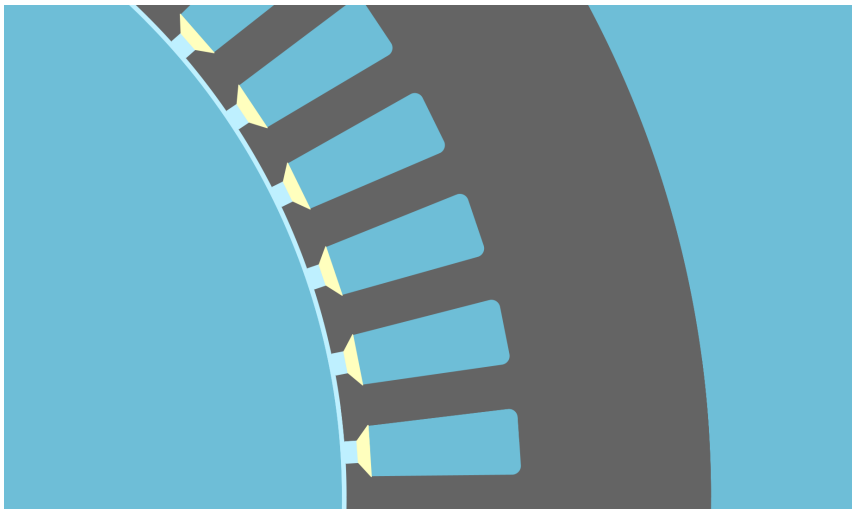

Figure 2.3: Representation of the stator from a model built in the FEA software Flux-Motor.

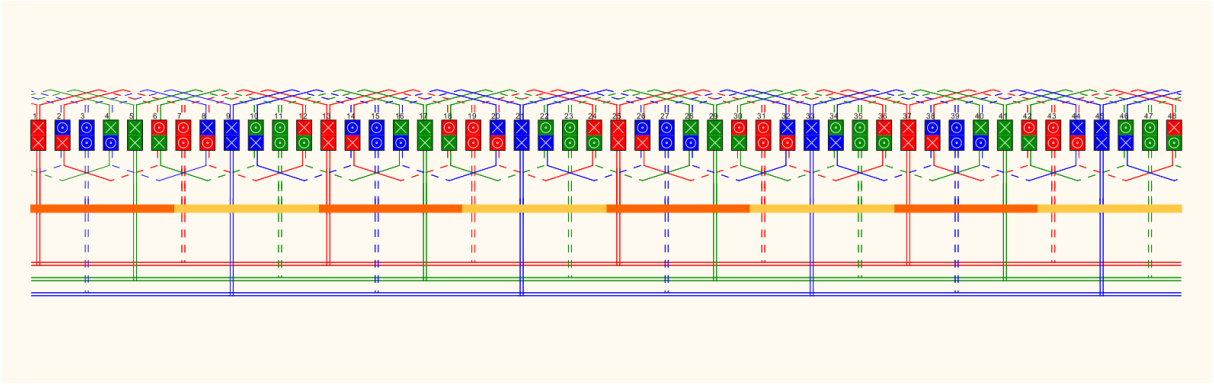

Figure 2.4: Double layer stator winding scheme chosen for the motor under study.

The slot pitch of the winding is set to 5. All these considerations allow to reach a shape of the spatial MMF which is close to a sinusoidal waveform. The waveform of the MMF is reported in Fig. 2.5.

The comparison of the normalized output torque obtained from a single-layer motor and a double-layer one is reported in Fig. 2.6. This choice allowed the reduction of the peak-to-peak torque ripple from 43.4% of the single-layer winding to 36.2% of the double-layer one.

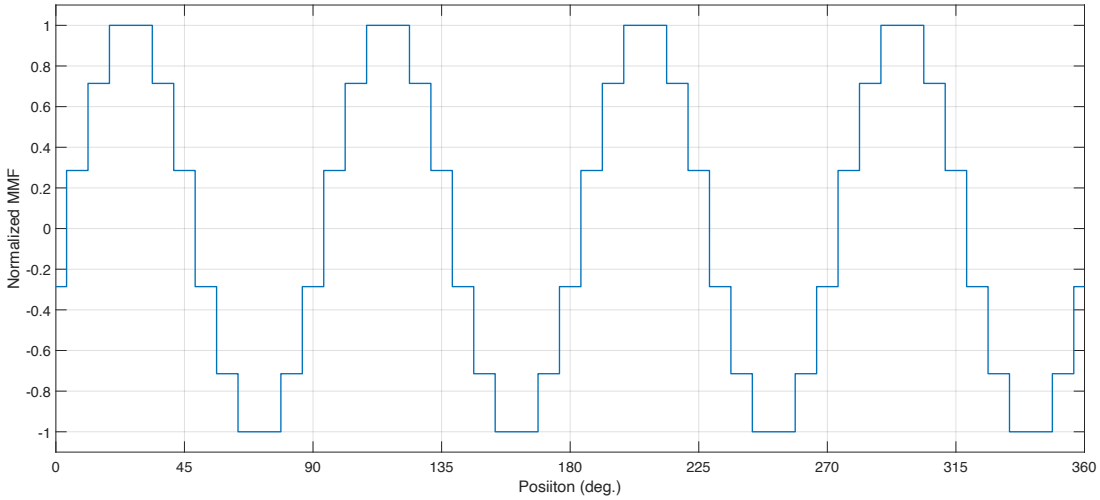

Figure 2.5: Sum of the spatial MMF of the three phases (normalized values).

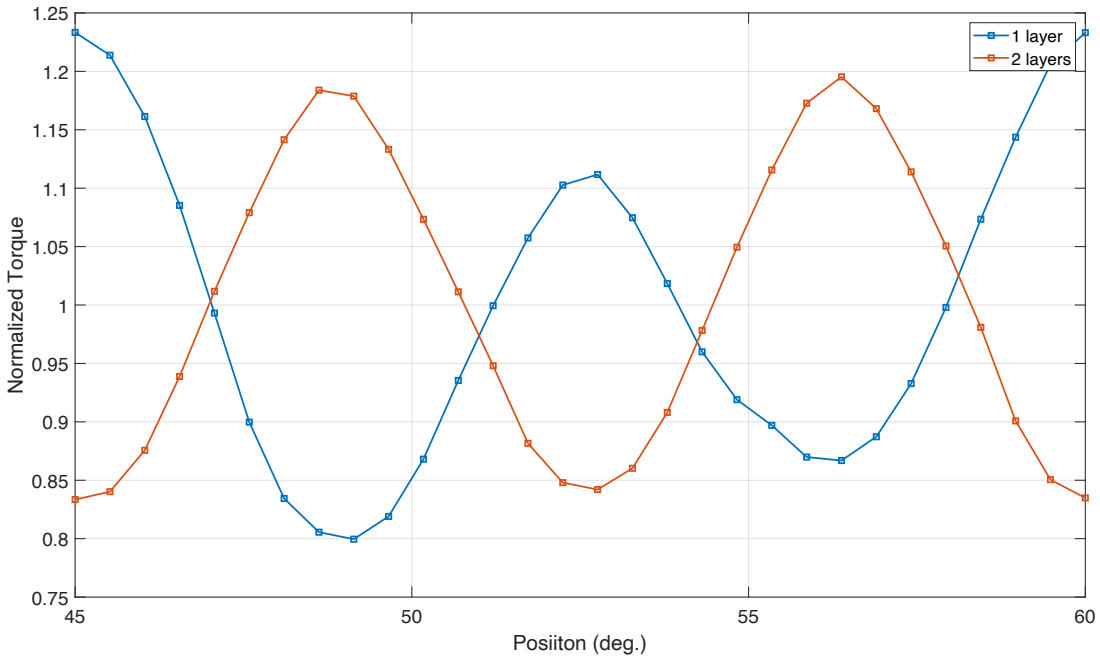

Figure 2.6: Comparison of the normalized shapes of the output torque for the single-layer winding configuration (blue) and the double-layer winding configuration (orange).

2.2.2 Number of poles

As can be noticed from Fig. 2.4, where the winding scheme has been introduced, the analyzed motor has 48 slots and 8 poles, so the number of slots per pole phase is equal to two). As already reviewed in section 1.5, a proper choice between the number of stator slots and the number of poles of the machine can lead to a general improvement of the

performance. At the same time, the analysis of the performance of a brushless motor with 48 stator slots was already investigated by the author in [82]. In this work, a comparative analysis between four-poles and eight-poles IPM motors with the same stator has been carried out, through 2D-FEA software. For both the machines under analysis, the same amount of materials for the permanent magnets was chosen, in order to obtain a comparison that is not influenced by this parameter. In table 2.2, the main characteristics of the studied machines are given. Some of the results for the analysis at the rated speed (940 rpm) are summarized in Table 2.3.

Results in Table 2.3 were obtained by changing only the rotor configuration and the number of poles of the machine, without modifying any other stator geometry or parameter. The analyzed eight-poles machine offers better performance in terms of output torque (both mean value and ripple torque), efficiency and power factor with respect to the 4-poles one.

Considering the available literature and this previous analysis, where the number of stator slots was equal to 48, the number of poles for the motor designed in this part of the thesis has been chosen equal to eight.

Table 2.2: Characteristics of the analyzed motors.

Parameter	**4-poles machine**	**8-poles machine**
Base speed point [rpm]	940	940
Lamination axial length [mm]	345	345
Turns per slot	14	14
Number of slots	48	48
Winding connection	wye	wye
Current RMS [A]	70	70
Output power [kW]	27.4	31.2

Table 2.3: Comparison between the performance of a 4-poles machine and an 8-poles machine.

	4-poles machine	**8-poles machine**
Output torque [Nm]	278.0	317.3
Power factor	0.74	0.85
Torque ripple [%]	29.1	2.3
Machine efficiency [%]	87.6	90.8

2.3 Rotor topology and material considerations

2.3.1 Rotor topology

As described in section 1.4, brushless IPM motors can have different shapes for the barriers of the poles. Essentially, each configuration allows to reach the proper performance based on the specific application. Moreover, for each configuration, it is possible to design further variations in the shape or in the number of layers for the barriers in each pole. An example is represented in Fig. 2.7.

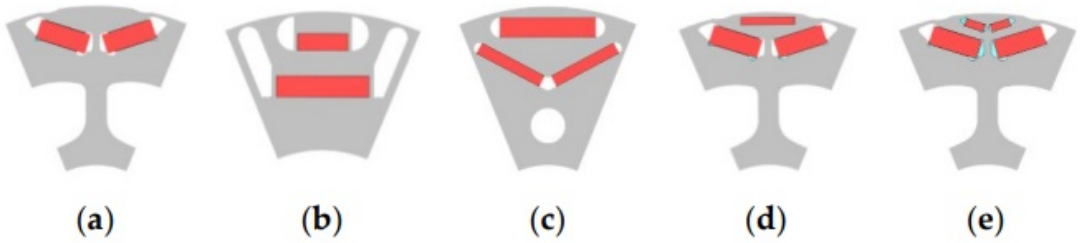

Figure 2.7: Variation of the V-shape rotor pole: simple V-shape (a); double U-shape (b); different delta-shape configurations (c),(d); double V-shape (e) [83].

Fig. 2.7a represents the most simple configuration of the V-shape pole, while the others are variations that involve more magnet segments in the rotor having multiple layer configuration. These configurations usually achieve good results along the torque-speed characteristics of the motor in terms of performance. Involving more magnet segments, however, makes the manufacturing process more complicated, increasing the costs with respect to a motor with the same amount of materials and a lower number of segments.

Table 2.4: Electric and mechanic properties of copper wires at the reference temperature of 20°C.

Properties	**Values for copper**
Mass density $[kg/m^3]$	8890.0
Electrical resistivity $[\Omega m]$	$1.724 \cdot 10^{-8}$
Resistivity temperature coefficient $[K^{-1}]$	$3.93 \cdot 10^{-3}$

In the first case study of this thesis, reported in chapter 3, in which the goal is to obtain a good compromise between performance and industrial interest, only single V-shape rotors are analyzed. This rotor topology allows the reduction of manufacturing costs (having only two rectangular magnets per pole and a simple barrier geometry) if compared to other types of rotor geometries. At the same time, the performance of the machine can be improved if the design process is properly made.

2.3.2 Analysis of the materials

Regarding the costs of manufacture, another important aspect is related to the choice of materials for the components of the machine. In particular, the cost of an electrical machine strongly depends on the costs of the active materials that are used in its construction. The analysis in this section considers three main components of the IPM machine:

- stator winding;
- magnetic circuit (stator and rotor core);
- permanent magnets.

Regarding the stator winding, for all the analysis carried out in this thesis, a copper random-wound wire has been chosen, whose main mechanic and electric properties are reported in Table 2.4.
For the design process of the motor reported in chapter 3, the lamination is made of M250-50A steel. This material has been chosen to keep quite low losses and temperatures at high

speed, being characterized by a value of specific losses (at 50 Hz of supply frequency) equal to 2.50 W/kg. The lamination sheet has a thickness equal to 0.50 mm, and the selected stacking factor (that is the percentage of active material for the length of the lamination) is equal to 95%, which is coherent with a real stacking factor for a manufactured motor. The value of the stacking factor is then used by the software to calculate the B-H curve of the laminated material from the solid one [84]. For this material, the saturation magnetic polarization (J_s) for the M250-50A in lamination is equal to 1.73 T. The magnetization curve of the laminated M250-50A chosen to build the FEA model is reported in Fig. 2.8.

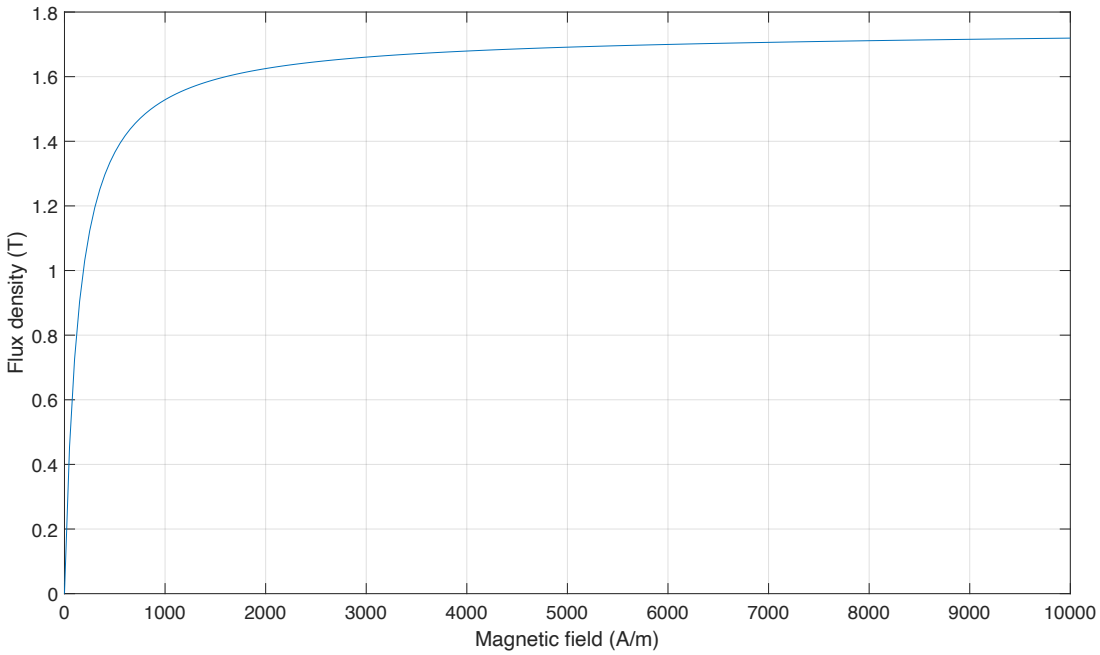

Figure 2.8: B-H curve of laminated M250-50A steel, obtained from the datasheet [85].

The iron losses are defined in the FEA software according to the Bertotti model, which is widely used as the reference model for iron losses in finite element analysis. The mathematical equation used in the material database of Altair software to compute the iron losses is [86]:

$$P = k_h \cdot B_{pk}^{\alpha_h} \cdot f_s^{\beta_h} + k_c \cdot (B_{pk} \cdot f_s)^{\alpha_c} + k_e \cdot (B_{pk} \cdot f_s)^{\alpha_e} \tag{2.1}$$

where:

- f_s is the supply frequency;

- k_h, α_h, β_h represent respectively the hysteresis loss coefficient, the exponent of the flux density for the hysteresis losses and the exponent of the frequency for the hysteresis losses;
- k_c, α_c are respectively the eddy current loss coefficient and the exponent of the flux density and the frequency for the eddy current losses;
- k_e, α_e are respectively the excess loss coefficient and the exponent of the flux density and the frequency for the excess losses;
- B_{pk} is the peak value of the flux density in the electric period, expressed in T.

By adopting this equation and neglecting the excess losses term (not taken into account during the work of this thesis, since they usually have lower values if compared to the other terms in equation 2.1), the losses per unit for the M250-50A are obtained as displayed in Fig. 2.9.

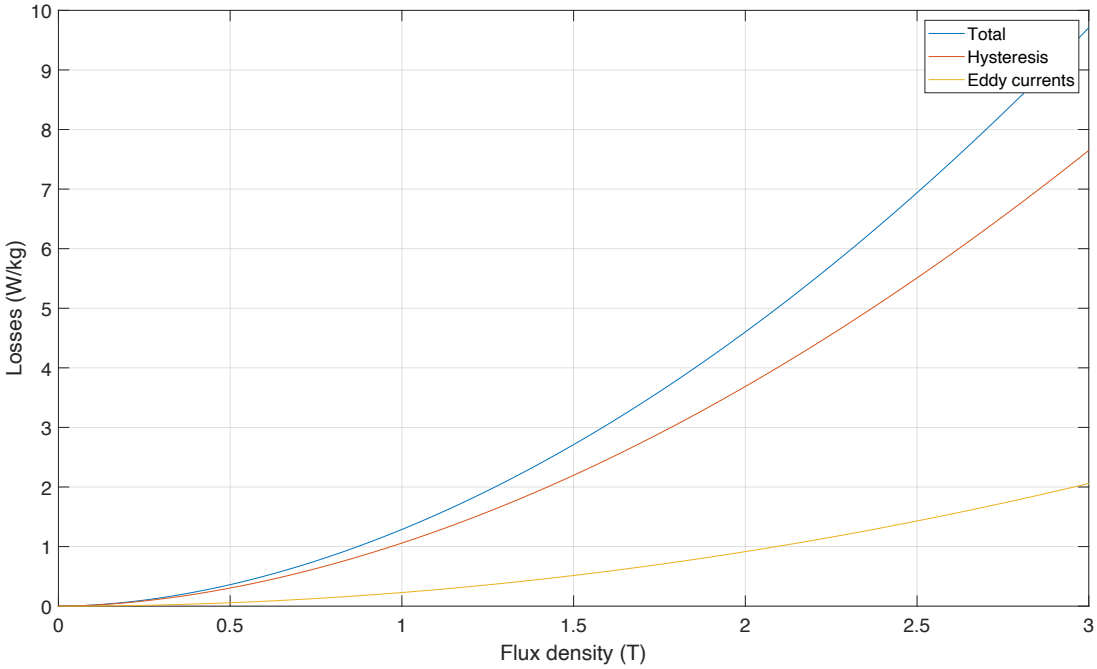

Figure 2.9: Losses for the laminated M250-50A steel at 50 Hz obtained through the Bertotti model, obtained from the datasheet [85].

These losses are referred to a motor with a supply frequency of 50 Hz; through the Bertotti method, introduced in [87], the analysis can be extended to the electric frequency at the

Table 2.5: Properties of the M250-50A laminated steel.

Properties	**Values for M250-50A**
Mass density $[kg/m^3]$	7650.0
Sheet thickness [mm]	0.50
Stacking factor [%]	95.0
Saturation magnetic polarization J_s [T]	1.73
Relative permeability μ_r	9500.0

analyzed working point of the motor. In Table 2.5 the most relevant properties of the selected M250-50A are resumed.

The last components under analysis in this section are the permanent magnets. If compared to the other active materials, these components have the highest price-per-unit in a brushless PM machine. For this reason, the choice of a proper permanent magnet can have a crucial role in the design of an IPM machine, impacting both the final price and the performance of the motor. In this thesis, three main topologies of permanent magnet materials have been analyzed inside an IPM motor:

- ferrite magnets;
- sintered NdFeB magnets;
- bonded NdFeB magnets.

Ferrite materials are currently the cheapest permanent magnets on the market. Their residual flux density B_r (that is the flux density of the magnetized material when the magnetic field is turned to zero) is generally low, with values in the range of $0.3 - 0.5$ T. However, they have the quality of having a coercive field H_c (the magnetic field required to remove the residual induction B_r) that increases as the temperature increases, unlike other materials used for permanent magnets.

Sintered NdFeB are the magnets that ensure the highest residual energy in the market. They exhibit residual induction values up to $1.35 - 1.45$ T and are the most widely used for permanent magnet machines. However, the use of rare earth elements, especially in the recent past, has increased the costs of this type of magnet. The sintering process,

which consists of forming a solid mass of material from powder through heat and pressure without melting it to the point of liquefaction, allows sorting granules of the material, improving the magnetization results. On the other hand, the complex process further increases the overall bill of materials in the final machine manufacture. Moreover, being formed of compressed powder, sintered magnets can be more fragile if compared to other materials. Finally, sintered neodymium magnets generally work at lower temperatures than ferrite ones. In fact, the maximum working temperature of NdFeB magnets is usually around $150 - 180°C$, while for ferrite it can also reach $250°C$ before demagnetization problems arise [88].

Bonded neodymium are a particular typology of magnets where NdFeB powders are enclosed into resins, forming the permanent magnets. One of the strengths of this type of material is the possibility of forming the magnet's shape using the lamination barriers directly. Moreover, compared to the other neodymium magnets, the costs are lower, not having the sintering process. However, since the rare earth materials within the resins are not properly oriented, the remaining flux density is lower than the one offered by sintered neodymium magnets (generally, it can be around $0.6 - 0.8$ T). Table 2.6 summarizes the main properties of the materials chosen for the analysis.

Table 2.6: Main magnetic properties of the three permanent magnet materials under analysis [89–91].

	$\mathbf{B_r}$ **[T]**	$\mathbf{H_{cJ}}$ **[kA/m]**	$\mathbf{(BH)_{max}}$ **[kJ/m³]**
Ferrite	0.41	270	29.7
Sintered NdFeB	0.75	796	95.5
N45SH	1.35	1592	354

As a sintered neodymium material, the N45SH magnet has been chosen for this analysis. This commercial material offers a very high remaining flux density ($1.32 - 1.38$ T, while the nominal value from the datasheet is 1.35 T). The Curie temperature T_c, that is the maximum value of the temperature before the magnet loses permanently its magnetic properties, is $310°C$. However, the maximum operating temperature suggested by

the manufacturer is around $150 - 180°C$ [91]. As highlighted in Table 2.6, despite ferrite and bonded Neodymium magnets are cheaper with respect to classical sintered NdFeB magnets, this last type allows to obtain very high B_r and $(BH)_{max}$ (this last value from the datasheet is equal to 354 kJ/m^3). These properties allow to obtain a very high power density if compared to the other types of magnets. This high power density could be seen in a reduced volume of the motor for the same power required. In this way, the motor becomes more compact and less heavy, allowing use in more applications such as automotive that require more lightweight components and reduced volume of devices. The study carried out in this paragraph has kept the goal of reaching the same torque at the nominal speed of the motor by inserting the three different materials under analysis into the V-shape barriers. All the other parameters and dimensions in the radial section of the motor, such as the diameter of the rotor and the thickness of the air gap, have been kept fixed for all the analyzed models. In Fig. 2.10 the different shapes of the rotor poles chosen for the analysis of the materials in the motor are shown.

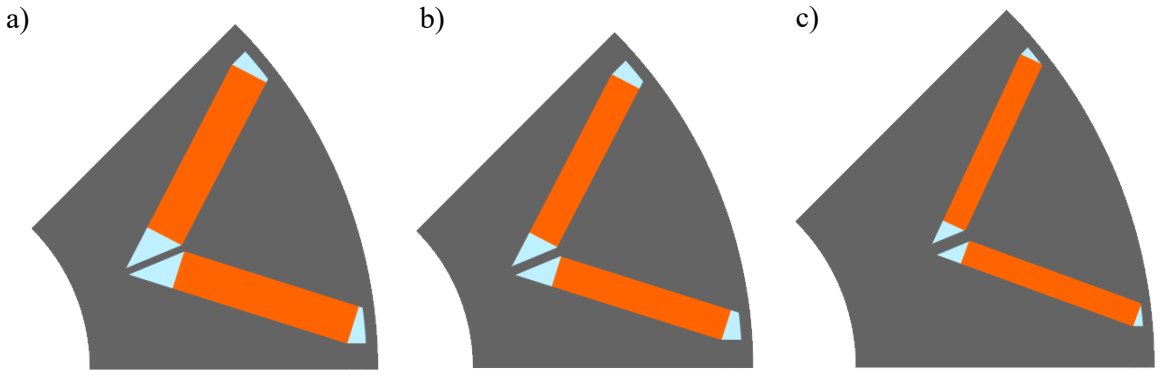

Figure 2.10: Different shapes of the V-pole rotors: Ferrite model (a); Bonded neodymium model (b); N45SH model (c).

As can be noticed, the thickness of the magnets decreases as the energy density of the magnet material used for the model increases. Moreover, the magnet segment of the model with ferrite is slightly wider if compared to the reference value of the motor designed with N45SH. The results of the main performance obtained through 2D-FEA simulation are reported in Table 2.7. In this table, the values of the geometrical parameters are normalized by taking the motor with the sintered NdFeB magnets as a reference.

Table 2.7: Main results of the simulations during the study of materials at the base speed point.

	Ferrite	Bonded NdFeB	N45SH
Rated torque [Nm]	435.1	437.5	439.4
Power density [kW/kg]	1.10	1.32	1.68
Machine efficiency [%]	97.2	97.7	98.0
Power factor	0.64	0.81	0.99
Normalized lamination length	1.60	1.30	1
Normalized magnet thickness	1.60	1.33	1
Normalized magnet width	1.04	1.03	1

The power density of the N45SH motor is significantly higher than the others, reaching the value of 1.68 kW/kg in the base speed point analyzed. Another important aspect is represented by the power factor at the rated working point. A high power factor allows to reduce significantly the dimension of the whole power drive for the same active power output. Again, the motor with sintered neodymium magnets offers better results for this parameter, reaching values that are close to 1. Moreover, as can be seen, to achieve a similar output torque by keeping fixed the axis height and power supply constraints, a higher lamination stack length combined with a larger cross-section of the magnets in the rotor is needed for ferrite and bonded Neodymium magnets.

To reach the same output torque as the model of the motor with N45SH magnets, the one designed with ferrite requires 60% more lamination length, while for the motor with bonded neodymium 30% more is necessary than the motor with sintered magnets. This fact is reflected in the higher usage of active materials, as can be noticed in Table 2.8. To obtain a motor that can give the same torque at the rated speed in the same condition, more materials are needed in the case of ferrite and bonded Neodymium magnets with respect to N45SH ones. This can be also seen as a partial compensation of the total cost of the machine, reducing the costs of copper and iron by about 35% in comparison to ferrite and 21% in comparison to bonded NdFeB magnets.

Based on the results of this analysis of the magnet materials, all the design studies car-

Table 2.8: Masses of the active materials for different permanent magnets type in the rotor.

	Winding [kg]	**Lamination [kg]**	**Magnets [kg]**
Ferrite	14.6	110.4	6.9
Sintered NdFeB	12.5	91.4	6.0
N45SH	10.6	72.4	4.0

ried out in this thesis for IPM motors are made by adopting high-energy density sintered neodymium magnets. In fact, despite their higher price compared to the others, the lower mass needed for all the active materials can compensate the total costs of the machine. Moreover, the higher power factor also reduces the costs of the whole electrical drive (since the apparent power required is lower) and the consumption during operation.

Chapter 3

Design procedure: case 1

In this chapter, the design procedure carried out through 2D finite element analysis for a motor that requires a high speed range is explained. In particular, an extract from this work has been published in [92]. As discussed in chapter 2, the case study explained in this chapter requires a compromise between performance, costs and easiness in manufacture; for this reason, all the modeled motors have V-shape rotor poles. The design procedure is summarized in Fig. 3.1.

The first step during the design process was to analyze the electromagnetic behavior of different rotor pole geometries through finite element analysis. Some geometrical parameters of the V-shape pole have been chosen in order to be modified. This allowed to identify if, by increasing or decreasing a certain parameter keeping fixed the others, it is possible to create a trend in the behavior of the motor performance. Once the geometry that ensures the best electromagnetic performance has been identified, the mechanical thrusts on the rotor lamination during operation have been checked. Finally, the study has been completed with the analysis of the electromagnetic performance along the flux-weakening region of the motor, together with a thermal analysis to check the possibility of operation.

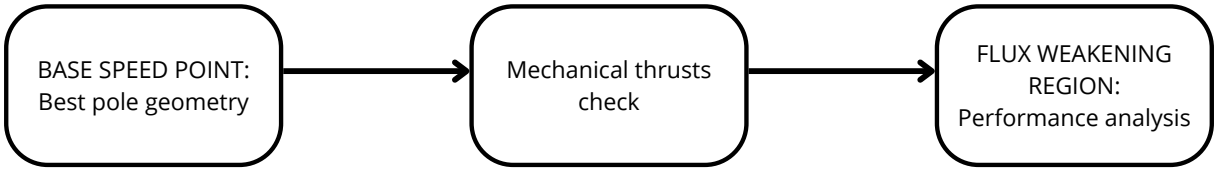

Figure 3.1: Design procedure for the V-shape IPM rotor.

3.1 V-shape pole geometry

The first steps of the design procedure are explained in this section. As described in section 2.2.1, the inner diameter of the stator lamination adopted for the design procedure is equal to 190 mm. For the rotor, a fixed rotor diameter, equal to 188.7 mm, has been chosen during the preliminary study of the design. The resulting air gap of the machine is 0.65 mm.

Regarding the geometrical parameters involved in the analysis of the V-shape pole geometry, the study has been conducted keeping fixed the winding configuration, the axial length of the machine and the RMS value of the current supply. These values will be changed later, once the final geometry has been determined. Also, the value of the base speed point set for the analysis of the geometry equal to 1500 rpm, will be changed later by modifying the number of turns per slot. In Table 3.1 the values chosen for the analysis are summarized.

Table 3.1: Starting values for the parameters.

Parameter	**Value**
Base speed point [rpm]	1500
Lamination axial length [mm]	250
Turns per slot	11
Winding parallel paths	4
Winding connection	wye
Current RMS [A]	93

Concerning the current, despite the RMS value has been kept fixed during the analysis, a different value for the control angle has been chosen for each geometry, in order to maximize the torque for each configuration. This parameter is defined as the angle between the electromotive force E and the electrical current, as shown in Fig. 3.2. The value of the control angle, which is constant in the region of the torque speed characteristics between zero rpm and the rated working point, is generally increased in the constant power region, allowing to keep constant the stator voltage of the machine.

The geometrical parameters involved in the study of the best pole geometry are shown

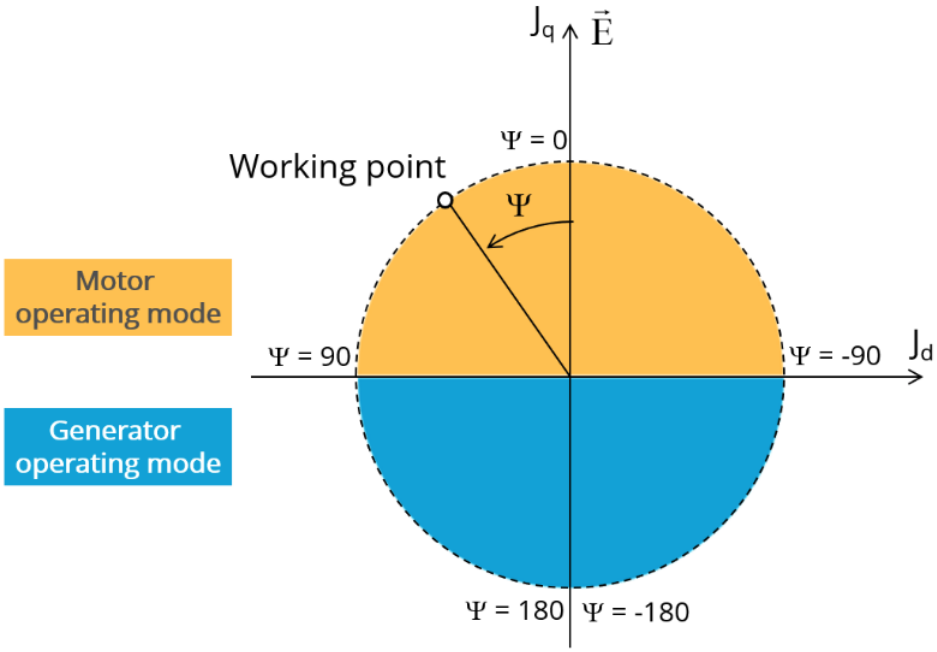

Figure 3.2: Vector representation for the control angle for IPM motors.

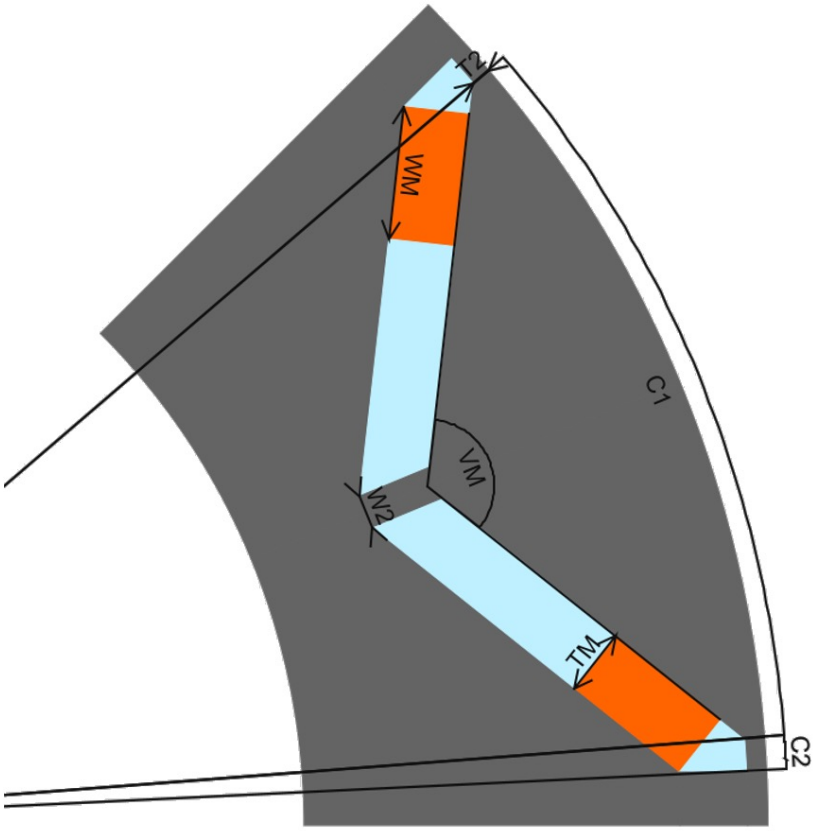

Figure 3.3: Parameters under analysis for the V-shape rotor.

in Fig. 3.3. Among these parameters, the dimensions of the radial ribs (W2) and the tangential ribs (T2) have been kept fixed to ensure mechanical stability to the structure. In particular, these values have been chosen:

- W2 = 1.9 mm
- T2 = 1.6 mm.

For the other parameters, the study is reported in the next subsections. In particular, regarding the magnet thickness TM and the magnet width WM, the study has been carried out by modifying both simultaneously to keep the total amount of magnet material inside the rotor constant. This choice allowed defining which parameter impacts more the performance of the machine. For the other parameters, instead, the study has been carried out by modifying one-by-one the angle or dimension under study, keeping fixed the others.

3.1.1 Pole shoe opening

In Table 3.2, the main results of the simulations carried out by modifying the pole shoe opening C1 are reported, while the trend of the average torque as a function of C1 is displayed in Fig. 3.4.

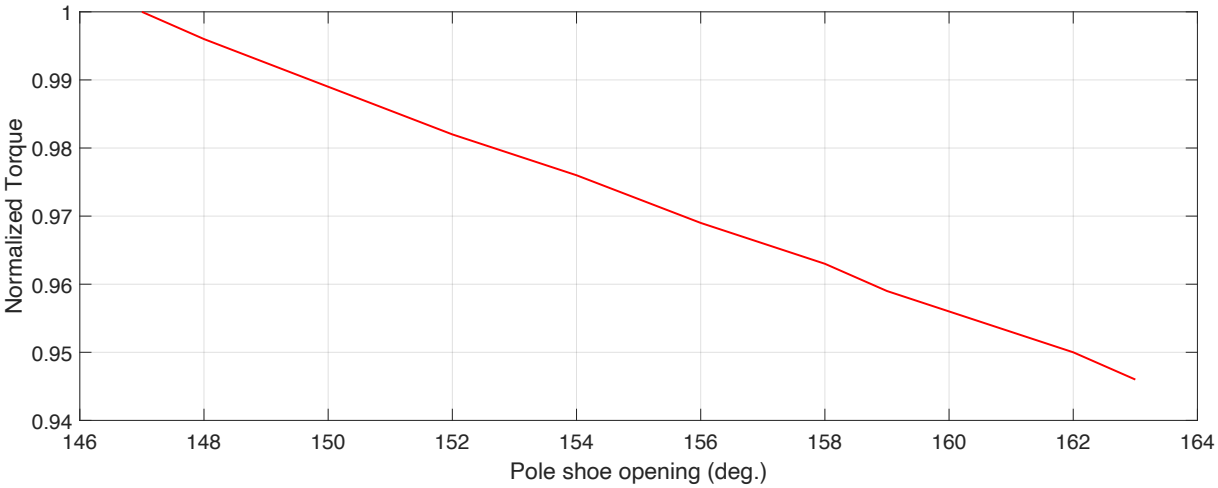

Figure 3.4: Trend of the normalized average torque as a function of C1.

Based on the simulations conducted, it emerged that the geometry that ensures the best results is the one with a C1 angle equal to 147 electrical degrees of the pole, which is the smallest among those analyzed. In particular, from Fig. 3.4, it can be noted that

Table 3.2: Main results of the analysis for the variation of the pole shoe opening C1.

C1 [deg.]	Normalized torque	Torque ripple [%]	Power factor	Efficiency [%]
147	1.000	62.6	0.948	97.1
148	0.996	62.8	0.948	97.1
150	0.989	61.8	0.943	97.1
152	0.982	58.8	0.938	97.1
154	0.976	52.3	0.937	97.1
156	0.969	43.6	0.932	97.0
158	0.963	33.8	0.930	97.0
159	0.959	29.2	0.929	97.0
160	0.956	24.4	0.929	97.0
161	0.953	19.2	0.928	97.0
162	0.950	13.8	0.927	97.0
163	0.946	14.1	0.923	96.9

the torque of the simulated machines (that has been normalized on the maximum value reached during the study of the pole shoe opening) shows an increasing trend as the C1 angle examined for this initial analysis decreases. Also, the power factor and the efficiency studied during the analysis show an increasing trend as the C1 angle decreases. As for the percentage ripple of torque, instead, it tends to increase significantly as the average torque provided by the machines during the simulations increases. In particular, for the machine with C1=147°, it reaches a value exceeding 62%, which is very high and not compatible with proper mechanical operation. Based on the results obtained from the analysis conducted, it has been decided to set the C1 angle at 147° for the subsequent simulations, while modifying the other parameters accordingly.

3.1.2 Angle between magnets

Once the optimal C1 angle was found and fixed, the behavior of the machine was analyzed as VM varied, representing the angle formed by the magnets that make up the V-shape

of the pole. With the C1 angle held constant, a variation in this parameter allows for the modification of the radial depth of the magnets within the rotor laminations. Results of the analysis are reported in Table and Fig. 3.5.

Table 3.3: Main results of the analysis for the variation of the pole shoe opening VM.

VM [deg.]	Normalized torque	Torque ripple [%]	Power factor	Efficiency [%]
110	0.979	61.4	0.940	97.1
114	0.983	61.6	0.943	97.1
118	0.988	62.2	0.946	97.1
122	0.991	62.6	0.948	97.1
126	0.994	64.4	0.951	97.1
130	0.997	65.5	0.952	97.1
134	0.998	67.3	0.951	97.1
138	1.000	68.1	0.952	97.1
140	1.000	68.3	0.953	97.1

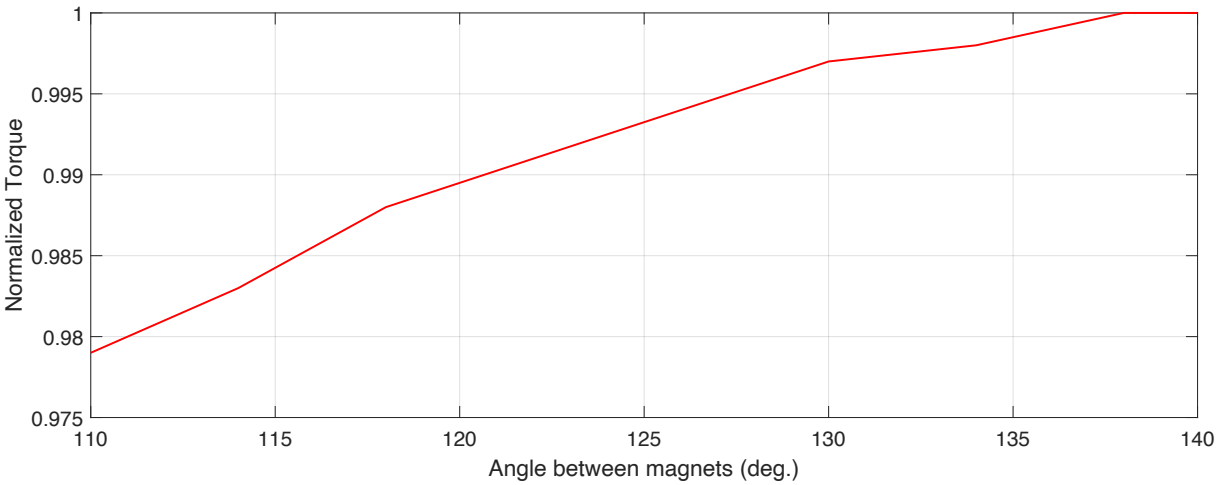

Figure 3.5: Trend of the normalized average torque as a function of VM.

As can be noticed from Table and Fig. 3.5, it emerged that an increase in the VM angle corresponds to a significant improvement in the performance of the machine. An improvement in the average torque of the machine corresponds to an increase in the power factor and efficiency as the VM angle increases. Additionally, the percentage torque ripple

increases as the VM angle increases. However, the increase in this parameter does not significantly impact the performance of the machine as markedly as the variation of the pole shoe opening C1 that has been previously analyzed.

3.1.3 Magnet width and thickness

The last parameters analyzed for the study of the geometry are the magnet width, WM, and the magnet thickness, TM. As already discussed, these parameters have been modified simultaneously during the study in order to analyze which one has more influence on the performance when the total mass of permanent magnets in the rotor is fixed. The main results of this analysis are summarized in Table 3.4, while the trend of the normalized torque as a function of the ratio WM/TM is shown in Fig. 3.6.

Table 3.4: Main results of the analysis for the variation of the ratio between magnet width and magnet thickness (WM/TM).

WM/TM	Normalized torque	Torque ripple [%]	Power factor	Efficiency [%]
4.66	0.976	67.2	0.947	97.1
4.82	0.983	67.7	0.950	97.1
4.99	0.990	68.0	0.952	97.1
5.17	0.996	68.0	0.957	97.1
5.34	1.000	67.1	0.961	97.1

From the study conducted while keeping the volume of the magnets inside the rotor constant, it emerged that increasing the length of the magnet and decreasing its thickness results in increased torque, as well as improved power factor and efficiency.

3.2 Final geometry and working point

3.2.1 Geometry considerations

From the study conducted in section 3.1, it emerged that the most significant variations in the electromagnetic performance of the studied machine are obtained through a reduction

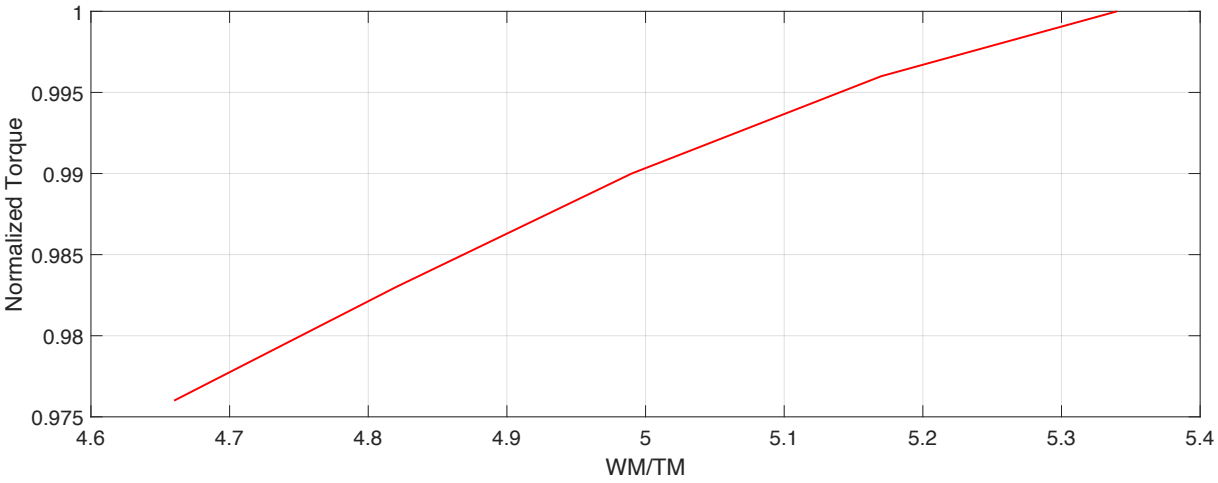

Figure 3.6: Trend of the normalized average torque as a function of the ratio WM/TM.

of the polar shoe C1 and an elongation of the magnet within the laminations, increasing the value of the parameter WM. For this reason, subsequently, the geometry was further modified following a trend dictated by these analyses. An example of geometry that ensures high electromagnetic performance is reported in Fig. 3.7.

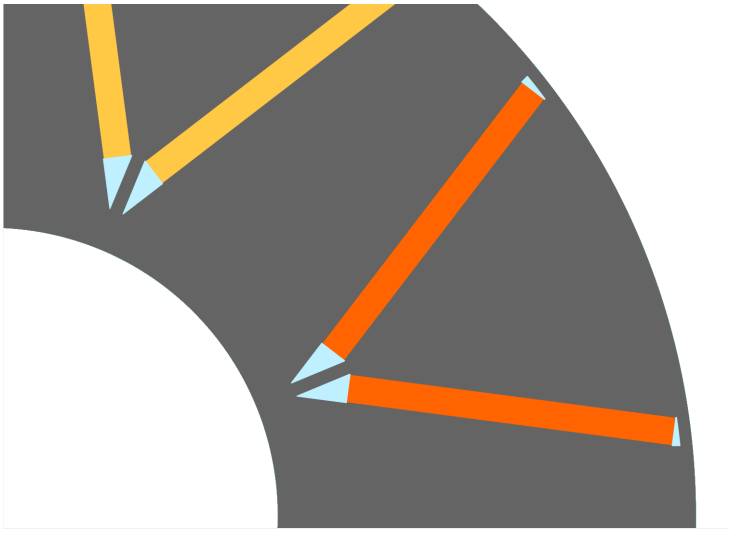

Figure 3.7: V-shape pole with magnets deep in the lamination.

The rotor shown in Fig. 3.7 presents a small angle between magnets (VM=60°), which is required to reduce the pole shoe opening C1, set to 115°. Moreover, the ratio between magnet width and magnet thickness is extremely high, equal to 11.5. These parameters for the geometry allow to obtain a mean value of the torque 10% higher than the highest obtained during the study carried out in the previous phase of the design. Also, the power

factor at the simulated operating point is higher, increasing from 0.961 to 0.989. Finally, the efficiency decreases by a small amount, remaining nonetheless very high.

Once an initial electromagnetic analysis was conducted, this type of rotor was subsequently studied from a mechanical perspective. From this study, it emerged that the forces exerted by the magnets on the laminations during operation at the required operating points are very high, thus not ensuring the mechanical stability and robustness required for the machine manufacture. The study of the mechanical thrusts of the magnets in the lamination was not carried out by the author. For this reason, only this consideration has been reported in this thesis.

Following the considerations about the mechanical thrusts on the lamination, it has been decided to analyze a rotor that maintains geometries derived from the study conducted previously (with V-shape magnets deep inside the laminations), while ensuring the necessary mechanical stability for proper operation at all required operating points. The final rotor pole geometry is reported in Fig. 3.8. The polar shoe opening occupied by the magnets in the pole has remained practically unchanged compared to the geometry studied previously (C1=120°). However, the width of the magnet has been significantly reduced together with the ratio between WM and TM (equal to 6.9). The internal angle of the V-shape formed by the magnets (VM) has been increased to reduce the area of the portion inside the pole and the forces due to centrifugal forces during operation.

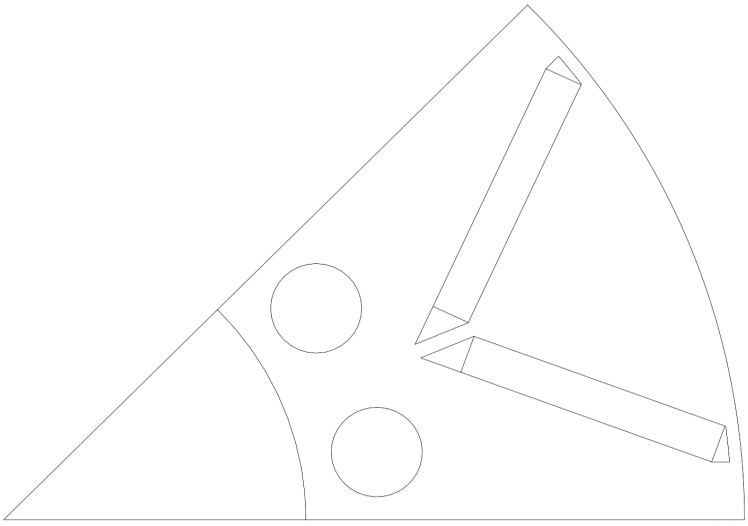

Figure 3.8: Final geometry of the V-shape pole.

Despite the lower depth of the magnets inside the rotor compared to the previously studied case, the performance is comparable between the different geometries concerning all analyzed quantities at the operating point. The obtained torque is almost unchanged if compared to the one obtained by the rotor with deeper magnets. The power factor obtained from the two geometries is almost identical, while the efficiency of the current geometry is slightly higher than that of the previous one.

3.2.2 Base speed point definition

The motor has to be designed in order to have a constant torque region up to 3500 rpm and a flux-weakening region from 3500 rpm to 9000 rpm. The target rated torque (T_n) in the constant torque region has to be at least 400 Nm, while at the maximum speed point the minimum acceptable value will be 50 Nm. Efficiency (η) and power factor ($cos\phi$) at 3500 rpm should be 94% and 0.92, respectively. The value of the maximum line-to-line RMS voltage (V_{Lmax}) is fixed to 600 V for electrical insulation related reasons, while the maximum current density (J_{max}) is 9.7 A/mm^2, mainly for thermal reasons. In Table 3.5 the characteristics of the motor under analysis in this chapter are highlighted.

Table 3.5: Main characteristics of the IPM motor under study.

Base speed point	3500 rpm
Maximum speed point	9000 rpm
Rated torque (T_n)	$\geq$400 Nm
Torque @ 9000 rpm	$\geq$ 50 Nm
Efficiency (η) @ base speed point	$\geq$ 94%
Power factor ($cos\phi$) @ base speed point	$\geq$ 0.92
Maximum line-to-line voltage (V_{Lmax})	600 V
Maximum current density (J_{max})	9.7 A/mm^2

To increase the speed from 1500 to 3500 rpm at the rated working point, a change of the winding scheme was necessary in order to keep under acceptable values the line voltage. Following this purpose, the number of turns per coil has been reduced from 11 to 8, and the parallel path in the stator winding increased from 4 to 8. Moreover, thanks to the

high current density available, which allows increasing torque and power density, the axial length of the lamination has been reduced from the starting value of 250 mm to 200 mm. Due to this selection of design parameters, the resulting design renders a motor topology that is more suitable for applications that require high power density, such as traction and propulsion applications. The changes adopted for the final configuration are summarized in Table 3.6.

Table 3.6: Comparison between starting and final values of the parameters.

Parameter	**Starting value**	**Final value**
Base speed point [rpm]	1500	3500
Lamination axial length [mm]	250	200
Turns per slot	11	8
Winding parallel paths	4	8
Winding connection	wye	wye
Current density [A/mm^2]	6.9	9.5

3.3 Torque ripple and skewing

Simulations implemented in the first part of the work, as can be noted from the tables in section 3.1, highlighted a high level of torque ripple at the base speed point. A high value in the torque ripple is not compatible with the proper operation of the machine. In order to reduce and bring it to an acceptable level, a skewing procedure became necessary.
The procedure has been made by dividing the rotor lamination stack into slices along the rotational axis. As discussed in chapter 1, the step-skew in the rotor lamination allows the reduction of the torque oscillations if properly implemented. Moreover, having barriers with a straight shape along the axial dimension, the construction methodology results easier than the one necessary for the continuous skewing technique. In fact, both lamination and magnets are divided into straight segments. During the proposed design process, the rotor lamination has been divided into three slices, that have the same axial dimension (1/3 of the total stack length of the lamination) and are skewed one with

the other by the same rotational angle. The rotational angle that occurs from the first lamination sheet and the last one has been set equal to one stator slot pitch:

$$skewing\ angle = \frac{360°}{slots\ number} = \frac{360°}{48} = 7.5° \tag{3.1}$$

Finally, the middle segment of the rotor lamination is placed in an angular position in the middle between the others: it is displaced by half a slot pitch from each of the segments at the extremes of the lamination. The configuration of the rotor skewing is shown in Fig. 3.9 and Fig. 3.10.

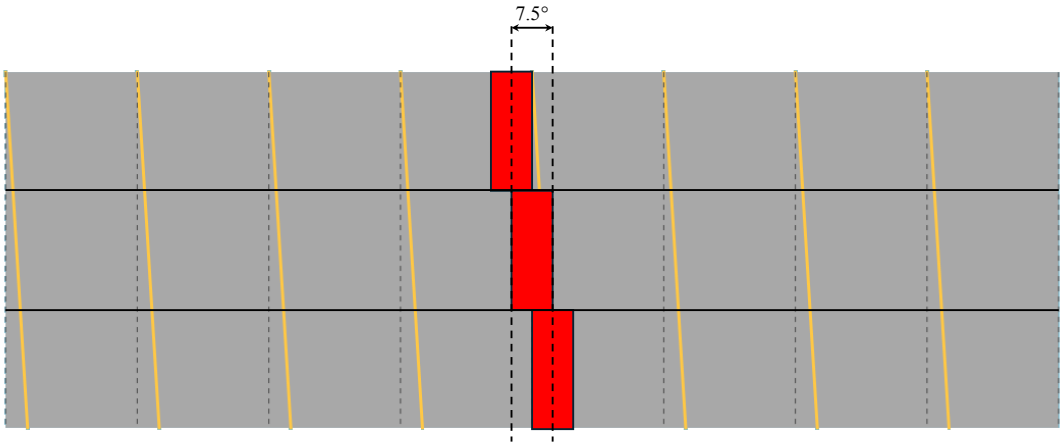

Figure 3.9: Axial view of the step-skew: segments of the magnets are represented in red. Lines in yellow represent the continuos-skew rotor model.

The comparison between normalized torque waveforms from the model with a skewed rotor and with a straight rotor is shown in Fig. 3.11. This analysis has been carried out at the base speed point of 3500 rpm, and in the figure two periods of the waveforms are reported. As expected, a period corresponds to one stator slot pitch, because the torque ripple strongly depends on the electromagnetic interaction between the rotor pole and the stator teeth.

In the plot shown in Fig. 3.11, the torque has been normalized to analyze the difference in percentages of the ripple concerning the average torque of the two models.

The torque ripple peak-to-peak for the non-skewed rotor simulated at 3500 rpm is 162.3 Nm, equal to 36.2% of the average torque. For the skewed motor, the resulting simulated torque ripple peak-to-peak is 13.0 Nm, equal to 3.0%. As to average torque, the non-

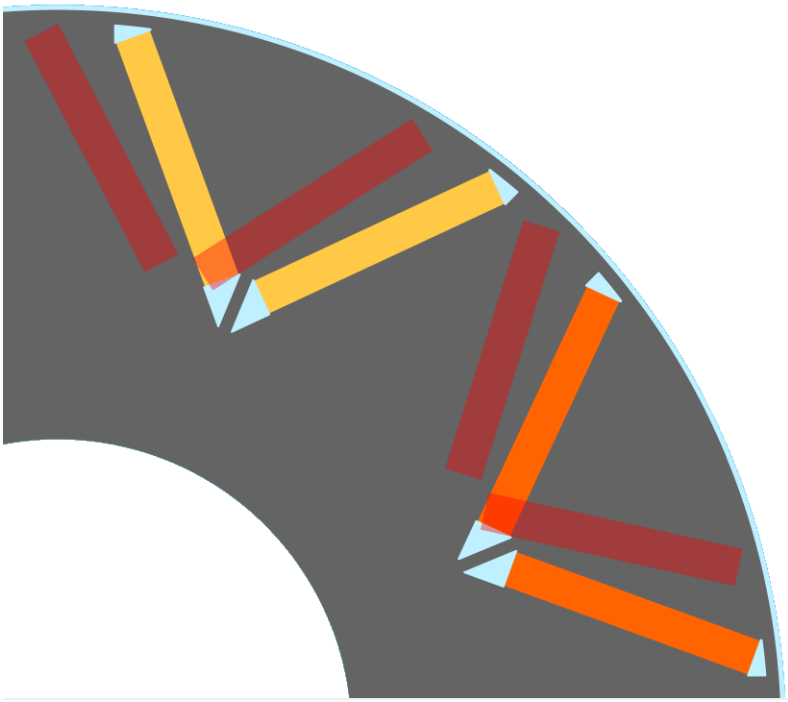

Figure 3.10: Representation of the first and last segment of lamination in the plane.

skewed model develops 448.1 Nm at the base speed point, while the skewed one reaches 439.4 Nm with the same current density. For both models, the average torque obtained at the base speed point from the simulation is much higher than the one required in the motor's initial specifications. While a reduction in the average torque is expected for a skewed motor concerning a non-skewed one, the reduction obtained from the IPM model considered is around 2%. Moreover, 3.0% of peak-to-peak ripple torque is a value that allows the safe continuous operation of the motor, especially in terms of noise and vibration, which are strictly related to this problem in rotating electrical machines.

3.4 Flux weakening region analysis and results

In this section, the results of the simulations carried out to analyze the behavior of the machine in the flux-weakening region are presented. For this study, the simulations have been carried out just for the base speed point and every 1000 rpm from 4000 rpm to the maximum speed of 9000 rpm. All the simulations have been carried out by studying both the electromagnetic and thermal behavior of the machine by inserting the appropriate parameters to simulate an adequate cooling system. In particular, the hypothesized cool-

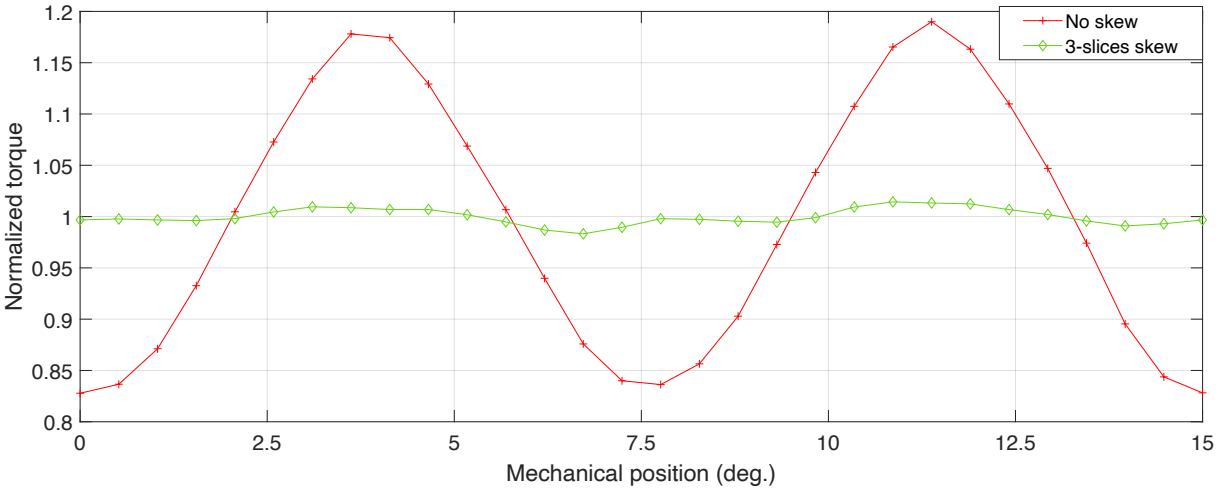

Figure 3.11: Normalized ripple period for non-skewed and skewed rotor at the base speed point (3500 rpm).

ing system of the machine involves both a liquid jacket, which consists of a spiral liquid circuit within the thickness of the frame, and forced air through a ventilation fan, improving the airflow inside the frame. A maximum operating temperature for the magnet has been chosen and set to 120°C, to avoid demagnetization risks (the maximum operating temperature of N45SH magnets from the datasheet is around 180°C). If the temperature of the magnets in the simulation exceeds this reference value, the current density is reduced to decrease at the same time the Joule losses in the stator and, consequently, the operating temperature.

3.4.1 Torque - speed characteristics and torque ripple

Fig. 3.12 shows the torque - speed characteristics of the analyzed motor with skewed rotor geometry.

As already described in section 3.4, up to the base speed point, the output rated torque of the motor is 439.4 Nm, offering a power density at 3500 rpm equal to 1.68 kW/kg. In the first part of the flux-weakening region, the decrease of the torque is linear with the increasing speed of the rotor, creating a constant power region where the control angle is increased to keep the voltage constant. As will be shown in subsection 3.4.3, the current density in the last part of the characteristics has been reduced for thermal reasons. Thus, from around 6000 rpm the reduction of the torque is much higher than the increase of

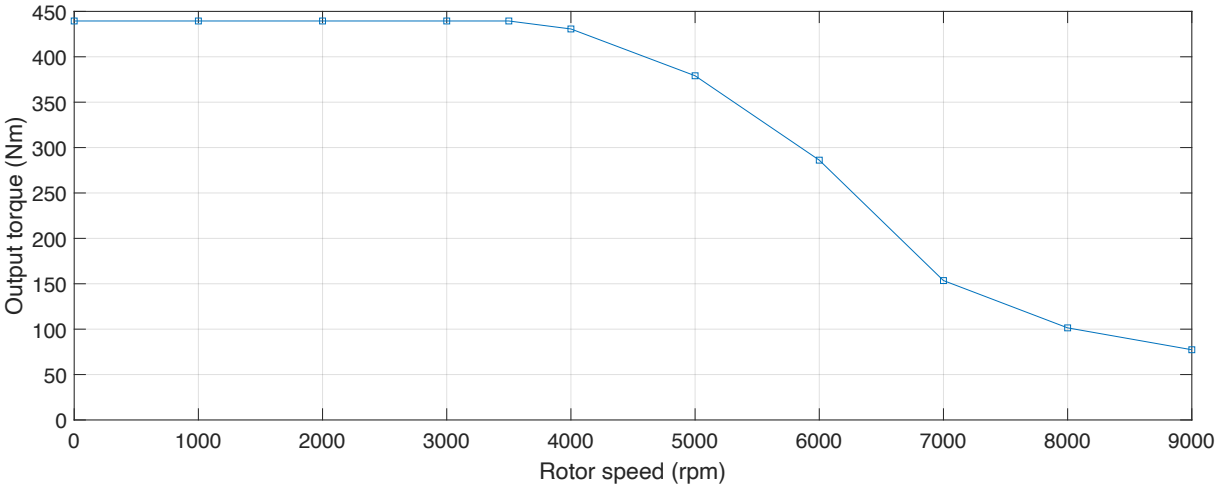

Figure 3.12: Torque - speed characteristics of the motor under thermal constraints.

the speed. However, at the maximum speed point, the output torque of the motor after simulations is 77.3 Nm, which is still higher than the required one reported in Table 3.5. The first analysis carried out after the construction of the characteristics of the motor is about the torque ripple of the machine along the flux-weakening region. The results of this study are summarized in Fig. 3.13.

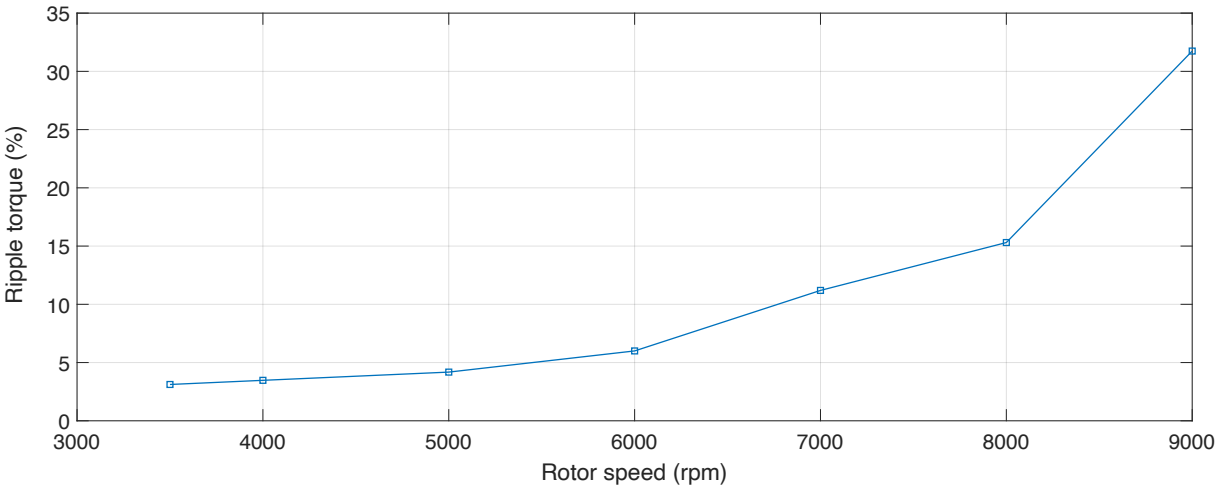

Figure 3.13: Torque ripple percentage vs. speed for the skewed rotor model in the flux-weakening region.

As already explained in section 3.3, the peak-to-peak ripple obtained from the simulations at the base speed point is 13.0 Nm, equal to 3.0% of the rated mean torque of the motor at this speed. For the plot reported in Fig. 3.13, the percentages have been calculated on the average torque of the motor in all the working points of the torque - speed curve

analyzed in Fig. 3.12. The torque ripple remains low in percentage up to 8000 rpm, where the maximum value in percentage is around 15%. At the working point at 9000 rpm (maximum speed point), it grows up to 31.7%, due to the low average torque developed at that point (77.3 Nm). In fact, the peak-to-peak value of the torque for the simulation at the maximum speed point is only 24.5 Nm, which is still much lower than the one obtained by the starting motor at the base speed point.

3.4.2 Efficiency and power factor

Two other important parameters to evaluate the global performance of the machine in the flux weakening region are the efficiency of the machine and the power factor. In particular, as already discussed, keeping the values for these parameters high allows to reduce the dimensions of the global electrical drive, being the apparent power in input close to the mechanical power at the shaft of the motor. The trend of the efficiency as a function of the rotor speed in the flux weakening region is displayed in Fig. 3.14.

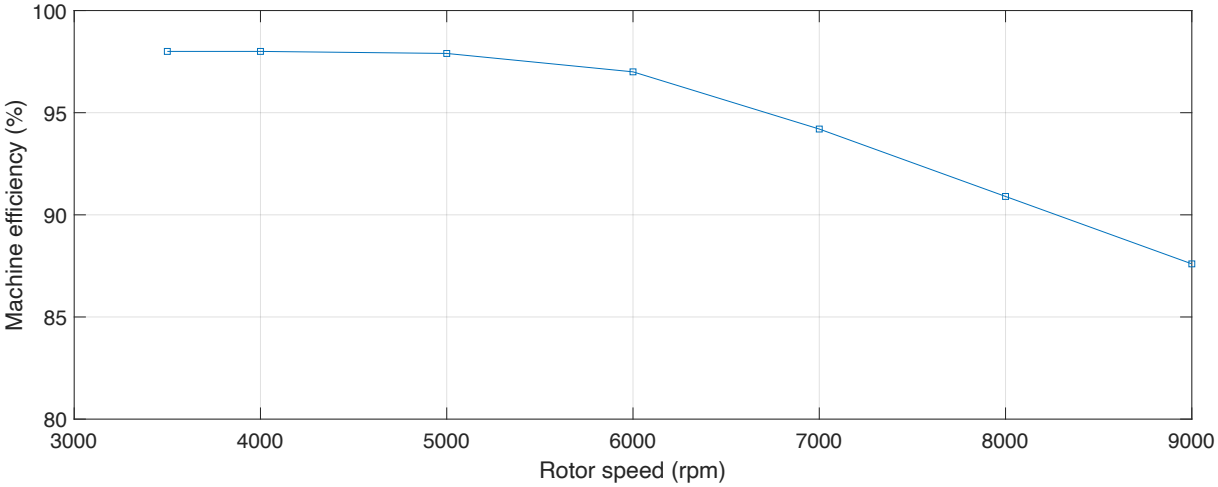

Figure 3.14: Efficiency vs. speed for the skewed rotor model in the flux-weakening region.

As can be seen, the efficiency remains high for all the torque-speed characteristics, starting from a peak value of 98% in the base speed point. Reduction in efficiency can be seen starting from 7000 rpm to 8000 rpm. This is mainly due to iron losses, which represent the majority of power losses in the high supply frequency (f_s) region. Iron losses increase from about 5.2 kW at 7000 rpm ($f_s = 466.7$ Hz) to 6.9 kW at 8000 rpm ($f_s = 533.3$ Hz) and 8.7 kW at 9000 rpm ($f_s = 600.0$ Hz) despite the mechanical power decrease during

this range from 112.5 kW at 7000 rpm to 72.9 kW at 9000 rpm. Even though iron losses increase as the speed increases,the efficiency remains high throughout the torque-speed characteristics. Its minimum value, calculated in the maximum speed point, is higher than 87%.

Power factor behavior as a function of rotor speed in the flux-weakening region is shown in Fig. 3.15

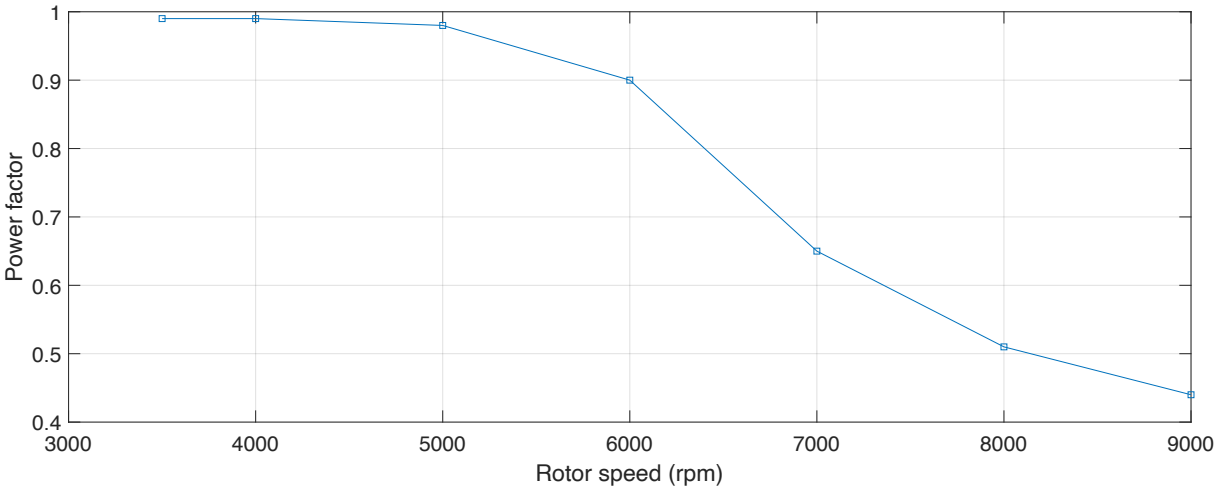

Figure 3.15: Power factor vs. speed for the skewed rotor model in the flux-weakening region.

At the base speed point the power factor is close to 1. This is mainly due to the high remanent flux density B_r of the N45SH magnets. Extremely high values of power factor result from simulations up to the speed of 6000 rpm, in which $cos\phi$ is equal to 0.90. Starting from this point, the power factor begins to decrease reaching its minimum value of 0.44 at 9000 rpm.

The quick reduction in the value of the power factor is due to the simultaneous increase of the control angle Ψ (the angle between the electromotive force E and the current I vectors), which is required in order to keep under safety limits the line voltage of the machine. At 7000 rpm, where the power factor is equal to 0.65, Ψ is set to 76°; in the maximum speed point, the control angle is equal to 82°.

3.4.3 Current density and flux density

Finally, some considerations can be written about the current density and the map of the flux density inside the machine pole. Regarding the current density from the simulations, it is directly related to the imposed thermal constraint. When the temperatures of the machine exceed the limit in the speed point analyzed, the current density has been reduced, therefore lowering the Joule losses of the stator winding during operation. In particular, as already explained, the temperature of the magnets has a crucial role in thermal considerations, since the demagnetization process is strongly affected by it. In Fig. 3.16, an example of a map of the temperature in different regions of the motor is reported.

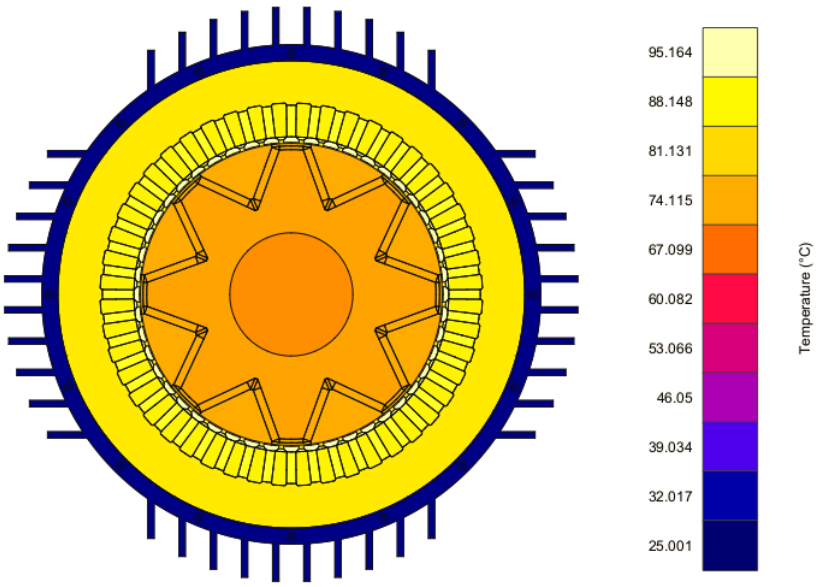

Figure 3.16: Thermal analysis of the motor model at 8000 rpm speed.

Following the previous considerations, the plot of the imposed value of the current density as a function of the rotor speed is reported in Fig. 3.17.

The maximum value of the current density is set to 9.5 A/mm^2, fixed until 6000 rpm. In the maximum speed point, it decreases to 7.7 A/mm^2, allowing to reduce the Joule losses in order to compensate the increase of temperatures due to the increasing speed and, because of the high supply frequency, iron losses.

Finally, in Fig. 3.18 the map of the flux density at the rated working point for the studied machine is represented. Hotspots in the rotor are located in the ribs, and in particular in

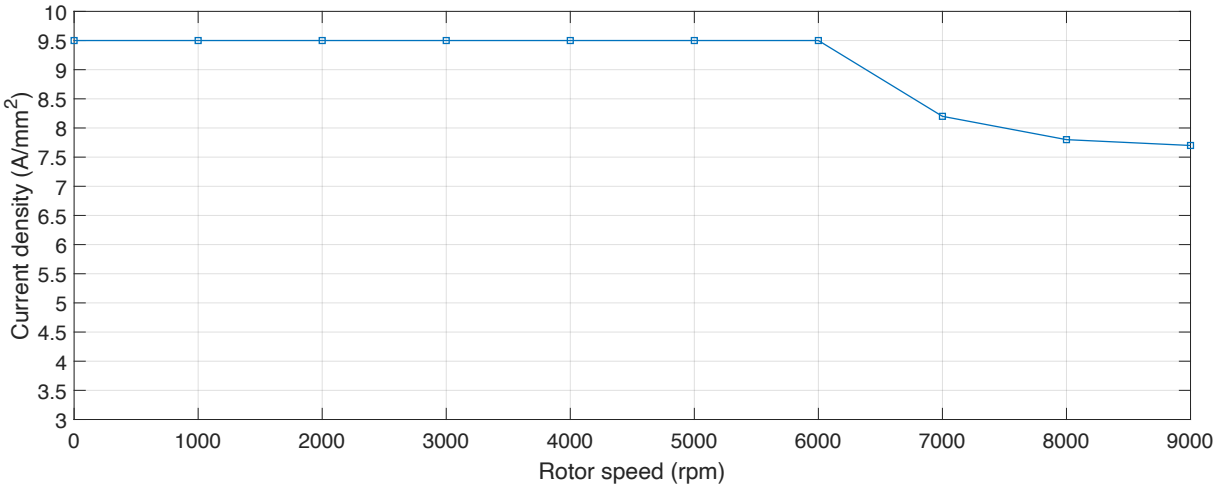

Figure 3.17: Current density vs. rotor speed for different speed conditions of the motor.

those closest to the air gap. In those regions, saturation is reached and the flux density has maximum values of about 2.7 T.

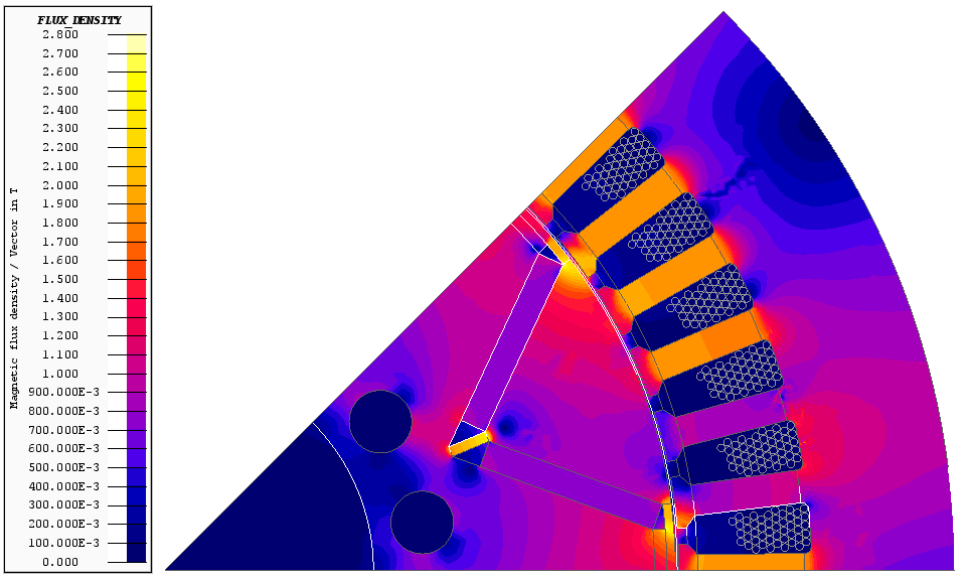

Figure 3.18: Map of the flux density in the lamination obtained through a 2D FE simulation at the base speed point.

3.5 Conclusions

The work presented in this chapter, together with the considerations explained about the materials in section 2.3, highlighted that IPMSMs can satisfy high performance over a wide speed range when their magnet topology is optimized by FEA and combined with rotor skewing and suitable choice of ferromagnetic materials. A complete FEA-based procedure for the design of a 160 kW IPMSM with high performance over a wide speed range is presented. In the first part of the research, different types of permanent magnet materials have been investigated to achieve the same rated torque, by changing the dimensions of the machine. The results of the simulations prove that the lower B_r of ferrite and bonded Neodymium magnets involves higher active materials weight and axial length, despite the largest cross-section, in comparison to high-energy sintered N45SH. The low mass of permanent magnets in the rotor, combined with the high power density of the motor, allows to keep low the overall material cost of the machine. The simple V-shape rotor pole geometry permits to obtain high performance (summarized in Table 3.7) in the base speed point thanks to the study of the optimal geometry, and to simplify the construction of the rotor with a single magnet layer. The high efficiency and the high power factor reached allow to reduce the costs of the entire drive, by coupling the motor to an inverter with an apparent power close to the maximum active power required.
Finally, the introduction of the 3-step skewing in the rotor has led to a net lowering in torque ripple, with a slight decrease of 10 Nm in the average torque (2%). Moreover, torque ripple can be considered acceptable even in the flux-weakening region.

Table 3.7: Main parameters of the designed motor obtained from 2D-FE simulations.

Permanent magnet mass (N45SH)	4.0 kg
Base speed point	3500 rpm
Maximum speed point	9000 rpm
Rated torque (T_n)	439.4 Nm
Torque @ 9000 rpm	77.3 Nm
Efficiency (η) @ base speed point	98%
Power factor ($cos\phi$) @ base speed point	0.99
Maximum line-line voltage (V_{Lmax})	600 V
Maximum current density (J_{max})	9.5 A/mm^2

Chapter 4

Design procedure: case 2

In this chapter, the design procedure of an IPM carried out through 2D finite element analysis is explained. The study involved the modeling and design of an interior permanent magnet synchronous motor for a high speed test bench. In particular, this study has been published in [93]. The main characteristics of the motor are summarized in Table 4.1. The analysis of this case study focused firstly on the optimal choice of the number of poles. The study of the number of poles has been carried out simultaneously with an analysis of different rotor pole topologies through simulation over the whole required speed range. After these analyses, some geometrical parameters of the rotor poles have been modified to improve performance. Once again, the geometries that offered the best performance in the base speed point have been evaluated together over the flux-weakening region. This analysis allowed to determine which configuration offers the best performance at high speed. All the analyses explained so far for the case study reported in this chapter have

Table 4.1: Main characteristics of the motor of the high speed test bench.

Rated power	350 kW
Base speed point	5000 rpm
Constant power region	5000 rpm $\leq$ speed $\leq$ 8000 rpm
Maximum speed	$\geq$ 15000 rpm
Rated torque	670 Nm
Shaft axial height	160 mm

included the use of Altair software FluxMotor.
In order to obtain more accurate results, a final analysis has been conducted on the definitive geometry using Altair Flux, which allowed to implement in the model some non-ideality.

4.1 Poles number and shape

As already explained, in the initial analysis, it is necessary to determine the number of poles that best suits a motor with such characteristics. In this case study, a comparison was made between motors with 6 and 8 poles, as solutions with a number of poles greater than 8 could be excluded a priori due to the high losses that would occur at the high frequency at which the current circulates, especially at the maximum speed point. Similarly, it has been decided to avoid solutions with a number of poles lower than 6, due to the results of the previous research explained in section 2.2.
Simultaneously to the analysis of number of poles, two possible rotor geometries were evaluated:

- V-shape rotor;
- Delta-shape rotor.

The reason for this choice lies, like for the case study explained in chapter 3, in the ease of magnet insertion within the rotor stack during the construction phase of rotors with these configurations. As already discussed in chapters 1 and 2, both configurations have their advantages and disadvantages, and there is no absolute best configuration. Therefore, it is essential to conduct an extensive study to find the best design for each case study.

4.1.1 Stator configuration

Regarding the stator, during the analysis conducted in this case study, two different types were modeled: one for the machine with 6 poles and another one for the machine with 8 poles. In order to change the smallest number of parameters during the analysis and make the influence of the stator less significant, two stators with the same number of slots

per pole and per phase were chosen: specifically, stators with 2 slots per pole and per phase, meaning 36 stator slots for the 6 poles motor and 48 stator slots for the 8 poles one. The geometries of the stators chosen for the analysis are depicted in Fig. 4.1.

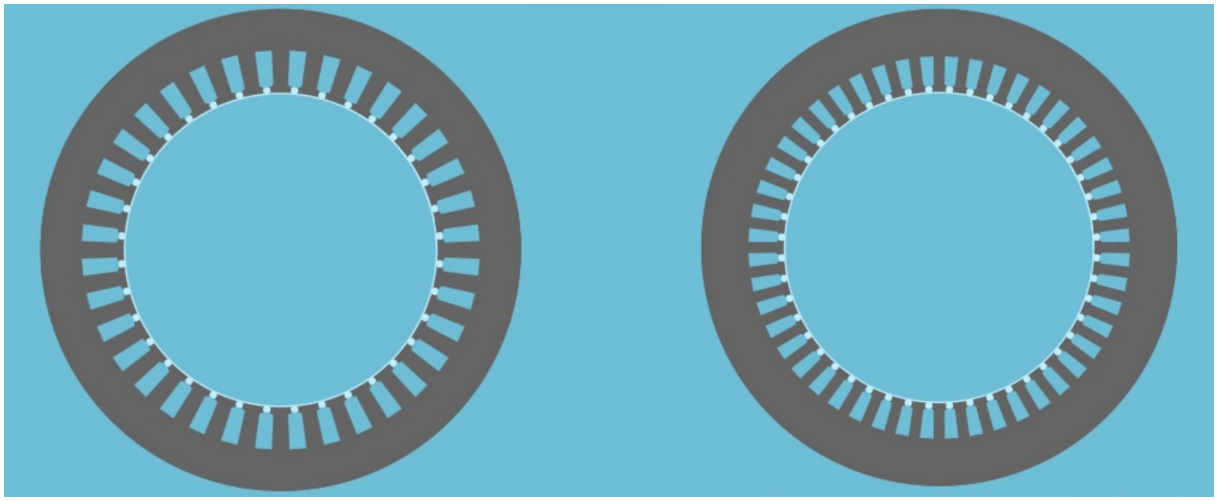

Figure 4.1: Different stator configurations chosen for the analysis: 6 poles (left); 8 poles (right).

Once the geometries of the slots for both configurations have been chosen, the type of winding has been analyzed to have similar results in terms of voltage and current density at the same reference speed. The parameters chosen are presented in Table 4.2.
For both the motors with 6 and 8 poles, except for the number of slots and their geometries, other geometrical parameters are identical. The outer diameter of the stator has been set to 295 mm, while the inner diameter is equal to 195 mm. Finally, the length of the stator laminations stack has been chosen, equal to 300 mm. For the stator core, NO20-1350N laminations with a thickness of 0.2 mm were used. This material has relatively

Table 4.2: Winding parameters for the analyzed configurations.

Parameter	**6 poles**	**8 poles**
Slots per pole per phase	2	2
Turns per coil	10	10
Parallel paths	3	4
Slot fill factor	36%	36%

low specific losses even at high supply frequency, essential for a high speed permanent magnet synchronous motor. When the motor is supplied at 50 Hz, the specific value of iron losses at 1.5 T ensured by the manufacturer is 2.24 W/kg. Some of the specific losses for different supply frequencies as a function of the flux density are summarized in Fig. 4.2.

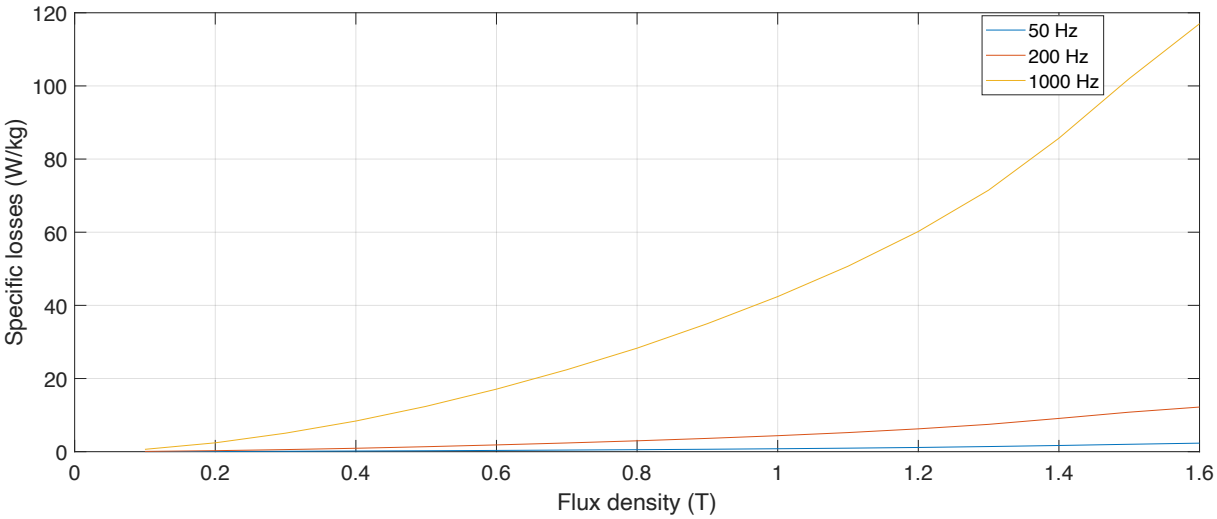

Figure 4.2: Specific losses for the NO20-1350N at different supply frequencies [94].

4.1.2 Rotor initial configurations

As mentioned previously, for the first analysis, four different rotors have been modeled and coupled to their respective stators:

- 6-poles V-shape to the 36-slots stator;
- 8-poles V-shape to the 48-slots stator;
- 6-poles Delta-shape to the 36-slots stator;
- 8-poles Delta-shape to the 48-slots stator;

In modeling the V-shape rotors, efforts were made to make the geometries proportionally equal so that the number of poles was the only varying parameter. The weight of the magnets also remained constant. The same principle was applied to model the two rotors with Delta-shape configuration. The shape of the rotors chosen for the analysis is shown

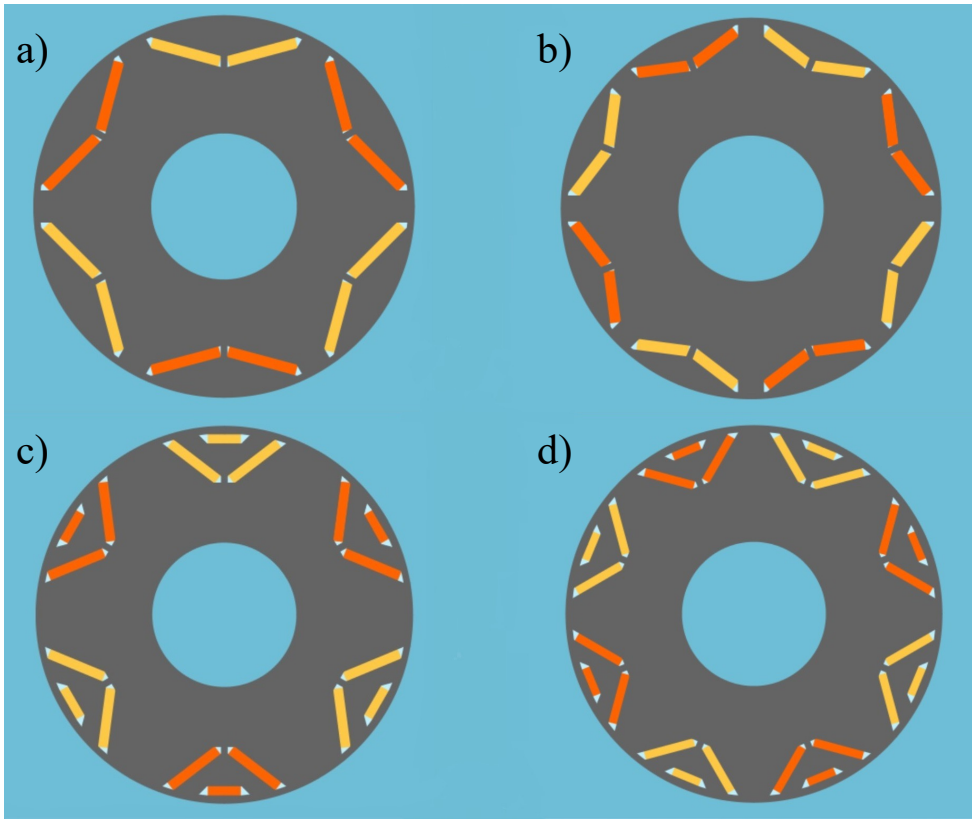

Figure 4.3: Rotors chosen for the analysis of the number of poles: V-shape and 6 poles (a); V-shape and 8 poles (b); Delta-shape and 6 poles (c); Delta-shape and 8 poles (d).

in Fig. 4.3.

For the rotor, the same lamination material adopted for the stator (NO20-1350N) has been employed, along with N45SH permanent magnets that, as already explained in chapter 2, offer a nominal residual induction of 1.35 T, ensuring a combination of excellent magnetic performance and moderate costs.

Table 4.3: Winding parameters for the analyzed configurations.

Stator lamination	NO20-1350N
Rotor lamination	NO20-1350N
Permanent magnets	N45SH
Cooling system	Forced air + water
Water flow rate	35 l/min

Finally, to conduct the thermal analysis in addition to the electromagnetic one, the cooling system was also modeled. This system includes an internal forced air cooling generated by a fan located on the shaft and an external forced water cooling system. In Table 4.3 materials and cooling parameters of the model are resumed.

4.2 Results of the first analysis

4.2.1 Definition of the working points

In order to carry out an adequate performance comparison between the different proposed configurations, it is necessary to define a series of operating points at which the machine must operate, establishing three main parameters: the stator current density, the control angle, and the rotor speed. The RMS value of the nominal current density was chosen to be 9.5 A/mm^2 as in the case study analyzed in chapter 3. For a current density set to this value, the machine is correctly sized from a thermal perspective, ensuring that neither the insulation nor the magnets will reach critical temperatures.

As already discussed in the previous chapters, when the machine operates at speeds higher than the rated one, losses due to eddy currents within the permanent magnets increase the temperature inside them. Indeed, when exposed to high temperatures, permanent magnets partially or completely lose their magnetization, with obvious negative repercussions on the motor's performance. For this analysis, a temperature higher than 120-150°C has been considered as critical for the proper operation of the magnets. Since only simulated software behavior was known during the design process and not the actual machine behavior, a cautious maximum value of 75°C was imposed.

The simulations were therefore carried out, like for the analysis explained in chapter 3, while constantly monitoring the temperature, lowering the current density value at those operating points where the temperature of the magnets exceeded 75°C.

To determine the optimal "control angle" value for controlling the machine at each speed, in the present case, some simulations have been carried out by changing it in order to obtain the highest value available for the torque. As for the rotor rotation speed, a range of values was taken from 5000 rpm (base speed point) to 15000 rpm with steps of 1000 rpm between one working point to the other. Once the three parameters defining the

operating point were inputted, initial temperatures of the magnets, conductors, external air, and coolant liquid were set at 25°C.

4.2.2 Simulation results

To make the comparison between the two motors with a V-shape configuration and the two motors with a Delta-shape configuration, the analysis has been carried out by studying along the flux-weakening region the torque behavior, power factor behavior, and efficiency behavior as functions of rotor speed. The results of the simulations are shown in Figs. 4.4-4.6.

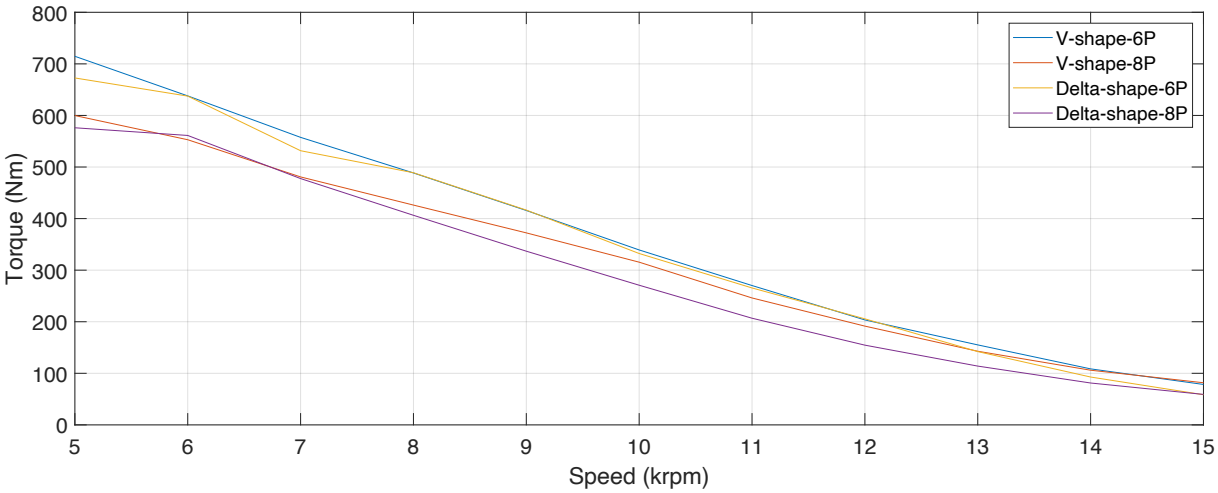

Figure 4.4: Torque behavior of the different configurations in the flux-weakening region.

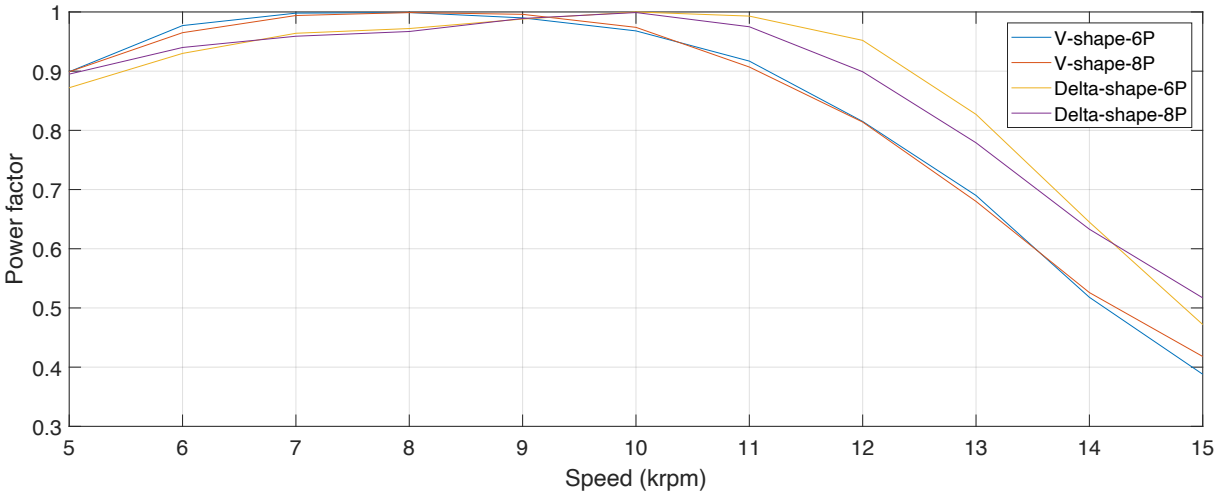

Figure 4.5: Power factor behavior of the different motors in the flux-weakening region.

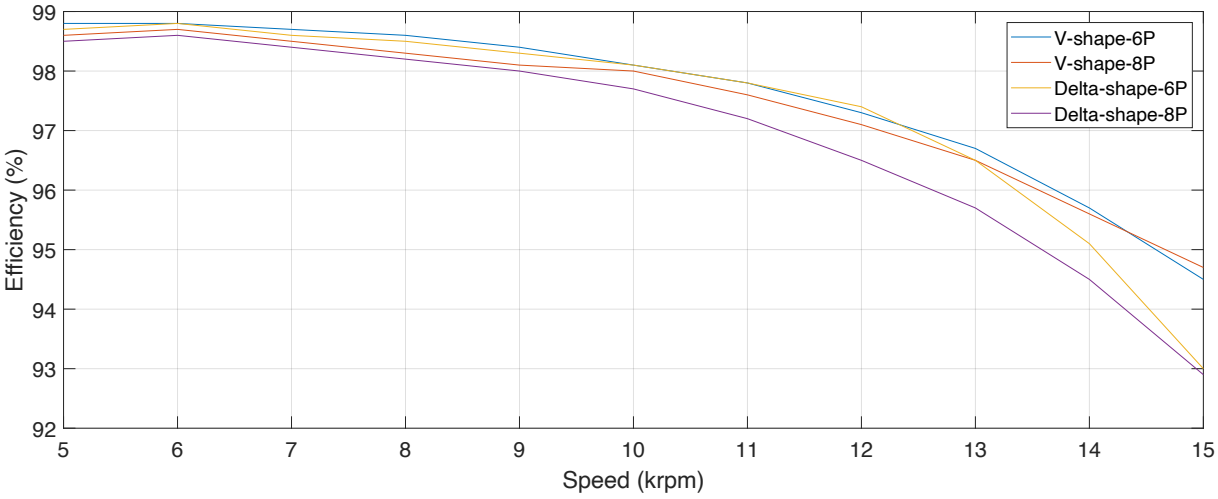

Figure 4.6: Efficiency behavior of the different configurations in the flux-weakening region.

Regarding the V-shape configuration, all analyzed quantities exhibit better results in the 6-poles motor. The torque remains higher across all operating points until it practically reaches the same value at 15000 rpm. The same applies to efficiency, with the only difference being a slightly lower value around 14500 rpm. The power factor values are almost identical across all operating points.

Similarly, for the Delta-shape rotor configuration, the results highlight the superior performance of the 6-pole motor in practically all operating points. Especially for what concerns efficiency, these results were expected, since the lower supply frequency involves lower iron losses in the lamination.

From this preliminary analysis, it can be concluded that 6 poles is the ideal number for the machine during the design phase. Therefore, only motors with this number of poles will be further analyzed.

4.3 Analysis of the pole shapes

As already explained in chapter 3, each geometric parameter influences the electromagnetic behavior and performance of the interior permanent magnet machine. Due to this fact, each parameter of the rotor was analyzed to understand its influence on the machine's performance. Each geometric parameter was examined at a time, varying it in small intervals while keeping all other parameters constant. Through careful analysis of

the results, it was possible to understand which parameter modifications positively or negatively affect the performance and thereby derive geometries best suited for operation at the rated speed. In all simulations, the weight of the magnets was kept constant and equal to 6 kg. The current density and the rotor speed were kept constant in all simulations, set respectively at 9.5 A/mm^2 and 5000 rpm (rated speed). The control angle was calculated before each simulation since varying the geometry might slightly alter its optimal value.

Regarding the analysis for the V-shape rotor, results achieved in this case study follow the trend already discussed in section 3.1 for the previous case study. The efficiency, torque, mechanical power, and power factor increase as the angle formed by the magnets increases. Additionally, considering that, to keep the weight of the magnets constant, an increase in their thickness results in a shortening and vice versa, it was found that a reduction in thickness accompanied by an increase in length improves the electromagnetic performance of the motor.

Parameters of the Delta-shape rotor configuration are shown in Fig. 4.7.

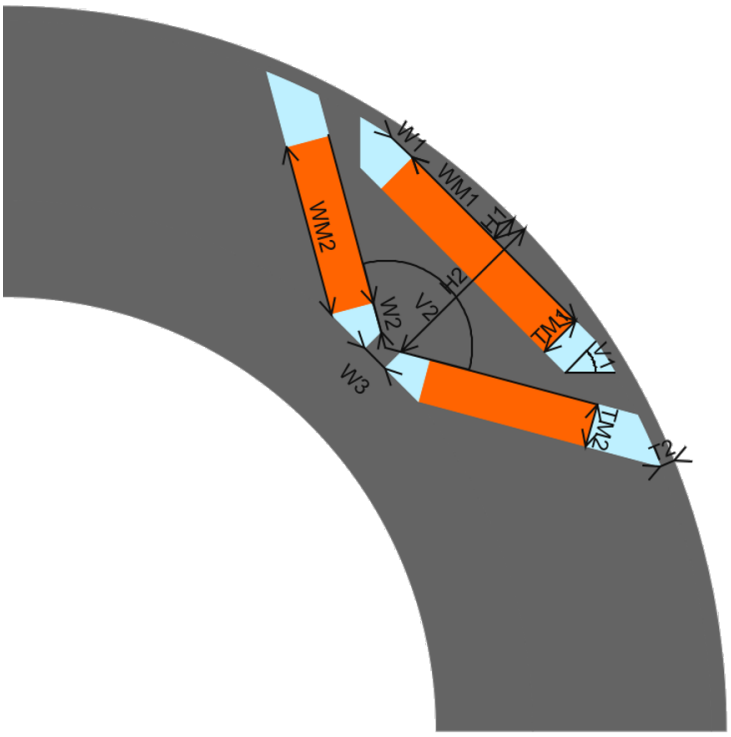

Figure 4.7: Geometrical parameters for the Delta-shape pole configuration.

In the Delta-shape configuration, to vary the angle formed by the magnets, it is necessary

to slightly modify the thickness and length of the magnets as well. The results obtained confirm that, even with this configuration, increasing the angle formed by the magnets improves the motor's performance. However, the increase in torque, efficiency, mechanical power, and power factor is much lower compared to the increase observed in the V-shape rotor configuration. This phenomenon can be attributed to the increase in the thickness of the magnets. As previously demonstrated for the V-shape configuration, the narrower and longer the magnets, the better the performance at the nominal speed operating point. In practice, there are two opposing effects: on one hand, increasing the angle between the magnets improves performance. On the other hand, increasing the thickness worsens it. Regarding the variation in magnet thickness with the Delta-shape configuration, two rotors were modeled where the only different parameters were the thickness and length of the two magnets that compose the "V" geometry, keeping the geometry of the central magnet constant. The simulation results confirm that, for the Delta-shape rotor as well, decreasing the thickness and increasing the length of the magnets lead to an improvement in performance, as shown in Fig. 4.8.

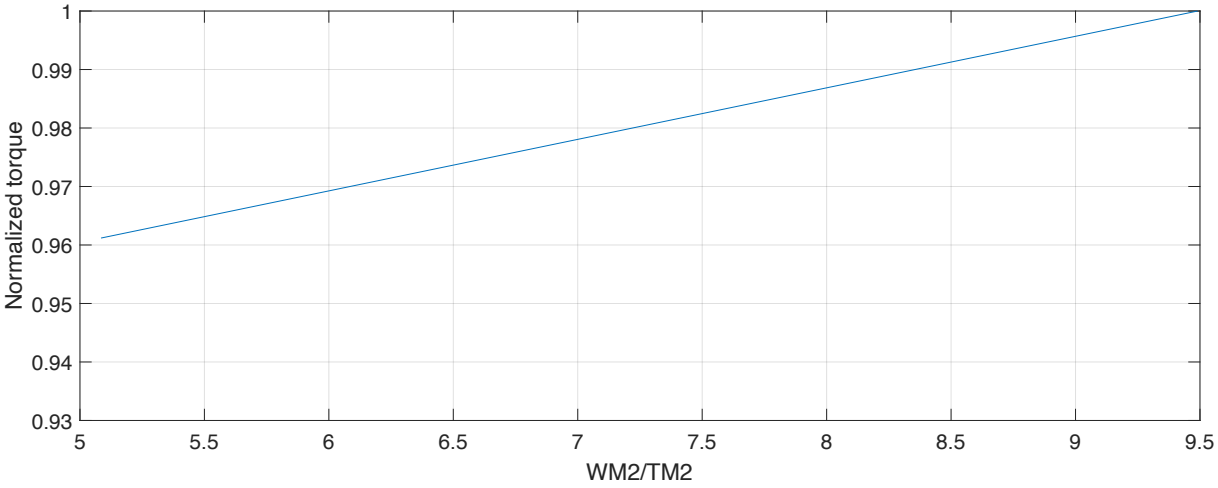

Figure 4.8: Trend of the normalized average torque as a function of the ratio WM2/TM2.

After this first analysis, a study was conducted on the following three geometric parameters related to a rotor with magnets arranged in the Delta-shape configuration:

- radial rib thickness (W3 in Fig. 4.7);
- pole shoe opening;

- thickness of the central magnet (TM1).

The parameter W3 was modified starting from a value of 4 mm down to 2.5 mm with a step of 0.15 mm: this thickness was not further reduced because, being a motor designed to operate at high speeds, a lower thickness could make the radial rib too fragile from a mechanical point of view. The results show that tightening the rib improves the overall performance of the motor. In Fig. 4.9 the behavior of the torque as a function of this parameter is reported.

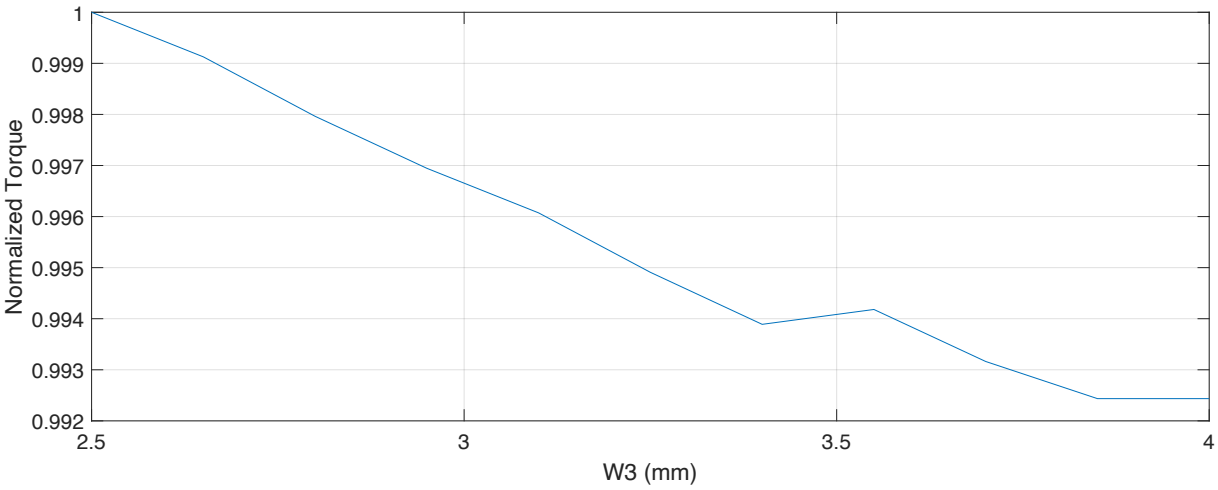

Figure 4.9: Trend of the normalized average torque as a function of W3.

Regarding the modification of the pole arc occupied by the magnets in the Delta-shape configuration, it is only possible to vary the occupied pole arc of the magnets by also modifying the thickness and length of the magnets. From the results, which are shown in Fig. 4.10, it can be observed that, by decreasing the pole arc and consequently making the magnets shorter and narrower, torque decreases. In particular, in Fig. 4.10 the normalized torque is represented as a function of the radial height of the magnets inside the lamination. This parameter is inversely proportional to the pole arc opening: as H2 increases, the pole shoe opening decreases.

It can be hypothesized that the positive contribution of decreasing the pole arc is not sufficient to counteract the negative contribution given by the shortening and increase in thickness of the magnets. Furthermore, the presence of the third magnet could be the cause of further performance degradation because by greatly reducing the pole arc occupied by the magnets, the portion of iron directly facing the air gap becomes very

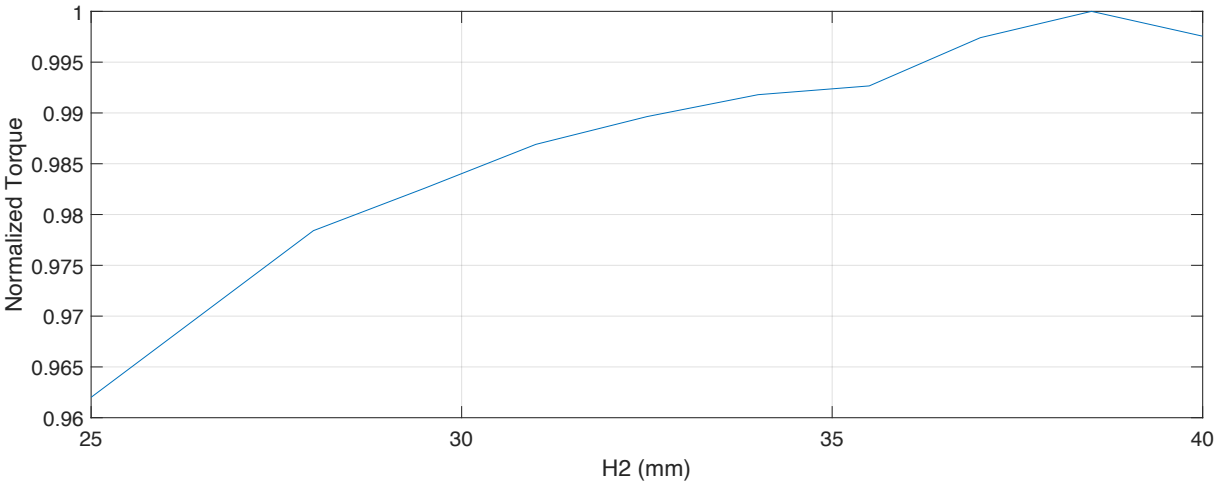

Figure 4.10: Trend of the normalized average torque as a function of H2.

small and subject to saturation. It is therefore possible to state that, unlike the V-shape rotor (studied in subsection 3.1.1), in this case, reducing the pole arc occupied by the magnets does not produce positive effects on the performance of the motor.

Finally, to study the influence of the thickness of the central magnet on the performance, the parameters TM1 (thickness) and WM1 (length) have been modified. It was necessary to also modify the parameter H1, which regulates the distance of the central magnet from the air gap, to maintain constant the thickness of the ribs dividing the air gap from the air barrier where the magnets are inserted, and to prevent the flux from not properly linking with the winding. In Fig. 4.11, the two extreme simulated geometries are shown. The results demonstrate that a thinner and longer magnet leads to an increase in torque (as shown in Fig. 4.12), mechanical power, power factor, and efficiency.

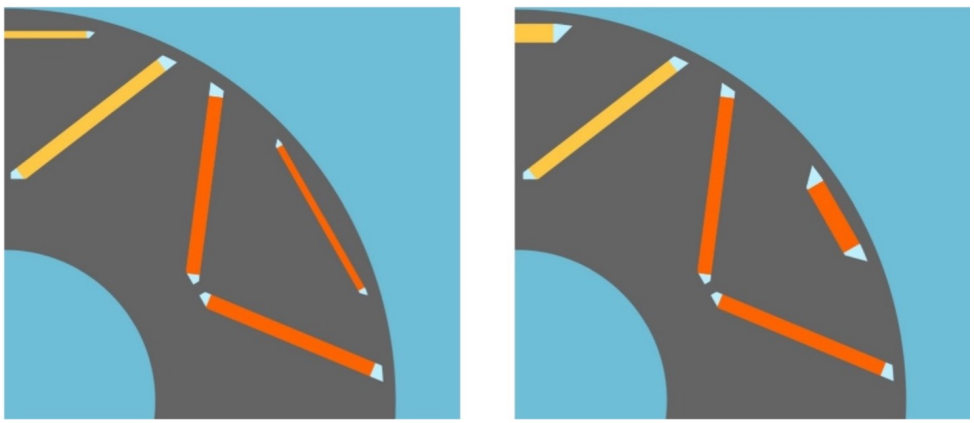

Figure 4.11: Extreme geometries designed for the analysis of the central magnet.

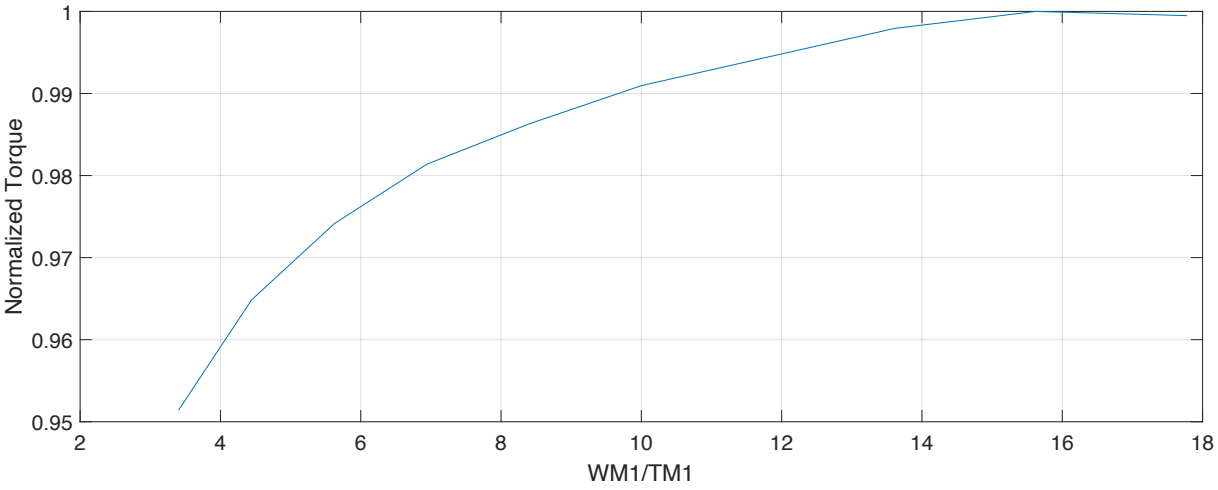

Figure 4.12: Trend of the normalized average torque as a function of the ratio WM1/TM1.

4.4 Analysis in the flux-weakening region

Following the analyses conducted at the operating point at nominal speed, four V-shape rotor configurations and six Delta-shape configurations have been selected. These geometries were simulated at various operating points, as in the preliminary analysis of section 4.1, with speeds ranging from 5000 rpm to 15000 rpm, with a step of 1000 rpm, to study the behavior of the machine under flux-weakening conditions. The current density was kept constant at 9.5 A/mm^2 in the first analyzed region, while in the high speed region it has been reduced to lower the total losses of the machine and, consequently, the temperatures.

The various configurations have been compared based on the torque, power factor, and efficiency as a function of rotor speed. The first comparison was made between the motors with the V-shape configuration, while the second comparison was made between the motors with the Delta-shape configuration. From the analysis of these plots, the two geometries offering the best performance were selected: the best among the V-shape rotors and the best among the Delta-shape rotors. Configurations for the V-shape geometries have been named from "V1" to "V4", while configurations for the Delta-shape geometries have been named from "D5" to "D10". In Figures 4.13-4.18 the results of the analysis for V-shape and Delta-shape configurations are shown. Finally, once selected "V4" and "D6" as the best geometries, a comparison between these has been carried out, highlighting "D6" as the best geometry of the whole analysis.

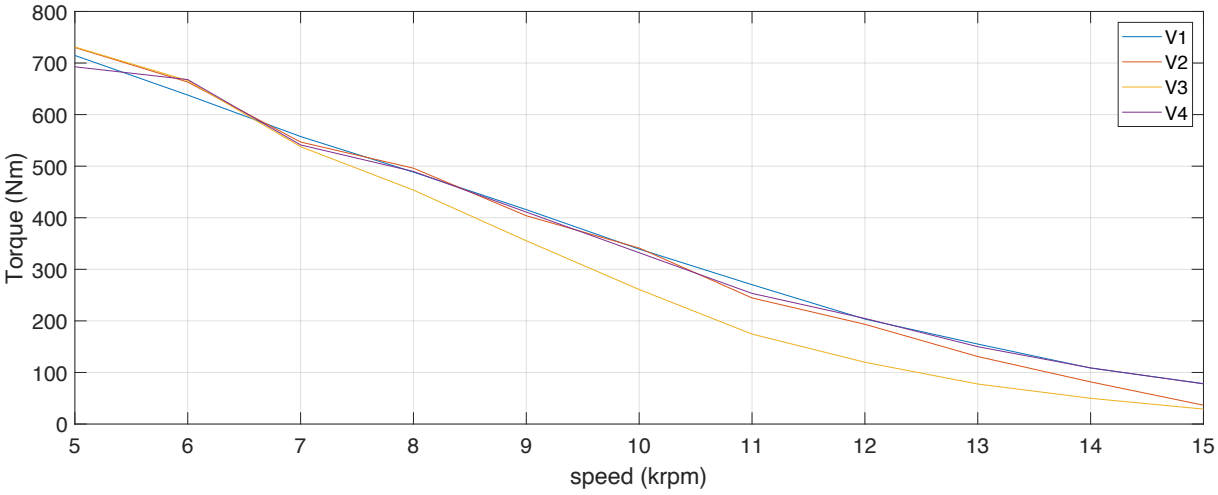

Figure 4.13: Analysis of the torque along the flux-weakening region for the selected V-shape geometries.

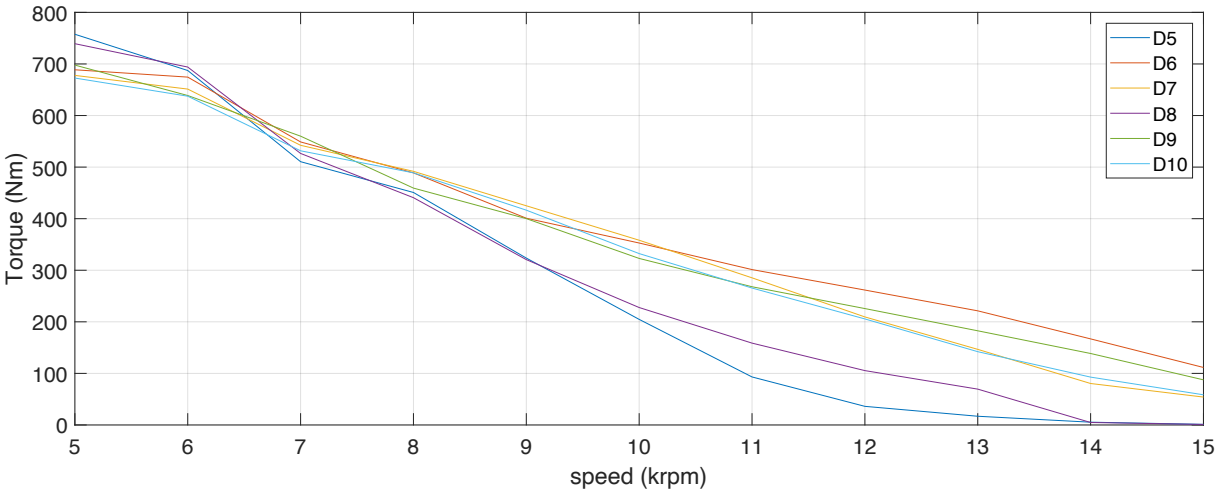

Figure 4.14: Analysis of the torque along the flux-weakening region for the selected Delta-shape geometries.

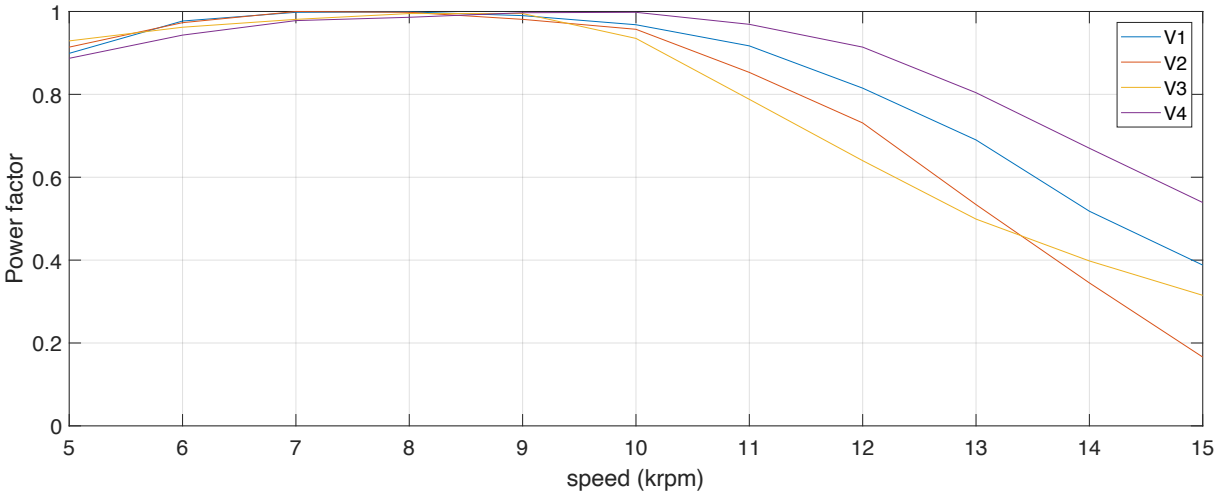

Figure 4.15: Analysis of the power factor along the flux-weakening region for the selected V-shape geometries.

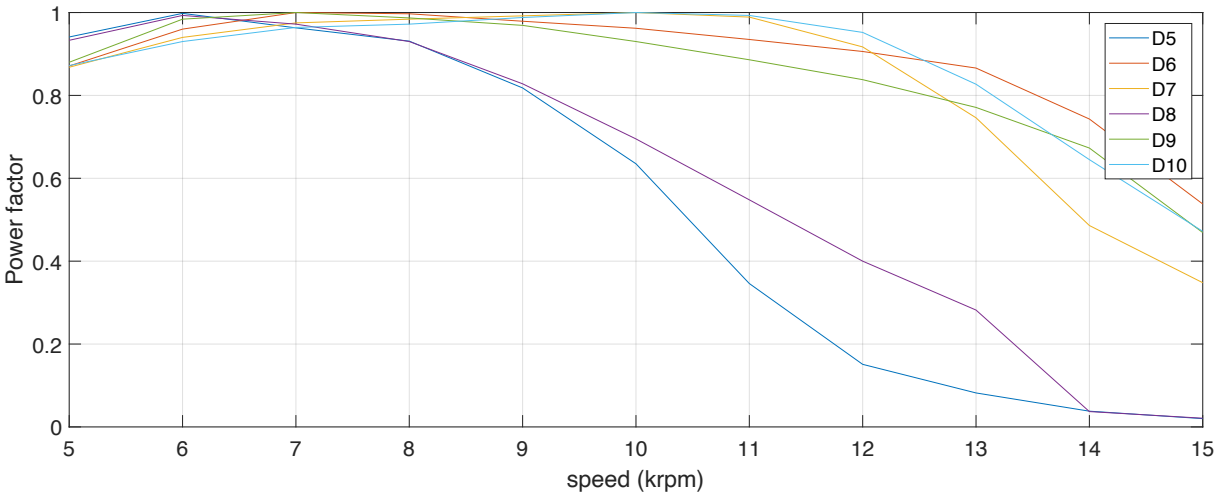

Figure 4.16: Analysis of the power factor along the flux-weakening region for the selected Delta-shape geometries.

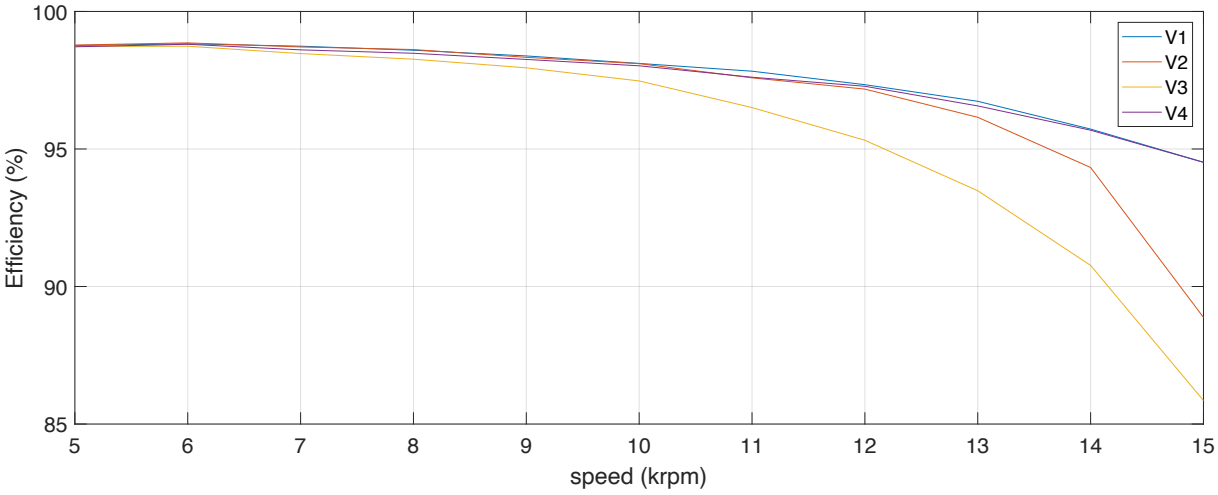

Figure 4.17: Analysis of the efficiency along the flux-weakening region for the selected V-shape geometries.

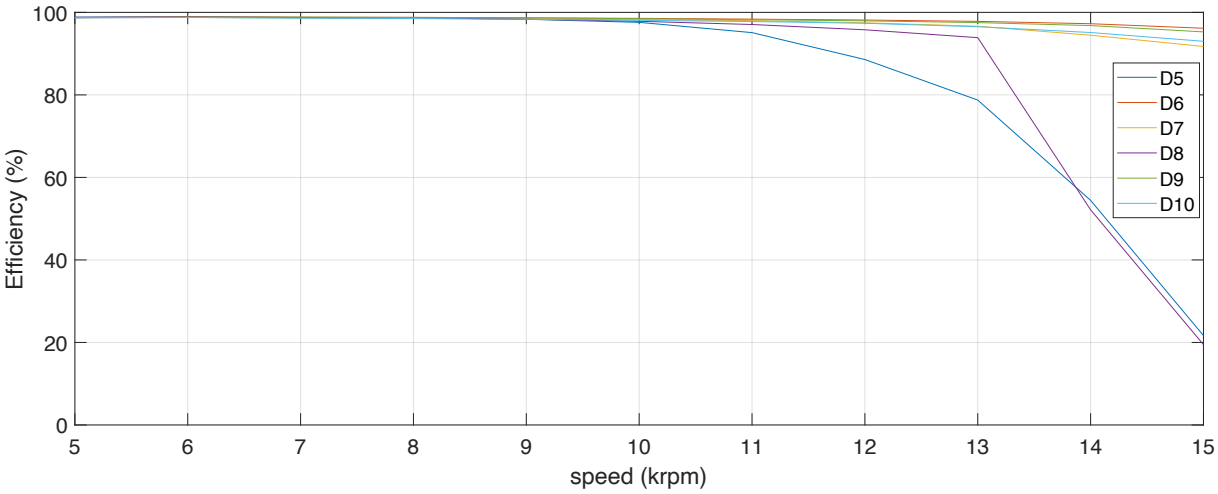

Figure 4.18: Analysis of the efficiency along the flux-weakening region for the selected Delta-shape geometries.

4.5 Final geometry modeling and simulation

Finally, the rotor geometry that provided the best results along the flux-weakening region ("D6") was studied in detail, representing the configuration that best suits the operation of an internal permanent magnet synchronous motor with the required characteristics. To conduct a more accurate study, Altair Flux software was used, allowing for the implementation of some non-idealities in the model, such as a rotor geometry that does not neglect the presence of air between the edge of the slot where the permanent magnets are inserted and the magnets themselves.

The geometries of the slots where the permanent magnets are inserted were slightly modified to ensure an air gap of 0.15 mm on each side (Fig. 4.19), allowing the insertion of the magnets during assembly. This air gap thickness is not modeled in the geometries simulated in FluxMotor but could significantly affect the performance of the motor.

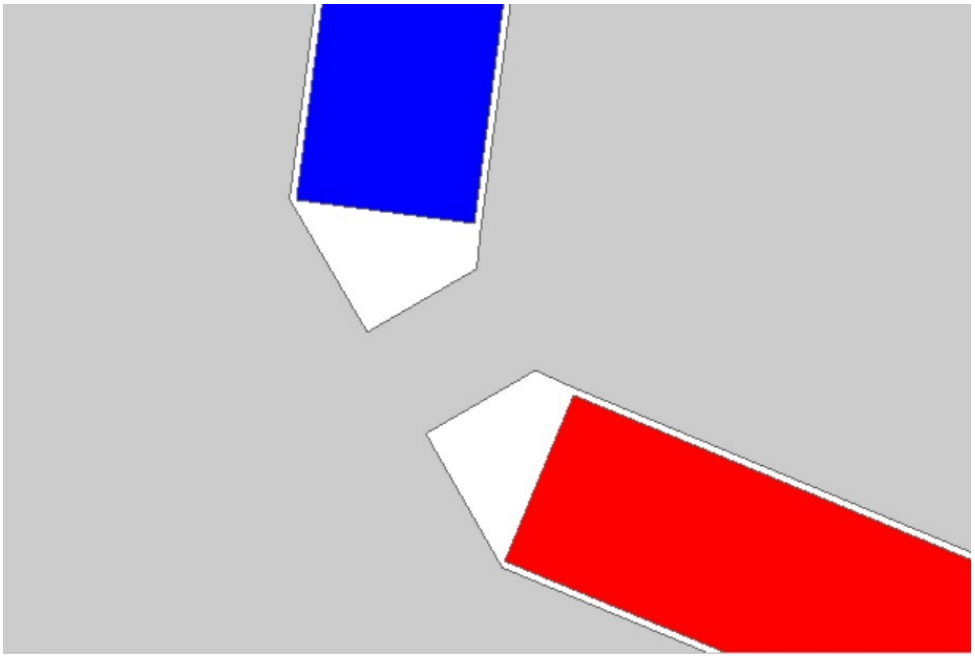

Figure 4.19: Detail of the air gap inside the pole barriers.

The main results of the simulations are presented in Table 4.4. It can be observed that the simulation in Flux returns an average torque value which, compared to the value obtained in FluxMotor (688.7 Nm), is lower, as expected, due to the inclusion of the air gap between the magnets and the slots where they are inserted. Furthermore, there is a high percentage torque ripple (45%), which significantly deteriorates the motor's performance.

Table 4.4: Main results for the 2D-FE simulation carried out in Altair Flux at the base speed point.

Torque mean value	665.2 Nm
Iron losses	1819 W
Magnet losses	119 W
Electrical input power	362.6 kW
Mechanical output power	349.5 kW
Efficiency	96.9 %

As for the case study of chapter 3, it should be reduced by adopting the step-skewing technique on the rotor, since for this analysis has not been analyzed and adopted. The study conducted has revealed a rotor geometry that allows for excellent performance, especially in terms of torque, power factor, and efficiency. From the flux density map in Fig. 4.20, it can be noted that there are some points subject to saturation concentrated near the radial and tangential ribs of the rotor. The magnetic flux density at the saturation points highlighted in Fig. 4.20 could be reduced by slightly modifying the geometric shape of the radial and tangential ribs of the rotor.

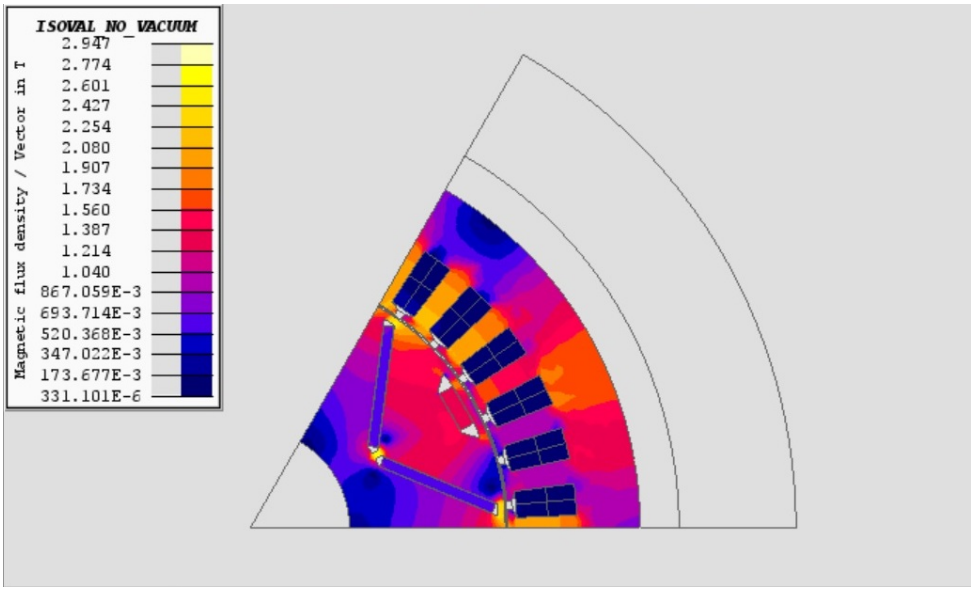

Figure 4.20: Flux density map of the motor at the base speed point.

4.6 Conclusions

This chapter has outlined a different procedure for the design of an interior permanent magnet synchronous motor concerning the case study presented in chapter 3. Initially, the selection of the optimal number of poles for the specific application was analyzed, carrying out both electromagnetic and thermal studies. Subsequently, various rotor geometries were examined at the operating point at nominal speed to find the magnet arrangement that best suits the motor's required characteristics. Following this, the best-performing geometries found in the previous analysis were studied regarding their behavior along the flux-weakening region. This latter study highlighted the best geometry, which was subsequently modeled and analyzed in a more precise software, allowing to reduce the non-idealities and reaching results that are closer to a real motor prototype.

Part II

Diagnostics of inverter-fed induction motors

Chapter 5

Diagnostics of induction machines: state of the art

Diagnostics and fault detection have been studied in electrical machines since their earlier applications, evolving alongside the development of the of the broader AC electrical machines family. In the early stages, users and manufacturers primarily depended on basic safeguards like over-current and over-voltage protection, as well as earth-fault detection, to maintain reliability and safety during operation. As the tasks performed by machines grew over time, there arose a need for advancements in fault diagnosis as well.

5.1 Concepts on diagnostics of electrical machines

Some definitions of key concepts behind the diagnostics of electrical machines will be given in this section. The diagnostics of electrical machines are closely related to condition monitoring and various maintenance practices.

Condition monitoring of a machine involves observing specific parameters such as vibration, line current, temperature or acoustic emission. The aim is to detect any significant changes that may indicate the development of a fault. This process is a crucial part of predictive maintenance. By utilizing condition monitoring, maintenance tasks can be scheduled proactively, or necessary actions can be taken to prevent damages and mitigate their potential consequences. One of the key advantages of condition monitoring is its ability to identify conditions that could shorten the normal lifespan of a machine [95].

Condition monitoring can be defined as the actions carried out to monitor the status of the machines. This process involves two main phases: data acquisition and data pre-processing of machine parameters. Decision-making, which is typically part of diagnostics, is separate from the condition monitoring process. Condition monitoring can be conducted in two modes: online and offline:

- Online monitoring involves continuous data acquisition during normal machine operation. This data is typically visualized and processed remotely, often in real-time.
- Offline monitoring, on the other hand, involves intermittent measurements taken when the machine is not operational. Data collected during offline monitoring is often processed at a later time.

Regarding the definition of diagnostics of electrical machines, it can be seen as the general issue related to the detection localization and identification of various kinds of faults in the machine. Additionally, the concept of diagnostics includes also the decision-making process regarding which actions should be taken after identifying a fault. This decision-making can be carried out by trained personnel or by algorithms, such as machine learning techniques.

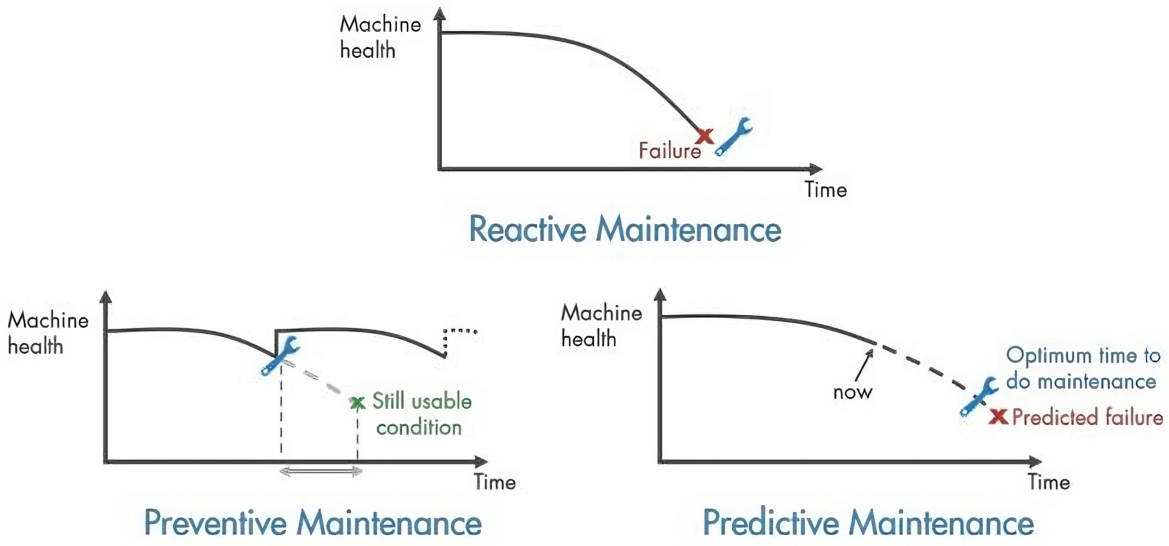

Figure 5.1: Three different types of maintenance approach [96].

Finally, predictive maintenance is closely related to the concepts of condition monitoring and diagnostics. It enables the estimation of a machine's time-to-failure, often referred to as Remaining Useful Life (RUL). This information allows for optimal scheduling of maintenance activities for the system. Predictive maintenance stands in contrast to reactive and preventive maintenance. Reactive maintenance involves using the machine until it fails, with repair or replacement occurring only after the failure has happened. Preventive maintenance, on the other hand, involves regular checks on the equipment and planned maintenance at set intervals to prevent potential failures. In simpler terms, predictive maintenance is highly effective for expensive and safety-critical equipment because it minimizes machine downtime by anticipating issues before they occur (unlike reactive maintenance) and maximizes the lifespan of machine components by scheduling maintenance based on actual usage patterns (unlike preventive maintenance) [96]. The predictive maintenance approach has similarities with the concept of the prognosis of the machines. The latter is the process that allows the prediction of a failure of the machine through the continuous monitoring of the variables and parameters of the system, using these informations to predict the time until a failure occurs, i.e. the RUL [97, 98]. Prognostics involves assessing the rate of degradation in a machine, which allows it to continue operating normally until the point of failure. This approach helps reduce costly and unnecessary maintenance interventions, as well as unexpected equipment failures [99].

In recent years, there has been a remarkable surge and advancement in the development of diagnostic techniques used for monitoring the condition of rotating electrical machines. Predictive maintenance is becoming increasingly prevalent across various industries, including the industrial sector and fields like electric traction. This approach, as previously explained, relies on advanced diagnostic techniques, preferably non-intrusive and conducted online. These techniques allow for the continuous monitoring of machine conditions, enabling early fault detection and proactive maintenance interventions to prevent costly downtime and equipment failures [100]. Moreover, thanks to the growth of worldwide electrification, electrical machines are present in almost any application [101]. Finally, thanks to the developments in the technologies of electronics and computer engineering, the sensors needed to measure the quantities to be monitored to predict the condition of the machines are now more reliable. This allows the extension to a wider

range of applications than in the past, including also medium and small power machines.

5.2 Diagnostic techniques

In this section, a brief overview of some techniques used to diagnose faults will be illustrated. Parameters to be monitored in a machine vary, and the effectiveness of each parameter depends on the type of fault being addressed. Different faults may require monitoring different parameters for accurate detection and diagnosis. Some complete reviews about the usage of different quantities for diagnostic purposes have been made in the past few years. According to some of these (i.e. [102, 103], among the parameters that can give useful information on the machine's condition, it is worth to mention:

- vibration;
- acoustic emission (which can be strictly related to vibrations);
- temperature;
- chemical analysis;
- mechanical displacement;
- stator current;
- voltages;
- magnetic stray fluxes.

Some of these will be analyzed in the following subsections. A particular focus will be given later on the Motor Current Signature Analysis (MCSA), since the stator current signal is the main signal analyzed during the work of this thesis.

5.2.1 Vibration analysis

Together with the thermal analysis of the machine, the analysis of vibrations of the machine during operation has been the main online condition monitoring technique for a long period. Vibrations can be produced in a machine from various factors, such as

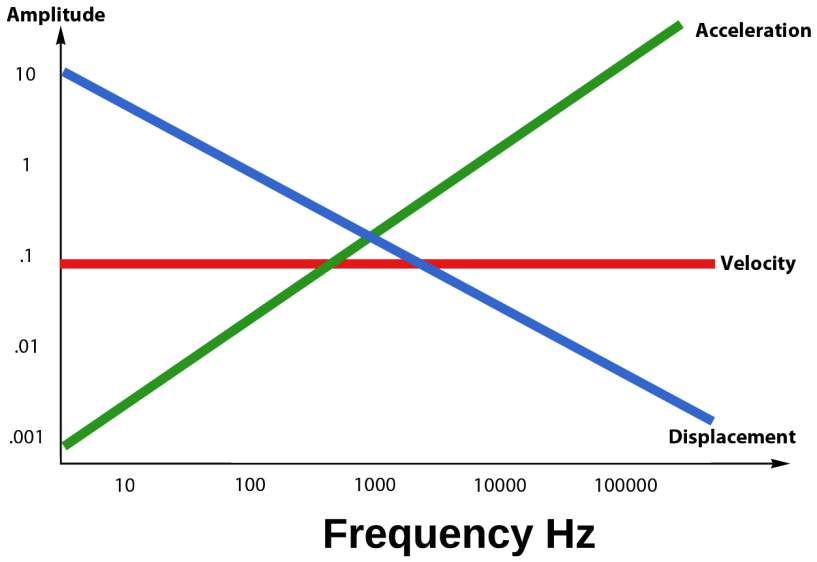

Figure 5.2: Frequency ranges for various indicators of vibration [105].

mechanical and electromagnetic but also fluid-dynamic. Vibrations refer to mechanical oscillations occurring around a reference position. Three main factors characterize them:

- displacement;
- velocity;
- acceleration.

According to the frequency range of the vibration, they can be measured through these three parameters, as resumed in Fig. 5.2. At low frequencies, generally lower than 10 Hz, the displacement is the most important quantity to be measured. For the range of frequencies between 10 Hz and 1 kHz, the velocity of the vibration is generally acquired. Finally, in the high-frequency range (>1000 Hz), the acceleration of the vibration contains the most important information for the analysis [104].

Regarding measurements for rotating electrical machines, however, even for vibrations at a frequency below 1 kHz the analysis of the acceleration is usually adopted. Vibration analysis can be conveniently conducted by placing one or multiple accelerometers on the mechanical component to be measured. One example of multi-sensor approach that involves the usage of two accelerometers in the analysis can be seen, as an example, in [106]

by Minervini et al., where the goal of the study was the detection of bearing faults.
Despite simple mechanical parts can be modeled through software and the vibration analysis carried out analytically, the study of real systems is usually more complex. Most of the machines and systems, in fact, have elastic parts that increase the number of degrees of freedom to infinite (generally referred to as continuous systems).
As already described, the natural frequencies of the system can enhance the characteristic frequencies of bearing faults, which are among the main causes of faults in rotating electrical machines. In order to do this, it is essential to filter the Frequency Response Function, FRF (which is a measurement function based on frequency used to identify the resonant frequencies, damping characteristics, and mode shapes of a structure), using a bandpass filter focused around the resonant frequency of the system.
One of the most used techniques to analyze vibrations is the so-called envelope analysis, which consists of the analysis of low-frequency harmonics through four main steps [107]:

- raw time signal acquisition;
- bandpass filtering;
- full wave rectification;
- power spectrum of the processed signal.

Finally, it is worth to mention the main causes of vibrations in a rotating electrical machine. In addition to the already-mentioned bearing faults, other mechanical factors can be related to vibrations. Among the others, mechanical imbalance of the rotor, defects of coupling and manufacturing defects are some examples. Also, aerodynamic factors can cause vibrations, especially in applications such as pumps or fans. Lastly, vibrations can also be related to electromagnetic factors, like Lorenz and Maxwell forces, which can be related, i.e., to eccentricity [108] or to a non-optimal choice of the number of rotor poles and stator slots, but also to unbalanced magnetic pull in conditions of asymmetry (airgap eccentricity), and imbalances in the power supply.

Figure 5.3: Commercial stray flux probe M343F from Emerson [110].

5.2.2 Stray flux analysis

Since their first applications during the 1980s, the usage of stray magnetic fluxes to monitor conditions of electrical machines has grown rapidly [109]. The usage of this signal, which can be taken in different positions of the machine's frame (axial stray flux, radial stray flux, circumferential stray flux), has some advantages if compared to other possible measurements. First of all, stray flux sensors can be easily installed on the outer surface of the machines. Moreover, the measurement of stray flux is an easy and flexible method of measurement, since it is possible to locate the sensor while the machine is operating. Lastly, sensors involved in the measurement of stray flux are generally cost-effective compared to other probes, such as piezoelectric ones for the acquisition of vibrations or some clamps involved in the analysis of stator currents. An example of a commercial stray flux probe is shown in Fig. 5.3.

This commercial probe basically consists of a simple circular coil without any ferromagnetic core (air coil), which has to be located perpendicularly to the rotating axis of the machine. An extensive analysis of magnetic fluxes for condition monitoring and identification of multiple faults in various induction motors has been carried out in the doctoral dissertation [111] from Kokko, in 2003. From this research, he stated that air-core coils can be considered the optimal sensor for such applications because they exhibit mini-

mal signal attenuation, particularly in frequencies below 20 kHz, which are crucial for diagnostic purposes. However, a drawback of using flux coils is their inability to detect continuous or very low-frequency signals.

When measuring a machine's stray flux with a coil probe, what is actually measured is not directly the magnetic flux, but rather an electromotive force generated by the change in flux over time. Typically, it is not always essential to calculate the exact value of the flux linked with the coil. Instead, focusing on the variation (i.e., the time derivative) of the flux analyzed in the frequency domain can highlight relative changes in the harmonics at the same frequency as the flux itself [95]. Various sensors can be utilized besides air-core flux probes. One of the most common is the ferrite-core coil one. Various analyses have been carried out using this kind of sensor. For example, in [112], Frosini et al. carried out an analysis on the stator intern-turn stator short circuit on low voltage motors, using both air-core and ferrite-core probes. The authors stated that, despite the signals acquired with both the probes give important information on the status of the machines, the amplitude of the fault-related harmonics in the spectra is higher for the signal acquired from the custom ferrite-core probe.

5.3 Motor Current Signature Analysis (MCSA)

In this thesis, the main signal analyzed for diagnostic purposes is the one from the stator current. Methods that involve the use of these signals are generally referred to as Motor Current Signature Analysis, MCSA [113].

MCSA is a non-invasive technique, which constitutes its main advantage over other monitoring schemes. This technique involves two main steps: firstly, the acquisition of the current signal from the stator of a machine and, secondly, its elaboration through various signal analysis methods (generally, these methods use the spectrum analysis of the acquired signal) [114]. The current signal is typically obtained using current transformers already in place for protection purposes, such as overload protection. Alternatively, permanent or temporary sensors can be installed directly to facilitate continuous or periodic condition monitoring. Continuous monitoring, also known as online condition monitoring, involves the permanent installation of sensors and signal conditioners to acquire data

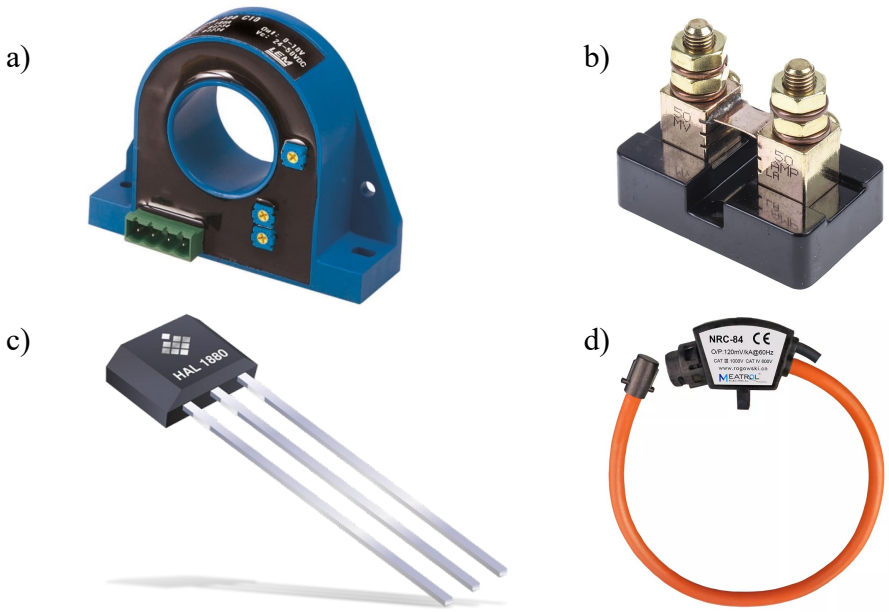

Figure 5.4: Different types of sensors to measure the stator current: current transformer (a) [115], shunt resistor (b) [116], Hall effect sensor (c) [117], Rogowski coil (d) [118].

continuously and regularly. In the current transformer, of which an example is shown in Fig. 5.4a, the primary winding is connected in series with the circuit where the current to be measured flows, while the instruments or equipment are connected in series to its secondary winding [119].

Concerning the other types of sensors shown in Fig. 5.4, the working principle is different from one to the other. Regarding the shunt resistor, shown in Fig. 5.4b, the value of the resistance is used to determine the electrical current flowing through the load. This is done by measuring the voltage difference across this resistance, applying Ohm's law [119]. Hall effect sensors (Fig. 5.4c) are capable of detecting and quantifying magnetic fields and can be used for various applications. In this particular application, the sensor is employed to measure an electric current by sensing the magnetic field produced by a conductor carrying the current. Generally, a Hall effect sensor incorporates a magnetic core to guide the flux around the wire and direct it towards the Hall effect element. When this magnetic circuit is not saturated, the flux is directly proportional to the current passing through the sensor. Consequently, the reading obtained from the Hall element can be translated into a current measurement [120]. Finally, the Rogowski coil (Fig. 5.4d) is an electronic device used to measure alternating current or rapid current pulses. It

consists of a coil of wire in a helical shape, around a circumference, like a toroid, but with an air core, and the two terminals are close to each other; this coil wraps around the conductor cable carrying the current to be measured [121]. It is generally cheaper if compared to other current sensors. Nevertheless, one of its main disadvantages is the frequency bandwidth, which generally starts from 10 to 30 Hz [122].

Typically, MCSA focuses on analyzing the current of a single phase. A single current sensor is utilized and placed on any of the three phases. This approach is adopted because the rotating flux waves resulting from various machine failures intersect all three stator phase windings, inducing corresponding currents in each phase. Therefore, analyzing the current of one phase provides insights into the overall condition of the machine [123]. When the analyzed currents are the Park ones, derived from the three phases, the analysis is commonly known as negative sequence analysis [100].

MCSA began its development between the late 1970s and the mid-1980s in both the USA and Europe. According to [124], numerous researchers collaborated during this period to establish the foundation of this novel diagnostic approach. Among the other research, it is worth citing the ones from Kliman and Stein [125], Vas [126], Cameron et al. [127] and Filippetti et al. [128]. An important and complete work of review, in which more works from different research groups in the early stages of MCSA are included, has been presented in 2000 from El Hachemi Benbouzid [129]. Moreover, this review also includes citations from more recent studies.

5.3.1 Signal processing steps

The implementation of the MCSA technique can be summarized in the following steps:

1. data acquisition capturing data at an appropriate sampling frequency and with a sufficient number of samples to accurately represent the signal;
2. filtering of the analog signal (i.e. antialiasing);
3. digital filtering and/or resampling;
4. windowing of the signal;
5. application of signal analysis techniques;

6. individuation of the fault characteristic harmonics in the spectrum.

Regarding the first point of the previous list, the sampling frequency strongly influences the bandwidth which can be analyzed from the spectrum analysis. Referring to algorithms to compute the Discrete Fourier Transform (DFT), such as the Fast Fourier Transform (FFT), the Shannon-Nyquist theorem proves that the maximum frequency that the DFT can show lies at half of the sampling frequency. The relation is that [130]:

$$F_s \geq 2BW_{max} \tag{5.1}$$

where F_s is the sampling frequency and BW_{max} is the maximum bandwidth that can be analyzed. For what concerns the range of frequency $> F_s$, the problem that arises is the so-called aliasing phenomenon (Fig. 5.5), which is the effect that causes distinct signals to become indistinguishable (aliases of each other) when sampled.
In practical applications, however, it is usual to set a higher sampling frequency, generally satisfying the equation [131]:

$$F_s \geq 10BW_{max} \tag{5.2}$$

The other key aspect of the acquisition step concerns the acquisition time. The acquisition time is related to the equation:

$$f_{res} = \frac{F_s}{N} = \frac{1}{T_{acq}} \tag{5.3}$$

where:

- f_{res} is the frequency resolution of a DFT;
- N is the number of samples acquired;
- T_{acq} is the duration in time of the acquisition.

Following the equation 5.3, it is clear that the frequency resolution of this frequency transformation only depends on the total time duration of an acquisition. Having a good frequency resolution means being able to distinguish very closely spaced peaks in the spectrum as separate peaks. Conversely, a bad frequency resolution results in peaks that are close to each other being identified as a single peak, which can be translated into a loss of information from the machine under analysis. Moreover, it is important to have a

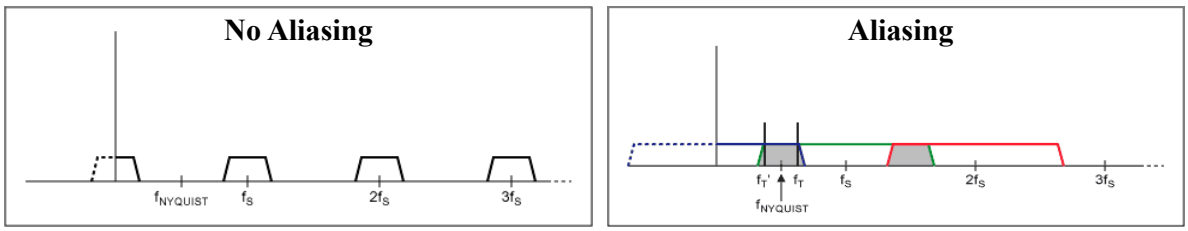

Figure 5.5: Representation of the aliasing phenomena [131].

frequency resolution that is as close as possible to a sub-multiple of the frequency to be analyzed. This allows the reduction of the so-called spectral leakage effect, of which the wrong choice of a proper frequency resolution can be a cause.
Regarding the other points outlined at the beginning of this subsection, they will explained later in the thesis.

5.4 Types of fault in induction motors

In this section, an overview of the components subject to failures in electrical machines will be given. Since the diagnostic analysis presented in this thesis focuses on methods for fault detection of induction motors, this section will focus on faults that occur in this kind of machine. Roughly 90% of industrial motors belong to this type. Additionally, it holds significant importance in traction, particularly in railways, where the majority of high-speed locomotives are outfitted with this motor type. Due to its widespread use in many sectors, many techniques have been developed over the last decades to identify various types of faults. The most common are [132]:

- stator winding faults (i.e. intern-turn short circuits);
- bearing faults;
- eccentricity;
- faults in the rotor cage.

Every fault that occurs causes a magnetic imbalance in the machine during the operation. Any asymmetry occurring in the motor due to a fault, such as unbalanced loads or

mechanical issues, will introduce specific harmonic components into the current. Therefore, the MCSA method is particularly effective for identifying faults that manifest as spectral components at characteristic frequencies known in advance, such as those caused by asymmetry in the motor. In Table 5.1, some of the main characteristic frequencies of different types of faults for induction motors, to which it is possible to apply MCSA, are reported. Despite these fault harmonics are present also in healthy motors, they generally have higher amplitudes in faulty motors.

To detect the fault, signal processing techniques should be employed to determine the harmonic content of the induction motor's stator current. Processing of this signal can be carried out in the time domain (relying on analysis through statistical measures), the frequency domain (i.e. applying DFT) or the time-frequency domain. The techniques used for the signal analysis during the study of this work will be presented and explained later in chapter 6.

Table 5.1: Main fault-related characteristic frequencies of some induction motor type of faults [102], [125], [127], [133], [134], [135].

Fault component	**Characteristic frequency of the fault**
Static eccentricity	$\left[kR\left(\frac{1-s}{p}\right) \pm n\right] f_s$
Dynamic & static eccentricity	$\left[(kR \pm n_d)\left(\frac{1-s}{p}\right) \pm n\right] f_s$
Mixed eccentricity	$nf_s \pm kf_r = \left[n \pm k\frac{1-s}{p}\right] f_s$
Bearing out race	$f_s \pm k\frac{N}{2} f_r \left(1 - \frac{D_b}{D_c} cos\beta\right)$
Bearing inner race	$f_s \pm k\frac{N}{2} f_r \left(1 + \frac{D_b}{D_c} cos\beta\right)$
Bearing ball element	$f_s \pm k\frac{D_c}{D_b} f_r \left[1 - \left(\frac{D_b}{D_c} cos\beta\right)^2\right]$
Broken bars & end ring damage	$\left[\frac{k}{p}(1-s) \pm s\right] f_s$

In the table: f_s is the fundamental supply frequency; f_r is the rotational frequency of the rotor; s is the rotor slip; p is the number of pole pairs; R is the number of rotor slots, k is an integer number ($k = 1, 2, 3 \dots$), n is the harmonic order ($n = 1, 3, 5 \dots$); n_d is the dynamic eccentricity order ($n_d = 1$: dynamic eccentricity, $n_d = 0$: static eccentricity); N is the number of balls of the bearing; D_b is the ball diameter; D_c is the ball pitch diameter; β is the ball contact angle.

5.4.1 Eccentricity faults

Concerning the different types of fault, rotor eccentricity can exist in two forms: static and dynamic, depending on whether the rotor's center of rotation remains fixed during rotation. Static eccentricity arises from factors like an ovalized internal stator circumference or incorrect rotor installation, causing the rotor's center of rotation to stay fixed but misaligned with respect to the stator (Fig.5.6b).

In contrast, dynamic eccentricity occurs when the geometric center of the rotor fails to coincide with its center of rotation, leading to a shifting center of rotation relative to the stator as the rotor spins (Fig.5.6a).

The presence of both static and dynamic eccentricities is generally known as mixed eccentricity. The most used equation to detect eccentricity-related harmonics (as also reported in Table 5.1) is:

$$f_{ecc} = \left[(kR \pm n_d) \left(\frac{1-s}{p} \right) \pm n \right] f_s \tag{5.4}$$

Harmonics identified through this equation are called Rotor Slot Harmonics (RSH). As reported for example in [124], it is not possible to distinguish between static and dynamic eccentricity through the MCSA method, since their harmonics are present at the same frequencies, and their amplitude is not dependent on the type of eccentricity.

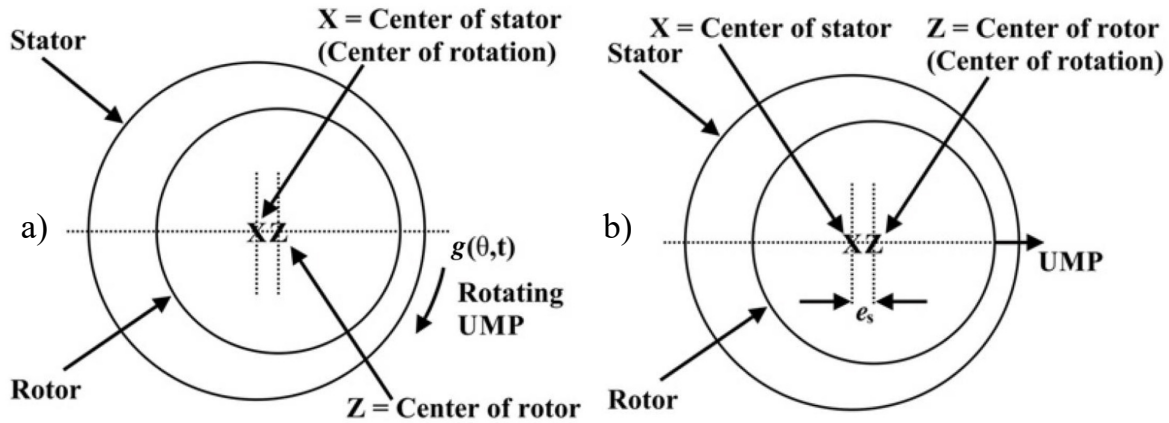

Figure 5.6: Representation of dynamic eccentricity (a) and static eccentricity (b) [124].

5.4.2 Stator winding faults

Regarding the stator winding, symptoms of insulation degradation such as partial discharges (PDs) are not present for low-voltage motors (V≤690 V) when directly mains-fed. However, several studies have shown the possibility of utilizing stator current and stray flux for detecting stator short circuits. Various signal processing techniques have been employed to analyze these signals and identify the presence of stator faults. For example, in [136], the authors proposed a Wavelet Transform-based pre-processing method to prove the effectiveness in filtering the stator current and stray flux signals in order to diagnose stator shorts in an induction motor supplied by an electronic converter, through the typical harmonics of this fault.

Following a coil short-circuit in a motor, the motor can still function close to optimal conditions, with only a slight increase in current and minor magnetic field distortion at the air gap. However, the short-circuited coils generate heat and electrical discharge due to current passing between them. This accelerates the aging of the thin insulating layer. The heat initiates a chain reaction, causing more turns to short-circuit until a complete phase-to-ground or phase-to-phase short circuit occurs. The degradation time of the insulator after the initial short circuit between turns is very short and challenging to estimate since it varies across different machines. However, empirical evidence suggests that, in low-voltage machines, there may be enough time to prevent a sudden failure.

The rapid degradation of a fault in the stator winding of a machine, which often necessitates downtime for repairs, can discourage the adoption of expensive online diagnostic devices. However, in certain critical production environments, any improvement in condition monitoring of the machine can offer significant advantages in preventing unexpected downtime. The harmonics related to this fault can be found through the equation:

$$f_{sc} = f_s \left[\frac{n}{p}(1 - s) \pm k \right] \tag{5.5}$$

5.4.3 Bearing faults

For what concerns bearings, on low voltage motors bearings with rolling elements are usually mounted, which can be balls or cylindrical elements. This kind of bearing provides the highest percentage of failures in electrical machines, in the order of 40% according

to the IEEE report published in the Transaction on Industry Applications in 1985 [137]. Since failure in the bearings is a completely mechanical fault, its identification through electromagnetic signals such as stator currents or stray fluxes is much more complicated if compared to the already described faults. Nevertheless, a bearing fault also induces secondary effects, such as air gap eccentricity [138] and torque oscillations [139]. These effects can be identified through the MCSA or through Stray Flux Signature Analysis (also known as SFSA). Bearing faults can be categorized into two main types: localized (or cyclic) faults and generalized roughness (or non-cyclic) faults. Localized faults involve a specific point-type defect, such as a crack or flaking, occurring on one part of the bearing. On the other hand, generalized roughness faults manifest more uniformly through erosion, typically resulting in increased internal mechanical clearances across the bearing.

Since the work presented in this thesis refers to broken rotor bar detection in induction motors, this type of fault will be presented in the next section. Moreover, an overview of the state of the art in the literature will be given for motors operating in non-stationary conditions.

5.5 Broken rotor bar fault: theory and literature review

5.5.1 Broken rotor bar fault

Failures in the rotor cage of induction motors have been studied since the half of the 1940s. From this period, for example, the work published in 1946 by Trickey [140] can be mentioned, in which the author studied the broken rotor bar (BRB) fault by measuring the resistance of the circuit. According to various researches, among which the ones in [141–143], faults in the rotor cage occur in percentages that oscillate from 7% to 12% of the total amount of faults in induction motors.

As reviewed in the Ph.D. thesis [144], the primary cause of this fault can be attributed to weak connections between the bars of the cage and its end rings. These connections tend to deteriorate further during machine operation due to excessive overheating and

thermal stresses. The probability of occurrence of this fault highly depends on the rotor manufacturing process: normally it can happen in fabricated rotors, as a breakage of a bar close to the welding between the bar and the end ring. Conversely, die-cast rotors are more robust and can hardly be subject to this fault. A particular case is given by deep well submersible motors: these motors have fabricated copper bars, but, instead of an end ring made of a solid piece, they use several copper sheets with the same shape as the ferromagnetic laminations. This type of end ring wears very often due to internal cooling water and high-speed rotation [145]. Additionally, manufacturing defects such as material impurities, the presence of porosity (air bubbles), magnetic anisotropy of the laminations, or imperfections can contribute to deficiencies in the rotor cage.

Over prolonged operation, these factors become more pronounced, particularly in the presence of magnetic stresses induced by magnetic forces, variable frequency content, or additional harmonics (leading to magnetic saturation effects), local maxima of magnetic fields at sharp edges and corners, and uneven distribution of eddy currents [146]. Ambient conditions also play a significant role, as the rotor of a machine may experience fatigue and corrosion when exposed to harsh environments such as humidity, dust, high pressures, toxic fumes, etc. [144, 147].

The asymmetry resulting from the breakage of rotor bars affects the distribution of magnetic fields. The rotor flux perceives this disruption as an open or partially open circuit, particularly if the bar is cracked rather than completely broken. These distorted rotor fields contribute to the generation of electromagnetic torque, leading to higher ripple in torque and speed. Consequently, this results in heightened levels of noise and vibration within the motor. Moreover, the breakages can also affect the lamination material at the points where they occur.

As already discussed, a defect in the rotor cage of the induction motor produces a distortion in the rotor magnetic field. The torque production in a motor primarily relies on the stator and rotor magnetic fields, which are interrelated by the slip (and so, by the speed). As these two fields interact, any non-uniformity and distortion in the rotor flux causes ripples in the stator magnetic field. These fluctuations are then transmitted to the stator current, as explained in [148], [149].

These fluctuations manifest as additional harmonics, which are also injected into the ax-

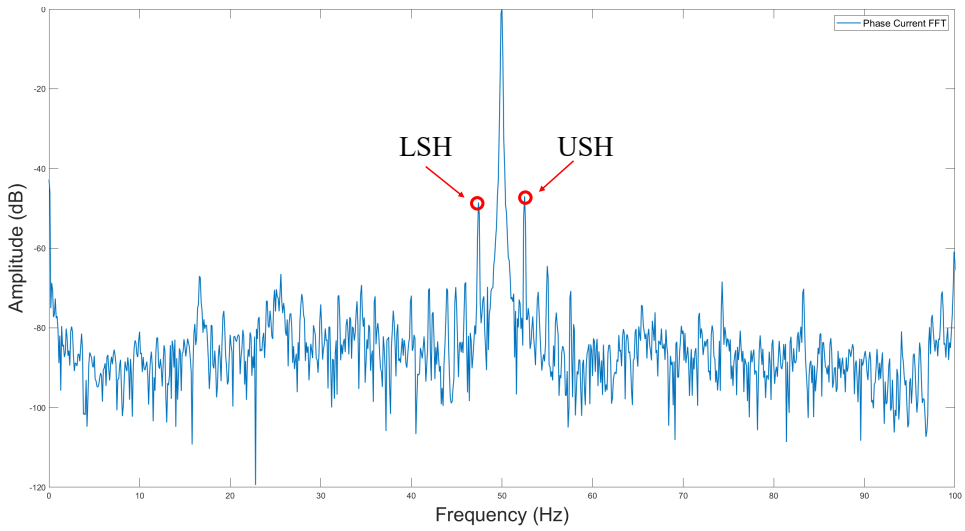

Figure 5.7: Identification of LSH and USH for a stationary signal of a motor with a broken rotor bar.

ial flux and stray magnetic flux of the machine. Due to the pulsating ripples, harmonics emerge in the current. The general equation to determine broken bars (or end ring) related fault harmonics is [133]:

$$f_{bb} = \left[\frac{z}{p}(1-s) \pm s\right] f_s \tag{5.6}$$

Where:

- f_s is the fundamental supply frequency;
- s is the slip;
- p is the number of pole pairs;
- $\frac{z}{p}$ assumes integer values $\left(\frac{z}{p} = 1, 3, 5, \dots\right)$.

Another equation related to the broken rotor bar fault is the one that defines the sidebands around the fundamental supply frequency, given by [150]:

$$f_{bb} = (1 \pm 2ks) f_s \tag{5.7}$$

Where the only undefined variable so far is k which assumes integer values ($k = 1, 2, 3, \dots$). Usually, these sidebands are studied for $k = 1$, since their amplitude is higher if compared

to the other harmonics obtainable from equation 5.7. In particular, the harmonic placed at $-2sf_s$ from the fundamental one is known as the Lower Sideband Harmonic (LSH), while the one in $+2sf_s$ is the Upper Sideband Harmonic (USH). According to [148, 151], the appearance of USH is mainly due to the speed oscillation that occurs due to the fault, while LSH is related to the fault itself, and specifically to the counter-rotating magnetic field which is created at $-sf_s$ from the fundamental.

The amplitude of the fault-related harmonics strongly depends on the number of adjacent broken rotor bars [152]. Moreover, a threshold can be defined to determine when the rotor has to be considered faulty. For instance, if the detected harmonics exhibit an amplitude difference from the fundamental of at least 45 dB, the motor is regarded as healthy. However, it is important to note that these thresholds may vary depending on factors such as the number of rotor bars and the number of poles in the machine. Three important studies, summarized in Table 5.2, have been conducted on this topic.

The presence of multiple adjacent consecutive broken bars results in an escalation of the amplitude of the fault harmonics. This increase continues until the number of broken bars surpasses the ratio R/p, where R is the number of rotor bars and p are the pole pairs of the machine [153]. The analysis of LSH and USH is not always an indicator of the broken rotor bar fault. For example, Sizov et al. in [154] stated that, for two non-adjacent broken bars placed at 90° (electrical degrees) from each other, LSH and USH tend to cancel in the spectrum. However, in this case, there is an increase in the amplitude of harmonics with $k = 2$.

Broken rotor bar related harmonics not only appear in the spectrum of the current signal. In fact, they are also present, for example, in the spectrum of the stray flux signal. Moreover, in this signal, other types of harmonics related to the fault can be found. As reported in [155] from Ceban et al., two fault-related harmonics appear in the spectrum of the stray flux at low frequencies:

$$f_{bb} = sf_s \tag{5.8}$$

$$f_{bb} = 3sf_s \tag{5.9}$$

The very low frequency harmonics are produced by the mechanical speed oscillations induced by the rotor bar breakage. These harmonics are only observable in the flux spectrum and not in the current one. However, all other characteristic harmonics are

Table 5.2: Summary of the studies carried out by ABB, Nicholas and EASA on the correlation between the severity of a fault and the difference in amplitude of the sidebands from the fundamental [131].

(dB)	ABB (> 70% load)	Nicholas (> 75% load)	EASA (> 50% load)
60	Healthy	Excellent	Good
54	Healthy	Good	Marginal condition
49	High resistance spots	Good	Marginal condition
48	High resistance spots	Moderate	Marginal condition
46	Several high resistance spots	Moderate	Marginal condition
45	Several high resistance spots	Moderate	Marginal condition
44	A lot of high resistance spots or a BRB	Moderate	At least one BRB
42	A lot of high resistance spots or a BRB	BRB or high resistance surfaces	At least one BRB
40	A lot of high resistance spots or a BRB	BRB or high resistance surfaces	At least one BRB
39	At least one BRB	BRB or high resistance surfaces	More than one BRB
36	At least one BRB	Multiple high resistance surfaces	More than one BRB
35	Several BRB	Multiple high resistance surfaces	More than one BRB
30		Multiple BRB	Severe damage

visible in both current and flux spectra because the flux signal is influenced by the stator current and carries the same diagnostic information.

The rotor bar breakage, moreover, could introduce mechanical vibrations, as presented in [156]. The authors hypothesized that vibrations in the axial direction may occur when bars break and current flows between them, particularly within the rotor laminations situated between the broken bar and the two adjacent bars. In the study, various signals were analyzed, including current, flux, and radial and axial vibration. Despite expectations based on Lorentz's law that axial vibrations would be present in the event of a broken bar and transverse current flow between bars, the axial vibration component was absent in the findings. Consequently, the authors concluded that the current flow between bars remains minimal, even in the case of a broken bar failure, especially in small motors.

Among the studies carried out to detect this fault, some interesting works have been made on delta-connected motors. In this context, certain studies, like [157], have focused on utilizing higher-order harmonics to detect fault conditions characterized by singular harmonic content. Additionally, the use of zero sequence current (ZSC), as discussed in [158–160], has been proposed as an alternative approach with promising outcomes. However, implementing the ZSC method typically necessitates multiple sensors to capture and analyze the zero sequence current. Another interesting work on the detection of the BRB fault for delta-connected motors has been recently published in [161]. In this work, the authors proposed a method based on the analysis of the components that appear around the odd triple harmonics of the fundamental.

5.5.2 Broken rotor bar detection in non-stationary conditions

Most of the works on the detection of broken rotor bars cited so far in this thesis refer to motors operating in stationary conditions. When this condition is not fulfilled, the identification through frequency domain techniques (as the Discrete Fourier Transform) of the sidebands and, in general, of the fault-related harmonics, is much more difficult. This is the case, for example, of motors fed by mains during the start-up transient, where the slip of the motor has great variations in a short time interval ($s = 1$ at $t = 0$ and $s \simeq 0$ at the end of the initial transitory).

The same problems arise when the motor is fed by a power converter during the start-

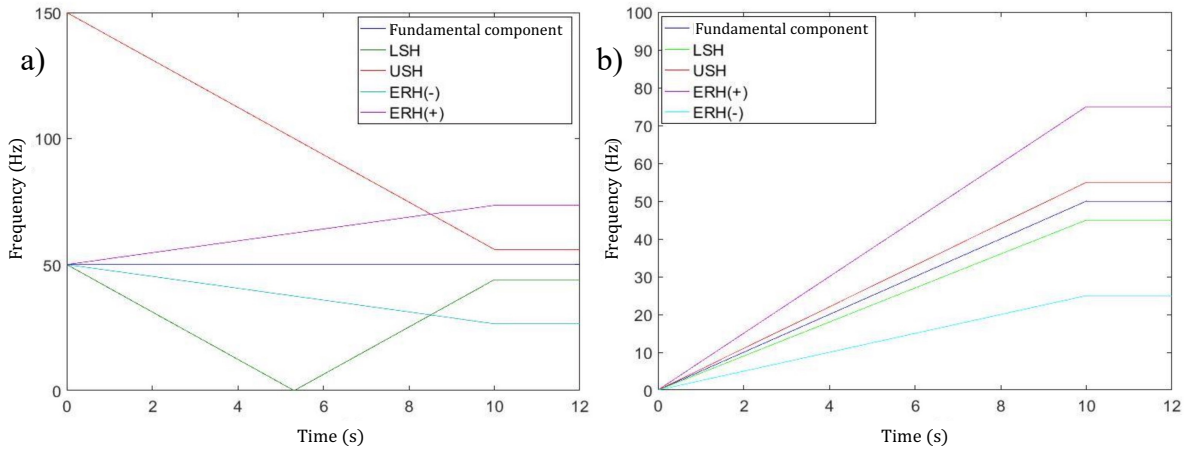

Figure 5.8: Theoretical trajectories of the harmonics related to the fault: mains-fed (a) and open-loop inverter-fed (b) [165].

up, despite the behavior of the slip is different. In fact, in this case, the frequency of the fundamental component of the current waveform is not constant during the start-up, moving from 0 Hz to the goal-selected frequency. When the harmonics do not have a fixed frequency, it is worth representing them in the time-frequency plane where, instead of fixed frequencies, trajectories are represented. In Fig. 5.8 the theoretical trajectories of the sidebands related to the broken rotor bar fault (LSH and USH) during the start-up are represented, both for mains-fed condition and power converter-fed condition (for an open-loop-controlled motor).

As already explained, in the case of motors directly fed from the grid, the fundamental frequency is constant and established from the moment the motor is connected to the line. During a direct start, some fault harmonics evolve in a very convenient way as their trajectories move away from the fundamental harmonic, which is the spectral component with the highest energy. For example, the Left Sideband Harmonic presents a trajectory in the time-frequency plane with a characteristic V-shape pattern (Fig. 5.8a)[162].

The evolution of the fault harmonics for inverter-fed start-up operation, instead, is completely different (Fig. 5.8b): broken bar-related harmonics, in this case, always lie close to the fundamental supply frequency [163, 164]. Moreover, during the transient, the rotor fault-related harmonics have low energy. This makes their detection particularly challenging: different works have been published in order to find a technique that allows to perfectly distinguish the different trajectories during the start-up.

Several time-frequency techniques have been used in the literature with the purpose of detecting the broken rotor bar fault. For example, in [166] by Panagiotou et al., the authors analyzed the results from a finite element model of a faulty motor through the Short Time Fourier Transform. The analysis have been finally validated with experimental tests on a real faulty motor in the laboratory. The analysis has been carried out analyzing faulty harmonics in a wide range of the spectrum by using the equation 5.6 and by applying it to both stator phase current and stray flux signals. The same research group has proposed a different approach in [167]. In this paper, the authors proposed a method based on signal estimation. The proposed approach is independent of motor slip and is based on isolating main harmonics rather than investigating signatures using traditional methods such as identifying fault-related sidebands.

Other examples of the ability of continuous time-frquency transforms can be seen in [168]. In this work, Pons-Llinares et al. stated that the detection of outer bar breakages in double-cage motors and the diagnosis of bar breakages in motors with rotor axial ducts through the usage of signal analysis tools such as the Short-Time Fourier Transform is much more efficient in transitory if compared, for example, to the analysis carried out using the Discrete Wavelet Transform (DWT). Another interesting work from the same research group can be found in the already-cited [163]. In this paper, the Chirplet Transform was proposed for the first time with diagnostic purpose to obtain the evolutions of the components' trajectories, even if they are too close in the time-frequency plane. The technique is validated in the paper through start-up tests, in which the presence of the fault has been quantified when analyzing the stator current.

Among the examples of atom-based techniques available in the literature, it is worth to mention the Dragon Transform (which will be explained in detail in chapter 6). The Dragon Transform is an energy atoms-based technique developed by Fernandez-Cavero et al. that exploits the adaption of the slope of the atoms according to the speed signal. This allows to perfectly follow the trajectories during the start-up transient in inverter-fed operation [169].

Most of the literature on the broken bar fault has dealt with motors supplied by the mains. Nevertheless, currently, it is fundamental to consider also motors fed by electronic power converters, especially in closed-loop operation. In fact, in closed-loop operation, the

control system ensures a safe operation even under an unbalance in both stator and rotor windings. Consequently, the typical fault harmonics in the stator current are reduced by the compensating action of the control system [170].

Two remarkable studies in the field of fault detection on motors running in closed-loop operation were published at the very beginning of the century. In [171], proposed by the research group of Bellini et al., simulation and experimental results prove that the spectrum of the field (magnetizing) current component (i_d) in a Field-Oriented Controlled (FOC) induction motor can be an effective diagnostic index. In fact, the amplitudes of the spectrum components at frequencies $2f_s$ and $2sf_s$ are almost constant with proportional gain variations and quite linearly dependent on stator and rotor faults degrees, respectively. Therefore, these fault indicators are quite independent of the control parameters, for the topology of the control system adopted, i.e. Direct Rotor Field-Oriented Control (DRFOC), and for a fixed bandwidth of the flux control loop.

In the paper published by Kral et al. in [172], a model-based diagnostic technique, called Vienna Monitoring Method (VMM), has been proposed to detect BRB in a vector-controlled induction motor. The fault indicator is based on the calculation of two values of the electromagnetic torque developed by the motor, one using a current model and the other one using a voltage model. The Vienna Monitoring Method was further improved by the same research group in [173], considering the possibility of its implementation without a position sensor, but some aspects related to the applicability of this method were not investigated, i.e. the role played by the tuning of the current, flux, and speed controllers of the drive.

The behavior of the magnetizing current component i_d for three types of vector-controlled drives has been analyzed in [174] by Cruz and Cardoso, finding that, although this quantity can be used to detect BRB in Indirect Rotor Field-Oriented Control with a Flux Control loop (IRFOC-FC) and DRFOC drives, the amplitude of the fault indicator is different for these two types of control system and depends on the parameters of the flux controller. A model-based technique to detect and quantify the BRB fault has been proposed later by the same research group in [175]. This technique is effective and independent of the operating conditions, such as load level, reference speed, and bandwidth of the control loops. However, it is only valid for specific control strategies.

A completely different approach is reported in [176], proposed by Gritli et al., where the detectability of BRB in Indirect Rotor Flux Oriented Control (IRFOC) is investigated for variable speed double cage induction motors, using vibration signature analysis techniques. The paper investigates the impact of the control system on the relevance of fault harmonics in the axial and radial vibration signals. Axial vibration analysis shows a more robust fault signature, under the control action, in separating healthy rotor from BRB in double squirrel cage induction motors.

In [177], proposed by Refaat et al., the stator line current is analyzed by means of a combination of empirical mode decomposition (EMD) and Wigner-Ville distribution (WVD) to detect BRB fault in open and closed-loop, along with a two-hidden layer feed-forward artificial neural network. This technique is preliminarily tested through finite element simulations and then experimentally, with a simple closed-loop system. In the latter case, the technique proved to be successful only when the motor was under full load and with two broken bars.

In [178] by Hou et al., a new online diagnosis method, based on both currents and voltages, is proposed to detect BRB in a closed-loop-controlled induction motor. Since in closed-loop the stator current fault harmonics propagate to voltage, a fault severity factor is proposed to evaluate the extension of the fault, which is obtained from the left sideband components and the fundamental ones of the motor currents and voltages. This method can be applied to different control strategies and is almost independent of the control parameters. In [179] the same research group proposed a method to detect and quantify BRB using zero-sequence voltage in a wye-connected induction motor in both open- and closed-loop, which can discriminate the BRB fault from a low-frequency load oscillation, even when these two phenomena occur simultaneously.

Based on the literature review presented above, the aim of this part of the thesis is to develop a method that can detect BRB in closed-loop induction motor operation. The method should rely solely on the analysis of one phase stator current without the need to measure or estimate any other variables. It should be applicable to all types of control and be as generalizable as possible.

Since techniques that analyze signals in the frequency domain, such as the DFT, often fail for closed-loop control operation motors (as will be proven in chapter 8), the traditional

motor current analysis is abandoned in favor of time-frequency approaches like the Short Time Fourier Transform (STFT) [180], the Dragon Transform [181] and the Min-Norm algorithm [182].

Chapter 6

Signal analysis techniques

In this chapter, the main signal analysis techniques employed during the work of this thesis will be presented and explained. Signal processing involves different steps in its development. During the process, the analog physical signal is sampled into a digital one and analyzed to monitor the system's condition and detect faults. The steps behind this process are summarized in Fig. 6.1. Signal analysis techniques have a crucial role in the digital signal processing step since implementing the correct technique allows finding the correct harmonic to indicate the ongoing fault in the machine.
In this thesis, three main types of signal analysis tools are evaluated:

- Fourier-based techniques: DFT (through the FFT algorithm implemented in MATLAB) and STFT;
- time-frequency atoms-based techniques: Dragon Transform;
- eigendecomposition-based spectral estimators: MUSIC and STMN.

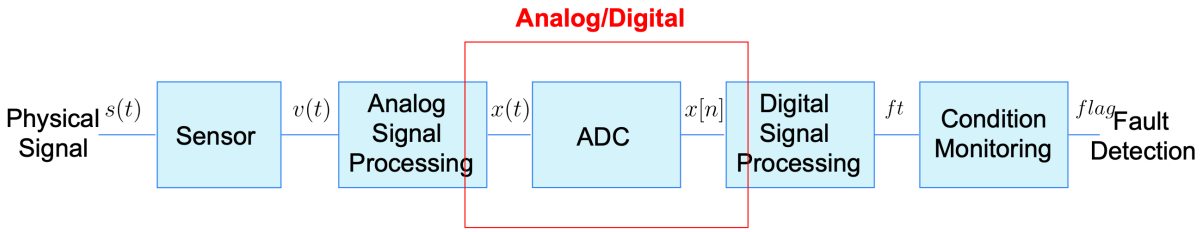

Figure 6.1: Steps to carry out the signal processing procedure [131].

6.1 Fast Fourier Transform

The Fourier Transform (FT) is a frequency transformation that allows to visualize harmonics in the frequency domain, as explained in chapter 5. According to the Fourier theorem, a steady-state wave can be represented as a series of sinusoidal components, each with frequencies corresponding to the fundamental frequency and its higher-order harmonic components. Each component possesses a certain amplitude and frequency. The continuous-time Fourier Transform (CTFT) of a signal is defined by:

$$X(f) := \int_{t=-\infty}^{\infty} x(t)e^{-j2\pi ft}dt \quad , \quad f = \frac{\omega}{2\pi} \tag{6.1}$$

Where the exponential term of the equation can be rewritten as:

$$e^{-j2\pi ft} = \cos(2\pi ft) - j\sin(2\pi ft) \tag{6.2}$$

The CTFT can be applied, as just mentioned, to continuous signals. The Fourier Transform for a discrete signal can be defined through a similar equation, linked to the continuous one:

$$X(f) := \sum_{k=-\infty}^{\infty} x(k)e^{-j2\pi fk} \tag{6.3}$$

In practical situations, where the acquisition of the signals is carried out by sampling it at a defined sampling frequency F_s, equation 6.3 cannot be applied, since it is defined in an infinite domain, while the actual frequency range that can be analyzed is strictly related to the sampling frequency, as discussed in subsection 5.3.1. To avoid this problem, the discrete digital signal is supposed to be periodic (N), and the integral in the infinite domain is converted into a sum between 0 and N through the already discussed Discrete Fourier Transform (DFT) [183]:

$$X[k] := \frac{1}{N}\sum_{k=0}^{N-1} x(n)e^{\frac{-j2\pi nk}{N}} \tag{6.4}$$

Equation 6.4 is valid under the following assumptions [131]:

- the bandwidth is limited;
- the sampling frequency is greater than 2 times the bandwidth of the signal;
- the time discrete signal $x(n)$ is stationary;

- the signal is periodic with period $T = \frac{N}{F_s}$;
- the estimated spectrum of $x(n)$ is also discrete with $n = 0, 1, 2, \ldots, \frac{N}{2} - 1$
- the frequency resolution is $\frac{F_s}{N}$.

The DFT presents, moreover, some limitations. First of all, since the bandwidth of real signals is not limited, there will be always spectral overlapping. Secondly, it is not always possible to choose N and F_s so that T is the actual period of the signal. This fact is one of the sources of spectral leakage. Lastly, since the frequency resolution is defined as $\frac{F_s}{N}$ and the real signal can contain components at frequencies that are not integer multiples of the frequency resolution, another source of spectral leakage is introduced [131]. In this thesis, the DFT is calculated with the Fast Fourier Transform (FFT) algorithm, which is available in commercial software such as MatLab from Mathworks. The FFT is an efficient algorithm that allows the reduction of the computational burden referring to the classical DFT [184].

As described previously, in practical situations, several problems introduce the so-called spectral leakage. The problem can be addressed during the signal processing stage using techniques like resampling [185] and windowing. Windowing is particularly relevant for the Short-Time Fourier Transform (STFT), explained in section 6.2.

6.1.1 Windowing

For the FFT analysis, a series of windowing functions can be used to improve the resolution and visual clarity of the analyzed signal, as they reduce the spectral leakage effects on a signal with a non-integer number of cycles. There exist various window functions (i.e., Hamming, Hann, Blackman-Harris)[186, 187], each suitable for different applications. It's crucial to recognize that the spectrum reflects not just the characteristics of the original signal but also those of the window function [188], including its shape and length. For example, the rectangular window, which is the simplest one, tends to introduce high spectral leakage due to discontinuities in the periodic windowed signal. In the work of this thesis, the Hann (or Hanning) window, shown in Fig. 6.2, has been employed during the signal analysis process. The Hann window is one of the most widely used windows because of its favorable trade-off between leakage and resolution. It is recommended by

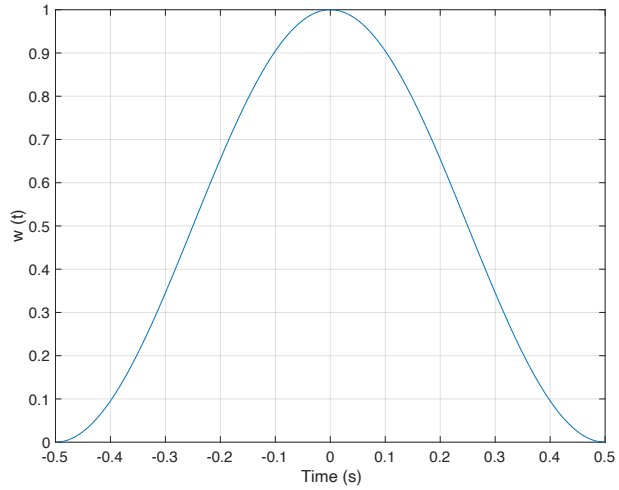

Figure 6.2: Representation of the Hanning window.

the standard IEC 61000–4–7 as a means to minimize spectral leakage [189].

Once a window has been created, it has to multiply the signal under analysis. Since, from this multiplication, the Hann window imposes the fictitious periodic signal to be continuous (the initial value and final value within a period are always zero), the spectral leakage in the analysis is reduced with respect to a not-windowed analysis.

6.2 Short-Time Fourier Transform

As previously discussed, the Fourier transform assumes that sinusoidal components persist throughout the entire time domain, which is suitable for steady-state conditions but inadequate for tracking transients, where the spectrum may vary over time. The goal of the STFT is to associate the instantaneous frequency spectrum with each moment in time. Consequently, the STFT enables the analysis of how the frequency content of a nonstationary signal changes over time, enabling the creation of a time-frequency distribution plot [190]. Time-frequency distributions (TFD) are functions of both time and frequency, necessitating a 3D plot. To clearly illustrate the behavior of the frequency component over time, the plots will be depicted in the time-frequency plane, with amplitude represented using a color map. This approach will be used for all the time-frequency techniques implemented during this thesis.

The STFT of a signal in time $g(t)$ is defined as:

$$S(t;f) := \int_{-\infty}^{\infty} w(\tau)g(t-\tau)e^{-j2\pi f\tau}d\tau \tag{6.5}$$

The STFT involves computing the Fourier transform of a signal multiplied by an appropriate window function $w(\tau)$ (which can be, for example, the already-cited Hann window) of finite duration. The procedure of the STFT can be summarized in the following four steps:

1. the signal $g(t)$ is multiplied by the window function $w(\tau)$, resulting in the product $w(\tau)g(t-\tau)$;
2. this product is zero outside of the window and is then Fourier transformed;
3. the Fourier transform provides the spectral representation of $g(t)$ at time $t = \tau$;
4. As time t increases, the function $w(\tau)g(t-\tau)$ shifts to the right, generating the spectrum for each point in time.

In a relative sense, the signal can be considered stationary while the window moves. Hence, the STFT is sometimes referred to as a sliding window Fourier transform.
Once again, the transformation reported in equation 6.5 refers to an analog signal. For a discrete-time signal $g[n]$, the STFT can be defined for a discrete-time window $w[n]$ of finite duration (N points):

$$S[n;f] := \frac{1}{N}\sum_{k=0}^{N-1} w[k]g[n-k]e^{\frac{-j2\pi kn}{N}} \tag{6.6}$$

The operational principle closely resembles the continuous case: the product $w[k]g[n-k]$ is zero outside of the window, and the DFT is applied. This transform represents the spectrum of $g[n]$ at $n = k$. As n increases, the function $w[k]g[n-k]$ shifts to the right, generating the spectrum for each n.
Finally, the spectrogram function is generally used to represent the energy of harmonics for the STFT. It is defined as the square of the magnitude of the previously defined STFT. Regarding the discrete-time signal $g[n]$, the spectrogram is defined as:

$$\left|S[n;f]\right|^2 = \left|\sum_{-\infty}^{\infty} w[k]g[n-k]e^{\frac{-j2\pi kn}{N}}\right|^2 \tag{6.7}$$

In general, larger time windows allow a better frequency resolution Δf. On the contrary, short windows allow the detection of sudden changes in the frequency of the trajectories of the harmonics, improving the time resolution Δt. Δf and Δt are related by the relationship [191–193]:

$$\Delta f \Delta t \geq \frac{1}{4\pi} \tag{6.8}$$

From this relation, known as the Heisenberg uncertainty principle, it is clear that, since there is a correlation between time and frequency resolutions, the fine-tuning of the parameters of the STFT has a key role in the identification of harmonics, especially when they lie one close to the other in the time-frequency plane.

An example of a result from a Short-Time Fourier Transform analysis is reported in Fig. 6.3.

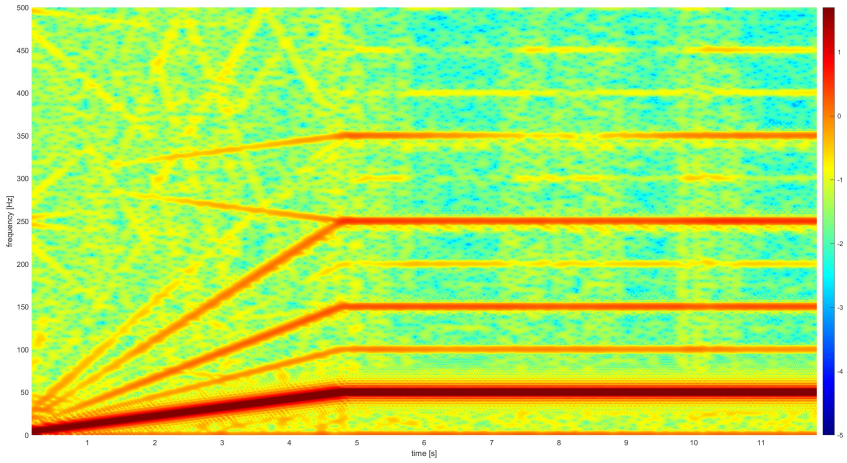

Figure 6.3: Example of STFT analysis carried out on current signal acquired at the motor's start-up.

6.3 Dragon Transform

The Dragon Transform (DT) is an atom-based signal transform [194], developed by Fernandez-Cavero, Pons-Llinares et al. [181]. Unlike the Wigner-Ville distributions (VWD), the atom-based techniques do not introduce cross-terms for the multi-component nonstationary signals. The cross-terms, for the WVD, are divided into outer-interference terms and inner-interference terms. Outer-interference terms arise with multiple mono-

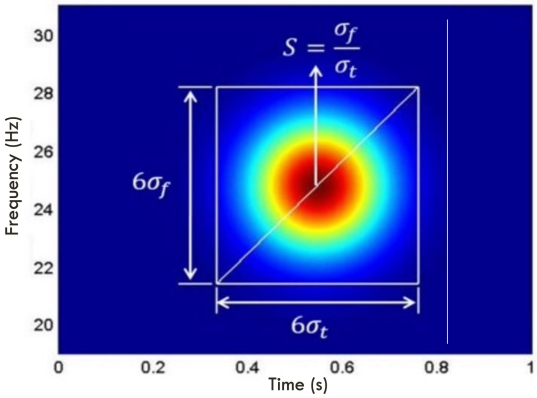

Figure 6.4: Example of a time-frequency atom (and its parameters) centered in a point of the plane [131].

components, while inner-interference terms occur due to nonlinear frequency-modulated (FM) components [193]. Removing cross-terms using kernels becomes particularly challenging when the harmonics are closely spaced, as in the case of the sidebands of broken bar-related harmonics.

A time-frequency atom is characterized as a function whose energy is concentrated around a specific point in the time-frequency plane. An example of a t-f atom is shown in Fig. 6.4.

An example of a t-f atom is given by the Gabor function:

$$g(t) = C_\sigma e^{-\frac{(t-t_c)^2}{2\sigma^2}} \longrightarrow \phi(t) = g(t)e^{j2\pi f_c(t-t_c)} \tag{6.9}$$

Where g is the Gaussian window that defines the Gabor function with a deviation parameter σ, centered in t_c and normalized with a constant $C_\sigma = \frac{1}{\sqrt[4]{\pi}\sqrt{\sigma}}$, while f_c is the modulation frequency of the Gabor function.

Each atom is characterized by its Heisenberg Box (HB), which describes how the energy of the atom disperses from its center along the plane. For a Gabor function, its HB sides are determined by:

$$\sigma_t = \frac{\sigma}{\sqrt{2}} \quad \text{s} \tag{6.10}$$

$$\sigma_f = \frac{1}{2\pi\sqrt{2}\sigma} \quad \text{Hz} \tag{6.11}$$

Finally, since a great amount of energy is usually located outside the HB, it is possible to define the Enlarged Heisenberg Box (EHB), introduced in [195] and defined by multiplying

by six the two sides of the original HB while keeping fixed its center.

The correlation between the atom and the signal being analyzed quantifies the energy of the signal within the EHB of the atom. Outside the EHB, the energy in the t-f plane is canceled, while only the energy carried inside the box is quantified.

Thus, the Dragon Transform is a technique based on the use of Dragon Atoms. These atoms are defined in such a way that their energy can follow the trajectory of any harmonic component to be detected. Then, the shape of these atoms is perfectly adapted to the trajectory of the harmonic to be followed, as specified. To achieve this, modulation must vary at each time instant. Specifically, the window must be modulated using an angle $\theta(t)$ in the complex exponential of the Gabor function, such that its time derivative corresponds to the time evolution of the frequency of the component $f(t)$[181]:

$$g(t) = C_\sigma e^{-\frac{(t-t_c)^2}{2\sigma^2}} \longrightarrow \phi(t) = g(t)e^{j2\pi\theta(t)} \longrightarrow \frac{d\theta(t)}{dt} = f(t) \tag{6.12}$$

Finally, a quantification method is introduced to obtain the instantaneous amplitudes of the harmonics. This provides a perfect resolution at each instant.

Therefore, the Dragon Transform is to be defined as the correlation between the signal to be analyzed (h) with a family of Dragon Atoms (ϕ), resulting in the following [181]:

$$\langle h, \phi \rangle = \int_{-\infty}^{+\infty} h(t)\phi^*(t)dt = \int_{-\infty}^{+\infty} h(t)C_\sigma e^{-\frac{(t-t_c)^2}{2\sigma^2}} e^{-j\theta(t)}dt \longrightarrow \frac{d\theta(t)}{dt} = f(t) \tag{6.13}$$

The deviation parameter σ is taken high enough to obtain a thin atom, while the constant that normalizes is defined as $C_\sigma = \frac{1}{\sqrt[4]{\pi}\sqrt{\sigma}}$. Finally, the other important remaining parameter from equation 6.13 is the angle of the complex exponent θ.

The key point in the adoption of the DT is the correct definition of the Dragon Atoms to be used. Therefore, the excellent time and frequency resolution of the Dragon Transform along the whole plane allows the correct visualization of the components to be studied as very thin lines, without interference from the energy of the first component. In Fig. 6.5 an example of Dragon Atoms applied to a synthetic signal is depicted [165, 181].

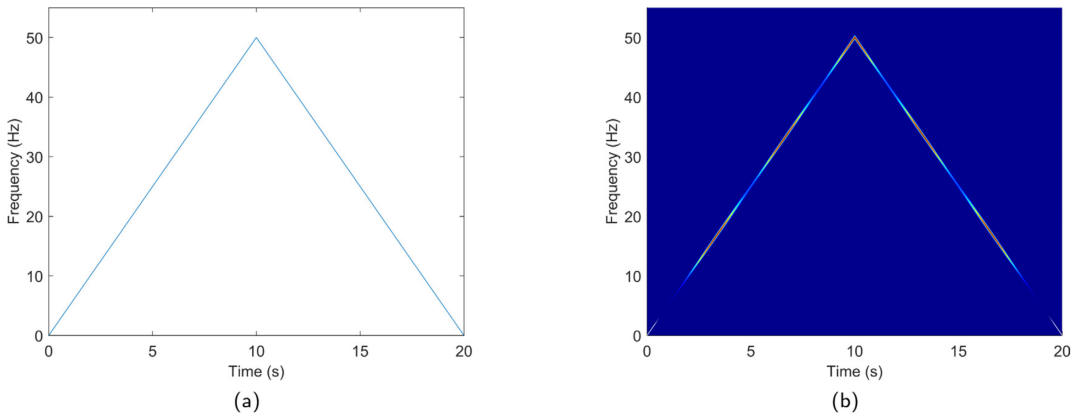

Figure 6.5: Time-frequency evolution of a mono-component synthetic signal (a) and energy distribution of Dragon Atoms following this evolution (b) [165, 181].

6.4 Short-Time Minimum Norm

The Minimum-Norm (Min-Norm, MN) algorithm is an advanced spectral estimator algorithm based on subspace decomposition, first developed by Reddi in 1979 [196]. Thanks to its high resolution, it can be used in the signal analysis process.

To apply this method, M observed data samples of a signal are assumed. Being t a certain time instant, the sequence can be modeled as:

$$s(t) = \sum_{p=1}^{P} v(\omega_p) s_p(t) + \eta(t) \tag{6.14}$$

In equation 6.14:

- $s_p(t)$ denotes the p-th harmonic component in the signal's spectrum;
- v is a uniformly sampled complex sinusoid array, whose angular frequency is: $\omega_p = \frac{2\pi f}{F_s}$, where F_s is the sampling frequency;
- $\eta(t)$ is the noise from the measurement.

The fault detection problem in an IM can be viewed as a power spectral density estimation problem, in which the fault-related frequencies f_f and its amplitudes $s_p(t)$ need to be estimated through the MCSA from the measured one-phase current [182].

Assuming $\mathbf{A}$ the $N \times M$ Vandermonde matrix [197] and $s(t) = [s_1(t), \ldots, s_P(t)]^T$ the vector of the amplitudes of the harmonics, the signal model can be written as:

$$\mathbf{S_x} = \mathbf{V}(\omega)\mathbf{A}s(t) + \eta(t), \quad t = 1, \ldots, M. \tag{6.15}$$

In the frequency domain, the model can be extended using eigenvalues and eigenvectors of the sample spectral covariance:

$$\mathbf{S_x} = \mathbf{V}(\omega)\mathbf{S}\mathbf{V}^H(\omega) + \sigma_w^2\mathbf{I} \tag{6.16}$$

Eigenvalues and eigenvectors must be estimated from the observed data since they are not known. The spectral matrix can be written in terms of its eigenvalues and eigenvectors as:

$$\mathbf{S_x} = \sum_{i=1}^{N} \lambda_i \mathbf{\Phi_i}\mathbf{\Phi_i^H} \tag{6.17}$$

In equation 6.17, λ_i are the eigenvalues, $\mathbf{\Phi_i}$ are the eigenvector. Assuming that D eigenvalues and eigenvectors are part of the signal (λ_i, Φ_i, $i = 1, 2, \ldots, D$), it is possible to define the signal subspace $\mathbf{U_s}$ and the noise subspace $\mathbf{U_n}$ as:

$$\mathbf{U_s} \triangleq \left[\mathbf{\Phi_1} \vdots \mathbf{\Phi_2} \vdots \cdots \vdots \mathbf{\Phi_D}\right] \tag{6.18}$$

$$\mathbf{U_n} \triangleq \left[\mathbf{\Phi_{D+1}} \vdots \mathbf{\Phi_{D+2}} \vdots \cdots \vdots \mathbf{\Phi_N}\right] \tag{6.19}$$

Different algorithms are based on this subspace decomposition, i.e. the MUltiple SIgnal Classification (MUSIC). The MUSIC algorithm employs all noise subspace eigenvectors and uniformly weights the norms of the projections of $v(\omega)$ onto the estimated eigenvectors [198].

The Min-Norm spectral estimation technique relies only on a single vector $\mathbf{d}$ in the noise subspace. This approach leads to more accurate estimates of ω_p and reduces the likelihood of spurious sinusoids resulting from zeros. In this technique, the signal subspace is spanned by the columns of $\mathbf{V}$. The vector $\mathbf{d}$ is defined as:

$$\mathbf{d} = [d_1, d_2, \ldots, d_N]^T \tag{6.20}$$

The vector is defined to have the property:

$$\mathbf{v}^H\mathbf{d} = 0, \quad i = 1, 2, \ldots, D \tag{6.21}$$

which means:

$$\mathbf{\Phi}_i^H\mathbf{d} = 0, \quad i = 1, 2, \ldots, D \tag{6.22}$$

The polynomial:

$$D(z) = \sum_{p=1}^{N} d_p z^{p-1} \tag{6.23}$$

has then zeros at:

$$z_p = e^{j\omega_p}, \quad i = 1, 2, \ldots, D \tag{6.24}$$

By finding the vector $\mathbf{d}$ as a linear combination of the $N - D$ in the subspace, the power spectral density will feature zeros at $\omega_1, \omega_2, \ldots, \omega_D$. It is imperative that d_1 equals to 1 while minimizing:

$$Q(\omega) = \sum_{p=1}^{N} |d_p|^2, \quad (d_1 = 1) \tag{6.25}$$

Finally, minimizing $Q(\omega)$, the null spectra of the Min-Norm is obtained as [198]:

$$\hat{Q}_{MN} = |\mathbf{v}^H(\omega)\mathbf{d}|^2 = \mathbf{v}^H(\omega)\hat{\mathbf{U}}_n\mathbf{W}\hat{\mathbf{U}}_n^H\mathbf{v}(\omega) \tag{6.26}$$

In equation 6.26:

- $\mathbf{W} = \mathbf{w}^{\frac{1}{2}}\mathbf{w}^{\frac{H}{2}}$
- $\mathbf{d} = \hat{\mathbf{U}}_n\mathbf{w}^{\frac{1}{2}}$

In Fig. 6.6 a pseudo-code for the practical implementation of the MN algorithm is reported, proposed by Garcia-Calva et al. in [182].

Once defined the spectral estimation, the time-frequency decomposition through the Short-Time Min-Norm (STMN) of $s(t)$ is given by [182] [199]:

$$S_{xx}(t, \omega) = \sum_{n=0}^{m=N_d-1} \frac{s(t)w(t - \tau l)}{\sum_{p=1}^{P} |v(\omega)\omega^2|} \tag{6.27}$$

Data: S_s, K, p
Result: $\hat{Q}_{MN}$
begin
  $nm = [(K+1), \cdots, (p+1)]$
  $\mathbf{T}_p = \text{Toeplitz}(S_s)$
  $\mathbf{F}_b = \left[\mathbf{T}_p \ \mathbf{T}_p^* \mathbf{J}_m\right]^T$
  $\mathbf{USV} = SVD(\mathbf{F}_b)$
  $g = \mathbf{V}(1, mn)$
  $\mathbf{G} = \mathbf{V}(2 : p+1, nm)$
  $\mathbf{d} = [1 \ (g^* g^T)^{-1} (G^* g^T)]^T$
  $\hat{Q}_{MN} = 20log_{10}|\mathbf{v}^H(\psi)\mathbf{d}|^2$

Figure 6.6: Min-Norm spectral estimation algorithm proposed in [182].

In equation 6.27:

- N_d is the data length of a sliding window analysis, w of the time signal $s(t)$;
- l is the leap size between successive windows;
- p is the number of frequency components inside the signal;
- ω is the frequency index.

An example of signal analysis carried out by applying the STMN technique is shown in Fig. 6.7.

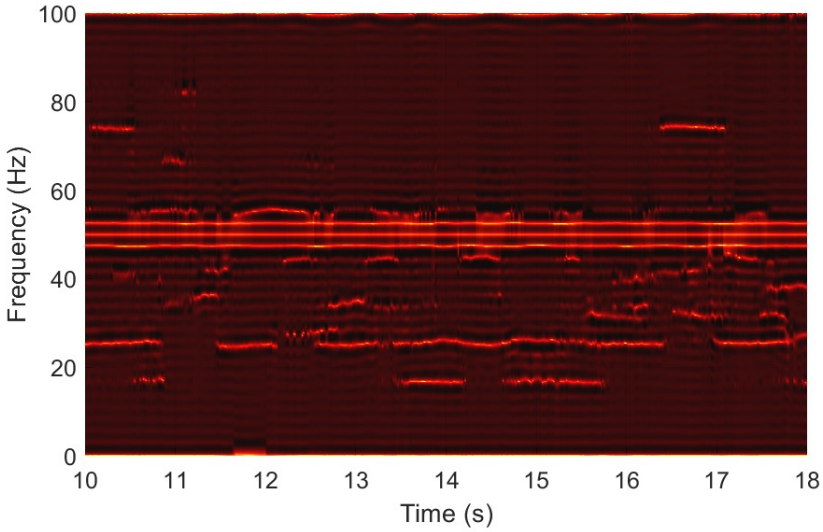

Figure 6.7: STMN analysis of a mains-fed IM with a broken rotor bar.

Chapter 7

Test bench and acquisitions

This chapter will present the test bench used by the author to acquire data. Moreover, the tests carried out in the laboratory will be outlined. A simple scheme of the power and data flow steps is shown in Fig. 7.1. In the scheme, the encoder signal is linked both to the data acquisition board and the encoder, since a speed feedback has been implemented to analyze the closed-loop operation of the motor.

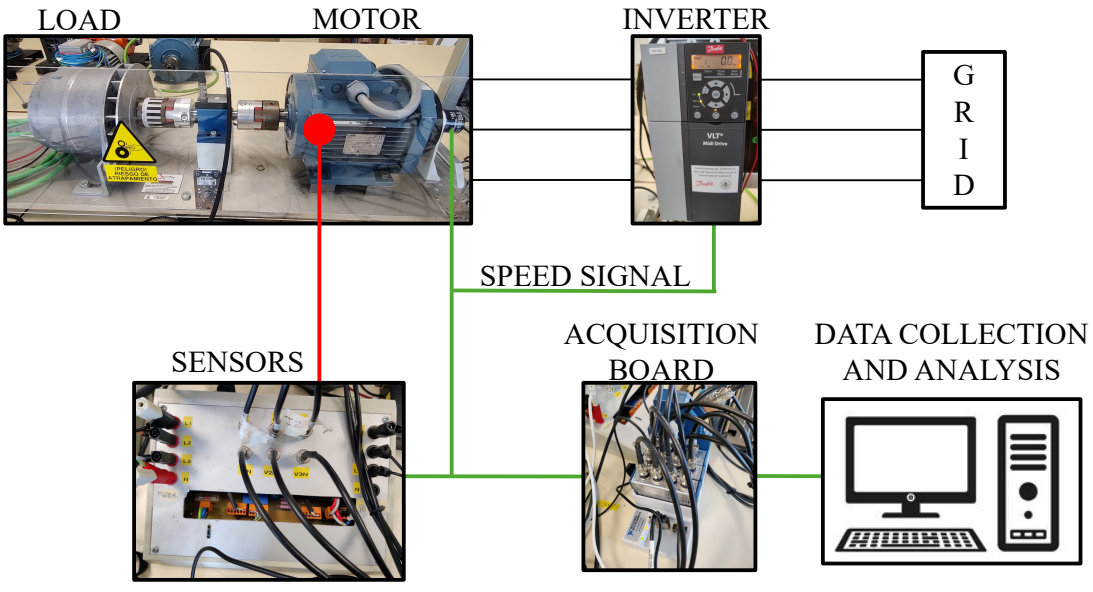

Figure 7.1: Scheme of the acquisition procedure: power flow links in black, data flow in green.

7.1 Test bench equipment

A general overview of the test bench employed for the work of this thesis is given in Fig. 7.2. The analyzed motors are two star-connected 4 poles 2.2 kW squirrel cage induction motors from ABB (3GAA102213-ASE): the model and the nameplate of the motor are shown in Fig. 7.3.

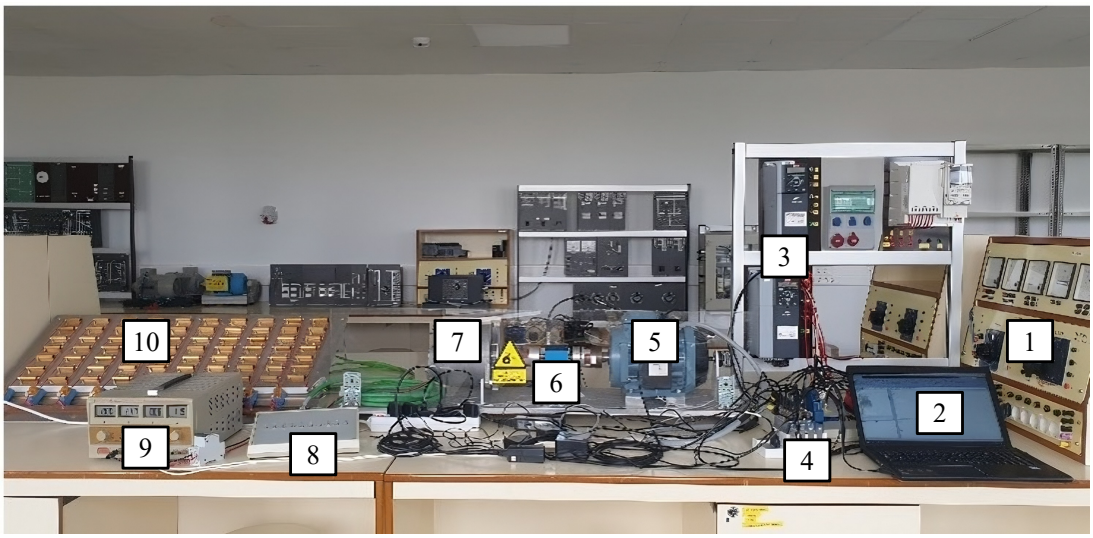

Figure 7.2: Overview of the test bench: 1.: mains supply; 2.: laptop; 3.: inverters; 4.: acquisition board (DAQ); 5.: ABB motor; 6.: torque sensor and mechanical joints (elastic coupling); 7.: DC alternator (load); 8.: resistors switches; 9.: alternator DC supply; 10.: bank of resistors.

a)

b)

Figure 7.3: Model of the motor under analysis (a) and its nameplate (b).

Trials have been carried out by using three different power converters: Danfoss VLT Midi Drive FC 280 (Fig. 7.4a), WEG CFW-08 (Fig. 7.4b) and Allen-Bradley PowerFlex 40 (Fig. 7.4c). However, only the analysis from the trials carried out with the Danfoss inverter will be presented in this thesis (in chapter 8).

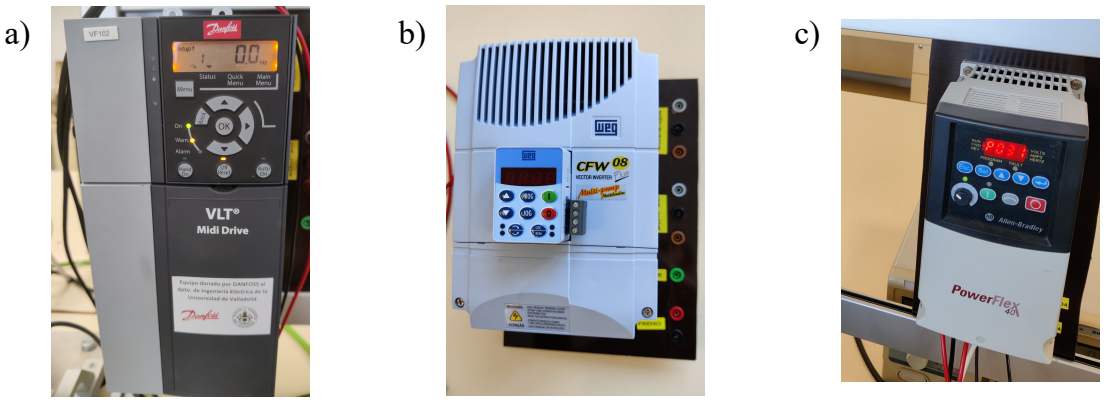

Figure 7.4: Inverters employed during the acquisitions: Danfoss VLT Midi Drive FC 280 (a), WEG CFW-08 (b) and Allen-Bradley PowerFlex 40 (c).

The motor is coupled through an elastic joint to a Delco Remy DC alternator (19025331) used as a mechanical load. The alternator is not self-excited and therefore it requires an external DC voltage source (24 V). It is specifically designed for automotive applications, with the output current (I_{alt}) adapting to load requirements within the limit curve depicted in Fig. 7.5. Meanwhile, the voltage (V_{alt}) remains constant at approximately 24 V thanks to an internal regulator that modulates the excitation current. Through a separate survey, various variables have been collected to provide a more comprehensive description of load variability. These include electrical and mechanical variables of the inverter, motor, and alternator under all considered load conditions, particularly in open-loop operation. Equations related to the model of the alternator are reported in Table 7.1. Apart from mechanical losses, power is also expended for the self-cooling system of the alternator, which can be modeled as a power function of the speed (ω). The total losses are denoted as P_{loss}. The current limit curve is almost linear in the considered speed range of the lab trials (900-1800 rpm). However, the limit curve depicted should never be exceeded under the imposed load conditions. Temperature exerts a discrete influence on such a curve. Ohm's law governs the required alternator current, and the dissipated power

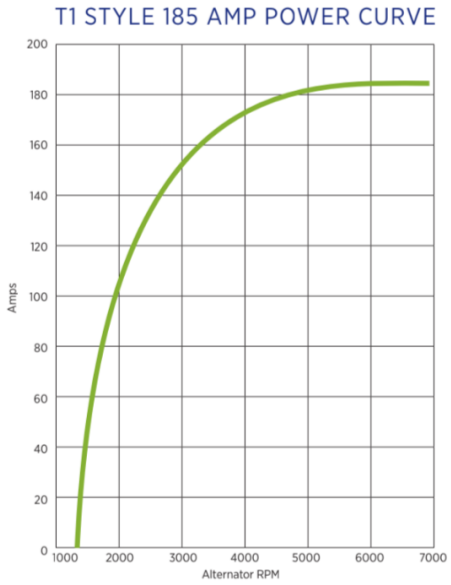

Figure 7.5: Alternator current limits as a function of the rotor speed.

Table 7.1: Characteristics equations that describe the behavior of the machine.

$$I_{alt} = \frac{V_{alt}}{R}$$
$$P_{IM} = (P_{loss} + P_R) = \omega T_m$$
$$P_R = \frac{V_{alt}^2}{R} = R I_{alt}^2$$
$$P_{loss} = k\omega^{\alpha}$$
$$T_l = T_l(R, \omega)$$

(P_R) is a consequence of the Joule effect. Although the voltage regulator may lack precision, the currents exhibit a relatively linear trend with the number of inserted resistors. Consequently, the required torque (T_{load}) does not exhibit an obvious relationship with the speed ω but depends on both speed and the inserted resistor banks (R). The bank of resistors consists of a variable stack of 70 resistors of 50 W. Ten rows of 7 resistors each can be inserted or removed manually, allowing the user to fix the load level. In order to not exceed the rated power of the ABB motor under test, the maximum number of lines inserted for the acquisitions of this thesis is equal to 5. An example of the dependence of the load on the number of rows of resistors linked to the stator circuit of the alternator is given in Table 7.2, where the experimental results for a rotor speed of 1500 rpm are given.

Table 7.2: Measured load depending on the number of resistors' rows linked to the DC alternator at 1500 rpm.

# lines of resistors	0	1	2	3	4	5
Load [Nm]	1.02	3.14	5.20	7.07	9.64	11.86

Finally, a National Instruments data acquisition system has been employed to acquire the signals (NI 9215 modules mounted on a NI cDAQ 9174). Referring to Fig. 7.6, a list of the sensors employed during the acquisitions is given below:

1. custom board with current and voltage Hall effect sensors;
2. incremental encoder (Omron E6C2-CWZ1X);
3. torque transducer;
4. custom stray flux sensor;
5. accelerometer (axial and radial acceleration measurements);
6. microphone.

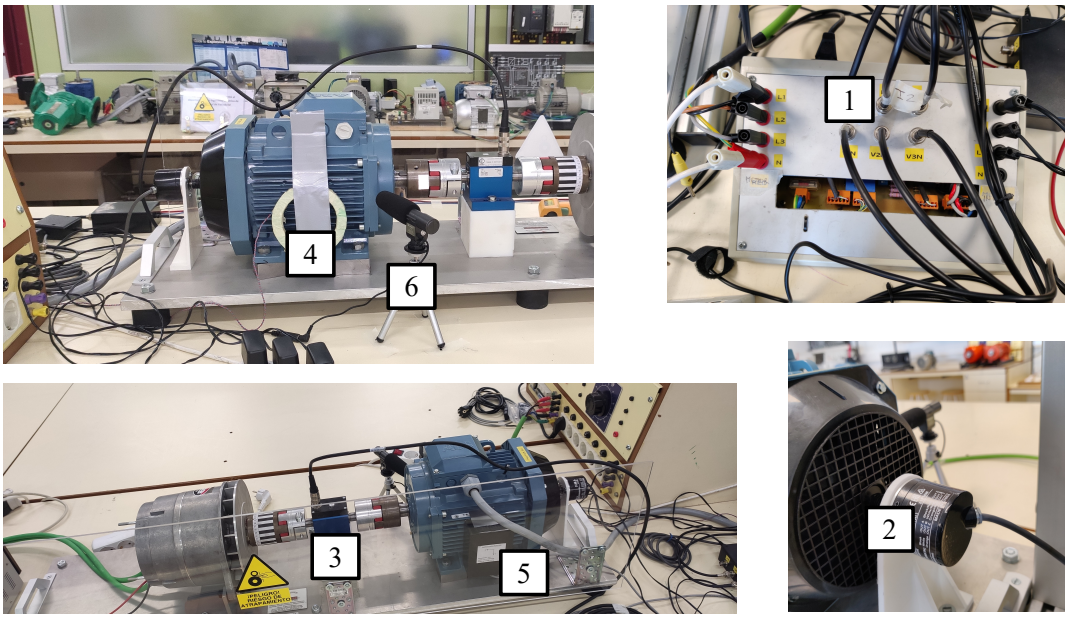

Figure 7.6: Sensors employed in the measurements.

7.2 Closed-loop inverter configuration

In this section, the tuning of the parameters of the speed closed-loop control of the Danfoss inverter used in the tests of this thesis will be explained. The tuning procedure, and in particular the choice of the parameters for the PID controller, has not been performed by the author of this thesis. The choice, in fact, has been made during another research carried out in the same laboratory (Laboratory of Diagnostics of Electrical Machines, University of Valladolid) and published in [200].

To visualize at best the Closed-Loop (CL) control operation, a block scheme model for the process is shown in Fig. 7.7. The process is the combination of the inverter, the induction motor and the load (alternator and resistances). The converter operates a vector control based on an equivalent circuit designed with a few parameters of the motor nameplate (rated voltage, current, power, speed) [201]. The employed Danfoss inverter requires a two-channel encoder with a delay of 1/4 of the rotational period to implement the CL control.

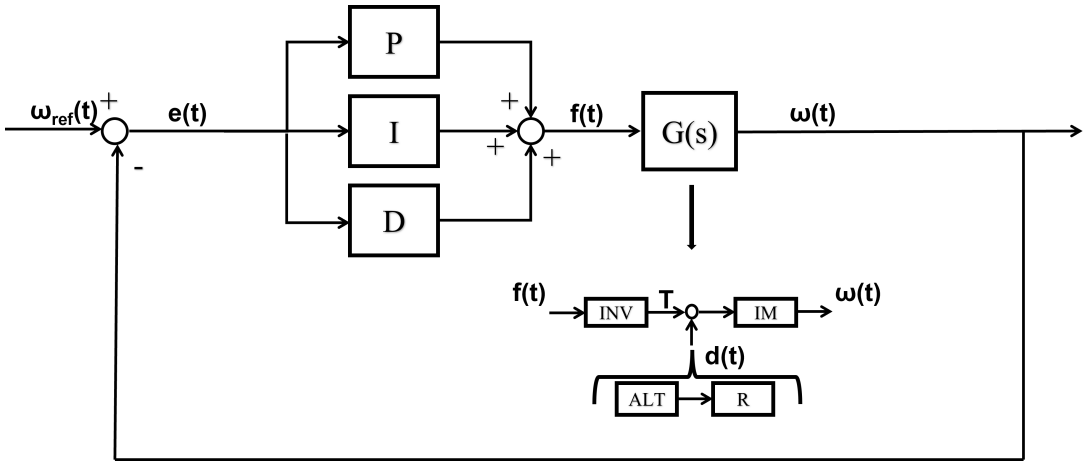

Figure 7.7: Process and control loop block scheme [200].

The inverter employs a PID digital controller, whose general transfer function is reported in equation 7.1.

$$R_{PID}(s) = K_P\left(1 + \frac{1}{sT_i} + sT_d\right) \tag{7.1}$$

Since the transfer function of the system was unknown, it was not possible to apply pole cancellation and root locus techniques to properly design the control.

Two different approaches have been used to find the correct tuning of the controller. The

first approach has been made by tuning manually the PID parameters and testing the response of the system with variations in the reference speed. Firstly, the proportional constant K_P has been modified and set to a proper parameter. Secondly, the integration time T_i has been decreased from the maximum value available from the inverter, with the purpose of having a fast response. Finally, also the derivative time T_d has been set to reduce overshoot during the operation. The transfer function of this first PID controller is the following:

$$R(s) = 0.300\left(1 + \frac{1}{0.033\ s} + 0.0165\ s\right) \tag{7.2}$$

Then, for the tuning of the second controller, the very general approach of the Internal Model Control (IMC) tuning rule has been used. The IMC rule allows to design a PID control, by only measuring the reaction curve for the open loop process [202]. A resume of the rules of the IMC method is given in Table 7.3. Regarding the parameters, T represents the time constant of the response to a variation in the goal frequency and τ the time delay of the response. Finally, T_f represents an arbitrary parameter that has to be chosen. From the tests, which have been carried out by applying 1 Hz of step from the inverter, a time constant $T = 0.234\ s$ and a time delay $\tau = 0.317\ s$ have been calculated to define the approximated transfer function. T_f was chosen equal to 0.25 s, giving the following final transfer function of the PID controller:

$$R(s) = 0.692\left(1 + \frac{1}{0.3925\ s} + 0.0945\ s\right) \tag{7.3}$$

This second controller allows to reach the reference speed without overshooting, but the response to system variations is much slower if compared to the one linked to the PID from

Table 7.3: IMC tuning rules for PI and PID controllers [200].

	$\mathbf{K_P}$	$\mathbf{T_i}$	$\mathbf{T_D}$
PI controller	$\frac{T}{\tau} + T_f$	T	-
PID controller	$T + \frac{0.5T}{\tau} + T_f$	$T + 0.5\tau$	$\frac{0.5T}{\tau} + T_f$

the first attempt. The first one indeed, due to the fast response, introduces also slight variations in the frequency of the fundamental component while trying to keep constant the speed read from the encoder. Both the settings of the PID for the Danfoss inverter have been used to acquire data for the work of this thesis. The parameters of the two controllers are resumed in Table 7.4, while the speed during the start-up transient for a healthy motor in both the control conditions (reference speed of 1500 rpm) is shown in Fig. 7.8. From the latter, the difference between the two controls implemented in terms of behavior in response to a change in the reference speed is clear. Due to their responses, in this thesis, we refer to the first controller as "Fast Loop" (FL) and to the second one as "Slow Loop" (SL). The FL reaches the reference speed faster than the Slow Loop, taking approximately 1 s less than the other. Nevertheless, the SL has a smoother behavior, offering less speed oscillations than the fast one.

Table 7.4: Resume of the parameters of the PID controllers.

	$\mathbf{K_P}$	$\mathbf{T_i}$	$\mathbf{T_d}$
Fast Loop (FL)	0.300	0.033 s	0.0165 s
Slow Loop (SL)	0.692	0.3925 s	0.0945 s

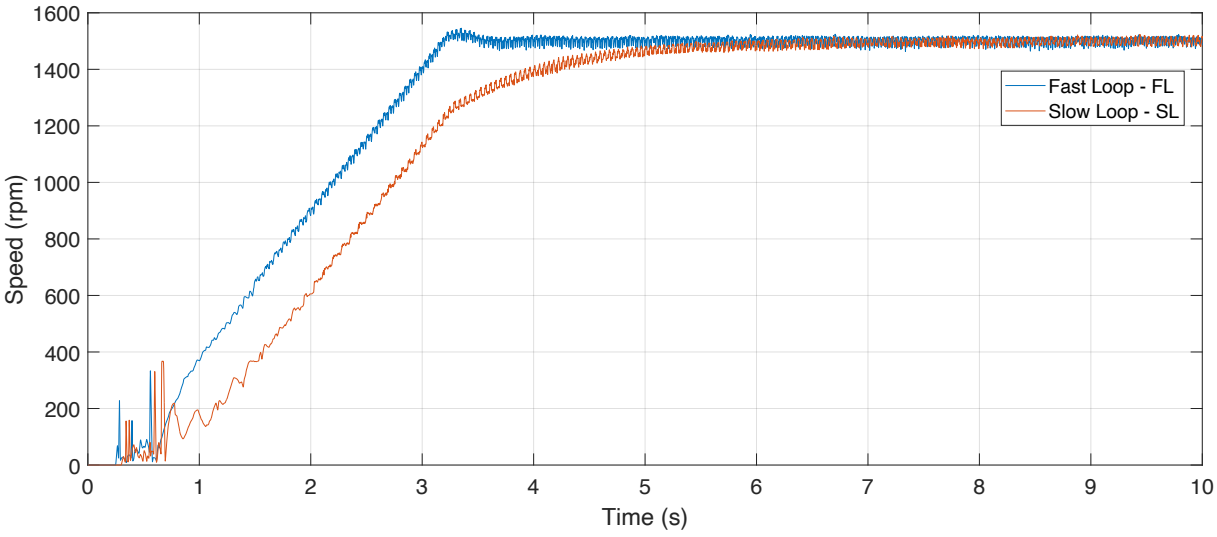

Figure 7.8: Different speed responses to the different control loops: Fast Loop in blue and Slow Loop in orange, with the same load level (5 rows of resistors) and the same reference speed (1500 rpm).

7.2.1 Speed signal issues and filtering

Closed-loop operation introduces an extremely high noise level in the signals, including the speed of the machine. Since having proper speed feedback is essential for the correct operation of the control, it has been necessary for the author to find a solution for this issue. Fig. 7.9 shows an example of a speed signal acquired from the encoder while the motor is operating under closed-loop control. Several high spikes are present in the time window analyzed. From the zoomed window, it is possible to see that even the reference speed is not reached due to interferences in the input signal of the converter. In this condition, the proper operation of the motor was not even possible. Several attempts have been implemented to reduce the noise to improve the quality of the control loops, among which:

- shielding the cables of the encoder (Fig. 7.10a);
- change the point in the grid for the encoder power supply;
- isolate the encoder power supply by adopting an UPS (uninterruptible power supply);
- change the DC power supply of the encoder.

Finally, it has been necessary to adopt two RC lowpass filters, one for each input to the converter, to reduce the noise level. Despite the fact that this filter introduces a delay and an error in the measurement, it allows the correct operation of the controller. The implementation is shown in Fig. 7.10b.

The speed signal has been filtered after its acquisition. This step was crucial to calculate the theoretical harmonics (and trajectories) of the faults and also to properly apply the Dragon Transform technique that, as already explained in section 6.3, requires the computation of the instantaneous slip.

A distinction has been made for signals acquired during the start-up and signals acquired while the motor was already operating around the reference speed. Regarding speed signals from motors running close to the reference speed, the `hampel` function, together with `smoothdata`, allows to reach good results in filtering the signal. The Hampel identifier (Hampel filter) is a function implemented in Matlab that allows the removal of outliers in

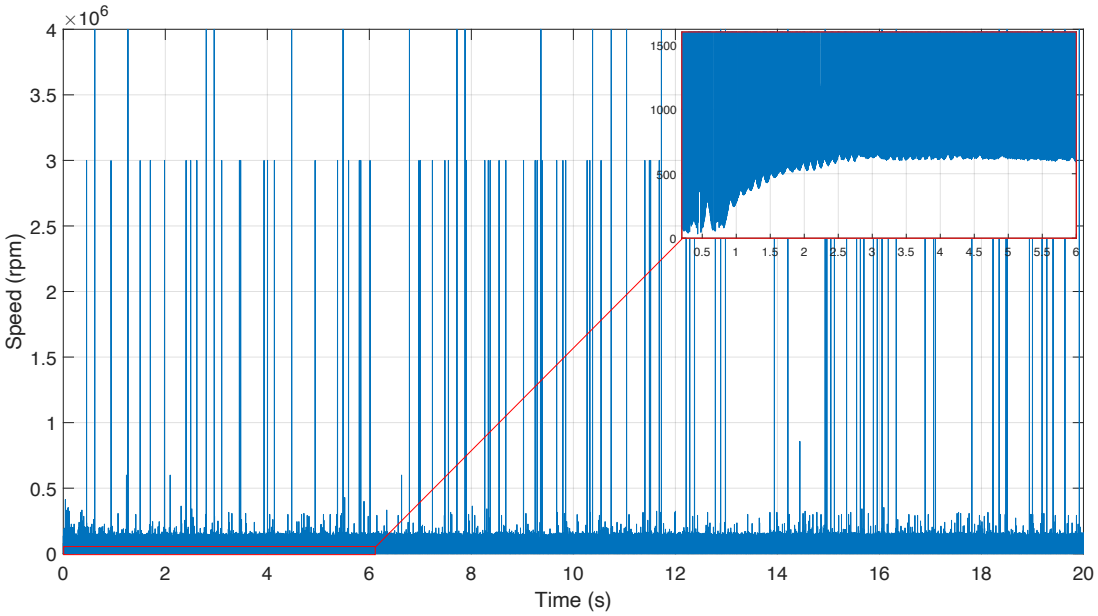

Figure 7.9: Speed signal acquired from closed-loop operation (SL) without filtering, reference speed equal to 1500 rpm.

a signal. For each sample of the signal, this function computes the median of a window composed of the sample and a defined number of surrounding samples, half of the defined number per side. It also estimates the standard deviation of each sample about its window median using the median absolute deviation. If a sample differs from the median by more than the standard deviation, it is replaced with the median. In the analysis of this work, it has been implemented as follows:

```
>      speed_f = hampel (speed, pnts, nsig);
```

In the Matlab function reported:

- `speed_f` is the output filtered signal;
- `speed` is the original signal;
- `pnts` is the number of surrounding samples of the point under analysis;
- `nsig` is a factor to multiply the standard deviation.

Regarding the function `smoothdata`, it allows to smooth the shape of a signal dividing it into windows. Depending on the selected method, the smoothing of the signal can be computed in different ways. It has been implemented as follows:

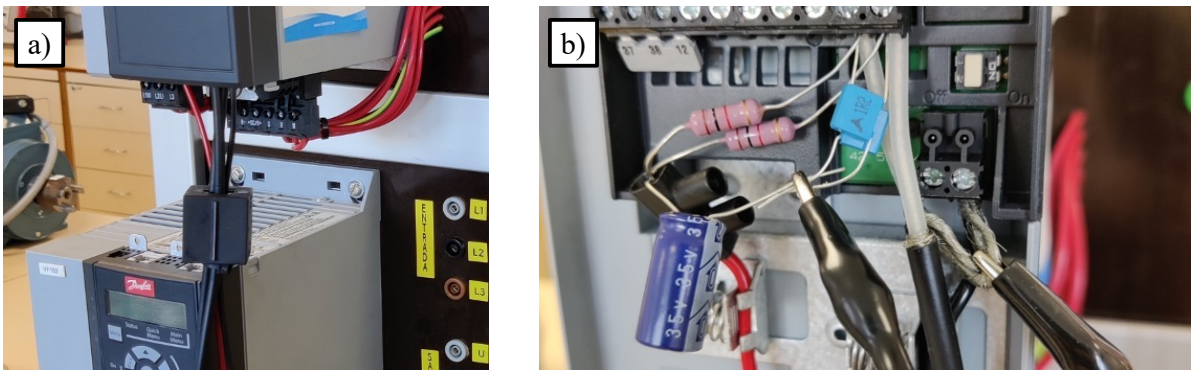

Figure 7.10: Shielding device on the encoder connection to the power converter (a) and the solution adopted to improve the control behavior (b).

```
>    for I = 1 : c
>        s1 = smoothdata (speed,  'gaussian', win);
>    end
```

Where:

- `'gaussian'` is the applied method, which computes the Gaussian-weighted average over each window of the signal;
- `win` is the window length where the Gaussian-weighted average is computed.

To not modify the real shape of the speed signal, the function has been computed into cycles with a reduced window length.
The most critical part to obtain an acceptable speed signal was the start-up, in which spikes from the encoder are high (especially during closed-loop operation), and it is not possible to use a traditional filtering technique. During the start-up, the speed signal has been reconstructed starting from the local minimum of the original one. The last point of this reconstruction has been chosen depending on the supply frequency of the acquisition. Starting from the last point of the signal, when it reaches a value below the reference one, a flag is activated to know the portion of the signal to be reconstructed.
In this portion, the signal is divided into windows of a certain number of points. In this window, just the minimum value and its position in the vector are saved. Then, the

signal is reconstructed by linear interpolation between two adjacent minimum points of the original signal. The results of the digital filtering process are shown in Fig. 7.11.

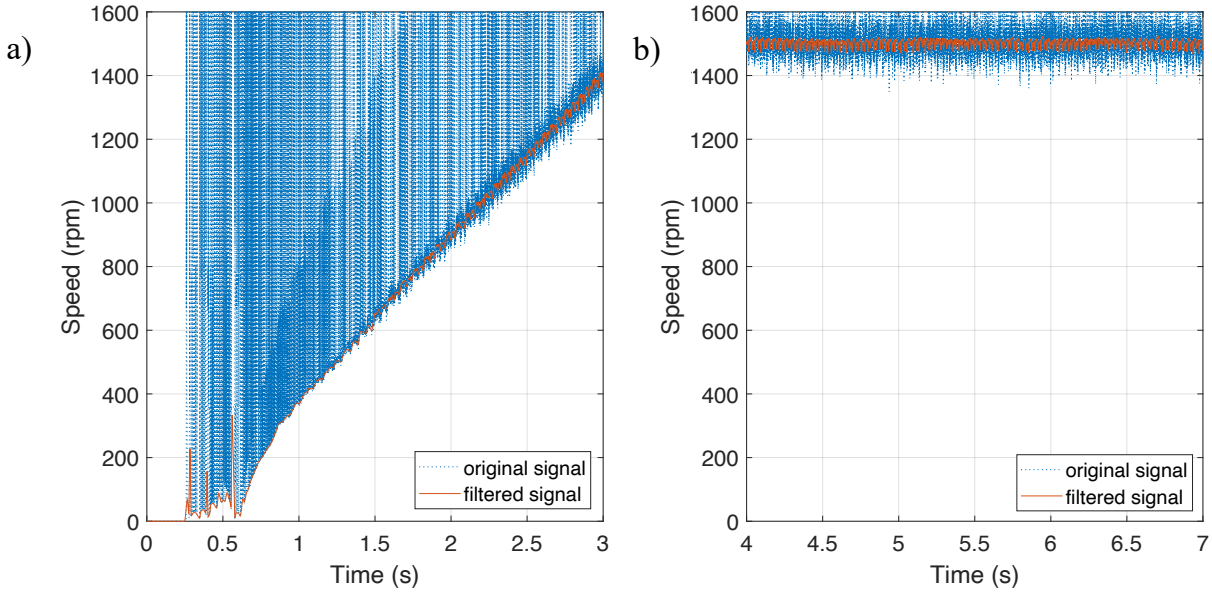

Figure 7.11: Results of the filtering methods applied: a) start-up; b) normal operation. Signals from a healthy motor operating in Fast Loop, 1500 rpm reference speed.

7.3 Emulation of the fault and acquisitions

7.3.1 Emulation of the broken bar fault

As already discussed, the analysis of this work focuses on the broken rotor bar fault detection while the induction motor is operating under closed-loop conditions. To replicate the fault accurately, alterations were made to the rotor of one of the ABB induction motors in the laboratory. Specifically, the alteration involved drilling a hole into the end ring of the squirrel cage, precisely targeting a rotor bar end.

The modification was implemented within the end ring of the squirrel cage to avoid potential damage to the rotor lamination. Such damage has the potential to induce undesirable magnetic imbalances within the motor during its operation. This operation allowed the increase of the resistance of the circuit in proximity of the bar, simulating a scenario of bar breakage.

Several attempts at the severity of the fault have been made in a preliminary analysis,

increasing step-by-step the severity of the fault while analyzing the current spectra for each condition under analysis. Finally, once the definitive faulty condition has been reached, it has not been modified among all the tests carried out.

The definitive faulty rotor is shown in Fig. 7.12.

Figure 7.12: Detail of the fault provoked in the laboratory for the analysis.

7.3.2 Acquired signals

Several acquisitions were made during the tests in the laboratory, capturing both the behavior of the healthy and the faulty motors. For every condition monitored, three acquisitions were made to create redundance of data. Each acquisition was carried out without varying time and sampling frequency of the trial. The following values were chosen:

- $T_s = 20\ s$ (acquisition period);
- $F_s = 100\ \frac{kS}{s}$ (sampling frequency).

Excluding the trials with the motor supplied from mains, the acquisitions were carried out including the start-up transient, in order to have the same condition in the control loop for all the analyzed cases. Then, the start-up transient was not taken into consideration, and only the last 10 seconds of the signals were analyzed (using the standard time required to achieve a frequency resolution of 0.1 Hz for a Fast Fourier Transform). After acquiring the signals, a resampling and/or decimation stage was performed to reduce the frequency range of the analysis and to decrease the computational burden for both the Fast Fourier analysis and time-frequency transformations. For the resampling stage, the function `resample` was used:

```
>    Ir = resample (I, p, q);
```

The latter function resamples the input signal, `I`, at `p/q` times the original sample rate. This function applies an FIR Antialiasing Lowpass Filter to `I` and compensates for the delay introduced by the filter.
Regarding the decimation process, the function `decimate` was used:

```
>    Id = decimate (I, dr);
```

The latter function reduces the sample rate of input signal `I` by a factor of `dr`. The function uses a lowpass Chebyshev Type I infinite impulse response (IIR) filter.
Finally, also fractional resampling was used to apply the Dragon Transform technique. The fractional resampling allows to reach the desired sampling frequency from the original one by applying linear interpolation and decimation by averaging [185, 203].
Tests were performed varying the load condition from no load "0R" (no rows of resistors linked to the stator of the alternator) to full load condition "5R" (5 lines of resistor linked), referring to Table 7.2 shown previously. Moreover, for each trial carried out with power converters, different reference frequencies were set: 30, 40, 50 and 60 Hz. Every condition of motor and inverter were so tested with all the combinations of load and supply frequency described.
Finally, for each trial, several signals were acquired:

- three phase currents;
- three phase voltages;
- radial stray flux;
- axial and radial vibrations;
- sound noise level;
- torque;
- speed.

Also the misalignment fault has been finally introduced by putting a 2.5 mm thick washer under the motor basement, to generate as a result an effect of eccentricity. Despite the presence of an elastic coupling that may have attenuated such an effect, sustained vibrations showed up at sight. A detail of the washer under the basement is shown in Fig. 7.13.

However, this thesis presents only the analysis of current signals, using also speed and torque. The only fault analyzed, moreover, is the broken rotor bar fault. In Fig. 7.14 an example of results from the acquisition of some signals is shown.

A final overview of the acquisition carried out in the laboratory is given in Table 7.5.

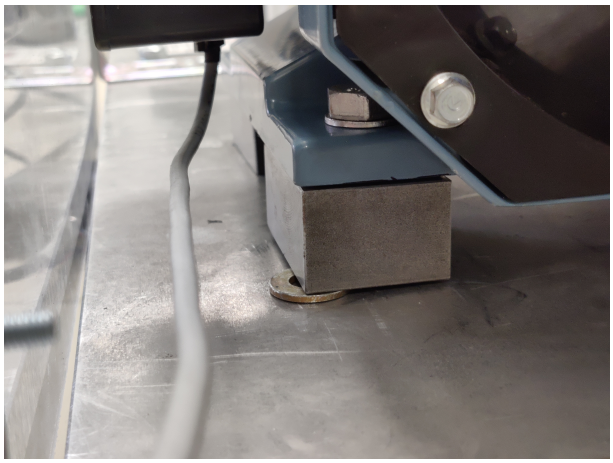

Figure 7.13: Detail of the washer under the basement of the motor.

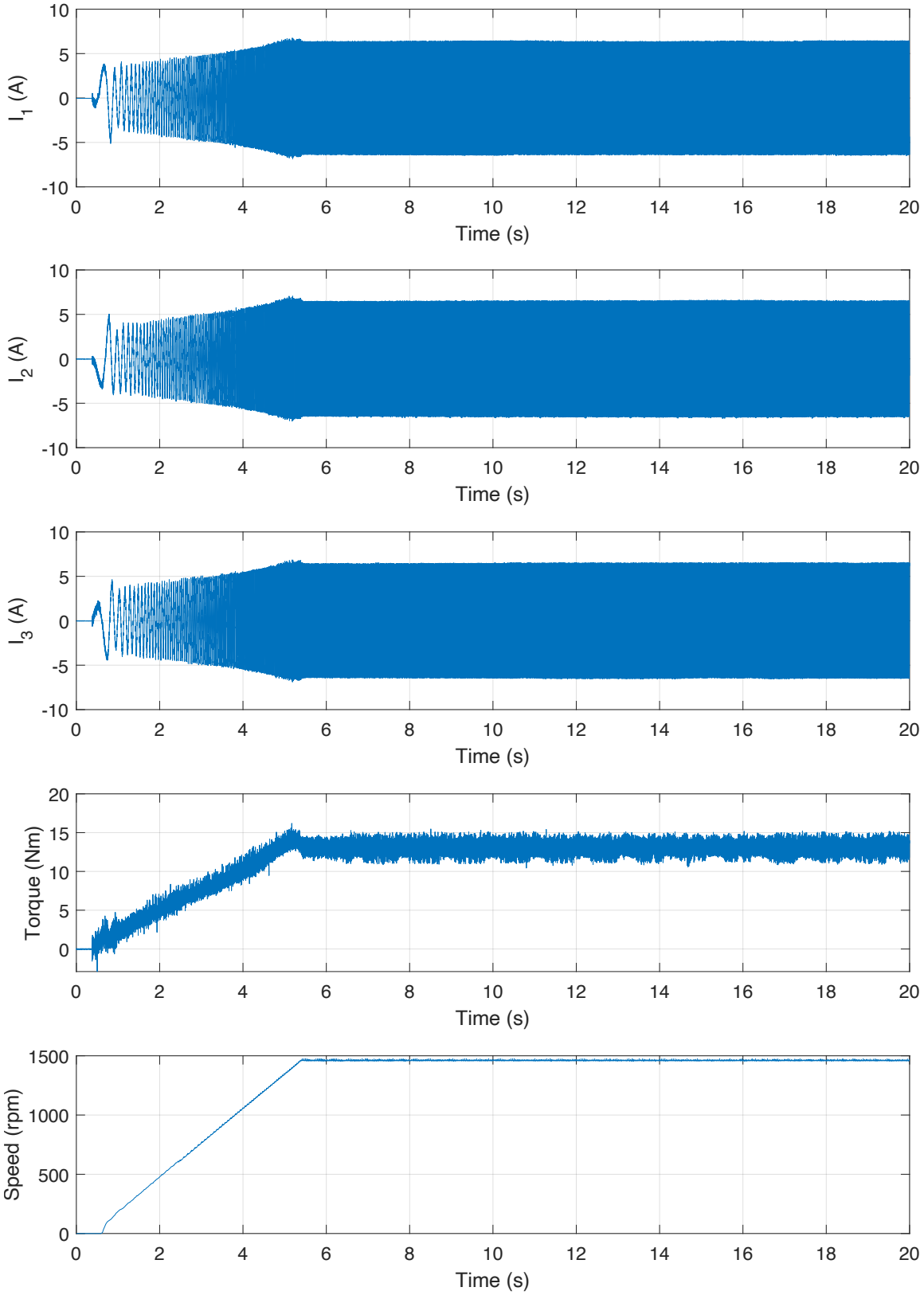

Figure 7.14: Phase currents, torque and filtered speed from an acquisition (healthy, open loop, 5R load, 50 Hz).

Table 7.5: Resume of the trials acquired in the laboratory.

	Control:	Healthy	BRB	BRB + Misalignment
Danfoss	OL	X	X	X
	OL - slip compensation		X	X
	FL	X	X	X
	SL	X	X	X
WEG	OL	X	X	X
Allen - Bradley	OL - slip compensation			X
Mains	-	X	X	

Chapter 8

Analysis of the signals

In this chapter, the analysis of the signals acquired will be presented. As already discussed, the analysis will focus on the detection of the broken rotor bar fault, mainly on closed-loop operation. Due to the high harmonic content and the oscillation of the harmonics introduced by the control, the identification of the fault-related harmonics may be more difficult than in the mains-fed or the open-loop fed operation of the motor. In the first part of the chapter, the analysis published by the author in [204] will be explained. In this work, FFT, STFT and Dragon Transform have been used to analyze the signals. Then a further analysis, not published yet, will be given, introducing also the STMN technique. Despite the trials were carried out by acquiring the behavior of the signals for a time equal to 20 s (including the start-up transient), only the last 10 s of the signals are used in the analysis of this thesis (not considering the start-up transient).
All the analyses have been conducted by using the Matlab - MathWorks software.

8.1 Preliminary analysis

The first part of the analysis of this chapter considers only current signals acquired from the faulty motor operating in closed-loop. Only the Fast Loop condition is considered in the first sections of this chapter: the parameters of its transfer function are reported in section 7.2, Table 7.4. The analysis focuses on finding harmonics related to the broken rotor bar around the fundamental supply frequency (f_s) in the phase current spectrum.

These harmonics are given by the equation 5.7, introduced in chapter 5:

$$f_{bb} = (1 \pm 2ks) f_s \tag{5.7}$$

Where s is the rotor slip at the working point and k assumes integer positive values. Generally, this equation is studied with a value of k equal to 1. As already explained in chapter 5, these two resulting harmonics usually have the highest amplitude among the BRB-related harmonics and are known as lower sideband harmonic (LSH, $(1-2s)f_s$) and upper sideband harmonic (USH, $(1+2s)f_s$).

However, when the analysis is focused on a closed-loop system, LSH and USH may be undetectable. In fact, the main supply frequency is not fixed also when the start-up is ended but has small variations to keep constant the output speed of the rotor. As a result, especially for low load conditions where slip has low values and BRB first harmonics are close to the fundamental one, it is usually not possible to distinguish them from the harmonics caused by the control loop even with time-frequency techniques.

For this reason, in this analysis, a value of $k = 3$ is considered. These harmonics are generally lower in amplitude with respect to LSH and USH but allow to better recognize the fault in closed loop inverter fed operation being furthest from the main harmonic.

8.1.1 Fast Fourier Transform analysis

This analysis was performed by studying the last 10 s of the current signal, in which the start-up transient is completed. The frequency resolution is given by:

$$\sigma_f = \frac{1}{10\ s} = 0.1\ \text{Hz} \tag{8.1}$$

To compute the theoretical frequency of the sidebands related to the broken rotor bar fault, the mean value of the acquired speed signal in the same time interval is calculated. This allows the computation of the average slip by calculating the component of the spectrum that carries the highest energy, using the latter as the reference supply frequency f_s. In Fig. 8.1 and Fig. 8.2 the results of the analysis for signals under different load conditions are shown.

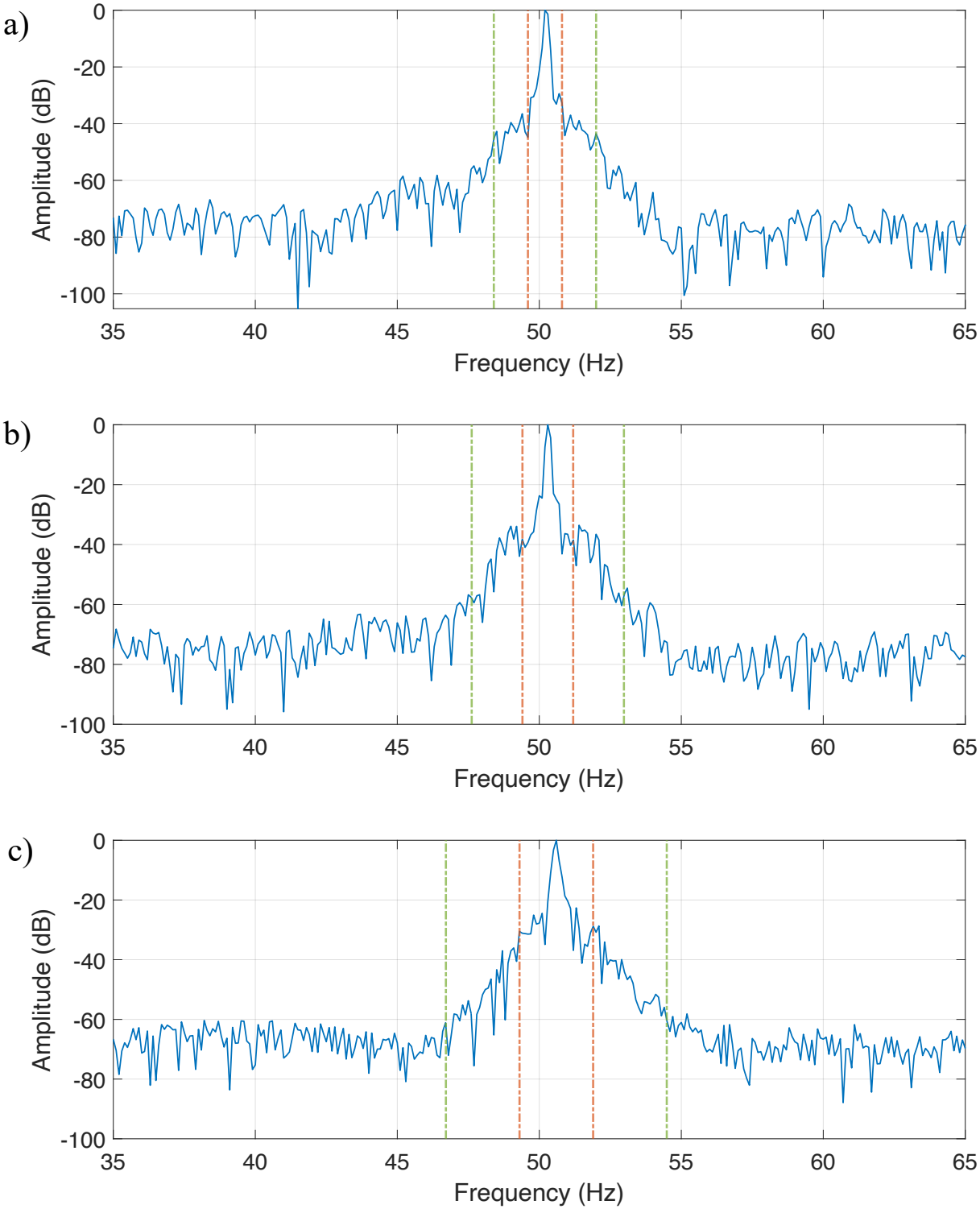

Figure 8.1: FFT of the current for different low load conditions: (a) no rows of resistors (0R) inserted (no load), (b) 1 row of resistors (1R) inserted and (c) 2 rows of resistors (2R) inserted. Theoretical frequencies of LSH and USH ($k = 1$) are reported in red while their third components ($k = 3$) are reported in green.

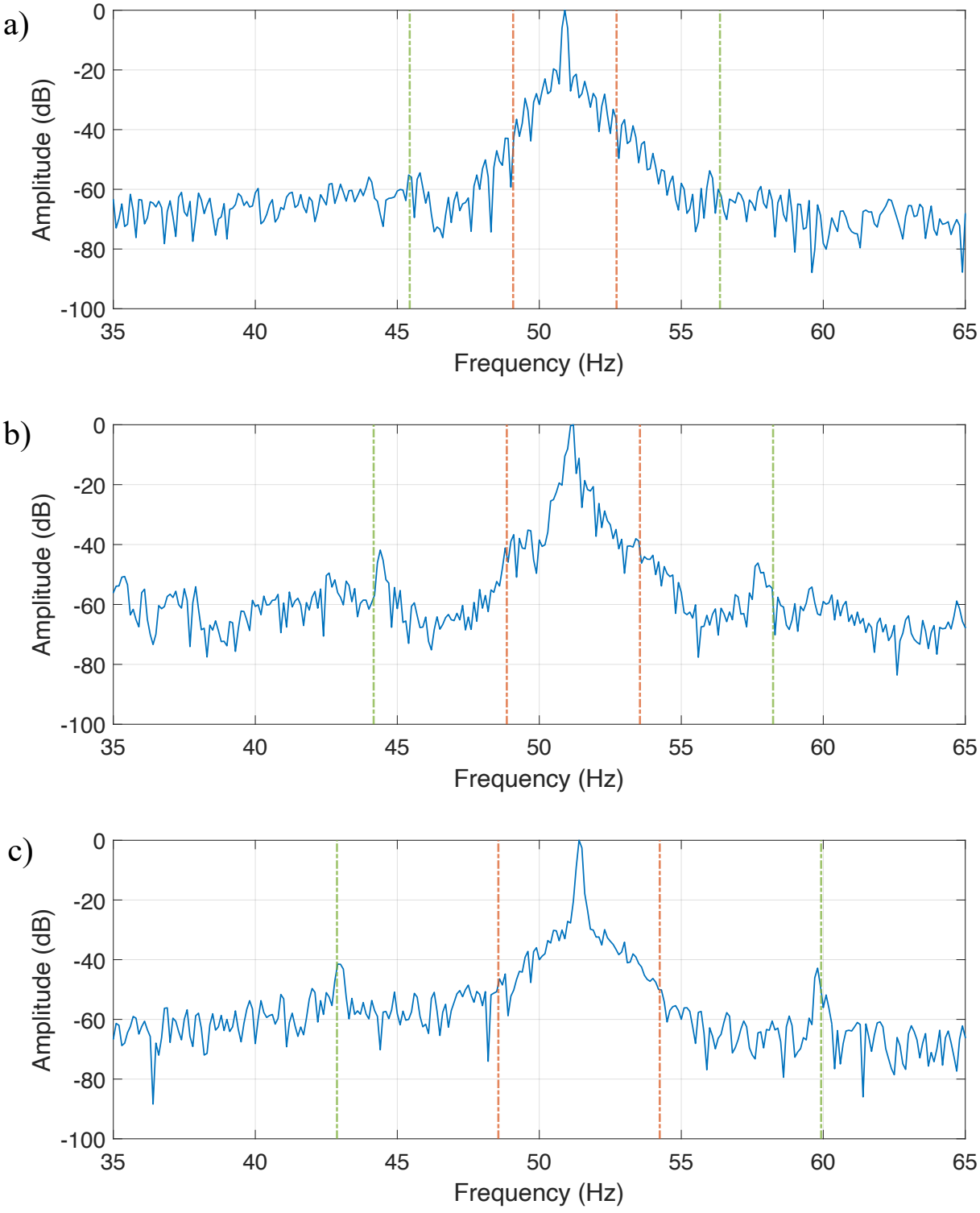

Figure 8.2: FFT of the current for different high load conditions: (a) 3 rows of resistors (3R) inserted, (b) 4 rows of resistors (4R) inserted and (c) 5 rows of resistors (5R) inserted. Theoretical frequencies of LSH and USH ($k = 1$) are reported in red while their third components ($k = 3$) are reported in green.

The best results for this analysis are achieved at full load, 5R ($T = 11.86$ Nm, $I_{rms} = 4.0$ A), the FFT of which is represented in Fig 8.2c. The calculated average slip in this condition is equal to 2.8%. For this load level, the fundamental component is located in $f_s = 51.4$ Hz and the rotor average speed is calculated equal to 1499 rpm. The theoretical LSH and USH are respectively located at 48.56 Hz and 54.24 Hz.

As mentioned before, these harmonics, especially with the classical discrete Fourier analysis at low load conditions, are not visible in the spectrum due to the not fixed supply frequency of the inverter current in closed-loop operation.

Expanding the study of the BRB-related harmonics to their third component around the fundamental harmonic ($f_{3bb} = (1 \pm 6s)f_s$), it is possible to better recognize the fault. For full load conditions, these harmonics are located at 42.87 Hz (the third component of the LSH) and 59.93 Hz (the third component of the USH). As can be seen from Fig. 8.2c, the sidebands of the third harmonic are detectable in the current spectrum of the full load trial, where the lower sideband has a normalized amplitude of -41.47 dB and the upper one reaches -42.83 dB.

In Fig. 8.1a and Fig. 8.2a the results of the analysis for no load condition, 0R (measured torque $T = 1.01$ Nm, $I_{rms} = 2.2$ A) and half load condition, 3R ($T = 7.1$ Nm, $I_{rms} = 3.0$ A) are shown. For no load condition, the fundamental component f_s is equal to 50.2 Hz, and the slip is equal to 0.6%. The fundamental component has a lower frequency (-1.2 Hz) than in the full load conditions because also the value of the slip is lower. Thus, the synchronous speed at the reference frequency of 50 Hz is reached with a lower value of compensation. The theoretical frequencies of LSH and USH are very close to the supply frequency (49.60 Hz and 50.80 Hz respectively), as well as their third components, located at 48.39 Hz and 52.01 Hz. In this situation, it is not possible to recognize the fault using the Fast Fourier Transform, not even analyzing the third component of the BRB harmonics. Harmonics to detect broken rotor bars are not recognizable also in the current signal acquired from the trial at half-load conditions. In this case, the slip has been estimated from the speed signal as 1.8%, with a supply frequency of 50.9 Hz. The third components are located at 45.42 Hz (lower) and 56.38 Hz (upper). As can be seen in the plot, their amplitude is not higher than the others in that frequency region, also because of very high noise in the signal given by the closed-loop control of the inverter.

8.1.2 Short-Time Fourier Transform analysis

The analysis carried out by using the FFT clearly shows the need to use a different technique to better detect the BRB fault in closed-loop operation. A decomposition in time windows is required, because of the small perturbations in the speed and consequently in the supply frequency that occur also when the goal speed is achieved by the motor. As already explained in detail in section 6.2, the Short Time Fourier Transform implements a windowing of the signal, computing the FFT for each shortened signal obtained. Each window can overlap adjacent ones for a certain percentage to have a better analysis. The STFT has been implemented for this work through the `spectrogram` function in Matlab:

```
>    [yI,fI,tI,~] = spectrogram (Ir, window, NWO, Fs);
```

Where the outputs `yI,fI,tI` are respectively the matrix of the amplitudes of the harmonics, the vector of the frequencies and the vector of the time instants of the windows. In input, `Ir` is the resampled or decimated current vector, `window` is the window selected (in this work, the hanging window has been used, so `window = hann(NW)`, where `NW` is the number of window point), `NWO` is the number of overlapping points between each consecutive window and `Fs` is the sampling frequency after the decimation/resample stage. To reach a good compromise between time and frequency resolution, the choice of the proper input parameter is crucial, and parameters may vary from one analyzed case to the other. For the percentage of overlap between adjacent windows, a value of 99.5% has been chosen (332 points). Each time window is composed of 333 points.
In this subsection, the same signals studied in the previous one are analyzed through the STFT method. In this case, since the harmonics related to the fault vary over time, theoretical time-frequency trajectories have been computed instead of a single theoretical steady state frequency from the average values of the speed. The speed signal has been divided into a certain number of overlapping windows, equal to the number of windows selected to compute the spectrogram. Then, the same approach used to compute the average slip used during the FFT analysis has been implemented to compute the slip for each window. The maximum value of each vector corresponding to a time window in the amplitude matrix has been computed and correlated to its value of frequency in the vector `fI`, allowing to compute the slip and so the theoretical trajectories of each

fault-related component. The results of this analysis are shown in Figs. 8.3 and 8.4. For the full load signal shown in Fig. 8.4c (left), two trajectories in the time-frequency plane related to the third harmonics of the BRB fault are clearly visible around 43 Hz and 60 Hz and follow the same path of the theoretical trajectories displayed in Fig. 8.4c (right). Lowering the load condition to half load (Fig. 8.4a), the sidebands related to the fault are still recognizable in the t-f plane considered.

To achieve this graphical result, however, a fully accurate analysis of the Matlab code is required, in particular regarding the color palette related to the amplitude of the harmonics and the range in which it is set. Finally, for the tests at low load conditions, whose results are shown in Fig. 8.3, the trajectories of the BRB fault-related third harmonics are not detectable with the STFT technique, as their theoretical trajectories lie close to the fundamental supply harmonic trajectory.

Even with high load values, and so high values in the slip, the LSH and the USH are still not easily recognizable with this technique, because of the suboptimal frequency resolution obtained. In fact, the decomposition of the signal in time windows leads to a compromise between time resolution and frequency resolution of the analysis: on one hand, short time windows are required to be able to detect variations in the frequency of the harmonics. On the other hand, reducing the windows opening results in a reduction of the frequency resolution. When operating in closed loop control, a trade-off between these two aspects is difficult to reach in the broken rotor bar detection analysis, even when the analyzed signal does not come from a start-up transient.

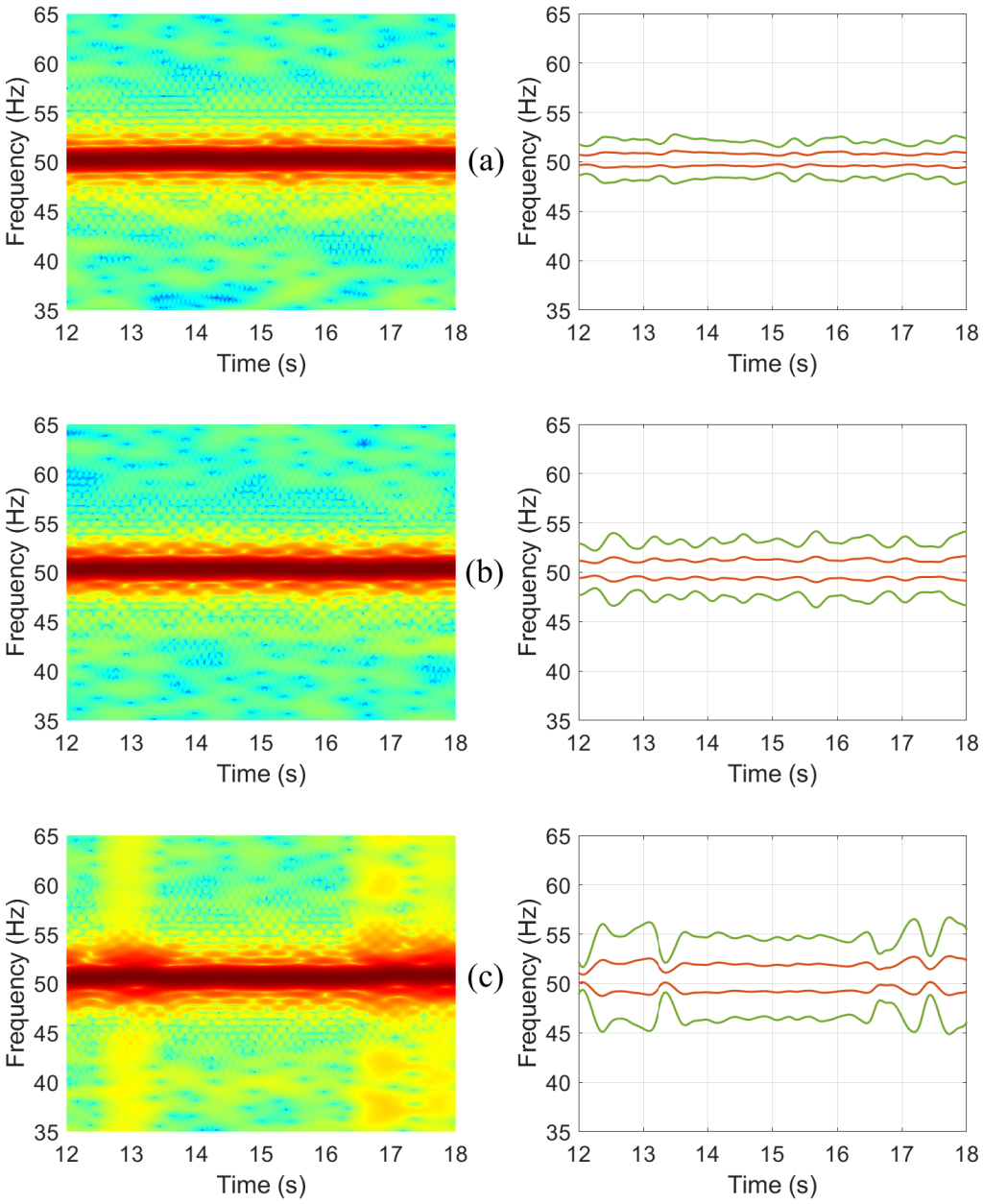

Figure 8.3: STFT analysis of the current for low load conditions (on the left) and theoretical trajectories of BRB-related harmonics (on the right, LSH and USH ($k = 1$) are reported in red while their third components ($k = 3$) are in green). Load conditions: (a) no rows of resistors (0R) inserted (no load), (b) 1 row of resistors (1R) inserted and (c) 2 rows of resistors (2R) inserted.

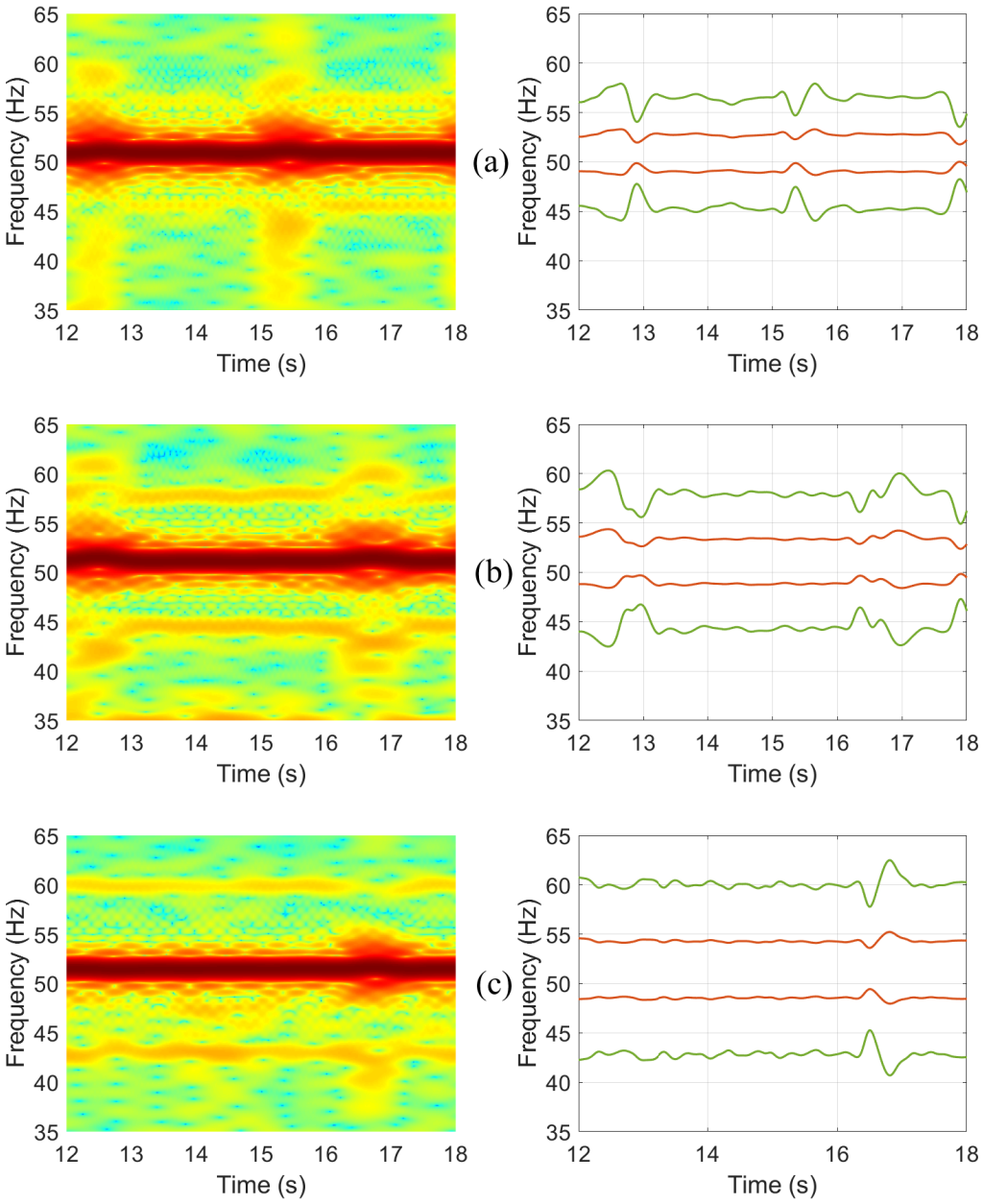

Figure 8.4: STFT analysis of the current for high load conditions (on the left) and theoretical trajectories of BRB-related harmonics (on the right, LSH and USH ($k = 1$) are reported in red while their third components ($k = 3$) are in green). Load conditions: (a) 3 rows of resistors (3R) inserted, (b) 4 rows of resistors (4R) inserted and (c) 5 rows of resistors (5R) inserted.

8.1.3 ST - MUSIC analysis

A last preliminary analysis, carried out implementing the Short-Time MUltiple SIgnal Classification (ST - MUSIC) is briefly reported in this subsection. The MUSIC algorithm is a spectral estimation technique similar to the Min-Norm, which has been presented in section 6.4. The algorithm has been implemented in Matlab in the following function:

```
>    [t,f,S] = wmusic(x,N,M,nfft,Fs,p);
```

Where `t,f,S` are respectively the time vector, the frequency vector and the matrix of the amplitudes in output while the inputs are:

- `x`: input signal;
- `N`: size of each window;
- `M`: overlapping points between consecutive windows;
- `nfft`: number of points of the estimated spectrum;
- `Fs`: sampling frequency;
- `p`: number of eigenvalues of the decomposition.

The key point in the usage of this technique is the proper choice of the number of eigenvalues, that are strictly related to the number of harmonics shown in the estimated spectrum. A wrong number of selected eigenvalues can lead to the appearance of harmonics not real in the spectrum. Moreover, the dependence of the spectrum on the number of eigenvalues is also related to the number of points selected for each window when the ST-MUSIC algorithm is applied. An example of a signal analyzed with this technique is shown in Fig. 8.5.

The application of this technique for the detection of the broken rotor bar fault required the implementation of a bandpass filter for the current signal under analysis. Based on preliminary tests conducted with this technique, harmonics close to the fundamental are not even identified without this solution. A Butterworth bandpass filter has been used during this analysis. This filter typology allows to filter the signal outside the desired frequency band without creating ripples in the filtered spectrum of the signal. The filter has been designed in Matlab using the function `butter`:

```
>    [aB,bB] = butter(Q,wn,'ftype');
```

Where `[aB,bB]` are the coefficient of the filter transfer function in output, `Q` is the filter order, `wn` is the vector of the selected band in per unit with respect to the whole bandwidth of the acquisition ($\frac{F_s}{2}$) and `'ftype'` is the selected type of filter. For the analysis of signals with a reference frequency of 50 Hz, these parameters have been selected to design the Butterworth filter:

- `Q = 4;`
- `wn = [35 65].*2/Fs;`
- `'ftype' = 'bandpass'`.

Then, the filter has been applied to the current signal using the coefficients of the filter transfer function through the function `filter`:

```
>    x = filter (aB, bB, Ir);
```

Where `x` is the output current filtered signal and `Ir` is the input resampled signal.
Despite from Fig. 8.5 it is clearly possible to distinguish two sidebands in the t-f plane close to 60 Hz and 43 Hz that may be related to the fault, but it is not possible to determine the actual amplitude of the harmonics using this technique. In fact, also the amplitude of the harmonics in the estimated spectrum strongly depends on the choice of the parameters presented previously.
For the reasons explained in this subsection, the ST-MUSIC technique has been abandoned for the study of this thesis.

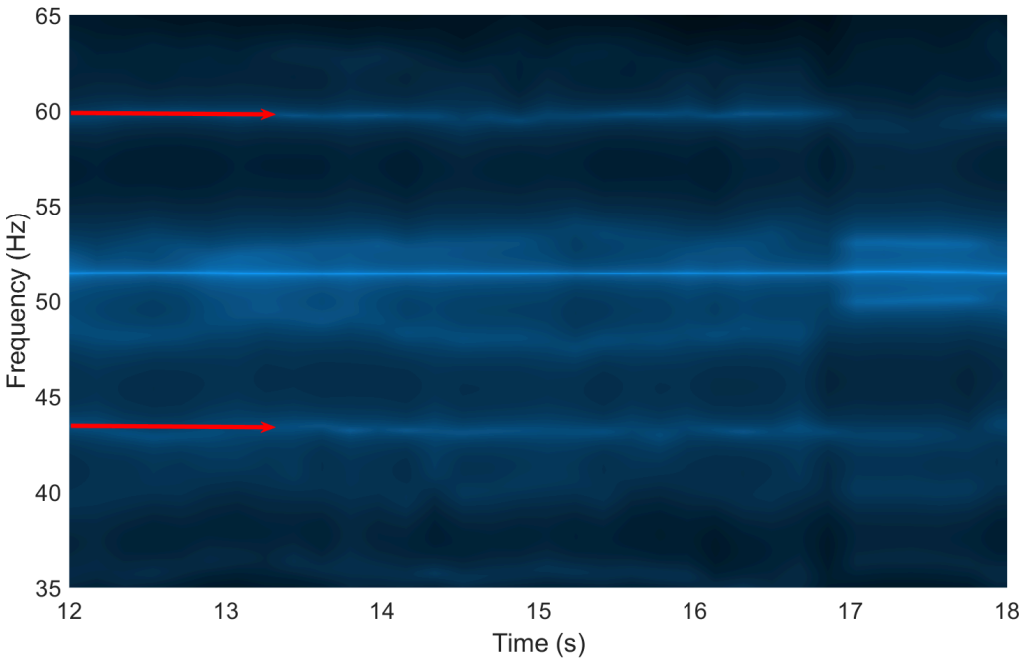

Figure 8.5: ST-MUSIC analysis of the current signal for full load conditions (5R). The red arrows denote the trajectories that can be related to the third component of the fault-related harmonics.

8.2 Dragon Transform analysis

As discussed in the previous part of this thesis, this study focuses on the harmonics generated by faults due to the BRB of the induction motors. These harmonics occur in the stator current of the machine and follow unique paths in the time-frequency plane. As demonstrated in section 8.1, because these harmonics are very close to the trajectory described by the first harmonic generated by the power supply and because of the high energy of this first harmonic, it is inadequate to visualize them using techniques such as FFT or STFT. Therefore, it is necessary to use more advanced techniques for their correct visualization. For this purpose, in this study, the Dragon Transform (introduced and explained in section 6.3) has been used as a technique to analyze the components present in the signal.

It is essential to employ a signal processing technique that is accurate enough to precisely track the trajectory of the harmonics, even when they are near the first high energy harmonic. The Dragon Transform is a technique that meets this requirement, as it allows trajectories to be tracked with excellent resolution over the entire time-frequency plane. To be able to apply the Dragon Transform by creating the atoms, a proper filtering procedure of the speed signal was necessary to compute a slip evolution in time that is as close as possible to the actual one. The procedure behind this step of the analysis has been already explained in subsection 7.2.1.

To apply the DT technique, a fractional resampling has been performed, reducing the sampling frequency to 256 Hz. This was made to reduce the computational burden of the calculations. With this value of F_s, the computational time required to compute the DT technique (by choosing $\sigma = 0.7979$ and $C_\sigma = 0.84$ in the construction of the Dragon Atoms) is around 5 minutes for a computer with an AMD 5800X CPU. The results from this analysis, where the same current signals considered previously are used, are shown in Figs. 8.6-8.11.

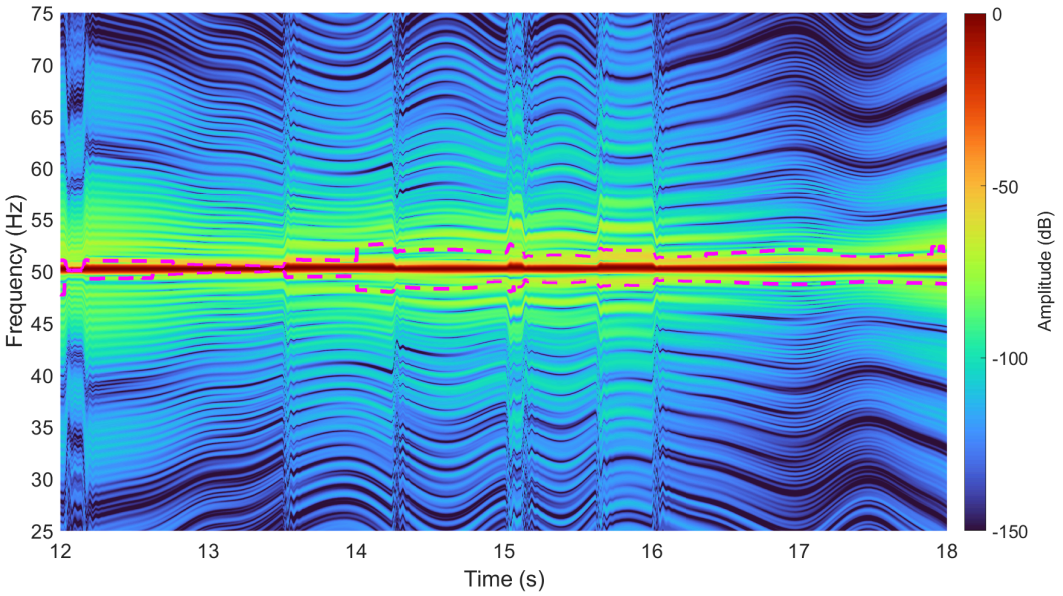

Figure 8.6: DT analysis of the current signal from a faulty motor under no load condition (0R). Dashed lines denote the theoretical trajectories of the third fault-related component.

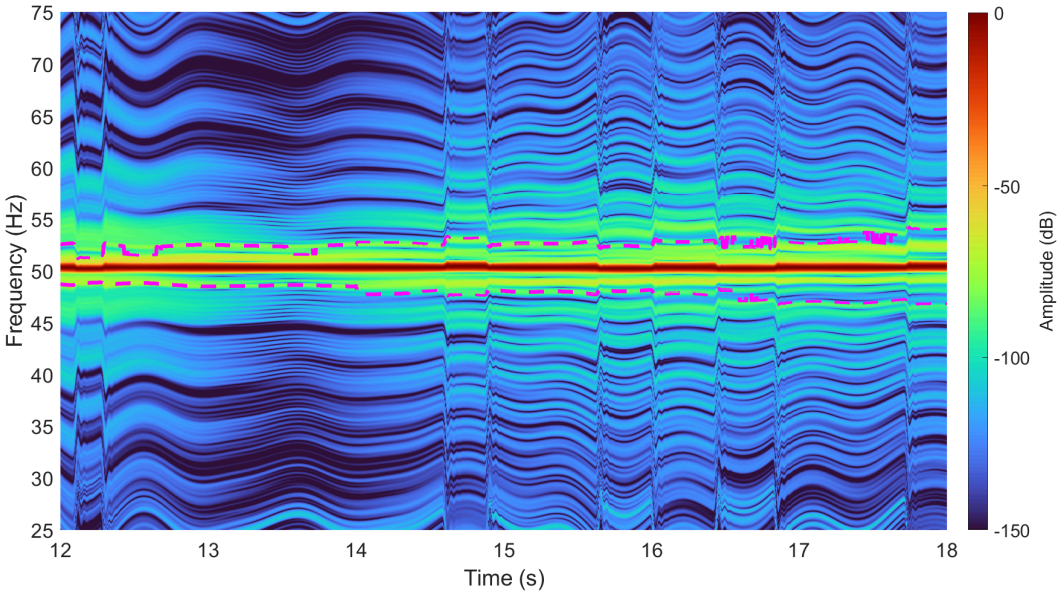

Figure 8.7: DT analysis of the current signal from a faulty motor under low load condition (1R). Dashed lines denote the theoretical trajectories of the third fault-related component.

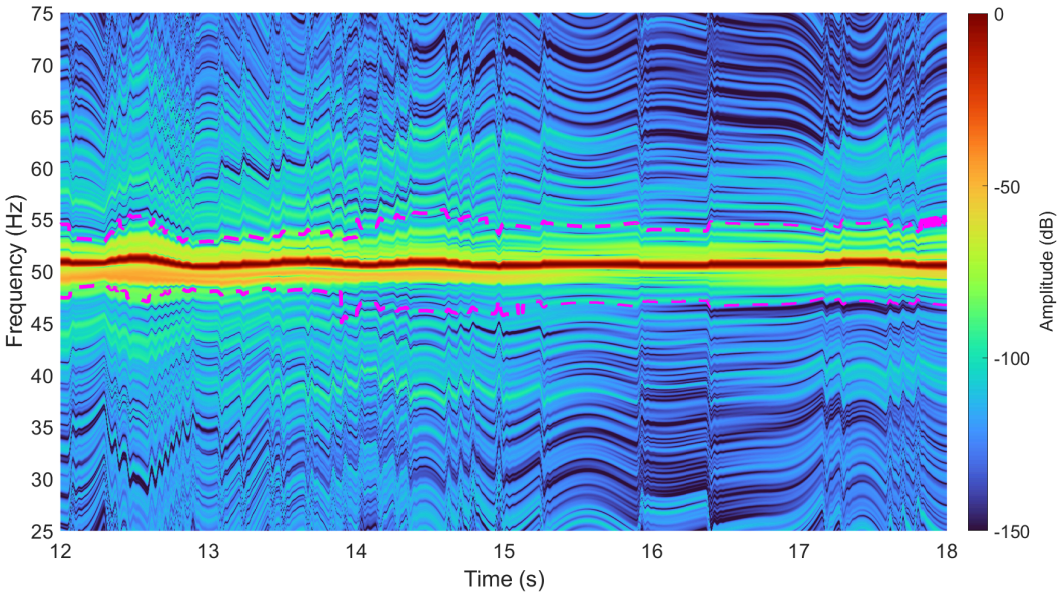

Figure 8.8: DT analysis of the current signal from a faulty motor under low load condition (2R). Dashed lines denote the theoretical trajectories of the third fault-related component.

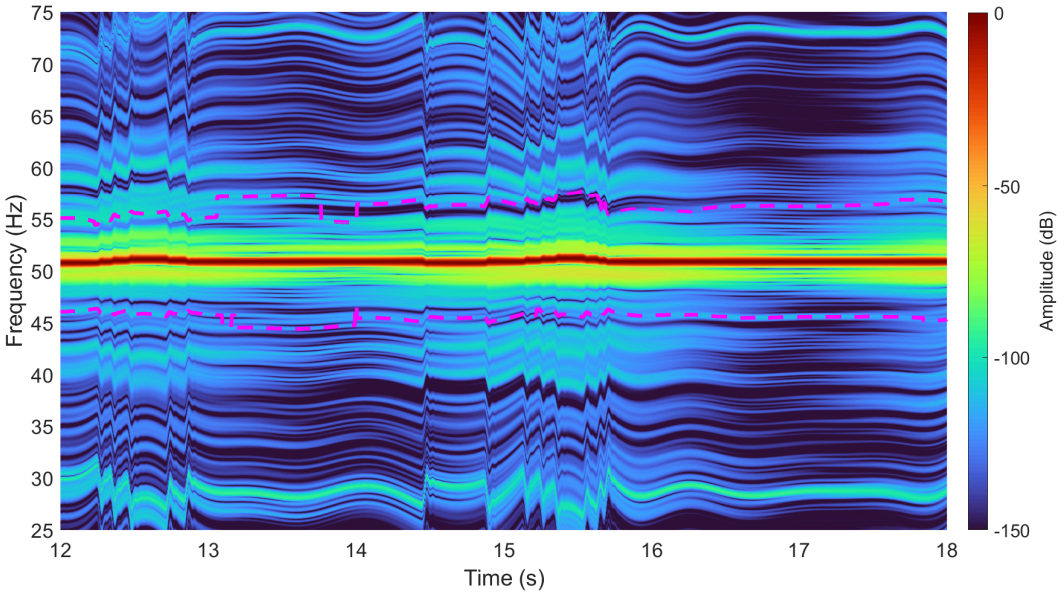

Figure 8.9: DT analysis of the current signal from a faulty motor under half load condition (3R). Dashed lines denote the theoretical trajectories of the third fault-related component.

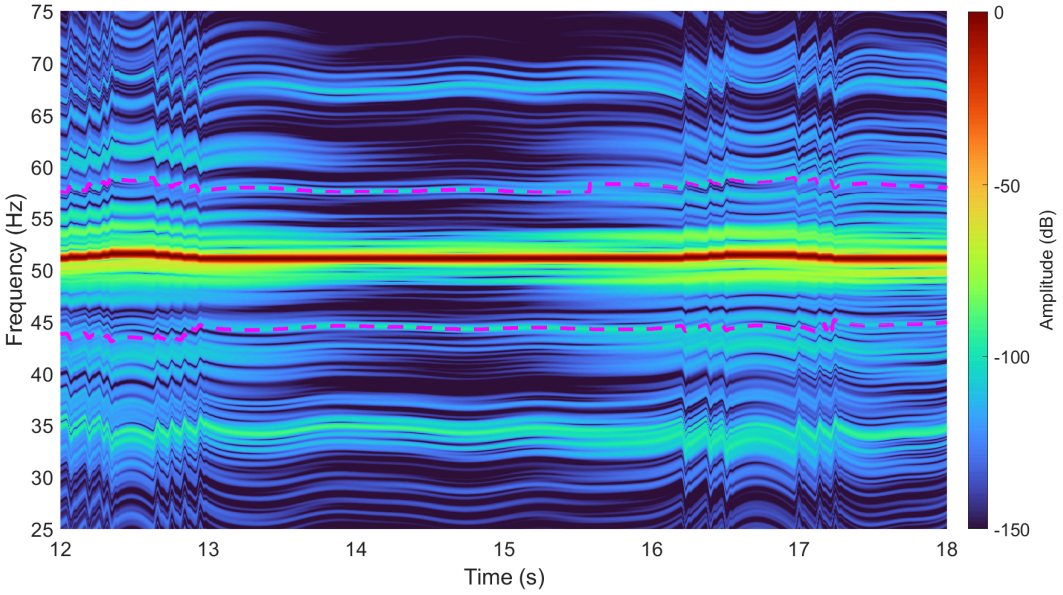

Figure 8.10: DT analysis of the current signal from a faulty motor under high load condition (4R). Dashed lines denote the theoretical trajectories of the third fault-related component.

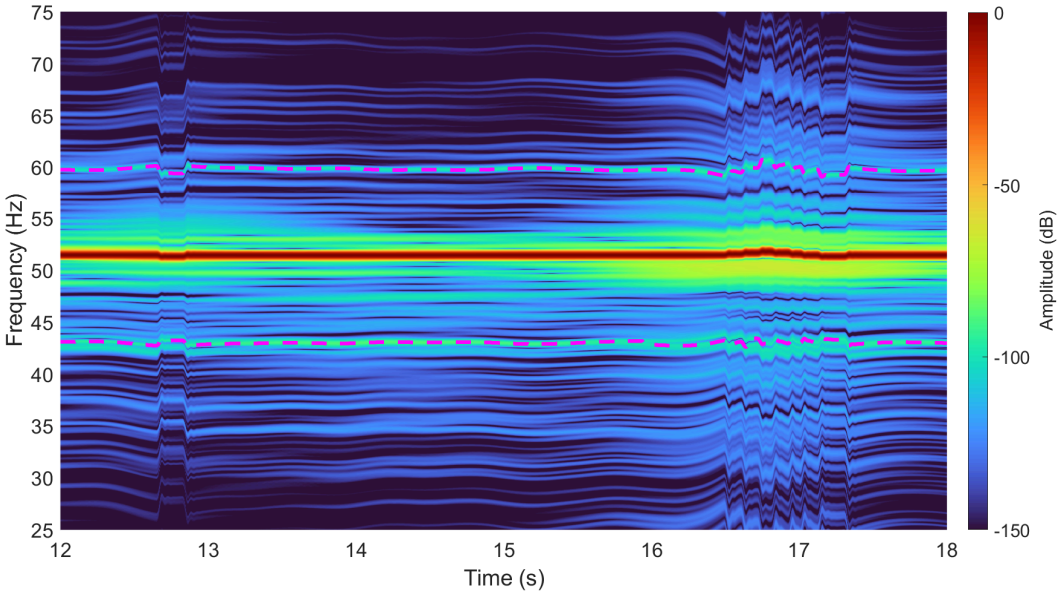

Figure 8.11: DT analysis of the current signal from a faulty motor under full load condition (5R). Dashed lines denote the theoretical trajectories of the third fault-related component.

As can be noticed from the previous figures, despite slight variations given by the closed-loop control, the trajectory of the fundamental harmonic at the output of the power converter is perfectly captured by the atoms. This allows to avoid uncertainties given by the harmonics around it, which are not distinguishable from the other analyzed techniques, due to the poor time-frequency resolution. Expectedly, for high load condition trials (3R, 4R and 5R load conditions), the third components of the BRB-related harmonics are perfectly visible in the Time-Frequency plane. Their trajectories follow the same path as the calculated theoretical ones, with a very precise frequency resolution.
The accuracy in the t-f plane given by the Dragon Atoms allows also to distinguish between different harmonics when their trajectories lie close to the main supply frequency given by the inverter. In this way, theoretical trajectories of the BRB harmonics with k=3 are distinguishable in the t-f plane of the Dragon Transform also with low load conditions (1R load, T=3.14 Nm and 2R load, T=5.20 Nm), despite instability in the analyzed signals (and also in the speed signal after the filtering stage) resulting in a very large number of small variations in the supply frequency from the inverter.
Finally, with the accurate tuning on the color map, which may be required also for the Dragon Transform technique to better highlight harmonics trajectories in dense regions of the time-frequency plane, harmonics related to the fault are also visible in the analysis made in no load conditions, although sidebands of the third harmonics are only 1.5 Hz apart from the inverter fundamental supply frequency.

In the next sections, a further analysis will be given on the identification of the broken rotor bar fault-related harmonics when the motor is closed-loop controlled by the power converter.

8.3 Control loops comparison

For this further analysis, the work has been focused not only on the signals from the faulty motor controlled with the Fast Closed Loop: signals acquired from both the closed-loop control implemented in the Danfoss power converter introduced in section 7.2 (Table 7.4) have been analyzed. A comparison between healthy and faulty analysis will be presented. Moreover, an overview of the main differences between open and closed-loop will be given. The analysis of the next sections only refers to motors operating at full load (5R), with a reference supply frequency equal to 50 Hz.

8.3.1 FFT and STFT observations

In the first part of this analysis, some observations will be reported on the detection of the fault through Fourier-based techniques in different control situations.
Fig. 8.12 shows the FFT analysis of the healthy and faulty motors operating in open-loop at the steady state.

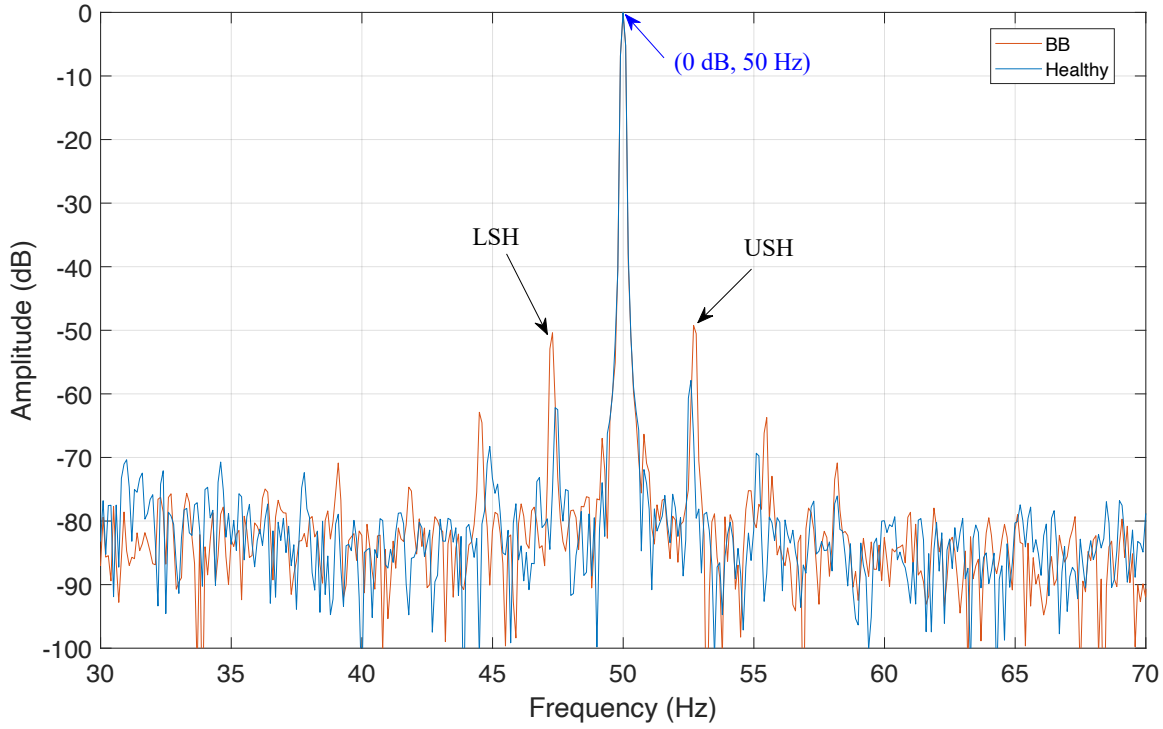

Figure 8.12: Spectra of motors at steady state for the open-loop control: comparison between spectra of healthy (blue) and faulty (orange) motor.

The mean value of the speed in the open loop test is 1465 rpm, while the load is set to 11.3 Nm. In this case, the difference in amplitude that occurs from healthy condition to faulty is clearly visible in LSH and USH (around 10 dB of increase). Moreover, these harmonics are visible, and no spectral leakage effect is present around the fundamental, meaning that the supply frequency is fixed. Finally, the noise level of the signal is low, around -80 dB.

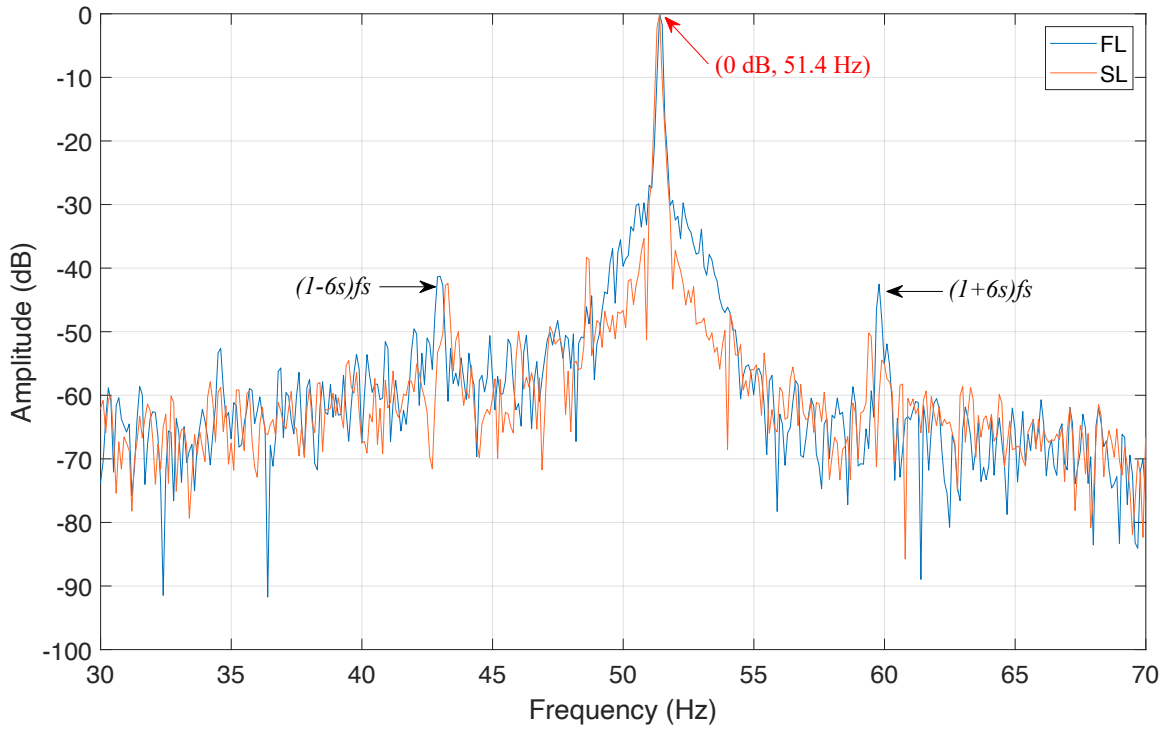

Figure 8.13: Spectra of the faulty motor at steady state for the two closed-loop controls: comparison between fast loop (blue) and slow loop (orange).

As displayed in Fig. 8.13, when the motor is controlled by the inverter through the speed closed-loop control, the noise level in the spectrum is higher, around -65 dB. However, also with the FFT, sidebands related to the fault with $k = 3$ are recognizable in the spectrum of a faulty motor. Furthermore, an effect similar to spectral leakage is present in a wide region close to the fundamental. This effect occurs when the supply frequency is not fixed in the analyzed time window of the signal. It is important to note that the fundamental component is not constant since the power modifies its frequency with respect to the load in order to achieve a constant motor speed. To overcome this effect, a different approach with respect to FFT is required. This can be done by adopting time-frequency techniques

such as the Short-Time Fourier Transform (STFT).

Finally, from Fig. 8.13 it is also possible to see how different closed-loop controls have different behaviors. The region with uncertainties close to the fundamental, in fact, is wider in the case of fast loop control than in the one of the slow control. This result is expected since the fast loop reacts also to sudden small changes in the reading of the speed while the slow loop keeps the fundamental frequency constant for a longer period before acting.

Figs. 8.14 and 8.15 show the STFT results for respectively healthy and faulty motor under open loop operation. For the faulty case, as already discussed in subsection 8.1.2, the theoretical trajectories of the fault are calculated by using the speed signal acquired from the encoder to compute the slip to put in equation 5.7. These trajectories are not detectable in the STFT time-frequency plane, not even for open loop operation, because of the low frequency resolution introduced by the STFT. This highlights the need to use techniques that allow to reach good frequency and time resolution at the same time, to be able to distinguish different trajectories of the harmonics also for motor operating in open-loop operation.

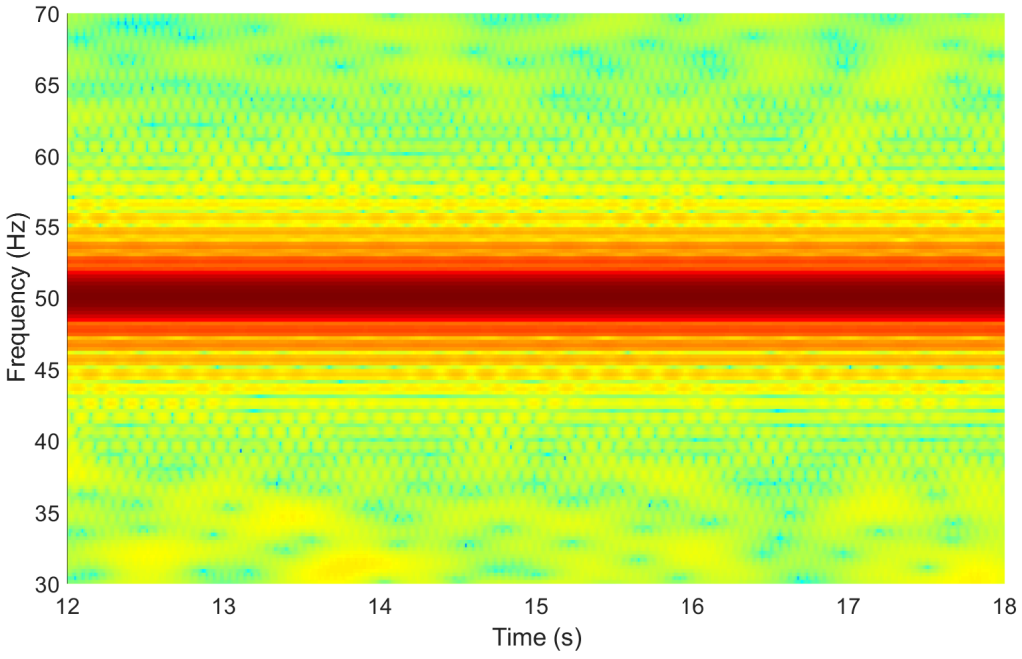

Figure 8.14: STFT of the healthy motor phase-current operating in open-loop at steady state.

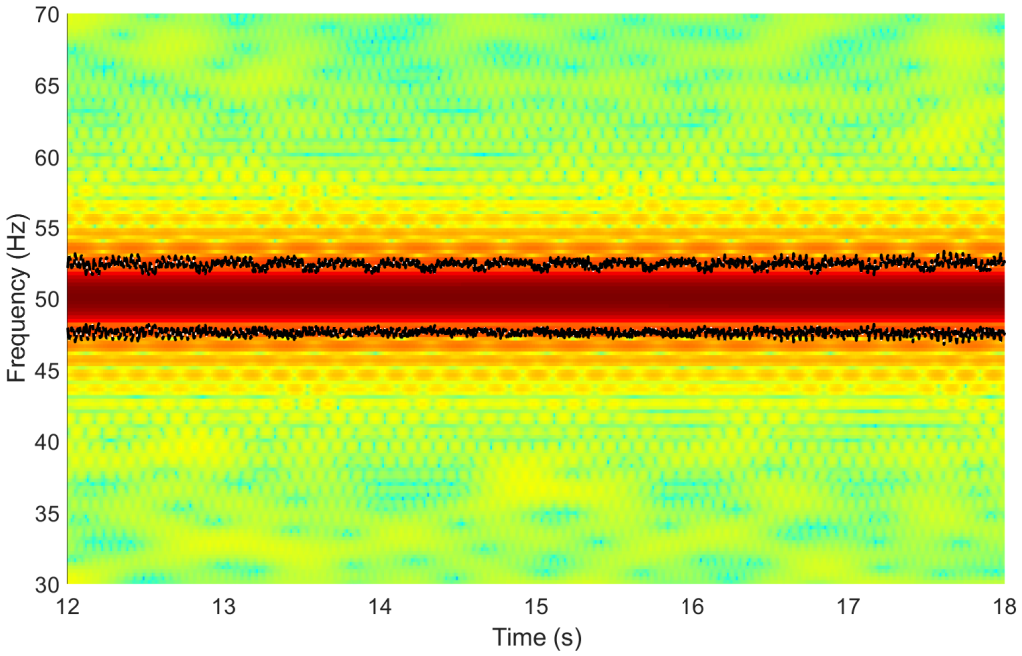

Figure 8.15: STFT of the faulty motor phase-current operating in open-loop at steady state. The theoretical fault trajectories are highlighted in black.

Moreover, sidebands with $k = 3$ are not present in the spectrum and spectrogram of the open-loop controlled faulty motor. These harmonics are generally lower in amplitude with respect to LSH and USH but, as discussed in the previous sections, allow to better recognize the fault in closed-loop inverter-fed operation being furthest from the fundamental supply frequency.

8.4 Time-frequency analysis

In this section, a complete analysis of the signals using more advanced time-frequency techniques will be given. Together with the already explained Dragon Transform analysis, the one with the Short-Time Min-Norm technique, whose theoretical explanation has been provided in section 6.4, will be used. STMN analysis provides good performance and, in general, requires more computational time than classic spectral estimators (such as Fourier transform-based) but less than non-linear or adaptive transformations (Wigner-Ville or DT). Unlike DT, STMN does not require information on the rate of change of frequency of the components within the signal to analyze. This makes STMN a useful high-resolution

technique for the time-frequency decomposition of time-varying stator-current signals. The STMN has been implemented in a script similar to the one used for the ST-MUSIC analysis. After the decimation stage, the STMN algorithm is computed through the following Matlab custom function:

```
>    L = stmn (Ir, w, h, nf, o, mm);
```

Where `L` is the output matrix of the amplitudes, `Ir` the decimated current signal, `w` is the number of points for each window, `h` is the number of non-overlapping points (`w - h` is the number of overlapping points), `nf` is the number of points in the frequency domain, `o` is the number of eigenvalues and `mm` the dimension of the data matrix. Once the resulting matrix of the function is obtained, a maximum and a minimum value of amplitude are set as saturation, and the amplitudes outside these boundaries are changed equal to those values. This last step is made to better visualize the trajectories of the components in the t-f plane and allows to change the "noise floor" of the results, by ignoring harmonics with extremely low amplitudes.

8.4.1 Open-loop analysis

Figs. 8.16 and 8.17 show respectively the DT analysis of the healthy and faulty motors operating at steady state under open-loop control. Despite they are recognizable, also in the healthy motor, in the faulty conditions the trajectories of the BRB-related harmonics for $k = 1$ have higher intensity and are clearly visible in the time-frequency plane. This is due to the good frequency resolution achieved by the Dragon Atoms, together with the optimal speed signal provided by the encoder for the open-loop control operation.
Fig. 8.18 and Fig. 8.19 report the analysis made with the STMN of the same signals in open loop operation for healthy and faulty motors, respectively. Like the DT, also the STMN technique allows for reaching good frequency resolution: this translates into the possibility of distinguishing the fault-related harmonics in faulty conditions. Even if the trajectories for the faulty case are less recognizable than the ones obtained with the DT for the same signal, the difference between the t-f planes of faulty and healthy condition are very marked. Due to the proper settings of the parameters, in the healthy spectrogram, these sidebands are not present because of their low amplitude.

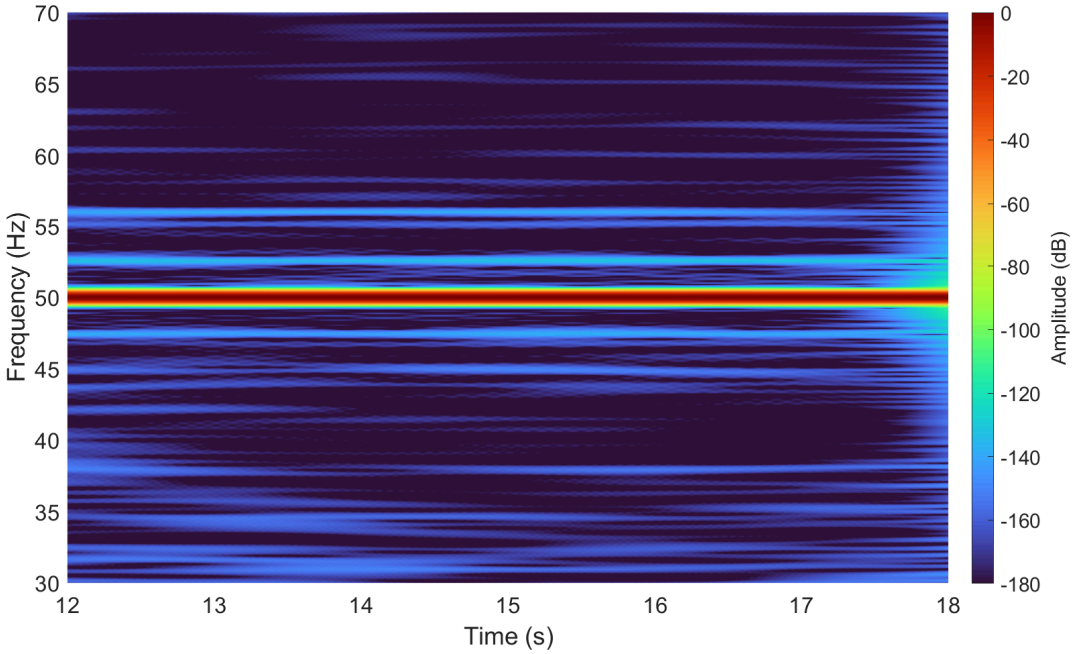

Figure 8.16: DT results of the healthy motor phase-currents operating in open loop at steady state.

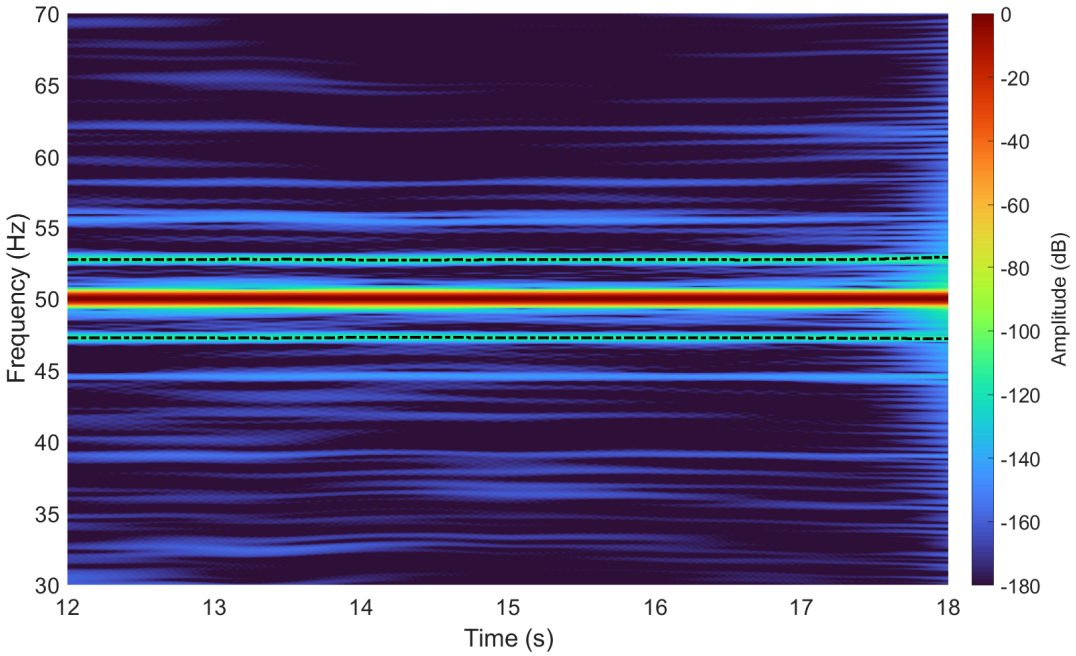

Figure 8.17: DT results of the faulty motor phase-currents operating in open loop at steady state. The theoretical fault trajectories are highlighted with dashed blue lines.

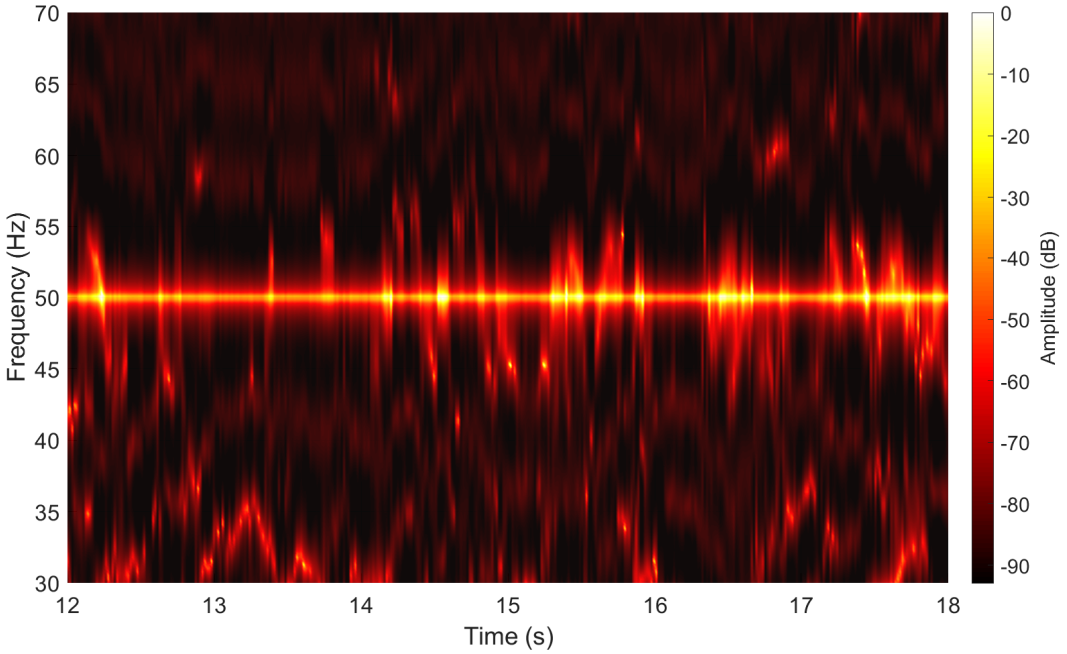

Figure 8.18: STMN results of the healthy motor phase-currents operating in open loop at steady state.

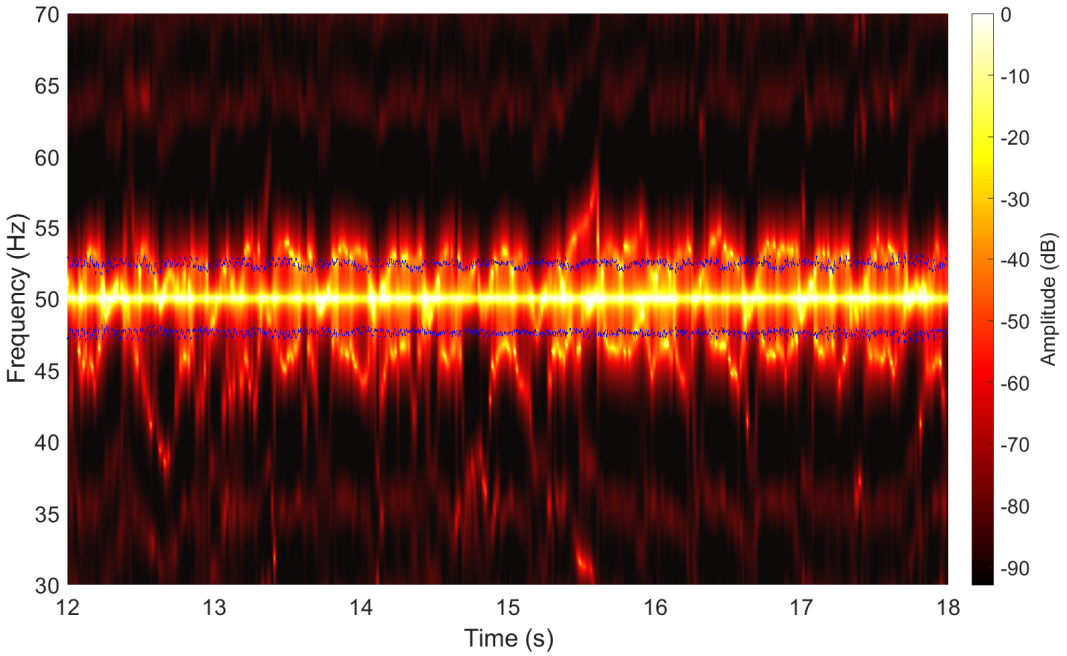

Figure 8.19: STMN results of the faulty motor phase-currents operating in open loop at steady state. The theoretical fault trajectories are highlighted with dashed blue lines.

8.4.2 Closed-loop analysis

Fig. 8.21 and Fig. 8.22 report, respectively, the analysis with the Dragon Transform technique for the healthy and faulty motor operating in closed-loop set to have a fast response. For this operating condition, even with the healthy motor, the spectrum of the current signal has a high level of noise floor along the analyzed frequency range. This is clearly visible in Fig. 8.21 where different harmonics are present, due to noise around the fundamental one.

Despite the noise content in the signal, in Fig. 8.22 two trajectories are clearly visible around 43 Hz and 60 Hz, but these are not detectable in the healthy time-frequency decomposition. These trajectories perfectly overlap the dashed red lines, representing the theoretical third trajectories related to the fault that, as previously explained, are computed by inserting the value of $k = 3$ in equation 5.7.

The two harmonics related to the broken bar fault still remain visible between 16 s and 17 s, where the trajectory of the fundamental has a very fast change in the frequency due to a perturbation in the speed, which is displayed in Fig. 8.20. This is possible thanks to the atoms that, by using the instantaneous slip computed from the speed measurement, allow to perfectly follow the shape trajectory of the harmonics related to the fault for every time step displayed in the plane.

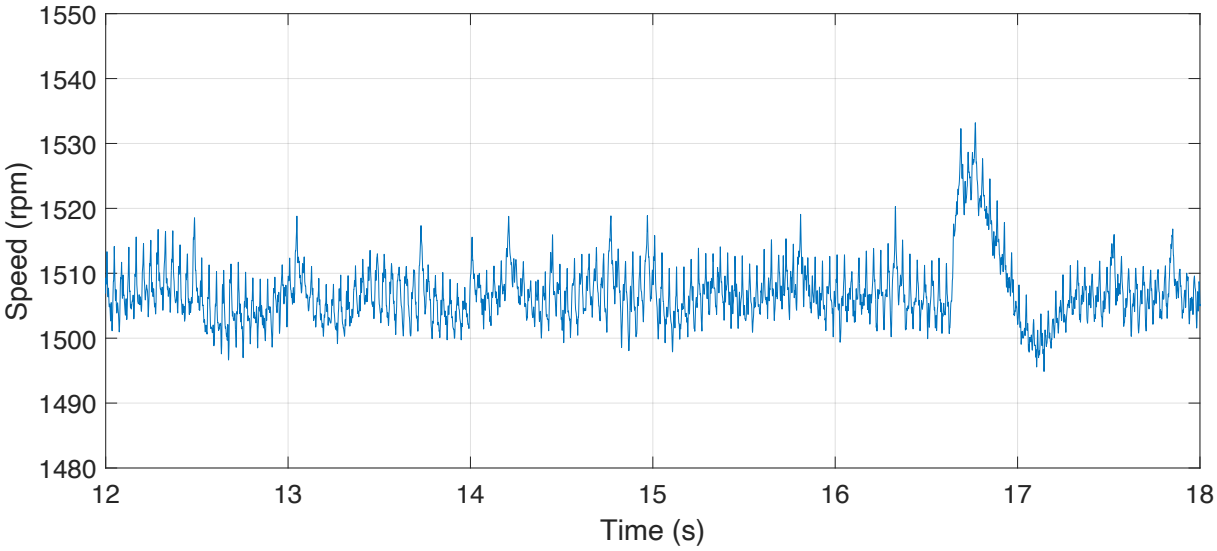

Figure 8.20: Speed signal of the faulty motor operating in fast closed-loop at steady state.

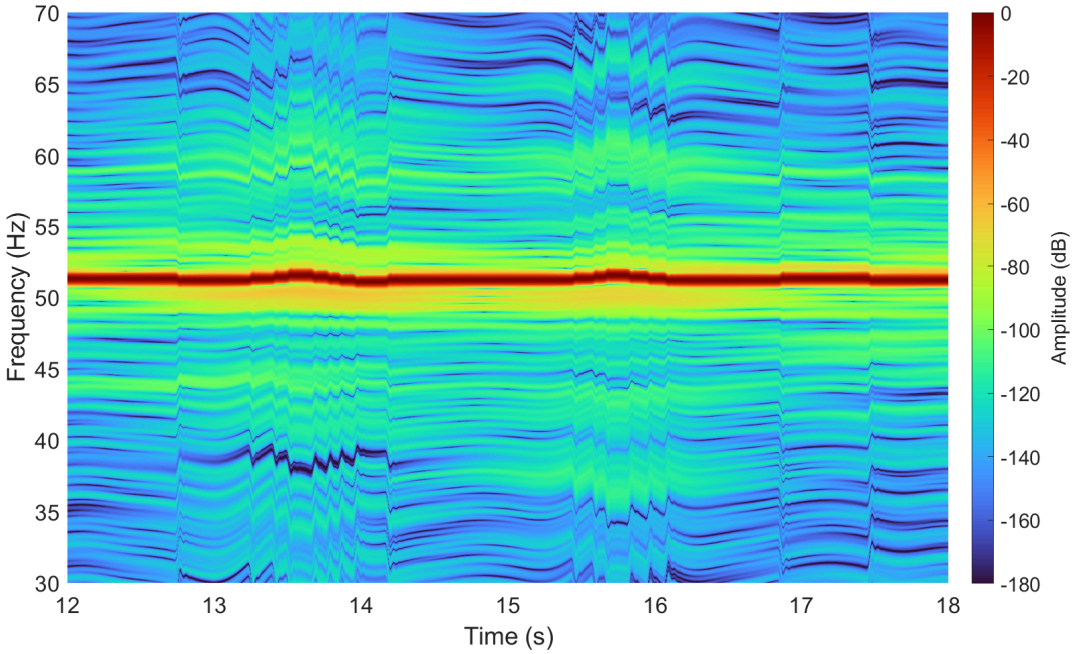

Figure 8.21: DT analysis results of the healthy motor phase-current operating in fast closed-loop at steady state.

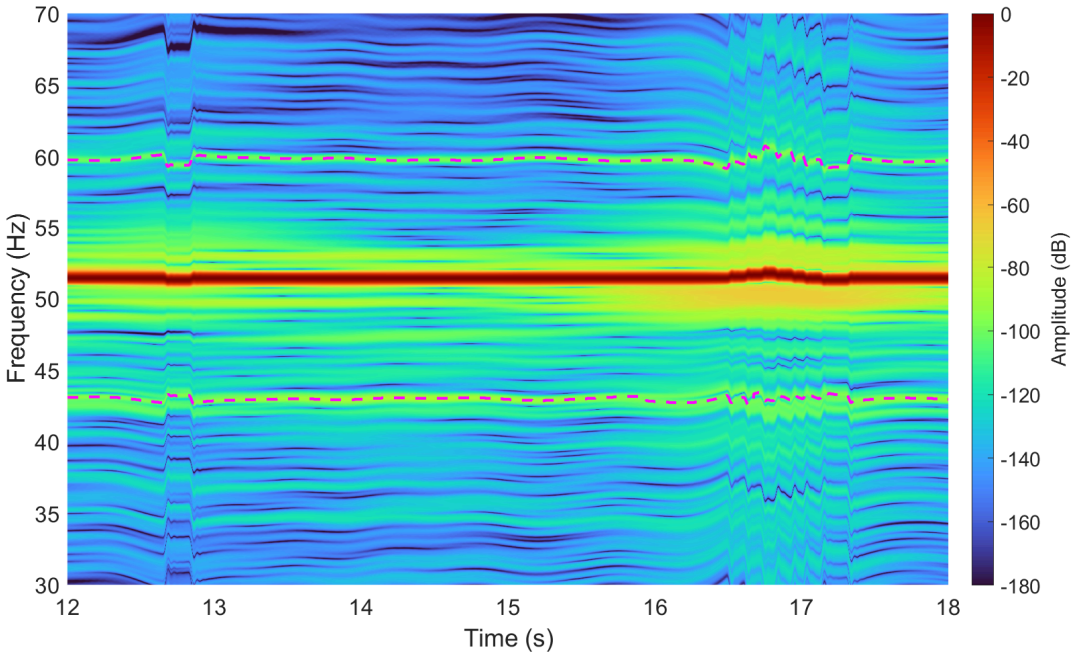

Figure 8.22: DT analysis results of the faulty motor phase-current operating in fast closed-loop at steady state. Theoretical fault trajectories are highlighted with dashed lines.

Figs. 8.23 and 8.24 show the results of the STMN decomposition for the same signals from fast loop operation analyzed with the DT technique. For the phase-current of the healthy motor, two sidebands are still present in the spectrogram of the analysis at $(1 \pm 6s)f_s$ Hz. Since these harmonics are a consequence of inherent asymmetries in the motor construction, the STMN algorithm is capable of distinguishing between noise and these harmonics close to the fundamental component. On the other hand, these sidebands are not so clear in the DT decomposition from the same signal, because in this region other harmonics related to noise are present.

Despite that, comparing it with the time-frequency decomposition of the stator current from the faulty motor, the difference in magnitude is still recognizable. In fact, for the faulty motor, the energy of the sidebands is higher, resulting in a better definition in the t-f decomposition. Moreover, in the region between the fundamental and the fault-related harmonics, there is less uncertainty and noise in the faulty motor current signal with respect to the healthy case.

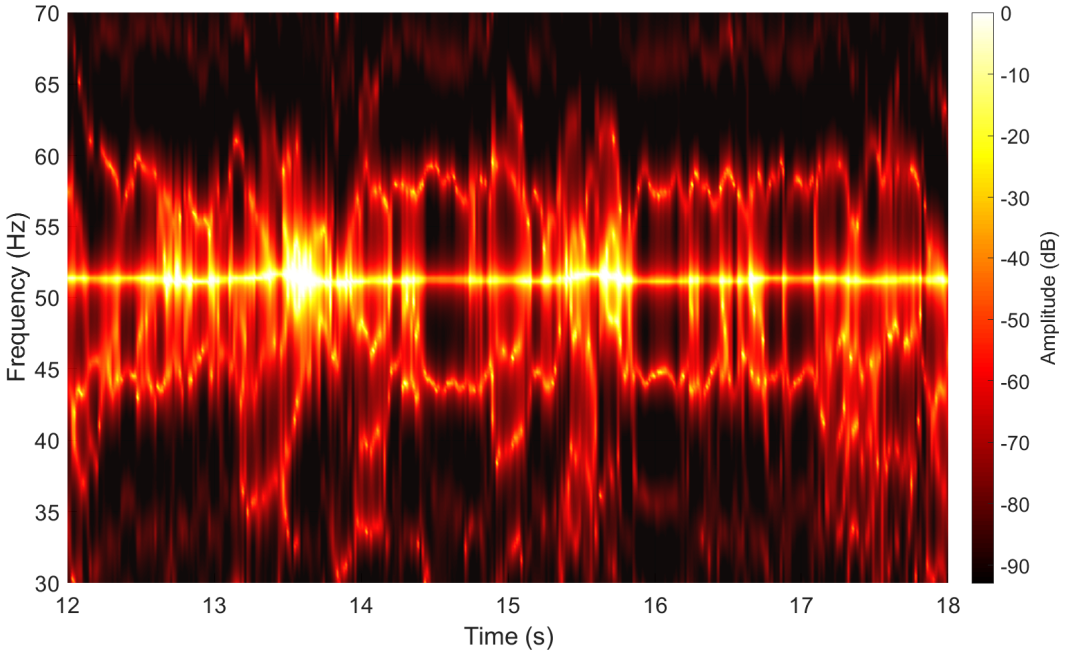

Figure 8.23: STMN analysis results of the healthy motor phase-current operating in fast closed-loop at steady state.

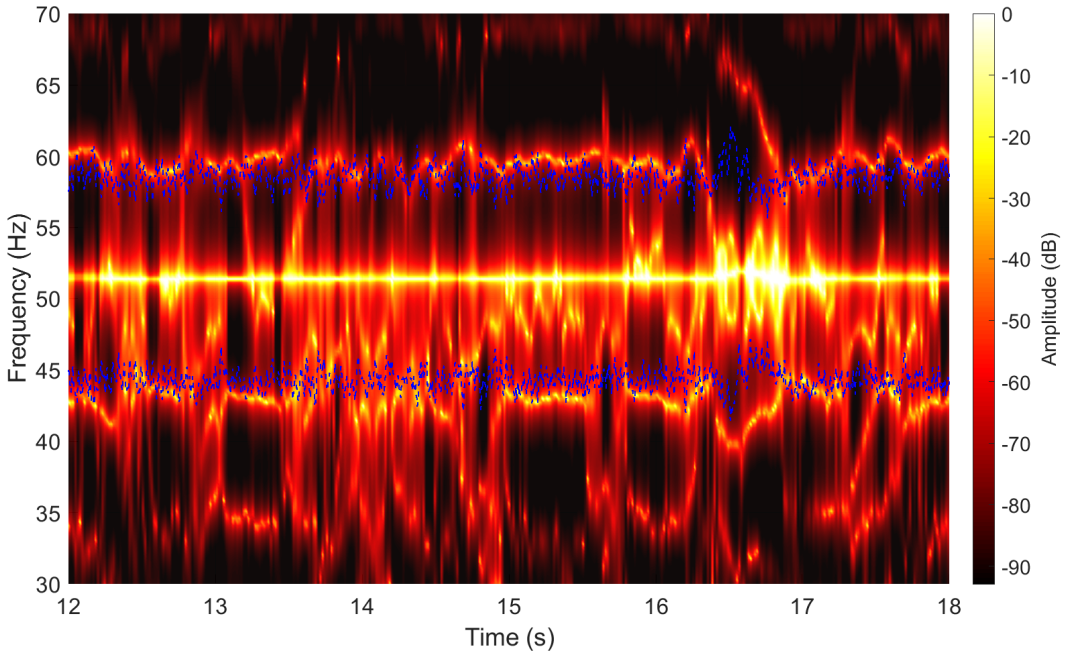

Figure 8.24: STMN analysis results of the faulty motor phase-current operating in fast closed-loop at steady state. Theoretical fault trajectories are highlighted with blue lines.

Fig. 8.25 and Fig. 8.26 show respectively the DT and STMN analysis of the faulty motor operating under closed-loop control (slow loop), which is set to have more stability in the fundamental frequency behavior. As can be noticed, despite the higher stability of the stator-current signal compared to the fast loop analysis (which can be verified in a lower number of perturbations at the fundamental frequency component) the noise level remains high along the time-frequency distribution. Also, in this situation, the third component of the fault-related harmonics is clearly distinguishable both with the DT and the STMN techniques, in case of the faulty motor current signal. In this faulty condition, harmonics in $f_s \pm 6sf_s$ have an increase in amplitude and so trajectories in the time-frequency plane are more precise. Finally, between the fundamental f_s and the fault component $f_s - 6sf_s$, it is possible to notice in the STMN decomposition (Fig. 8.26) a component that appears with a lower amplitude. This component is also present in the DT analysis (Fig. 8.25) and could be related to the Lower Side Harmonic, LSH, at $f_s - 2sf_s$.

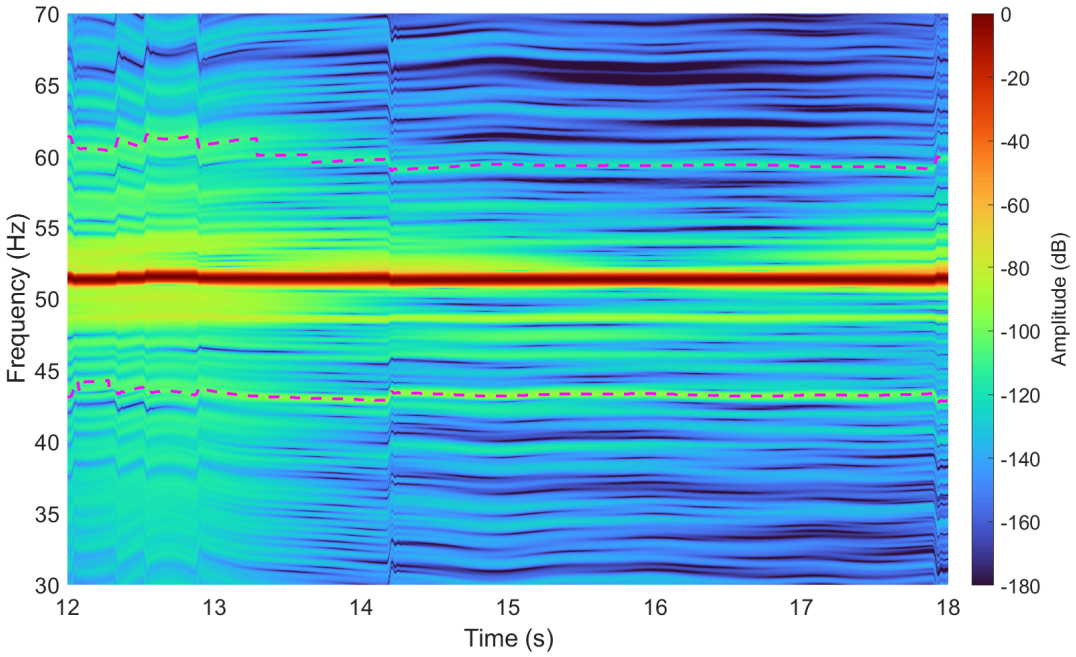

Figure 8.25: DT analysis results of the faulty motor phase-current operating in slow closed-loop at steady state. Theoretical fault trajectories are highlighted with dashed lines.

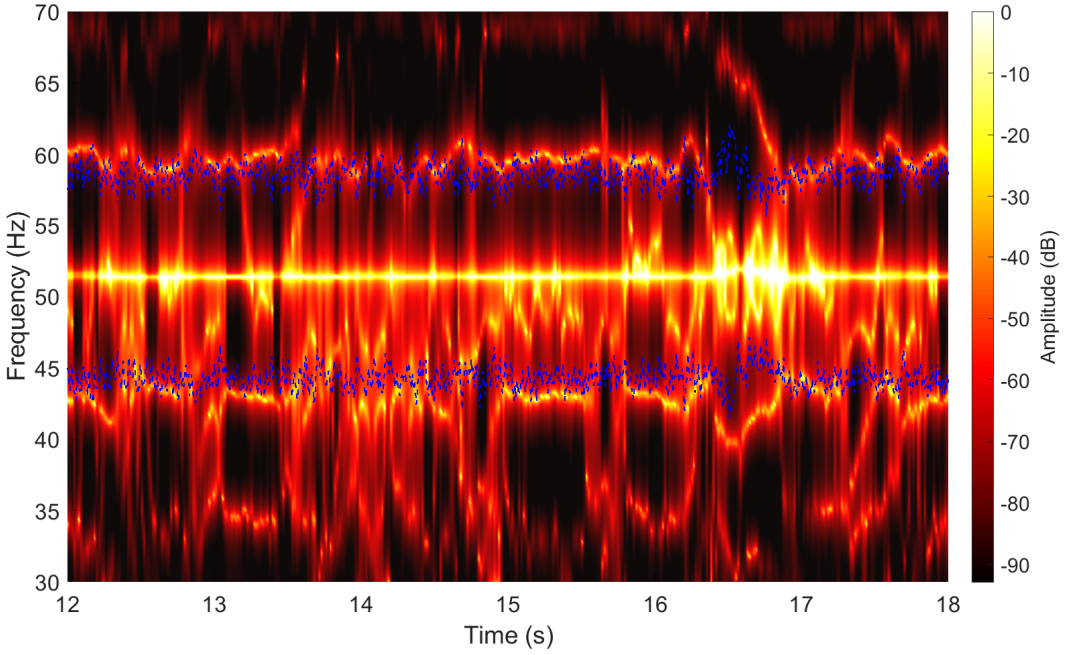

Figure 8.26: STMN analysis results of the faulty motor phase-current operating in slow closed-loop at steady state. Theoretical fault trajectories are highlighted with blue lines.

Finally, in Fig. 8.27 the speed signal from the faulty motor operating under slow-loop operation is depicted. Despite a spike between 12 s and 13 s, probably due to some electromagnetic interference during the acquisition, the behavior in time has a lower number of oscillations if compared to the one of the same motor under FL operation in Fig 8.20.

The smoother behavior of this control loop can be appreciated by comparing Figs. 8.25 and 8.26 with the speed signal of the same acquisition: despite the spike at 12.5 s, the fundamental harmonic in the t-f planes does not change frequency.

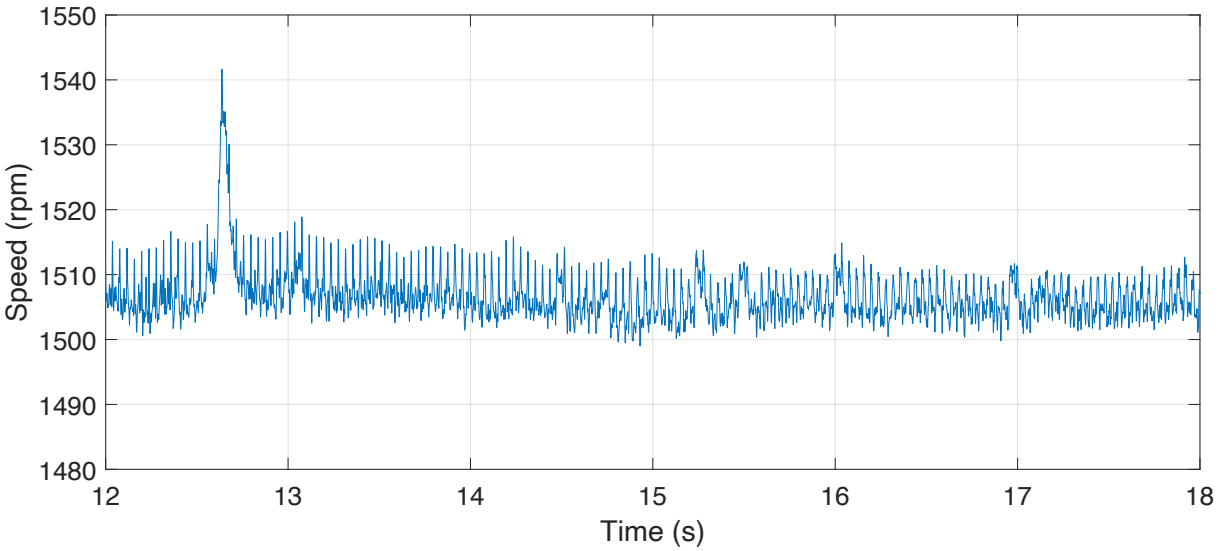

Figure 8.27: Speed signal of the faulty motor operating in slow closed-loop at steady state.

8.5 High frequency range analysis

A last analysis has been carried out in the high-frequency band of the stator-current, by studying the general equation for broken rotor bar harmonics (equation 5.6 introduced in section 5.5):

$$f_{bb} = \left[\frac{z}{p}(1-s) \pm s\right] f_s \tag{5.6}$$

Where $\frac{z}{p} = K$ assumes integer odd values $\left(\frac{z}{p} = K = 1, 3, 5, \dots\right)$.

Considering $K = 11$, two resulting harmonics can be identified at f_s $(11 - 12s)$ and

f_s $(11 - 10s)$. These harmonics are the fault sidebands around the 11th harmonic of the fundamental one. This analysis has been carried out using the STMN, because of the low computational burden of this technique with respect to the DT, which is not suitable for high frequency-band analysis due to this reason.

Fig. 8.28 and Fig. 8.29 report the results of the high-frequency band analysis for the fast loop control of respectively the healthy and the faulty motors. In this analysis, the same time window of the stator-current signals has been chosen as for the low-frequency range. For the healthy case (Fig. 8.28), only one trajectory is clearly visible in the spectrogram between 560 and 570 Hz, corresponding to the 11th harmonic of the fundamental frequency. In the t-f decomposition of the faulty motor (Fig. 8.29) the trajectory of a harmonic below the one that represents the 11th of the fundamental is clearly detectable. This lies in proximity to the theoretical trajectories of the broken rotor bar harmonics in $11f_s - 10sf_s$ and $11f_s - 12sf_s$.

However, due to the error in the speed signal introduced by both the noise and the filtering stage, it is difficult to identify which one of the two components is present in the t-f plane.

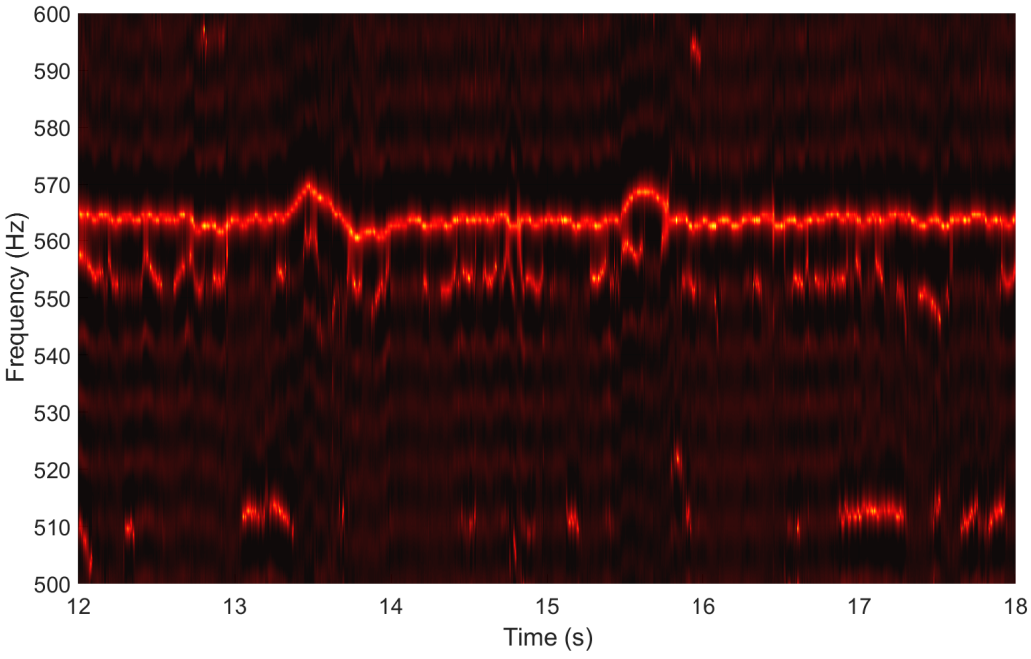

Figure 8.28: High-frequency range STMN results of the healthy motor phase-current operating in fast closed-loop at steady state.

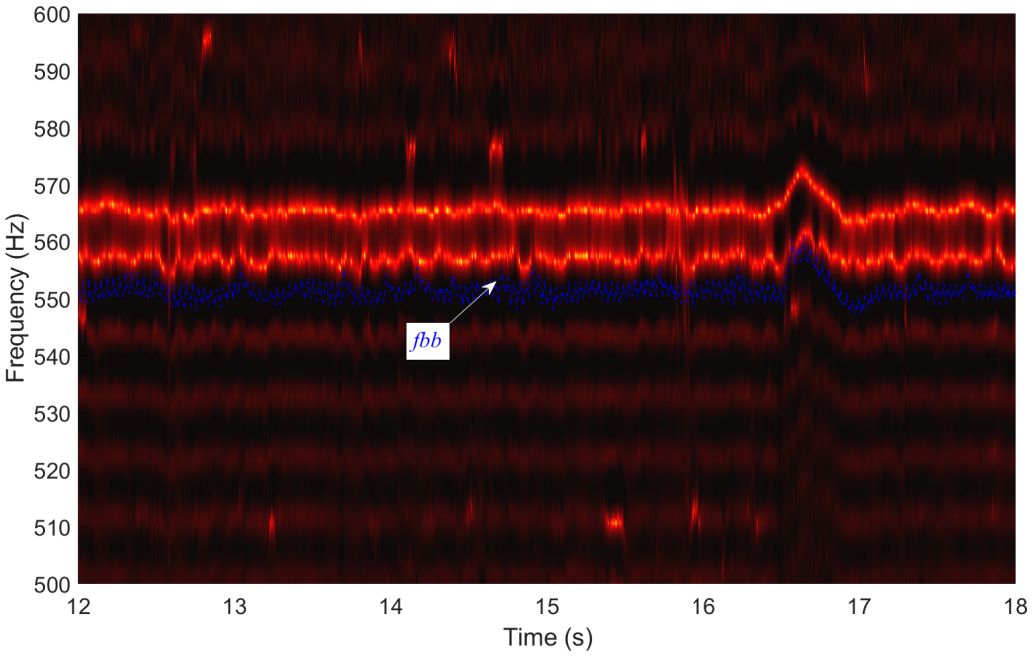

Figure 8.29: High-frequency range STMN results of the faulty motor phase-current operating in fast closed-loop at steady state. The theoretical fault trajectories are depicted in blue.

Finally, Fig. 8.30 (healthy) and Fig. 8.31 (faulty) show the results for the same analysis made on current signals from slow closed-loop operation. Also, in this supply situation, the 11th harmonic is clearly visible in the t-f decompositions, both for the healthy motor and the faulty one, whereas the harmonic related to the fault appears with high energy just in the stator-current decomposition of the faulty motor.

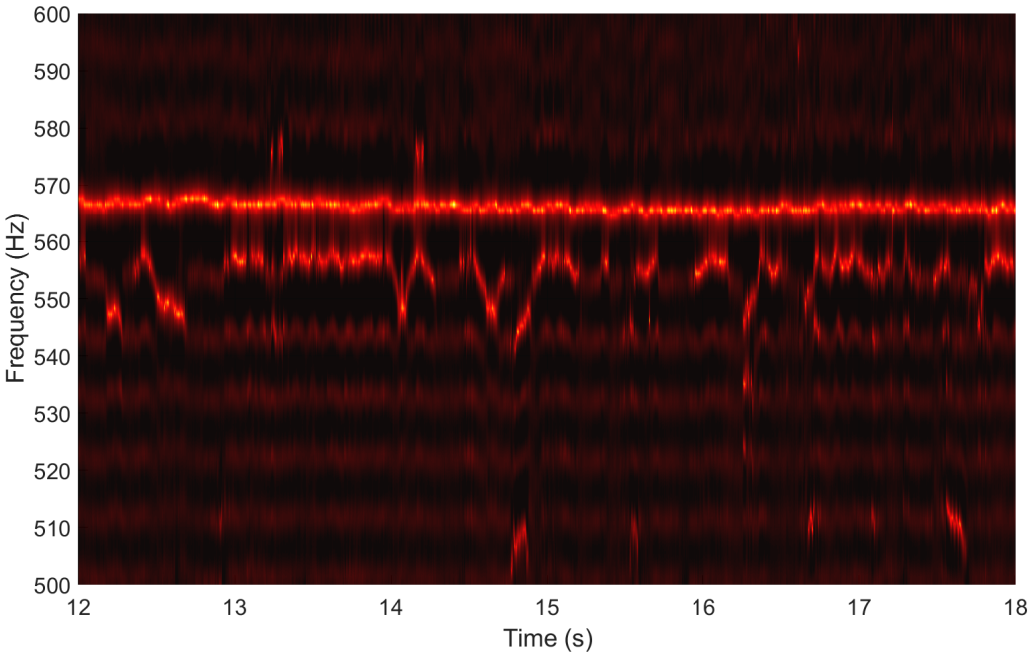

Figure 8.30: High-frequency range STMN results of the healthy motor phase-current operating in slow closed-loop at steady state.

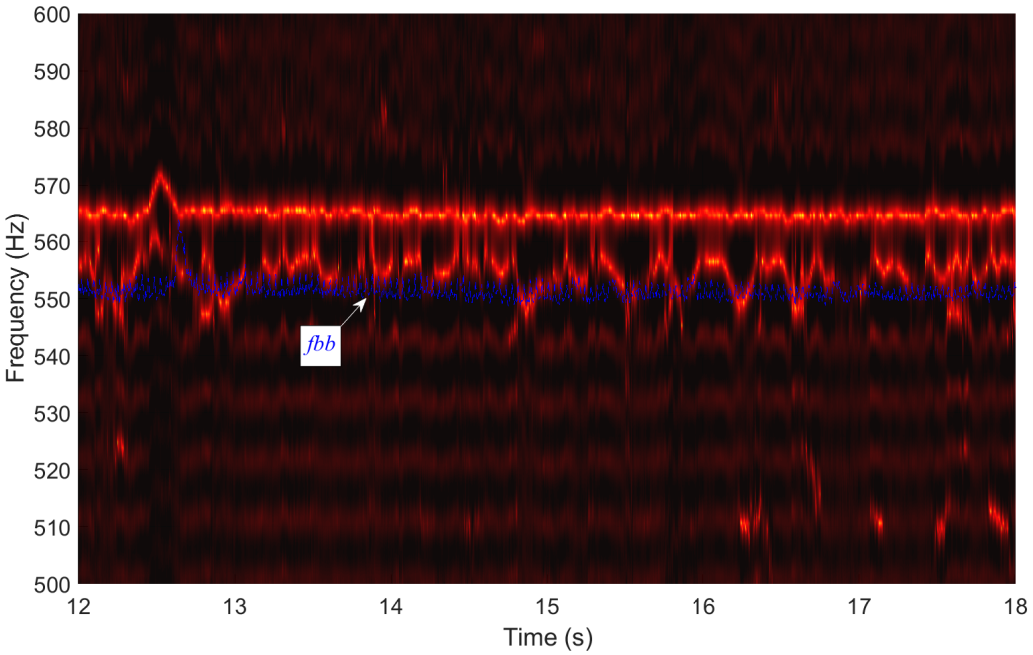

Figure 8.31: High-frequency range STMN results of the faulty motor phase-current operating in slow closed-loop at steady state. The theoretical fault trajectories are depicted in blue.

8.6 Conclusions

An analysis to detect broken rotor bar fault-related harmonics in closed-loop operating induction motors has been presented in this chapter. Due to sudden changes in the supply frequency of the inverter, classical analyses, such as the FFT, are not useful for this application, even if the start-up transient regime is not considered. As for transient regimes, a current signal from speed closed loop operation needs a time-frequency decomposition to be analyzed. Nevertheless, a technique such as the Short-Time Fourier transform, which requires a compromise between time and frequency resolution, is not the best option to analyze signals from this supply condition.

Due to the very high precision of the Dragon Transform and the high resolution of the Short-Time Min-Norm, it is possible to overcome above mentioned problems and detect the trajectories of the fault-related harmonics in the t-f plane. Moreover, for closed loop operation, harmonics located in $(1 \pm 6s)f_s$ appear clearly visible in the t-f decompositions of the stator-current, also for low load conditions. In fact, these harmonics have higher energy density if compared to the signals from the open loop operation of the motor, in which are almost undetectable.

Due to the low computational burden of the STMN, for closed-loop operation, this fault can be recognized by analyzing a wider range of frequencies in the spectrum, using the general equation of the broken rotor bars. Sidebands around the 11th harmonic of the fundamental are clearly visible in the t-f plane for the current signals acquired from faulty motors operating in closed-loop conditions. The result is a method that allows the detection of the broken rotor bar fault when the motor is operating in speed closed-loop control.

This result represents a novelty with respect to the literature since it presents the following advantages: it is based on the analysis of a single stator current (normally measured in all the electrical drives, without adding any other sensor) and it is valid for different types of closed-loop control schemes. The aim of future research will involve the application of this new method to other control strategies.

Chapter 9

Conclusions

In this thesis, the main scientific works carried out by the author during his doctoral course have been presented. Since the research activities varied from two different topics, which are the design and the diagnostics of inverter-fed electrical machines, the conclusions will be divided into two sections. More exhaustive conclusions for each of the works presented have been provided at the end of chapters 3, 4, 8.

9.1 Design of IPM machines

The design of electrical machines is a critical area of research and development that underpins numerous technological advancements in various industries, from automotive to renewable energy systems. Interior Permanent Magnet Synchronous Machines have emerged as a prominent solution in this field due to their high efficiency, superior performance, and wide speed range capabilities. However, the optimal design of IPMSMs involves intricate considerations regarding material selection (often dependent on the discontinuous market of rare-earth materials), geometric configuration, and manufacturing techniques.

In this context, understanding and improving the design procedures for IPMSMs is crucial. This research aimed to propose refined design procedures and evaluate their effectiveness through comprehensive case studies.

After an extensive review of the state of the art presented in chapter 1, two comprehensive design procedures detailed in chapters 2, 3 and 4 have been proposed. These chapters

collectively underscore the importance of various design considerations and innovative techniques in the development of IPMSMs.

The review highlighted the crucial role of selecting appropriate magnet materials and topologies for achieving high performance across a wide speed range. It was emphasized that the adoption of an optimal ratio between the number of slots and rotor poles is a fundamental step in the design process of IPMSMs. This ratio significantly influences the electromagnetic performance and efficiency of the machine.

Furthermore, the research demonstrated the benefits of implementing step-skewing, which facilitates straightforward manufacturing processes while yielding substantial performance improvements. Specifically, step-skewing was shown to nearly eliminate torque ripple, a common issue in traditionally designed PM machines, thereby enhancing the overall smoothness and efficiency of operation.

The comparative analysis of two distinct case studies revealed the profound impact of the number of poles and rotor topology on the machine's performance and suitability for specific applications. These choices are not solely determined by material and manufacturing costs but are also heavily influenced by the intended application and specific performance requirements. This underscores the need for a custom approach in each design process to meet diverse operational demands.

Additionally, the importance of thermal studies and the consideration of non-idealities in modeling and simulations was underscored. Manufactured machine performance often diverges from simulated results due to thermal effects and various non-ideal factors, such as undesired air gaps and non-uniform electric and magnetic properties of the materials. Incorporating these aspects into the design and simulation phases is crucial for achieving accurate performance predictions and ensuring the reliability and efficiency of the final product.

In conclusion, the proposed design procedures and techniques offer a robust framework for developing high-performance IPMSMs. By meticulously considering material selection, slot-to-pole ratios, step-skewing techniques, and constraints linked to non-idealities, designers can significantly enhance machine performance and reliability, paving the way for advanced applications in various industries.

9.2 Diagnostics of inverter-fed IMs

The detection and diagnosis of rotor faults in induction motors are fundamental for ensuring the reliability of industrial machinery. While much progress has been made in the analysis of motors operating directly from mains or under open-loop control, the complexities introduced by closed-loop control systems, increasingly widespread in industrial applications and transport, present unique challenges that necessitate advanced diagnostic approaches. In this thesis, following a comprehensive literature review reported in chapter 5, a novel approach has been proposed for identifying rotor faults in induction motors under this challenging control condition.

This approach consists of the measurement of a single-phase stator current, using advanced time-frequency signal analysis techniques to overcome the continuous fluctuation of the harmonics in the spectrum, which appear even when the start-up transient is concluded.

The research detailed in chapter 6 examines various signal analysis techniques to address these challenges. Classical Fourier-based methods were found to have limitations in terms of time or frequency resolution, even after the start-up transient stage has ended. These limitations interfere with the accurate identification of faults when the motor is operating under these conditions.

To address these limitations, advanced time-frequency analysis techniques such as the Dragon Transform and the Short-Time Min-Norm have been employed. These techniques, which implement completely different approaches to estimate the spectrum of a signal, are essential for accurately identifying fault-related harmonics, as the trajectories of these harmonics exhibit slight frequency variations over time. The advanced time-frequency methods provide superior resolution and accuracy, enabling the detection of subtle changes in harmonic frequencies associated with rotor faults.

However, some limitations in the application of such techniques have been found. The behavior of the DT, for example, is strictly related to the quality of the speed signal, which is strongly affected by the type of encoder when the motor is operating under speed closed-loop. Thus, an efficient filtering of this signal is required to properly define the Dragon Atoms along the $t - f$ plane. Moreover, the application of this technique implies a high

computational burden and, therefore, adequate hardware to carry out the calculations. On the other hand, being a parametric technique, the STMN requires a meticulous analysis by the user, to properly show the right trajectories of the fault-related component.
The experimental tests conducted in the laboratory revealed critical insights into the behavior of fault-related harmonics in closed-loop controlled motors. Notably, some harmonics associated with rotor faults appeared at different positions compared to open-loop operation. For instance, the third component of the broken bar-related sidebands ($f_s \pm 6sf_s$), which typically has lower amplitudes in open-loop controlled motors, emerged as a significant identifier in closed-loop operation.
Furthermore, since the analysis around the fundamental supply frequency can lead to ambiguous results, the analysis has been extended to the high-frequency range, finding that valuable diagnostic information about the machine's condition can be extracted around several harmonics related to the fundamental. Thus, high-frequency harmonics provided additional insights into the presence of a rotor fault, complementing the information obtained from traditional low-frequency analysis.
In conclusion, the proposed diagnostic approach lays the foundation for a robust framework for identifying rotor faults in induction motors operating under closed-loop control.

9.3 Future work

The work implemented in this thesis lays a solid foundation for a variety of future analyses and advancements in the fields of electrical machine design and fault diagnostics.
In the context of the design of IPM machines, this thesis has highlighted several areas for further research. Improvements can be made by developing more precise 3D FE models. These advanced models can provide a deeper understanding of the step-skewing technique analyzed in this thesis, allowing for optimization to eliminate harmonics in the output torque. Enhanced 3D modeling will also help in accurately predicting the electromagnetic behavior of the machine.
To better characterize the machine's behavior, future research should incorporate additional non-idealities such as the real voltage supply waveform from a power converter. This approach will provide a more realistic simulation of machine performance under ac-

tual operating conditions. The results of these simulations can then be validated in the laboratory manufacturing a machine prototype, ensuring that the theoretical advancements translate effectively into practical improvements.

Regarding the diagnostics of IMs operating under closed-loop control, this thesis has outlined a new research direction. While significant progress has been made in fault detection under steady-state conditions, the identification of fault-related harmonics during the start-up transient remains challenging due to the high level of noise introduced by the control loop. Future research should aim to develop advanced signal processing techniques that can effectively isolate and identify these harmonics during the transient stage.
Additionally, future studies should investigate the impact of various control loops, which may be correlated with the introduction of harmonics in the current spectrum of a machine, power converters, and encoders on fault diagnostics. By testing different configurations and varying the switching frequency of the power electronics, a more generalized diagnostic approach that is robust across different systems and conditions can be proposed.
In particular, regarding the encoder and the speed signal, an optimal filtering technique should be investigated in the future, to improve the results obtained from the application of the Dragon Transform.
Moreover, the detection and analysis of different types of harmonics, such as the RSH, present additional challenges under closed-loop operation [200]. Identifying these harmonics is crucial for comprehensive fault diagnostics.
Finally, fault indicators may be present in the spectra of other signals available to the power converter, such as the voltage signals. By applying the signal analysis techniques studied in the present thesis, different approaches can be proposed to overcome the challenging problem of detecting faults when the motor is operating under speed closed-loop control.

Bibliography

[1] A. H. Hoffmann, "Brushless synchronous motors for large industrial drives," *IEEE Transactions on Industry and General Applications*, vol. IGA-5, no. 2, pp. 158–162, 1969. DOI: 10.1109/TIGA.1969.4181006.

[2] S. P. Bordeau, "C. Truman Hibbard and the Invention of Automatic Control for Synchronous Motors," *IEEE Transactions on Education*, vol. 23, no. 3, pp. 163–169, 1980. DOI: 10.1109/TE.1980.4321402.

[3] K. T. Chau, C. C. Chan, and C. Liu, "Overview of permanent-magnet brushless drives for electric and hybrid electric vehicles," *IEEE Transactions on Industrial Electronics*, vol. 55, no. 6, pp. 2246–2257, 2008. DOI: 10.1109/TIE.2008.918403.

[4] R. H. Staunton, T. A. Burress, and L. D. Marlino, "Evaluation of 2005 Honda Accord hybrid electric drive system," U.S. Department of Energy Office of Scientific and Technical Information, Tech. Rep., 2006. DOI: 10.2172/891260.

[5] T. A. Burress *et al.*, "Evaluation of the 2008 Lexus LS 600H hybrid synergy drive system," U.S. Department of Energy Office of Scientific and Technical Information, Tech. Rep., 2009. DOI: 10.2172/947393.

[6] A. M. El-Refaie, "Motors/generators for traction/propulsion applications: A review," in *2011 IEEE International Electric Machines & Drives Conference (IEMDC)*, 2011, pp. 490–497. DOI: 10.1109/IEMDC.2011.5994647.

[7] T. A. Burress *et al.*, "Evaluation of the 2007 Toyota Camry hybrid synergy drive system," U.S. Department of Energy Office of Scientific and Technical Information, Tech. Rep., 2008. DOI: 10.2172/928684.

[8] L. Chong, "Design of an interior permanent magnet machine with concentrated windings for field weakening applications," Ph.D. dissertation, University of New South Wales, 2011.

[9] S. Morimoto, K. Kawamoto, and Y. Takeda, "Position and speed sensorless control for IPMSM based on estimation of position error," *Electrical Engineering in Japan*, vol. 144, no. 2, pp. 43–52, 2003. DOI: https://doi.org/10.1002/eej.10180. eprint: https://onlinelibrary.wiley.com/doi/pdf/10.1002/eej.10180. [Online]. Available: https://onlinelibrary.wiley.com/doi/abs/10.1002/eej.10180.

[10] A. M. El-Refaie, "High speed operation of permanent magnet machines," Ph.D. dissertation, University of Wisconsin-Madsion, 2005.

[11] D. Hanselman, *Brushless Permanent Magnet Motor Design*. Magna Physics Publishing, 2006.

[12] T. Jahns and R. Van Nocker, "High-performance EHA controls using an interior permanent magnet motor," *IEEE Transactions on Aerospace and Electronic Systems*, vol. 26, no. 3, pp. 534–542, 1990. DOI: 10.1109/7.106132.

[13] N. Alle, S. S. Hiremath, S. Makaram, K. Subramaniam, and A. Talukdar, "Review on electro hydrostatic actuator for flight control," *International Journal of Fluid Power*, vol. 17, no. 2, pp. 125–145, 2016. DOI: 10.1080/14399776.2016.1169743.

[14] N. Bianchi, S. Bolognani, and B. Ruzojcic, "Design of a 1000 HP permanent magnet synchronous motor for ship propulsion," in *2009 13th European Conference on Power Electronics and Applications*, 2009, pp. 1–8.

[15] B. Ruzojcic, D. Zarko, and D. Ban, "Interior permanent-magnet motor for ship propulsion, design and testing," in *2009 13th European Conference on Power Electronics and Applications*, 2009, pp. 1–10.

[16] M. Guarnieri, M. Morandin, A. Ferrari, P. Campostrini, and S. Bolognani, "Electrifying water buses: A case study on diesel-to-electric conversion in venice," *IEEE Industry Applications Magazine*, vol. 24, no. 1, pp. 71–83, 2018. DOI: 10.1109/MIAS.2017.2739998.

[17] T. Yamakawa, S. Wakao, K. Kondo, and T. Yoneyama, "A new flux weakening operation of interior permanent magnet synchronous motors for railway vehicle traction," in *2005 European Conference on Power Electronics and Applications*, 2005, 6 pp.–P.6. DOI: 10.1109/EPE.2005.219524.

[18] M. Barcaro, E. Fornasiero, N. Bianchi, and S. Bolognani, "Design procedure of IPM motor drive for railway traction," in *2011 IEEE International Electric Machines & Drives Conference (IEMDC)*, 2011, pp. 983–988. DOI: 10.1109/IEMDC.2011.5994950.

[19] S.-W. Lee, I.-J. Yang, and W.-H. Kim, "A study on reducing cogging torque of IPMSM applying rotating tapering," *IEEE Transactions on Magnetics*, vol. 58, no. 8, pp. 1–5, 2022. DOI: 10.1109/TMAG.2022.3179126.

[20] K.-J. Park, D.-S. Jung, H.-S. Chang, J.-N. Bae, and J. Lee, "A study on the reducing of cogging torque of IPMSM," in *2008 International Conference on Electrical Machines and Systems*, 2008, pp. 3137–3141.

[21] H.-S. Lee, M.-H. Hwang, and H.-R. Cha, "Electromagnetic field analysis and design of a hermetic interior permanent magnet synchronous motor with helical-grooved self-cooling case for unmanned aerial vehicles," *Applied Sciences*, vol. 11, no. 11, 2021, ISSN: 2076-3417. DOI: 10.3390/app11114856.

[22] S. Suzuki, T. Katane, H. Saotome, and O. Saito, "Electric power generating system using magnetic coupling, for medical electronic devices implanted deeply," in *2002 IEEE International Magnetics Conference (INTERMAG)*, 2002, FT13–. DOI: 10.1109/INTMAG.2002.1001368.

[23] P. Pillay and R. Krishnan, "Modeling, simulation, and analysis of permanent-magnet motor drives. i. the permanent-magnet synchronous motor drive," *IEEE Transactions on Industry Applications*, vol. 25, no. 2, pp. 265–273, 1989. DOI: 10.1109/28.25541.

[24] R. H. Park, "Two-reaction theory of synchronous machines generalized method of analysis-part i," *Transactions of the American Institute of Electrical Engineers*, vol. 48, no. 3, pp. 716–727, 1929. DOI: 10.1109/T-AIEE.1929.5055275.

[25] A. Hughes and B. Drury, *Electric Motors and Drives*. Elsevier, 2013.

[26] F. Amin, E. Sulaiman, and H. Soomro, "Field oriented control principles for synchronous motor," *International Journal of Mechanical Engineering and Robotics Research*, vol. 8, no. 2, pp. 284–288, 2019.

[27] J. R. J. Hendershot and T. J. E. Miller, *Design of Brushless Permanent-Magnet Machines*. Motor Design Books, 2010.

[28] V. Subrahmanyam, *Electric Drives: Concepts and Applications*. McGraw-Hill Education, 1996.

[29] R. Anguluri, A. Abraham, and V. Snasel, "A hybrid bacterial foraging - PSO algorithm based tuning of optimal FOPI speed controller," *Acta Montanistica Slovaca*, vol. 16, pp. 55–65, Nov. 2011.

[30] P. Vas, *Sensorless Vector and Direct Torque Control*. Oxford University Press, 1998.

[31] N. Mohan, *Advanced Electric Drives*. Wiley & Sons, 2014.

[32] S. Shen and Q.-Z. Chen, *Practical Control of Electric Machines for EV/HEVs: Design, Analysis, and Implementation*. Springer, 2023.

[33] R. Krishnan, *Permanent Magnet Synchronous and Brushless DC Motor Drives*. CRC Press, 2010.

[34] M. Meyer and J. Bocker, "Optimum control for interior permanent magnet synchronous motors (ipmsm) in constant torque and flux weakening range," in *2006 12th International Power Electronics and Motion Control Conference*, 2006, pp. 282–286. DOI: 10.1109/EPEPEMC.2006.4778413.

[35] T. M. Jahns, G. B. Kliman, and T. W. Neumann, "Interior permanent-magnet synchronous motors for adjustable-speed drives," *IEEE Transactions on Industry Applications*, vol. IA-22, no. 4, pp. 738–747, 1986. DOI: 10.1109/TIA.1986.4504786.

[36] T. Miller, "Field-weakening performance of brushless synchronous ac motor drives," English, *IEE Proceedings - Electric Power Applications*, vol. 141, 331–340(9), 6 Nov. 1994, ISSN: 1350-2352. [Online]. Available: https://digital-library.theiet.org/content/journals/10.1049/ip-epa_19941470.

[37] G. Pellegrino, E. Armando, and P. Guglielmi, "Optimal exploitation of the constant power region of ipm drives based on field oriented control," in *2007 IEEE Industry Applications Annual Meeting*, 2007, pp. 1335–1340. DOI: 10.1109/07IAS.2007.207.

[38] J. Pyrhönen, T. Jokinen, and V. Hrabovcová, *Design of Rotating Electrical Machines*. John Wiley & Sons, 2008.

[39] L. Chong, R. Dutta, and F. Rahman, "Design of a highly efficient 1kw concentric wound IPM machine with a very wide constant power speed range," Jun. 2010. DOI: 10.1109/IPEC.2010.5543119.

[40] W. Soong and N. Ertugrul, "Field-weakening performance of interior permanent-magnet motors," *IEEE Transactions on Industry Applications*, vol. 38, no. 5, pp. 1251–1258, 2002. DOI: 10.1109/TIA.2002.803013.

[41] C. Nevoloso, "Enhanced mathematical modelling of interior permanent magnet synchronous machines for loss minimization control," Ph.D. dissertation, Università degli Studi di Palermo, 2020.

[42] S. Morimoto, "Trend of permanent magnet synchronous machines," *IEEJ Transactions on Electrical and Electronic Engineering*, vol. 2, no. 2, pp. 101–108, 2007. DOI: https://doi.org/10.1002/tee.20116.

[43] K. Yamazaki, M. Shina, Y. Kanou, M. Miwa, and J. Hagiwara, "Effect of eddy current loss reduction by segmentation of magnets in synchronous motors: Difference between interior and surface types," *IEEE Transactions on Magnetics*, vol. 45, no. 10, pp. 4756–4759, 2009. DOI: 10.1109/TMAG.2009.2024159.

[44] G. Pellegrino, A. Vagati, P. Guglielmi, and B. Boazzo, "Performance comparison between surface-mounted and interior PM motor drives for electric vehicle application," *IEEE Transactions on Industrial Electronics*, vol. 59, no. 2, pp. 803–811, 2012. DOI: 10.1109/TIE.2011.2151825.

[45] T. Jahns and V. Caliskan, "Uncontrolled generator operation of interior PM synchronous machines following high-speed inverter shutdown," *IEEE Transactions on Industry Applications*, vol. 35, no. 6, pp. 1347–1357, 1999. DOI: 10.1109/28.806049.

[46] C. R. Steen, "Direct axis aiding permanent magnets for a laminated synchronous motor rotor," Patent US 4139790A, Aug. 1977.

[47] T. M. Jahns, "Flux-weakening regime operation of an interior permanent-magnet synchronous motor drive," *IEEE Transactions on Industry Applications*, vol. IA-23, no. 4, pp. 681–689, 1987. DOI: 10.1109/TIA.1987.4504966.

[48] R. Schiferl and T. Lipo, "Power capability of salient pole permanent magnet synchronous motors in variable speed drive applications," *IEEE Transactions on Industry Applications*, vol. 26, no. 1, pp. 115–123, 1990. DOI: 10.1109/28.52682.

[49] Z. Q. Zhu and D. Howe, "Electrical machines and drives for electric, hybrid, and fuel cell vehicles," *Proceedings of the IEEE*, vol. 95, no. 4, pp. 746–765, 2007. DOI: 10.1109/JPROC.2006.892482.

[50] G. Pellegrino, A. Vagati, B. Boazzo, and P. Guglielmi, "Comparison of induction and pm synchronous motor drives for EV application including design examples," *IEEE Transactions on Industry Applications*, vol. 48, no. 6, pp. 2322–2332, 2012. DOI: 10.1109/TIA.2012.2227092.

[51] W. Chlebosz and G. Ombach, "Demagnetization properties of IPM and SPM motors used in the high demanding automotive application," *The international journal for computation and mathematics in electrical and electronic engineering*, vol. 32, pp. 72–85, 1 2012. DOI: 10.1108/03321641311293759.

[52] X. Liu, H. Chen, J. Zhao, and A. Belahcen, "Research on the performances and parameters of interior PMSM used for electric vehicles," *IEEE Transactions on Industrial Electronics*, vol. 63, no. 6, pp. 3533–3545, 2016. DOI: 10.1109/TIE.2016.2524415.

[53] S.-I. Kim, G.-H. Lee, J.-P. Hong, and T.-U. Jung, "Design process of interior PM synchronous motor for 42-V electric air-conditioner system in hybrid electric vehicle," *IEEE Transactions on Magnetics*, vol. 44, no. 6, pp. 1590–1593, 2008. DOI: 10.1109/TMAG.2007.916136.

[54] Q. Chen, G. Liu, W. Zhao, L. Sun, M. Shao, and Z. Liu, "Design and comparison of two fault-tolerant interior-permanent-magnet motors," *IEEE Transactions on Industrial Electronics*, vol. 61, no. 12, pp. 6615–6623, 2014. DOI: 10.1109/TIE.2014.2314070.

[55] Y. Yang *et al.*, "Design and comparison of interior permanent magnet motor topologies for traction applications," *IEEE Transactions on Transportation Electrification*, vol. 3, no. 1, pp. 86–97, 2017. DOI: 10.1109/TTE.2016.2614972.

[56] S. M. Castano, J. W. Jiang, B. Bilgin, A. Sathyan, H. Dadkhah, and A. Emadi, "An investigation of slot-pole combinations for interior permanent magnet synchronous machines with different magnet topologies," in *2017 IEEE International Electric Machines and Drives Conference (IEMDC)*, 2017, pp. 1–8. DOI: 10.1109/IEMDC.2017.8002414.

[57] Z. Zhu and D. Howe, "Influence of design parameters on cogging torque in permanent magnet machines," *IEEE Transactions on Energy Conversion*, vol. 15, no. 4, pp. 407–412, 2000. DOI: 10.1109/60.900501.

[58] C. Hwang, S. John, and S. Wu, "Reduction of cogging torque in spindle motors for CD-ROM drive," *IEEE Transactions on Magnetics*, vol. 34, no. 2, pp. 468–470, 1998. DOI: 10.1109/20.667794.

[59] J. Xintong, X. Jingwei, L. Yong, and L. Yongping, "Theoretical and simulation analysis of influences of stator tooth width on cogging torque of BLDC motors," *IEEE Transactions on Magnetics*, vol. 45, no. 10, pp. 4601–4604, 2009. DOI: 10.1109/TMAG.2009.2022639.

[60] Z. Azar, Z. Q. Zhu, and G. Ombach, "Investigation of torque–speed characteristics and cogging torque of fractional-slot IPM brushless AC machines having alternate slot openings," *IEEE Transactions on Industry Applications*, vol. 48, no. 3, pp. 903–912, 2012. DOI: 10.1109/TIA.2012.2190962.

[61] X. Ge, Z. Q. Zhu, G. Kemp, D. Moule, and C. Williams, "Optimal step-skew methods for cogging torque reduction accounting for three-dimensional effect of interior permanent magnet machines," *IEEE Transactions on Energy Conversion*, vol. 32, no. 1, pp. 222–232, 2017. DOI: 10.1109/TEC.2016.2620476.

[62] W. Q. Chu and Z. Q. Zhu, "Investigation of torque ripples in permanent magnet synchronous machines with skewing," *IEEE Transactions on Magnetics*, vol. 49, no. 3, pp. 1211–1220, 2013. DOI: 10.1109/TMAG.2012.2225069.

[63] W. Fei and Z. Q. Zhu, "Comparison of cogging torque reduction in permanent magnet brushless machines by conventional and herringbone skewing techniques," *IEEE Transactions on Energy Conversion*, vol. 28, no. 3, pp. 664–674, 2013. DOI: 10.1109/TEC.2013.2270871.

[64] Y. Xiao, Z. Zhu, J. Chen, D. Wu, and L. Gong, "A novel V-shape interior permanent magnet synchronous machine with asymmetric spoke-type flux barrier," in *2020 International Conference on Electrical Machines (ICEM)*, vol. 1, 2020, pp. 382–388. DOI: 10.1109/ICEM49940.2020.9270679.

[65] Y. Xiao, Z. Q. Zhu, G. W. Jewell, J. T. Chen, D. Wu, and L. M. Gong, "A novel asymmetric interior permanent magnet synchronous machine," *IEEE Transactions on Industry Applications*, vol. 58, no. 3, pp. 3370–3382, 2022. DOI: 10.1109/TIA.2022.3147150.

[66] H. Zhou and D. Gerling, "Rotor flux-barrier design for improving field-weakening capability of an interior permanent magnet synchronous machine," in *2020 International Conference on Electrical Machines (ICEM)*, vol. 1, 2020, pp. 319–325. DOI: 10.1109/ICEM49940.2020.9270996.

[67] A. Abdelrahman, Y. Wang, D. Al-Ani, and B. Bilgin, "Comparative analysis of two rotor topologies for a high-power density dual three-phase IPM propulsion motor," in *2021 IEEE Transportation Electrification Conference & Expo (ITEC)*, 2021, pp. 1–5. DOI: 10.1109/ITEC51675.2021.9490049.

[68] S. Ruoho, E. Dlala, and A. Arkkio, "Comparison of demagnetization models for finite-element analysis of permanent-magnet synchronous machines," *IEEE Transactions on Magnetics*, vol. 43, no. 11, pp. 3964–3968, 2007. DOI: 10.1109/TMAG.2007.906749.

[69] C.-L. Jeong and J. Hur, "Optimization design of PMSM with hybrid-type permanent magnet considering irreversible demagnetization," *IEEE Transactions on Magnetics*, vol. 53, no. 11, pp. 1–4, 2017. DOI: 10.1109/TMAG.2017.2707102.

[70] G. K. Sakkas and A. G. Kladas, "Design considerations for cost effective radial flux interior permanent magnet motors with increased demagnetization robustness," in *2021 IEEE Workshop on Electrical Machines Design, Control and Diagnosis (WEMDCD)*, 2021, pp. 58–63. DOI: 10.1109/WEMDCD51469.2021.9425629.

[71] M. Kimiabeigi *et al.*, "High-performance low-cost electric motor for electric vehicles using ferrite magnets," *IEEE Transactions on Industrial Electronics*, vol. 63, no. 1, pp. 113–122, 2016. DOI: 10.1109/TIE.2015.2472517.

[72] H. Cai, B. Guan, and L. Xu, "Low-cost ferrite PM-assisted synchronous reluctance machine for electric vehicles," *IEEE Transactions on Industrial Electronics*, vol. 61, no. 10, pp. 5741–5748, 2014. DOI: 10.1109/TIE.2014.2304702.

[73] P. Sekerak, V. Hrabovcova, J. Pyrhonen, L. Kalamen, P. Rafajdus, and M. Onufer, "Comparison of synchronous motors with different permanent magnet and winding types," *IEEE Transactions on Magnetics*, vol. 49, no. 3, pp. 1256–1263, 2013. DOI: 10.1109/TMAG.2012.2230334.

[74] P. C.-K. Luk, H. A. Abdulrahem, and B. Xia, "Low-cost high-performance ferrite permanent magnet machines in EV applications: A comprehensive review," vol. 6, 2020, p. 100 080. DOI: https://doi.org/10.1016/j.etran.2020.100080.

[75] C. Robert D., M. David S., M. E. Plesha, and W. Robert J., *Concepts and applications of finite element analysis*. Wiley, 2001.

[76] *Altair Flux User Guide*. 2023. [Online]. Available: https://2023.help.altair.com/2023/flux/Flux/Help/english/UserGuide/English/topics/FluxSoftware.htm (visited on 2024).

[77] E. Costen. "FEA Mesh Elements & Nodes Guide | Intro to FEA." (2019), [Online]. Available: https://asrengineering.com/2019/09/23/fea-mesh-elements-nodes-guide-intro-to-fea/ (visited on 2024).

[78] G. Meunier, *The Finite Element Method for Electromagnetic Modeling*. Wiley & Sons, 2008.

[79] O. D. Kellogg, *Foundations of potential theory*. Springer, 1929.

[80] A. H.-D. Cheng and D. T. Cheng, "Heritage and early history of the boundary element method," *Engineering Analysis with Boundary Elements*, vol. 29, no. 3, pp. 268–302, 2005, ISSN: 0955-7997. DOI: https://doi.org/10.1016/j.enganabound.2004.12.001. [Online]. Available: https://www.sciencedirect.com/science/article/pii/S0955799705000020.

[81] D. Hanselman, "Minimum torque ripple, maximum efficiency excitation of brushless permanent magnet motors," *IEEE Transactions on Industrial Electronics*, vol. 41, no. 3, pp. 292–300, 1994. DOI: 10.1109/41.293899.

[82] L. Mantione, *Progettazione di motori sincroni a riluttanza mirata al miglioramento del rendimento e del fattore di potenza, Master thesis*, 2020.

[83] M.-H. Hwang, J.-H. Han, D.-H. Kim, and H.-R. Cha, "Design and analysis of rotor shapes for ipm motors in ev power traction platforms," *Energies*, vol. 11, no. 10, 2018, ISSN: 1996-1073. DOI: 10.3390/en11102601. [Online]. Available: https://www.mdpi.com/1996-1073/11/10/2601.

[84] "FluxMotor 2022.1 - User Guide - Materials." (2022), [Online]. Available: https://2022.help.altair.com/2022.1/fluxmotor/pdfUserGuides/Materials_2022.1.pdf (visited on 2024).

[85] "Tata Steel, M250 - 50A Datasheet." (2008), [Online]. Available: https://www.tatasteeleurope.com/sites/default/files/m250-50a.pdf (visited on 2024).

[86] "Altair FluxMotor - Define Iron Losses Parameters." (2023), [Online]. Available: https://help.altair.com/FluxMotor/topics/3500-DefineIronLossparameters.htm?hl=bertotti (visited on 2024).

[87] G. Bertotti, "General properties of power losses in soft ferromagnetic materials," *IEEE Transactions on Magnetics*, vol. 24, no. 1, pp. 621–630, 1988. DOI: 10.1109/20.43994.

[88] D. Brown, B.-M. Ma, and Z. Chen, "Developments in the processing and properties of NdFeB-type permanent magnets," *Journal of Magnetism and Magnetic Materials*, vol. 248, no. 3, pp. 432–440, 2002, ISSN: 0304-8853. DOI: https://doi.org/10.1016/S0304-8853(02)00334-7.

[89] "EclipseMagnetics - Ferrite Magnets/Ceramic Magnets Datasheet." (), [Online]. Available: https://www.eclipsemagnetics.com/site/assets/files/19602/ferrite_ceramic_datasheet.pdf (visited on 2024).

[90] "Advanced Magnets - Bonded NdFeB Magnets' Specifications." (), [Online]. Available: https://www.advancedmagnets.com/wp-content/uploads/2021/09/Bonded-Neodymium-Iron-Boron-NdFeB-Magnets-Specifications.pdf (visited on 2024).

[91] Arnold Magnetic Technologies. "N45SH datasheet." (2017), [Online]. Available: https://www.arnoldmagnetics.com/wp-content/uploads/2017/11/N45SH-151021.pdf (visited on 2024).

[92] L. Mantione, L. Frosini, and M. Minervini, "Evaluation of different magnet materials and skewed geometries for IPMSM at high speed," in *2022 International Conference on Electrical Machines (ICEM)*, 2022, pp. 2297–2303. DOI: 10.1109/ICEM51905.2022.9910949.

[93] L. Mantione, T. Emanuelli, L. Frosini, M. Minervini, and G. Pacinotti, "Geometrie rotoriche per motori sincroni a magneti permanenti ad alta velocità," *AEIT journal (Italian journal)*, 2023.

[94] Tata Steel Europe. "NO20-1350N datasheet." (2020), [Online]. Available: https://www.tatasteeleurope.com/sites/default/files/tata-steel-hi-lite-electrical-steel-no20-1350n-datasheet-en.pdf (visited on 2024).

[95] M. Minervini, "Multi-sensor analysis and machine learning classification approach for diagnostics of electrical machines," Ph.D. dissertation, University of Pavia, 2022. [Online]. Available: https://hdl.handle.net/11571/1464785.

[96] (), [Online]. Available: https://uk.mathworks.com/campaigns/offers/predictive-maintenance-with-matlab.html?s_tid=vid_pers_ofr_recs (visited on 2024).

[97] E. G. Strangas, S. Aviyente, J. D. Neely, and S. S. H. Zaidi, "The effect of failure prognosis and mitigation on the reliability of permanent-magnet ac motor drives," *IEEE Transactions on Industrial Electronics*, vol. 60, no. 8, pp. 3519–3528, 2013. DOI: 10.1109/TIE.2012.2227913.

[98] A. Muetze and E. G. Strangas, "The useful life of inverter-based drive bearings: Methods and research directions from localized maintenace to prognosis," *IEEE Industry Applications Magazine*, vol. 22, no. 4, pp. 63–73, 2016. DOI: 10.1109/MIAS.2015.2459117.

[99] W. R. Jensen, E. G. Strangas, and S. N. Foster, "A method for online stator insulation prognosis for inverter-driven machines," *IEEE Transactions on Industry Applications*, vol. 54, no. 6, pp. 5897–5906, 2018. DOI: 10.1109/TIA.2018.2854408.

[100] L. Frosini, "Novel diagnostic techniques for rotating electrical machines—a review," *Energies*, vol. 13, no. 19, 2020, ISSN: 1996-1073. DOI: 10.3390/en13195066. [Online]. Available: https://www.mdpi.com/1996-1073/13/19/5066.

[101] J. K. Nøland, M. Leandro, J. A. Suul, and M. Molinas, "High-power machines and starter-generator topologies for more electric aircraft: A technology outlook," *IEEE Access*, vol. 8, pp. 130 104–130 123, 2020. DOI: 10.1109/ACCESS.2020.3007791.

[102] S. B. Lee *et al.*, "Condition monitoring of industrial electric machines: State of the art and future challenges," *IEEE Industrial Electronics Magazine*, vol. 14, no. 4, pp. 158–167, 2020. DOI: 10.1109/MIE.2020.3016138.

[103] W. Zhou, T. G. Habetler, and R. G. Harley, "Bearing condition monitoring methods for electric machines: A general review," in *2007 IEEE International Symposium on Diagnostics for Electric Machines, Power Electronics and Drives*, 2007, pp. 3–6. DOI: 10.1109/DEMPED.2007.4393062.

[104] (2024), [Online]. Available: https://sensemore.io/what-is-vibration-analysis/#:~:text=Mechanical%20vibrations%20can%20be%20measured,%E2%89%A4%20f%20%E2%89%A4%201000%20Hz. (visited on 2024).

[105] (2020), [Online]. Available: https://www.ritec-eg.com/Library%20&%20Tools/Vibration-Unit-Converter.html (visited on 2024).

[106] M. Minervini, L. Frosini, L. Hasani, and A. Albini, "A multisensor induction motors diagnostics method for bearing cyclic fault," in *2020 International Conference on Electrical Machines (ICEM)*, vol. 1, 2020, pp. 1259–1265. DOI: 10.1109/ICEM49940.2020.9271000.

[107] S. McInerny and Y. Dai, "Basic vibration signal processing for bearing fault detection," *IEEE Transactions on Education*, vol. 46, no. 1, pp. 149–156, 2003. DOI: 10.1109/TE.2002.808234.

[108] D. Dorrell, W. Thomson, and S. Roach, "Analysis of airgap flux, current, and vibration signals as a function of the combination of static and dynamic airgap eccentricity in 3-phase induction motors," *IEEE Transactions on Industry Applications*, vol. 33, no. 1, pp. 24–34, 1997. DOI: 10.1109/28.567073.

[109] W. Bryan, "Condition monitoring of electrical drives," English, *IEE Proceedings B (Electric Power Applications)*, vol. 133, 142–148(6), 3 1986, ISSN: 0143-7038. [Online]. Available: https://digital-library.theiet.org/content/journals/10.1049/ip-b.1986.0019.

[110] (2004), [Online]. Available: https://www.emerson.com/documents/automation/product-data-sheet-csi-343-flux-coil-csi-technologies-en-38906.pdf (visited on 2024).

[111] V. Kokko, "Condition monitoring of squirrel-cage motors by axial magnetic flux measurements," Ph.D. dissertation, University of Oulu, 2003.

[112] L. Frosini, M. Magnaghi, and A. Albini, "An improved diagnostic system to detect inter-turns short circuits in low voltage stator windings," in *2015 IEEE Workshop on Electrical Machines Design, Control and Diagnosis (WEMDCD)*, 2015, pp. 220–225. DOI: 10.1109/WEMDCD.2015.7194533.

[113] D. Miljković, "Brief review of motor current signature analysis," *HDKBR Info magazin*, vol. 5, no. 1, pp. 14–26, 2015.

[114] P. Pillay and Z. Xu, "Motor current signature analysis," in *IAS '96. Conference Record of the 1996 IEEE Industry Applications Conference Thirty-First IAS Annual Meeting*, vol. 1, 1996, 587–594 vol.1. DOI: 10.1109/IAS.1996.557096.

[115] (), [Online]. Available: https://int.rsdelivers.com/product/lem/dhr-500-c10/lem-dhr-series-current-transformer-500a-input-5001/5278567 (visited on 2024).

[116] (), [Online]. Available: https://uk.rs-online.com/web/content/discovery/ideas-and-advice/shunt-resistors-guide (visited on 2024).

[117] (), [Online]. Available: https://www.mouser.it/new/tdk/tdk-hal188y-hall-effect-sensors/ (visited on 2024).

[118] (), [Online]. Available: http://www.rogowski.cn/Private/ProductFiles/637800018681934264406527974.pdf (visited on 2024).

[119] P. Purkait, B. Biswas, S. Das, and C. Koley, *Electrical and Electronics Measurements and Instrumentation*. McGraw Hill, 2013.

[120] R. Malarić, *Instrumentation and Measurement in Electrical Engineering*. Brown-Walker Press, 2011.

[121] D. G. Pellinen, M. S. Di Capua, S. E. Sampayan, H. Gerbracht, and M. Wang, "Rogowski coil for measuring fast, high-level pulsed currents," *Review of Scientific Instruments*, vol. 51, no. 11, pp. 1535–1540, Nov. 1980, ISSN: 0034-6748. DOI: 10.1063/1.1136119. eprint: https://pubs.aip.org/aip/rsi/article-pdf/51/11/1535/19263007/1535_1_online.pdf. [Online]. Available: https://doi.org/10.1063/1.1136119.

[122] "Pico Technology - TA325 / TA326 AC Current Probes User's Guide." (), [Online]. Available: https://www.picotech.com/download/manuals/ta325-ta326-ac-current-probe-users-guide.pdf (visited on 2024).

[123] W. T. Thomson and R. J. Gilmore, "Motor current signature analysis to detect faults in induction motor drives - fundamentals, data interpretation, and industrial case histories," *Texas A&M University. Turbomachinery Laboratories.*, 2003. DOI: 10.21423/R1CS91.

[124] W. T. Thomson and I. Culbert, *Current Signature Analysis for Condition Monitoring of Cage Induction Motors: Industrial Application and Case Histories*. IEEE press - Wiley, 2016. DOI: 10.1002/9781119175476.

[125] G. B. Kliman and J. Stein, "Methods of motor current signature analysis," *Electric Machines & Power Systems*, vol. 20, no. 5, pp. 463–474, 1992. DOI: 10.1080/07313569208909609.

[126] P. Vas, "Steady state and transient performance of induction motors with rotor asymmetry," *IEEE Transactions on Power Apparatus and Systems*, vol. PAS-101, no. 9, pp. 3246–3251, 1982. DOI: 10.1109/TPAS.1982.317508.

[127] A. Dow, "Vibration and current monitoring for detecting airgap eccentricity in large induction motors," English, *IEE Proceedings B (Electric Power Applications)*, vol. 133, 155–163(8), 3 1986, ISSN: 0143-7038. [Online]. Available: https://digital-library.theiet.org/content/journals/10.1049/ip-b.1986.0022.

[128] F. Filippetti, G. Franceschini, M. Martelli, and C. Tassoni, "An approach to a knowledge representation about induction machine diagnostics in expert systems," in *1988 International Conference on Electrical Machines*, 1988.

[129] M. El Hachemi Benbouzid, "A review of induction motors signature analysis as a medium for faults detection," *IEEE Transactions on Industrial Electronics*, vol. 47, no. 5, pp. 984–993, 2000. DOI: 10.1109/41.873206.

[130] L. Tan and J. Jiang, "Chapter 2 - signal sampling and quantization," in *Digital Signal Processing (Third Edition)*, L. Tan and J. Jiang, Eds., Third Edition, Academic Press, 2019, pp. 13–58, ISBN: 978-0-12-815071-9. DOI: https://doi.org/10.1016/B978-0-12-815071-9.00002-6. [Online]. Available: https://www.sciencedirect.com/science/article/pii/B9780128150719000026.

[131] D. Morinigo-Sotelo, V. Fernandez-Cavero, and T. García-Calva, *Seminar: Signal processing and condition monitoring of electrical machines, University of Pavia*, 2024.

[132] K. Yatsugi, S. E. Pandarakone, Y. Mizuno, and H. Nakamura, "Common diagnosis approach to three-class induction motor faults using stator current feature and support vector machine," *IEEE Access*, vol. 11, pp. 24 945–24 952, 2023. DOI: 10.1109/ACCESS.2023.3254914.

[133] G. Kliman, R. Koegl, J. Stein, R. Endicott, and M. Madden, "Noninvasive detection of broken rotor bars in operating induction motors," *IEEE Transactions on Energy Conversion*, vol. 3, no. 4, pp. 873–879, 1988. DOI: 10.1109/60.9364.

[134] A. Fernaindez, I. Bediaga, A. Gaston, and J. Hemaindez, "Evaluation study on detection techniques for bearing incipient faults," in *EUROCON 2005 - The International Conference on "Computer as a Tool"*, vol. 2, 2005, pp. 1566–1569. DOI: 10.1109/EURCON.2005.1630266.

[135] W. Thomson, D. Rankin, and D. Dorrell, "On-line current monitoring to diagnose airgap eccentricity in large three-phase induction motors-industrial case histories verify the predictions," *IEEE Transactions on Energy Conversion*, vol. 14, no. 4, pp. 1372–1378, 1999. DOI: 10.1109/60.815075.

[136] L. Frosini, S. Zanazzo, and A. Albini, "A wavelet-based technique to detect stator faults in inverter-fed induction motors," in *2016 XXII International Conference on Electrical Machines (ICEM)*, 2016, pp. 2917–2923. DOI: 10.1109/ICELMACH.2016.7732938.

[137] "Report of large motor reliability survey of industrial and commercial installations, Part I," *IEEE Transactions on Industry Applications*, vol. IA-21, no. 4, pp. 853–864, 1985. DOI: 10.1109/TIA.1985.349532.

[138] R. Schoen, T. Habetler, F. Kamran, and R. Bartfield, "Motor bearing damage detection using stator current monitoring," *IEEE Transactions on Industry Applications*, vol. 31, no. 6, pp. 1274–1279, 1995. DOI: 10.1109/28.475697.

[139] M. Blodt, P. Granjon, B. Raison, and G. Rostaing, "Models for bearing damage detection in induction motors using stator current monitoring," *IEEE Transactions on Industrial Electronics*, vol. 55, no. 4, pp. 1813–1822, 2008. DOI: 10.1109/TIE.2008.917108.

[140] P. H. Trickey, "Die cast rotor testing by test stator method," *Electrical Engineering*, vol. 65, pp. 483–484, 1946. [Online]. Available: https://api.semanticscholar.org/CorpusID:51672499.

[141] A. Bellini, F. Filippetti, C. Tassoni, and G.-A. Capolino, "Advances in diagnostic techniques for induction machines," *IEEE Transactions on Industrial Electronics*, vol. 55, no. 12, pp. 4109–4126, 2008. DOI: 10.1109/TIE.2008.2007527.

[142] V. Ghorbanian, G. Joksimović, and J. Faiz, *Fault Diagnosis of Induction Motors*. Institution of Engineering & Technology, 2017.

[143] H. A. Toliyat, S. Nandi, S. Choi, and H. Meshgin-Kelk, *Electric machines: modeling, condition monitoring, and fault diagnosis*. CRC press, 2002.

[144] P. Panagiotou, "Reliable detection of rotor electrical faults in induction motors using frequency extraction of stator current and stray magnetic flux signals," Ph.D. dissertation, Coventry University, 2020.

[145] J. Bonet-Jara, D. Morinigo-Sotelo, O. Duque-Perez, L. Serrano-Iribarnegaray, and J. Pons-Llinares, "End-ring wear in deep-well submersible motor pumps," *IEEE Transactions on Industry Applications*, vol. 58, no. 4, pp. 4522–4531, 2022. DOI: 10.1109/TIA.2022.3166876.

[146] S. B. Lee *et al.*, "Identification of false rotor fault indications produced by online mcsa for medium-voltage induction machines," *IEEE Transactions on Industry Applications*, vol. 52, no. 1, pp. 729–739, 2016. DOI: 10.1109/TIA.2015.2464301.

[147] I. Lomax, "Assessment of induction motor cage fatigue life," in *1991 Fifth International Conference on Electrical Machines and Drives (Conf. Publ. No. 341)*, 1991, pp. 281–284.

[148] F. Filippetti, G. Franceschini, C. Tassoni, and P. Vas, "Ai techniques in induction machines diagnosis including the speed ripple effect," *IEEE Transactions on Industry Applications*, vol. 34, no. 1, pp. 98–108, 1998. DOI: 10.1109/28.658729.

[149] M. Riera-Guasp, J. A. Antonino-Daviu, and G.-A. Capolino, "Advances in electrical machine, power electronic, and drive condition monitoring and fault detection: State of the art," *IEEE Transactions on Industrial Electronics*, vol. 62, no. 3, pp. 1746–1759, 2015. DOI: 10.1109/TIE.2014.2375853.

[150] W. Deleroi, "Squirrel cage motor with broken bar in the rotor – physical phenomena and their experimental assessment," in *V International Conference on Electrical Machines (ICEM)*, 1982, pp. 767–770.

[151] S. Nandi, S. Ahmed, and H. Toliyat, "Detection of rotor slot and other eccentricity related harmonics in a three phase induction motor with different rotor cages," *IEEE Transactions on Energy Conversion*, vol. 16, no. 3, pp. 253–260, 2001. DOI: 10.1109/60.937205.

[152] F. Filippetti, M. Martelli, G. Franceschini, and C. Tassoni, "Development of expert system knowledge base to on-line diagnosis of rotor electrical faults of induction motors," in *Conference Record of the 1992 IEEE Industry Applications Society Annual Meeting*, 1992, 92–99 vol.1. DOI: 10.1109/IAS.1992.244459.

[153] F. Filipetti, G. Franceschini, C. Tassoni, and P. Vas, "Impact of speed ripple on rotor fault diagnosis of induction machine," in *International Conference on Electrical Machines*, vol. 2, 1996, pp. 452–457.

[154] G. Y. Sizov, A. Sayed-Ahmed, C.-C. Yeh, and N. A. O. Demerdash, "Analysis and diagnostics of adjacent and nonadjacent broken-rotor-bar faults in squirrel-cage induction machines," *IEEE Transactions on Industrial Electronics*, vol. 56, no. 11, pp. 4627–4641, 2009. DOI: 10.1109/TIE.2008.2011341.

[155] A. Ceban, R. Pusca, and R. Romary, "Study of rotor faults in induction motors using external magnetic field analysis," *IEEE Transactions on Industrial Electronics*, vol. 59, no. 5, pp. 2082–2093, 2012. DOI: 10.1109/TIE.2011.2163285.

[156] A. Bellini, C. Concari, G. Franceschini, C. Tassoni, and A. Toscani, "Vibrations, currents and stray flux signals to asses induction motors rotor conditions," in *IECON 2006 - 32nd Annual Conference on IEEE Industrial Electronics*, 2006, pp. 4963–4968. DOI: 10.1109/IECON.2006.347365.

[157] N. Halem, S. Zouzou, K. Srairi, and K. Gyftakis, "Fem analysis for comparative investigation of the stator circuit connexion impact on the induction motor broken bar fault higher order signatures," English, *International Journal on Electrical Engineering and Informatics*, vol. 8, no. 4, pp. 739–752, 2016, The full text is available from: http://dx.doi.org/10.15676/ijeei.2016.8.4.3, ISSN: 2085-6830. DOI: 10.15676/ijeei.2016.8.4.3.

[158] K. N. Gyftakis, J. A. Antonino-Daviu, R. Garcia-Hernandez, M. D. McCulloch, D. A. Howey, and A. J. Marques Cardoso, "Comparative experimental investigation of broken bar fault detectability in induction motors," *IEEE Transactions on Industry Applications*, vol. 52, no. 2, pp. 1452–1459, 2016. DOI: 10.1109/TIA.2015.2505663.

[159] D. Morinigo-Sotelo, R. de J. Romero-Troncoso, P. A. Panagiotou, J. A. Antonino-Daviu, and K. N. Gyftakis, "Reliable detection of rotor bars breakage in induction motors via music and zsc," *IEEE Transactions on Industry Applications*, vol. 54, no. 2, pp. 1224–1234, 2018. DOI: 10.1109/TIA.2017.2764846.

[160] A. Duda and P. Drozdowski, "Induction motor fault diagnosis based on zero-sequence current analysis," *Energies*, vol. 13, no. 24, 2020, ISSN: 1996-1073. DOI: 10.3390/en13246528. [Online]. Available: https://www.mdpi.com/1996-1073/13/24/6528.

[161] R. P. Policarpo de Souza, D. Morinigo-Sotelo, V. Fernandez-Cavero, Ó. Duque-Perez, C. M. Agulhari, and A. Goedtel, "Broken rotor bar fault detection using odd triple harmonics in delta-connected induction motors," in *2023 IEEE 14th International Symposium on Diagnostics for Electrical Machines, Power Electronics and Drives (SDEMPED)*, 2023, pp. 49–55. DOI: 10.1109/SDEMPED54949.2023.10271506.

[162] J. Antonino-Daviu, M. Riera-Guasp, M. Pineda-Sánchez, J. Pons-Llinares, R. Puche-Panadero, and J. Pérez-Cruz, "Feature extraction for the prognosis of electromechanical faults in electrical machines through the dwt," *International Journal of Computational Intelligence Systems*, vol. 2, no. 2, pp. 158–167, 2009. DOI: 10.1080/18756891.2009.9727651.

[163] J. Pons-Llinares, D. Morinigo-Sotelo, O. Duque-Perez, J. Antonino-Daviu, and M. Perez-Alonso, "Transient detection of close components through the chirplet transform: Rotor faults in inverter-fed induction motors," in *IECON 2014 - 40th Annual Conference of the IEEE Industrial Electronics Society*, 2014, pp. 3386–3392. DOI: 10.1109/IECON.2014.7048999.

[164] J. Pons-Llinares, J. Antonino-Daviu, J. Roger-Folch, D. Moríñigo-Sotelo, and O. Duque-Pérez, "Mixed eccentricity diagnosis in inverter-fed induction motors via the adaptive slope transform of transient stator currents," *Mechanical Systems and Signal Processing*, vol. 48, no. 1, pp. 423–435, 2014, ISSN: 0888-3270. DOI: https://doi.org/10.1016/j.ymssp.2014.02.012. [Online]. Available: https://www.sciencedirect.com/science/article/pii/S0888327014000703.

[165] V. Fernandez-Cavero, "Técnicas de detección y diagnóstico de fallos en motores de inducción alimentados por inversor en estado transitorio," Ph.D. dissertation, University of Valladolid, 2018.

[166] Panagiotou PA and Arvanitakis I and Lophitis N and Antonino-Daviu JA and Gyftakis KN, "On the broken rotor bar diagnosis using time–frequency analysis: 'Is one spectral representation enough for the characterisation of monitored signals?'" *IET Electric Power Applications*, vol. 13, 932–942, 7 2019, Accessed on 2024/04/02. DOI: {10.1049/iet-epa.2018.5512}. [Online]. Available: %7Bhttp://dx.doi.org/10.1049/iet-epa.2018.5512%20%7D.

[167] P. A. Panagiotou, J. C. Mayo-Maldonado, I. Arvanitakis, G. Escobar, J. A. Antonino-Daviu, and K. N. Gyftakis, "A novel method for rotor fault diagnostics in induction motors using harmonic isolation," in *2023 IEEE 14th International Symposium on Diagnostics for Electrical Machines, Power Electronics and Drives (SDEMPED)*, 2023, pp. 265–271. DOI: 10.1109/SDEMPED54949.2023.10271499.

[168] J. Pons-Llinares, J. A. Antonino-Daviu, M. Riera-Guasp, S. Bin Lee, T.-j. Kang, and C. Yang, "Advanced induction motor rotor fault diagnosis via continuous and discrete time–frequency tools," *IEEE Transactions on Industrial Electronics*, vol. 62, no. 3, pp. 1791–1802, 2015. DOI: 10.1109/TIE.2014.2355816.

[169] V. Fernandez-Cavero, J. Pons-Llinares, O. Duque-Perez, and D. Morinigo-Sotelo, "Detection of broken rotor bars in nonlinear startups of inverter-fed induction motors," *IEEE Transactions on Industry Applications*, vol. 57, no. 3, pp. 2559–2568, 2021. DOI: 10.1109/TIA.2021.3066317.

[170] F. Filippetti, A. Bellini, and G.-A. Capolino, "Condition monitoring and diagnosis of rotor faults in induction machines: State of art and future perspectives," in *2013 IEEE Workshop on Electrical Machines Design, Control and Diagnosis (WEMDCD)*, 2013, pp. 196–209. DOI: 10.1109/WEMDCD.2013.6525180.

[171] A. Bellini, F. Filippetti, G. Franceschini, and C. Tassoni, "Closed-loop control impact on the diagnosis of induction motors faults," *IEEE Transactions on Industry Applications*, vol. 36, no. 5, pp. 1318–1329, 2000. DOI: 10.1109/28.871280.

[172] C. Kral, R. Wieser, F. Pirker, and M. Schagginger, "Sequences of field-oriented control for the detection of faulty rotor bars in induction machines-the vienna monitoring method," *IEEE Transactions on Industrial Electronics*, vol. 47, no. 5, pp. 1042–1050, 2000. DOI: 10.1109/41.873212.

[173] C. Kral, F. Pirker, and G. Pascoli, "Model-based detection of rotor faults without rotor position sensor-the sensorless vienna monitoring method," *IEEE Transactions on Industry Applications*, vol. 41, no. 3, pp. 784–789, 2005. DOI: 10.1109/TIA.2005.847316.

[174] S. M. A. Cruz and A. J. M. Cardoso, "Diagnosis of rotor faults in direct and indirect foc induction motor drives," in *2007 European Conference on Power Electronics and Applications*, 2007, pp. 1–10. DOI: 10.1109/EPE.2007.4417710.

[175] S. M. A. Cruz, A. Stefani, F. Filippetti, and A. J. M. Cardoso, "A new model-based technique for the diagnosis of rotor faults in rfoc induction motor drives," *IEEE Transactions on Industrial Electronics*, vol. 55, no. 12, pp. 4218–4228, 2008. DOI: 10.1109/TIE.2008.2003365.

[176] Y. Gritli, A. O. Di Tommaso, R. Miceli, F. Filippetti, and C. Rossi, "Closed-loop bandwidth impact on mvsa for rotor broken bar diagnosis in irfoc double squirrel cage induction motor drives," in *2013 International Conference on Clean Electrical Power (ICCEP)*, 2013, pp. 529–534. DOI: 10.1109/ICCEP.2013.6586904.

[177] S. S. Refaat, H. Abu-Rub, M. S. Saad, and A. Iqbal, "Open and closed-loop motor control system with incipient broken rotor bar fault detection using current signature," in *IECON 2014 - 40th Annual Conference of the IEEE Industrial Electronics Society*, 2014, pp. 774–780. DOI: 10.1109/IECON.2014.7048588.

[178] Z. Hou, J. Huang, H. Liu, T. Wang, and L. Zhao, "Quantitative broken rotor bar fault detection for closed-loop controlled induction motors," *IET Electric Power Applications*, vol. 10, no. 5, pp. 403–410, 2016. DOI: https://doi.org/10.1049/iet-epa.2015.0440. eprint: https://ietresearch.onlinelibrary.wiley.com/doi/pdf/10.1049/iet-epa.2015.0440. [Online]. Available: https://ietresearch.onlinelibrary.wiley.com/doi/abs/10.1049/iet-epa.2015.0440.

[179] Z. Hou, J. Huang, H. Liu, M. Ye, Z. Liu, and J. Yang, "Diagnosis of broken rotor bar fault in open- and closed-loop controlled wye-connected induction motors using zero-sequence voltage," *IET Electric Power Applications*, vol. 11, no. 7, pp. 1214–1223, 2017. DOI: https://doi.org/10.1049/iet-epa.2016.0505. eprint: https://ietresearch.onlinelibrary.wiley.com/doi/pdf/10.1049/iet-epa.2016.0505. [Online]. Available: https://ietresearch.onlinelibrary.wiley.com/doi/abs/10.1049/iet-epa.2016.0505.

[180] B. Yazici and G. Kliman, "An adaptive statistical time-frequency method for detection of broken bars and bearing faults in motors using stator current," *IEEE Transactions on Industry Applications*, vol. 35, no. 2, pp. 442–452, 1999. DOI: 10.1109/28.753640.

[181] V. Fernandez-Cavero, J. Pons-Llinares, O. Duque-Perez, and D. Morinigo-Sotelo, "Detection and quantification of bar breakage harmonics evolutions in inverter-fed motors through the dragon transform," *ISA Transactions*, vol. 109, pp. 352–367, 2021, ISSN: 0019-0578. DOI: https://doi.org/10.1016/j.isatra.2020.10.020. [Online]. Available: https://www.sciencedirect.com/science/article/pii/S0019057820304158.

[182] T. A. Garcia-Calva, D. Morinigo-Sotelo, O. Duque-Perez, A. Garcia-Perez, and R. d. J. Romero-Troncoso, "Time-frequency analysis based on minimum-norm spectral estimation to detect induction motor faults," *Energies*, vol. 13, no. 16, 2020, ISSN: 1996-1073. DOI: 10.3390/en13164102. [Online]. Available: https://www.mdpi.com/1996-1073/13/16/4102.

[183] F. Castanié, *Spectral analysis: parametric and non-parametric digital methods*. ISTE Ltd, 2003.

[184] C. Moler and S. Eddins. "Faster finite fourier transforms (matlab - mathworks)." (2001), [Online]. Available: https://it.mathworks.com/company/technical-articles/faster-finite-fourier-transforms-matlab.html (visited on 2024).

[185] R. de Jesus Romero-Troncoso, "Multirate signal processing to improve fft-based analysis for detecting faults in induction motors," *IEEE Transactions on Industrial Informatics*, vol. 13, no. 3, pp. 1291–1300, 2017. DOI: 10.1109/TII.2016.2603968.

[186] T. MVSR, A. Kumar, and C. Sai Prasanth, "Comparative analysis of windowing techniques in minimizing side lobes in an antenna array," in *2014 International Conference on Communication and Signal Processing*, 2014, pp. 1380–1383. DOI: 10.1109/ICCSP.2014.6950075.

[187] Sulistyaningsih *et al.*, "Performance comparison of blackman, bartlett, hanning, and kaiser window for radar digital signal processing," in *2019 4th International Conference on Information Technology, Information Systems and Electrical Engineering (ICITISEE)*, 2019, pp. 391–394. DOI: 10.1109/ICITISEE48480.2019.9003791.

[188] S. R. Chintakindi, O. Varaprasad, and D. Siva Sarma, "Improved hanning window based interpolated fft for power harmonic analysis," in *TENCON 2015 - 2015 IEEE Region 10 Conference*, 2015, pp. 1–5. DOI: 10.1109/TENCON.2015.7373150.

[189] A. Arranz-Gimon, A. Zorita-Lamadrid, D. Morinigo-Sotelo, and O. Duque-Perez, "Analysis of the use of the hanning window for the measurement of interharmonic distortion caused by close tones in iec standard framework.," *Electric Power Systems Research*, vol. 206, p. 107 833, 2022, ISSN: 0378-7796. DOI: https://doi.org/10.1016/j.epsr.2022.107833. [Online]. Available: https://www.sciencedirect.com/science/article/pii/S0378779622000633.

[190] R. J. Marks, *Handbook of Fourier Analysis & Its Applications*. Oxford University Press, 2009.

[191] L. Cohen, *Time Frequency Analysis: Theory and Applications*. Prentice Hall, 1994.

[192] P. Flandrin, *Time-Frequency/Time-Scale Analysis*. Academic Press, 1999.

[193] B. Boashash, *Time-Frequency Signal Analysis and Processing: A Comprehensive Reference*. Protoavis Productions, 2003.

[194] V. Fernandez-Cavero, D. Morinigo-Sotelo, O. Duque-Perez, and J. Pons-Llinares, "A comparison of techniques for fault detection in inverter-fed induction motors in transient regime," *IEEE Access*, vol. 5, pp. 8048–8063, 2017. DOI: 10.1109/ACCESS.2017.2702643.

[195] J. Pons-Llinares, M. Riera-Guasp, J. A. Antonino-Daviu, and T. G. Habetler, "Pursuing optimal electric machines transient diagnosis: The adaptive slope transform," *Mechanical Systems and Signal Processing*, vol. 80, pp. 553–569, 2016, ISSN: 0888-3270. DOI: https://doi.org/10.1016/j.ymssp.2016.05.003. [Online]. Available: https://www.sciencedirect.com/science/article/pii/S0888327016300863.

[196] S. Reddi, "Multiple source location-a digital approach," *IEEE Transactions on Aerospace and Electronic Systems*, vol. AES-15, no. 1, pp. 95–105, 1979. DOI: 10.1109/TAES.1979.308800.

[197] Z. Yang, L. Xie, and P. Stoica, "Vandermonde decomposition of multilevel toeplitz matrices with application to multidimensional super-resolution," *IEEE Transactions on Information Theory*, vol. 62, no. 6, pp. 3685–3701, 2016. DOI: 10.1109/TIT.2016.2553041.

[198] H. L. Van Trees, "Parameter estimation ii," in *Optimum Array Processing*. John Wiley & Sons, Ltd, 2002, ch. 9, pp. 1139–1317, ISBN: 9780471221104. DOI: https://doi.org/10.1002/0471221104.ch9. eprint: https://onlinelibrary.wiley.com/doi/pdf/10.1002/0471221104.ch9. [Online]. Available: https://onlinelibrary.wiley.com/doi/abs/10.1002/0471221104.ch9.

[199] T. A. Garcia-Calva, K. N. Gyftakis, G. A. Skarmoutsos, M. Mueller, D. Morinigo-Sotelo, and R. d. J. Romero-Troncoso, "Advanced signal processing techniques for demagnetization detection in pm generators at variable speed," *IEEE Transactions on Industry Applications*, vol. 60, no. 1, pp. 174–183, 2024. DOI: 10.1109/TIA.2023.3312362.

[200] G. De Boni, V. Fernandez-Cavero, L. Frosini, O. Duque-Perez, and D. Morinigo-Sotelo, "Fault harmonics current detection in closed-loop controlled induction motors," in *2023 IEEE 14th International Symposium on Diagnostics for Electrical Machines, Power Electronics and Drives (SDEMPED)*, 2023, pp. 443–449. DOI: 10.1109/SDEMPED54949.2023.10271455.

[201] J. Santisteban and R. Stephan, "Vector control methods for induction machines: An overview," *IEEE Transactions on Education*, vol. 44, no. 2, pp. 170–175, 2001. DOI: 10.1109/13.925828.

[202] D. E. Rivera, M. Morari, and S. Skogestad, "Internal model control: PID controller design," *Industrial & Engineering Chemistry Process Design and Development*, vol. 25, pp. 252–265, 1986.

[203] T. A. Garcia-Calva, D. Morinigo-Sotelo, and R. de Jesus Romero-Troncoso, "Non-uniform time resampling for diagnosing broken rotor bars in inverter-fed induction motors," *IEEE Transactions on Industrial Electronics*, vol. 64, no. 3, pp. 2306–2315, 2017. DOI: 10.1109/TIE.2016.2619318.

[204] L. Mantione, V. Fernandez-Cavero, D. Morinigo-Sotelo, and L. Frosini, "A time-frequency analysis for broken rotor bar detection in closed loop inverter fed induction motor at imposed speed," in *2023 IEEE 14th International Symposium on Diagnostics for Electrical Machines, Power Electronics and Drives (SDEMPED)*, 2023, pp. 450–456. DOI: 10.1109/SDEMPED54949.2023.10271474.